MODELLING AND MEASUREMENT OF UNCONFINED BUBBLY TWO-PHASE PLUME FLOW

By

YUANYI SHENG

A Thesis

Submitted to the School of Graduate Studies

in Partial Fulfilment of the Requirements

for the Degree

Doctor of Philosophy

McMaster University

September 25, 1992

To my dear grandmother

MODELLING AND MEASUREMENT OF UNCONFINED BUBBLY TWO PHASE PLUME FLOW

DOCTOR OF PHILOSOPHY (1992) McMASTER UNIVERSITY
(Materials Sci. & Eng.) Hamlton, Ontario

TITLE: Modelling and Measurement of Unconfined Bubbly Two-Phase Plume Flow

AUTHOR: Yuanyi Sheng,

B.Eng. (Beijing University of Iron and Steel Technology, CHINA)
M.Eng. (Beijing University of Iron and Steel Technology, CHINA)

SUPERVISOR: Professor G.A. Irons

NUMBER OF PAGES: xxiv, 279

ABSTRACT

Bubbly plume flow, which is encountered in many refining processes of the iron and steel making industry, has been studied with a water model ladle and simulated with a novel mathematical model. The main achievements of this project can be summarized as followings:

(1) A new experimental technique based on the Laser Doppler Anemometry and Electrical Probe has been developed to measure various flow parameters of the plume, such as: mean and turbulent liquid velocities, bubble velocities and distributions of void fraction and bubble frequency.

(2) The turbulence feature and bubble behaviour in the gas/liquid two-phase zone has been experimentally studied with the newly developed LDA/EP technique in a water model ladle. It has been found that turbulence in the plume zone is close to an isotropic one and the relative velocity of bubbles is not affected by the void fraction in the plume.

(3) A mathematical model based on the modified k-ϵ turbulence model has been developed to simulate the plume flow. The coefficients of the extra source terms of the modified k-ϵ model have been determined experimentally. The mathematical model yielded good predictions of both the mean and the turbulent liquid velocities. The behaviour of bubbles in the plume has also been dealt with to produce good predictions of the void fraction distributions.

ACKNOWLEDGEMENTS

The author wishes to take this opportunity to express his sincere gratitude to Professor G.A. Irons for his excellent guidance and encouragement in the past five years which led to the successful completion of this project. The author also wish to thank all those who have assisted him in the course of the work. In particular, the following people have made invaluable contributions in making this thesis a reality:

- Professor W.K. Lu who constantly offered critical comments, suggestions and guidance;

- Professor P.E. Wood who generously supplied the LDA equipment and his laboratory facilities as well as suggestions for the mathematical model;

- Professor M. Shoukri who served on the supervisory committee and offered many inspiring comments and suggestions;

- Professor Ö.F. Turan who also served on the supervisory committee and offered important comments and suggestions in the field of turbulence modelling.

Financial support of this project by the Canadian International Development Agency and the Natural Sciences and Engineering Council is gratefully acknowledged.

TABLE OF CONTENTS

LIST OF ILLUSTRATIONS

LIST OF TABLES

LIST OF SYMBOLS

a_{np}	Coefficients defined by Eq.(II.23) for neibouring grid points
A	Area
C_L	Lateral lift coefficient
$C_\mu, C_1, C_2, \sigma_k, \sigma_\varepsilon$	Constants used in k-ε model and defined in Table II.2
$C_{k1}, C_{k2}, C_{\varepsilon 1}, C_{\varepsilon 2}$	Extra source coefficients in modified k-ε model
d_o	Nozzle diameter
d_f	Fringe spacing in LDA measuring volume
D	Diameter of the model
D	Diffusive flux Coefficient or diffusivity
D_k	Diffusion term of k in k-ε model
D_B	Diameter of a bubble
E	Shape ratio of a bubble
f	Frequency
F	Convective flux coefficient
F_{Br}	Force on bubble in radial direction
g	Gravitation
h	Heat Transfer coefficient
h_m	Height of the LDA measuring volume
i.j.k	Unit vectors
k	Turbulent kinetic energy

k_m	Mass transfer coefficient
k_t	Thermal conductivity
l_b	Separation between two laser beams
l_f	Focal length of laser beam
l_m	Length of the LDA measuring volume
L	Length scale
M	Mass
M_{ik}	Drag force on k phase from i phase
Mo	$=g\mu^4\Delta\rho/\rho^2\sigma^3$, Morton Number
N	Numbers
N_D	Dispersion number defined by Eq.(II.33)
N_f	Number of the fringes in the LDA measuring volume
Nu	$=hD/k_t$, Nusselt Number
p	Pressure
p'	fluctuating component of pressure
P_k	Production of k
Pr	$=\mu c_p/k_t$, Prandtl Number
Q_g	Gas flowrate
Re	$=UL\rho/\mu$, Reynolds number
Sc	$=\mu/\rho D$, Schmidt Number
Sh	$=k_mD/D$, Sherwood Number
S_{ij}	Shear stresses
s_{ij}	Turbulent shear stresses
S^ϕ	Source term for variable ϕ
t	Time
T	Temperature

$\mathbf{U}$	Liquid velocity vector
U,V,W	Liquid velocity components
V_i	Same as U
V_j	Same as V
V_k	Same as W
$\mathbf{U_B}$	Bubble velocity Vector
U_B, V_B, W_B	Bubble velocity components
$\mathbf{U_r}$	Slip velocity vector
U_r, V_r, W_r	Slip velocity components
$\mathbf{u}$	Instantaneous liquid velocity vector
u,v,w	Components of $\mathbf{u}$
u',v',w'	R.M.S. components of $\mathbf{u}$
V	Volume
W	Power
x,r,θ	Scalar coordinates

Greek

α	Void fraction of bubble
Γ_ϕ,	Diffusivity of ϕ
γ_k	Eddy difusivity
δ_{ij}	Kronecker delta, $\delta_{ij}=1$, when $i=j$; $\delta_{ij}=0$, when $i\neq j$
ϵ	Dissipation of the turbulent kinetic energy
θ	Angle
λ	Wavelength of the laser beam

μ	Viscosity
μ_{eff}	Turbulent effective viscosity
ν	$=\mu/\rho$
ν_T	Turbulent kinemetic viscosity
ρ	Density
σ	Turbulent Prandtl number
ϕ	Variable used in various transport equations

Subscription

B	Bubble
e, w, n, s	East, west, north, south
g	Gas phase
l	Liquid
m	Mixtture
nb	Neighbouring
p	Particle
r	In the r-direction or relative values
s	Slip
T	Turbulent properties or terminal values
x	In the x-direction
∞	Single bubble values

Abbreviations

EP	Electric Probe
FG	Fritted Glass
LDA	Laser Doppler Anemometer
LHS	Left Hand Side
MV	Measuring Volume of LDA
PD	Photo Diodes
PMT	Photo Multiplier Tube
RHS	Right Hand Side

CHAPTER I
INTRODUCTION

Bubbly plumes are widely encountered in ferrous metallurgical processes. When gas is injected into the molten metal, a two-phase flow zone consisted of rising bubbles and entrained liquid metal is formed in the bath. The two-phase zone assumes a shape of a reversed cone and is named bubbly plume. Bubbly plumes are also important refining tools in the non-ferrous industry, such as the side blowing of air in copper and nickel converting processes. The physics of the multiphase bubbly flows has great significance in fields other than metallurgy, e.g. bubble driven flows play very important roles in many chemical engineering processes and power generation processes. In all of the above mentioned processes, a good understanding of the behaviour of bubbles in the plume, the interaction between bubbles and liquid as well as the liquid flow caused by the plume is vital for better design of the reactors and better control of the processes. As a result, a great deal of effort has been made to study the phenomenon which contributed greatly to our present understanding of it. However, more knowledge is needed for the purpose of modelling the process, which include the fundamental determination of the gas void fraction distribution inside the plume, the modelling of turbulent flow field inside the two-phase area and various transport rate phenomena inside the plume.

1.1 Importance of Gas Stirring in Iron and Steelmaking

During the last two decades, there has been a greater demand on steel makers to produce higher quality steels with fewer inclusions, and lower contents of sulphur, phosphorous and other impurities. There has been also a trend in the steelmaking industry to intensify the steelmaking processes for the purpose of attaining higher productivity. In addition, the ever increasing use of continuous casting technology has required closer control of the temperature and composition of the liquid steel. To meet the demands of these developments, various new steelmaking processes such as the bottom and top oxygen blown steelmaking converter and different types of ladle metallurgy techniques were developed in the last two decades. Many of these new techniques involve the use of gas injection into liquid metals, for the purposes of stirring the melt and intensifying mass and heat transfer during refining. The important roles played by gas injection in the development of the new iron and steel making technologies are discussed in the following sections.

The top and bottom blowing oxygen converter is one of the best examples of the newly developed steelmaking techniques. The principal structure of such a converter is illustrated in Figure I.1. The addition of the bottom blowing of various reacting and/or non-reacting gases, such as oxygen and argon, to the top oxygen blowing converter made the steelmaking process more efficient, more flexible and capable of producing more types of alloyed steels with better quality (Schlebusch and Hauck, 1989). A good example is the K-OBM process (Figure I.2) implemented at Dofasco Inc. (Wright, 1991). The heat size of the furnace is 300 tonnes and 30% of the total oxygen used is supplied through eight annular tuyeres in the furnace bottom. Either argon or nitrogen is blown from the furnace bottom. This bottom blowing makes it possible

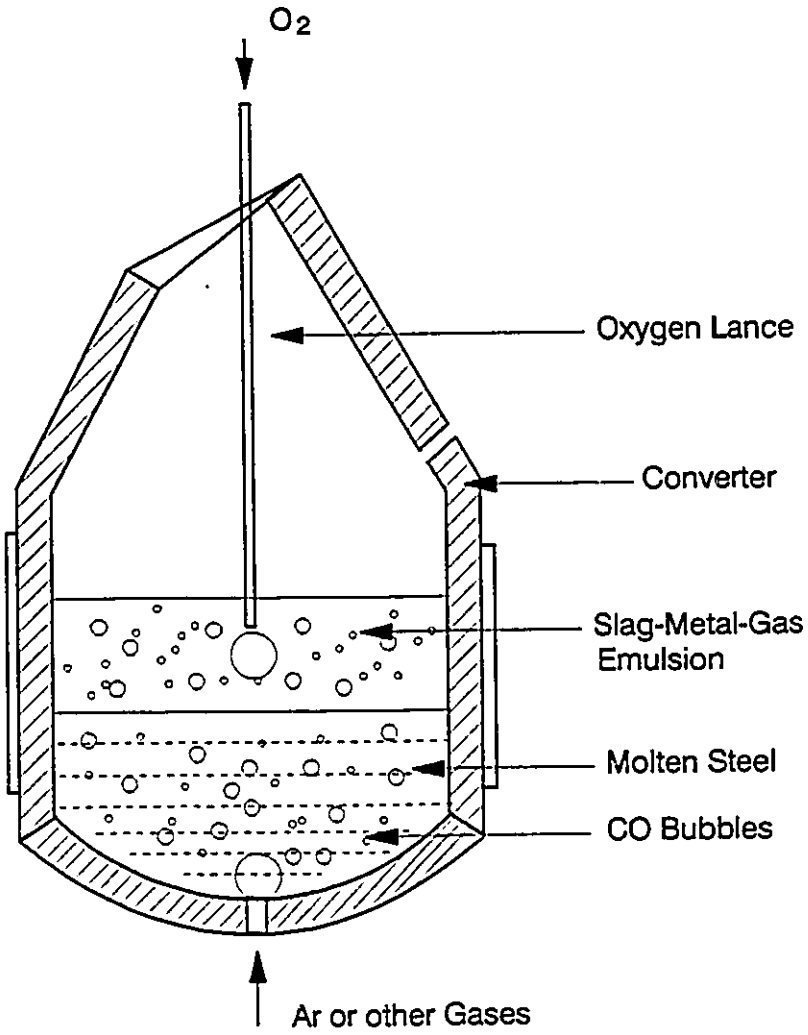

Figure I.1 Illustration of a combined blowing steelmaking converter

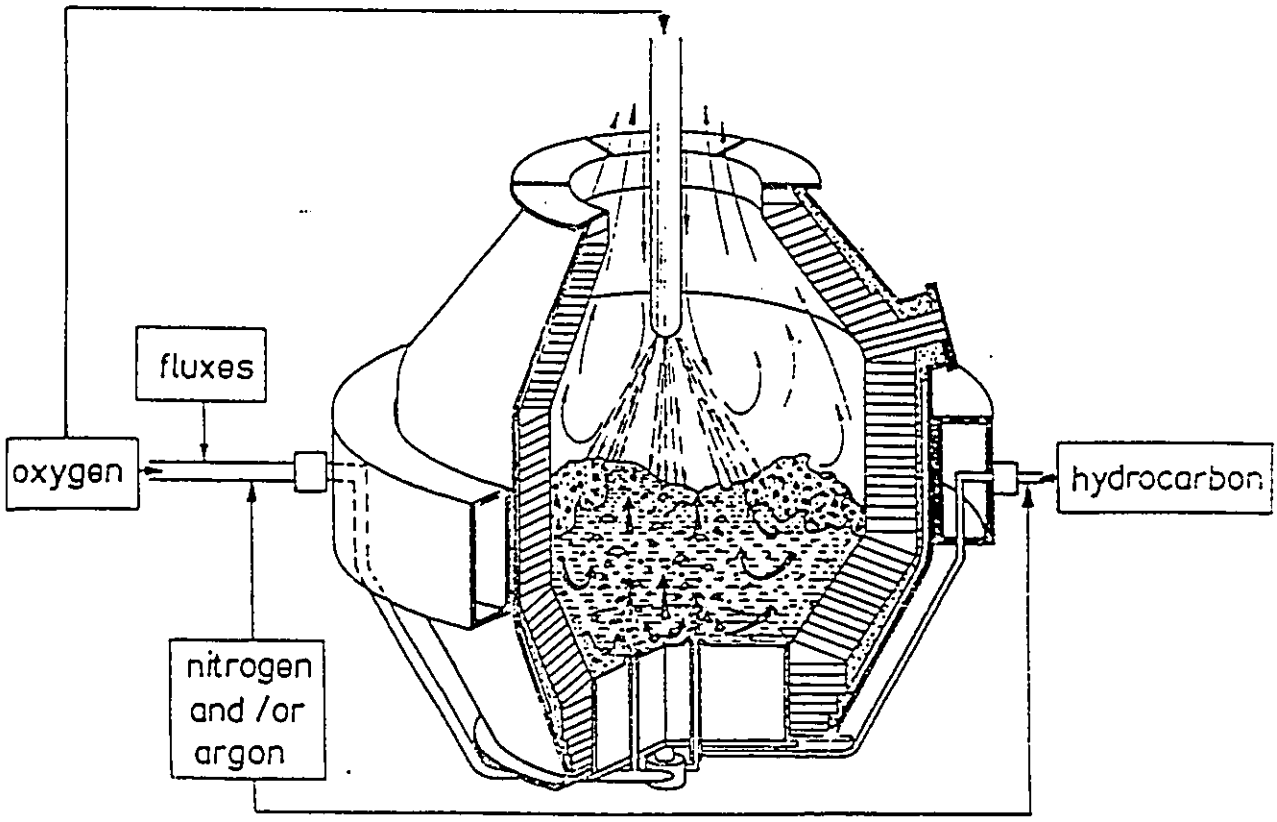

Figure I.2 Schematic diagram of the K-OBM steelmaking converter

to control the refining atmosphere inside the converter, and to bring more heat into the melt. As a result, this process obtained higher capability in reaching lower carbon content of steel and thermodynamic equilibrium between the slag and the liquid metal to yield better desulphurisation, dephosphorization and alloy composition adjustment.

To increase the productivity of electrical steelmaking processes, the residence time of the liquid steel in the main melting furnaces has been shortened by removing as many operations as possible from the main furnace to various ladle refining processes. Gas blowing is employed in most of these processes. Furthermore, many of the refining operations, e.g., alloying, deoxidation, inclusion removal, desulphurization, and so on, can be better performed in the ladle processes. Various types of the ladle treatment equipment have been brought into practice in the last two decades, among them, the simplest one is the ladle bottom stirring with argon, where gas is injected into bath either through an immersed lance or a nozzle located on the bottom of the ladle, and the more sophisticated ones include the ladle furnace (LF), which consists of an electric heating station equipped with a vacuum chamber and gas or powder injection facilities, and the vacuum oxygen decarburization (VOD), which employs oxygen blowing into the ladle inside a vacuum chamber to reach much lower carbon concentration of the steel. Argon stirring is employed for the purposes of removal of inclusions, homogenization of the melt and lower CO content in the furnace atmosphere. In Ladle Furnace or Vacuum Oxygen Decarburization processes, argon or oxygen blowing is used to stir the melt or to supply the oxygen for the decarburization. The gas bubbles produced by gas injection can also improve the metallurgical reactions in the furnace, such as decarburization, deoxidation desulphurization and hydrogen or nitrogen removal (Fruehan, 1985). With the help of these ladle refining techniques, it is possible

to produce very high quality steel with low impurity content, e.g., [O] < 10 ppm, [H] < 1 ppm, [S] < 10 ppm and [P] < 10 ppm, and high accuracy in alloy composition (Irons, 1986).

Another important role played by gas blowing in the ladle refining process is to carry solid powders into the melt to carry out the refining reactions and to decrease the loss of the powders such as calcium and magnesium due to oxidation in air and volatilization under high temperature. Calcium and magnesium are very powerful agents for deoxidation and desulphurisation as well as inclusion modifiers, but are very volatile under steel making temperatures. Along with the wire injection technique, powder injection is one of the few convenient techniques to send calcium and magnesium powders into the melt to achieve the above mentioned refining effects (Kirkaldy, 1979).

1.2 Bubbly Two-Phase Flow Study In Metals Processing

Although bubbly two-phase flow phenomena have been playing important roles ever since the invention of Bessemer converter in the middle of last century, both theoretical and experimental study of the phenomena have not received adequate attention until recently. The rapid development of modern fluid dynamics and numerical methods, together with the development of computer technology had great impact on the research in this area. At the same time, the development of the experimental techniques for two-phase flow study, such as various visualization and measurement techniques for two-phase flows also contributed to the progress of the research. For example, fast variations of the flow pattern can be recorded with

highspeed cinematography techniques. Various two-phase flows, such as particulate gas-solid flows and some gas-liquid flows, have been experimentally studied with Laser Doppler Anemometry (LDA), to obtain data of gas void fraction, particle concentration and separated two phase velocities. The early development of the above mentioned techniques occurred in the fields of chemical engineering or power generation industry where a wide range of the gas-liquid flows take place. Their success triggered the interests of metallurgists to apply the techniques to various metal processing studies.

The earliest studies on multiphase phenomena in a liquid metal bath may be those simulating the behaviour of an air jet inside liquid copper in a converter. Using water models, the investigators observed the dynamic behaviour of the air jet in liquid, and set up a mathematical model to predict the shape and trajectory of the jet based on momentum balance (Themelis et al., 1969). A numerical method was later reported being used to simulate the melt flow in the copper furnace (Szekely, 1979). In 1976, Szekely et al. published the results of their mathematical model of an argon stirred ladle. The two-phase bubbly plume zone was treated simply as a upward moving solid cylinder in this model. Following this, Deb Roy et al. (1978) considered the buoyant effect of the gas in the plume zone by treating the gaseous phase as a momentum source. They also set up a turbulent viscosity model based on the mixing length theory for the two-phase zone, and considered the relative movement of bubbles in the liquid. This model laid a fundamental base for most of the later research. The most extensive studies on the modelling of bubbly flow inside ladles were then carried out by the research group of Guthrie, since the early 1980's. They improved the computation techniques with new effective viscosity models (Sahai & Guthrie, 1982a; Mazumdar, 1989), and made the effort to apply the technique to the full scale flow field in ladles, in terms of axisymmetric flows (Sahai & Guthrie, 1982b), and three-dimensional flow with

heat transfer (Salcudean et al. 1983). Recently, some new approaches have been adopted for the modelling of the bubbly plume flows, which include those using a Lagrangian scheme to trace the bubbles' movement (Johansen et al., 1988), and those with modified turbulent models to take into account the extra generation of the turbulence in the plume zone (Burty et al., 1990). All these efforts contributed greatly to the understanding of the fluid dynamics of bubbly two-phase flow in a steel making ladle.

The present work is intended to further study the dynamic behaviour of the bubbles in the plume and the turbulent flow features in the two-phase zone with the Laser Doppler Anemometer (LDA) and Electric Probe (EP) technique, and develop a more plausible mathematical model for the prediction of the bubble void fraction distribution and the turbulent flow field in the ladle.

CHAPTER II
LITERATURE REVIEW

In this chapter, the following topics related to the experimental and theoretical study of multi-phase flows will be reviewed:

1. The basic equations used for the modelling of various flow problems, namely, the Navier-Stokes equations.
2. The most commonly used model for the turbulence in engineering flows, namely, the k-ϵ two-equation model.
3. The SIMPLE algorithm.
4. The computer code TEACH, which is based on the SIMPLE algorithm.
5. Models of the bubbly plume two-phase flows.
6. Bubbles behaviour in a plume.
7. Laser Doppler Anemometry (LDA) and Electrical Probe (EP) techniques.

2.1 Single Phase Flow Modelling

The models usually consist of either a group of integral equations or a group of differential equations, which are based on the conservation of mass, momentum and

energy. The analytical or numerical solutions of these equations simulate the characteristics of the flow.

In the early years before the advent of the computer technology, numerical solution of the engineering fluid flow problems was impractical due to extremely long time required, and therefore, solutions were only available for a few flow problems which could be solved analytically. The development of the computer technology and numerical techniques has changed this situation. Many of these problems can be solved numerically today with various computation codes as discussed in the following sub-sections.

2.1.1 Conservation Equations for Single Phase Flow

The derivation of the fluid flow equations is based on the conservation of mass, momentum and energy. Consider the fluid flow through a cubic control volume with sides Δx, Δy and Δz, as shown in Figure II.1, the general balance of variable ϕ with respect to the control volume may be expressed as follows (Szekely, 1979):

$$\begin{bmatrix} rate\ of \\ accumulation \end{bmatrix} = \begin{bmatrix} rate\ of \\ input \end{bmatrix} - \begin{bmatrix} rate\ of \\ output \end{bmatrix} \qquad \text{(II.1)}$$

The mathematical form of the Eq.(II.1) may be written as follows:

$$\frac{\partial \rho \phi}{\partial t} = - U \cdot \nabla \rho \phi + \nabla \cdot (\Gamma_{\phi} \nabla \phi) + S_{\phi} \qquad \text{(II.2)}$$

Where, ϕ may stand for mass, momentum and energy, or any other transportable variables of the fluid as shown in Table II.1. The first term on the right hand side (RHS) of Eq.(II.2) is the effect of convection, the second term represents accumulation due to the diffusion process and S^{ϕ} is the source term for the corresponding variable. When ϕ stands for momentum, Eq.(II.2) is usually called the Navier-Stokes Equation.

The classic Navier-Stokes equation can only be solved analytically for a very limited number of laminar flows, where local fluctuation of the velocity components or the turbulence intensity are almost negligible. When Re becomes larger, it becomes more difficult to obtain an analytical solution for the flow. Nevertheless, most of the engineering flow problems can still be numerically solved with various computational techniques and turbulence models.

Table II.1 Detailed Conservation Equations

	CONTINUITY	MOMENT	T.K.ENERGY	DISSIPATION
ϕ	1	**u**	k	ϵ
Γ_{ϕ}	0	μ	μ/σ_k	μ/σ_{ϵ}
S^{ϕ}	0	S^{u}	S^{k}	S^{ϵ}

2.1.2 k-ε Model for Turbulent Single Phase Flow

Among the various turbulence models (Rodi, 1984), the two-equation k-ε model has been used most widely for the solution of various engineering flow problems. To give a clear description of the model, one needs to go back to the Navier-Stokes Equation. In the following derivation, the Einstein convention is used for the vectorial expressions, where, x_i stand for the coordinate directions along x, y, and z direction for

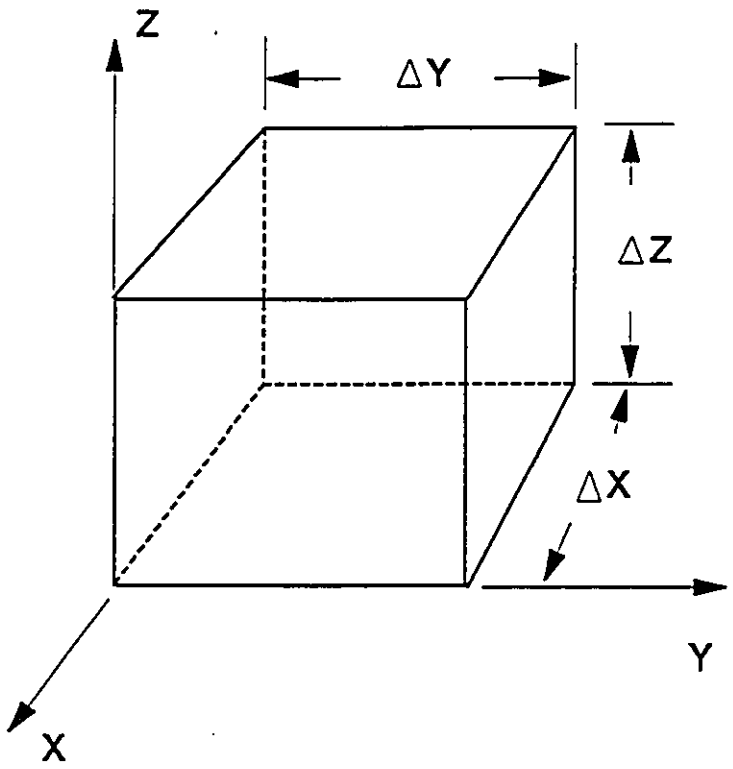

Figure II.1 Illustration of a cubic control volume

i=1, 2, and 3, respectively. V_i stands for time averaged velocity components and v_i for the instantaneous velocity components. The primed values stand for the corresponding turbulent components and is expressed as follows:

$$v_i = V_i + v_i' \tag{II.3}$$

The Navier-Stokes equations for turbulent and viscous flows assume the following form:

$$\frac{\partial v_i}{\partial t} + V_j\frac{\partial v_i}{\partial x_j} = -\frac{1}{\rho}\frac{\partial P}{\partial x_i} + \frac{\partial}{\partial x_j}\left(\nu\frac{\partial v_i}{\partial x_j}\right) \tag{II.4}$$

At high Reynolds numbers, the equations can be rewritten by using the Reynolds decomposition technique on the velocities v_i into the form:

$$\begin{aligned}&\frac{\partial(V_i + v_i')}{\partial t} + (V_j + v_j')\frac{\partial(V_i + v_i')}{\partial x_j}\\ &= -\frac{1}{\rho}\frac{\partial(p + p')}{\partial x_i} + \frac{\partial}{\partial x_j}\left(\nu\frac{\partial(V_i + v_i')}{\partial x_j}\right)\end{aligned} \tag{II.5}$$

For a steady flow, after time averaging and using the continuity equation:

$$\frac{\partial V_i}{\partial x_i} = 0 \tag{II.6}$$

Eq.(II.5) becomes:

$$V_j\frac{\partial V_i}{\partial x_j} = -\frac{1}{\rho}\frac{\partial p}{\partial x_i} + \frac{\partial}{\partial x_j}\left(\nu\frac{\partial V_i}{\partial x_j}\right) - \frac{\partial(\overline{v_i' v_j'})}{\partial x_j} \tag{II.7}$$

The above equations are not closed, since there are 10 unknowns (p, V_i, $(\overline{v_i' v_j'})$, i, j = 1,2,3) but only 4 equations for mass conservation, Eq.(II.6), and momentum conservation, Eq.(II.7). It is not possible to derive similar transport equations for the Reynolds' stresses $(\overline{v_i' v_j'})$ based on Eq. (II.1), and therefore, these variables must be modeled properly to obtain closure. Many attempts exist in the literature, but the most common practice until now has been to adopt Boussinesq's eddy-viscosity concept. This theory assumes that the turbulent Reynolds stress is a result of the mean flow stresses and proportional to the mean stresses:

$$-\overline{v_i' v_j'} = \nu_T\left(\frac{\partial V_i}{\partial x_j} + \frac{\partial V_j}{\partial x_i}\right) - \frac{2}{3}\delta_{ij}k \qquad \text{(II.8)}$$

$$= 2\nu_T S_{ij} - \frac{2}{3}\delta_{ij}k$$

where, μ_t is the turbulent viscosity or eddy viscosity, which depends strongly on the state of the local turbulence rather than being a property of the fluid. k is the turbulent kinetic energy defined with the following equation:

$$k = \frac{1}{2}\overline{v_i' v_i'} = \frac{1}{2}\left(\overline{v_1'^2} + \overline{v_2'^2} + \overline{v_3'^2}\right) \qquad \text{(II.9)}$$

For isotropic turbulence:

$$k = \frac{1}{2}\overline{v_i' v_i'} = \frac{3}{2}\overline{v_1'^2} \qquad \text{(II.10)}$$

$$S_{ij} = \frac{1}{2}\left(\frac{\partial V_i}{\partial x_j} + \frac{\partial V_j}{\partial x_i}\right) \qquad \text{(II.11)}$$

With this model, the last two terms in Eq.(II.7) can be re-written as one term representing both viscous and turbulent shear forces, and the remaining problem is to model the eddy viscosity. In the Two-Equation k-ε model, the eddy viscosity is calculated with the following equation:

$$\nu_T = C_\mu \frac{k^2}{\epsilon} \qquad \text{(II.12)}$$

where, the turbulent kinetic energy k and its dissipation ε may be modelled in the following way.

After some manipulation, the following equation can be obtained for the Reynolds stresses:

$$\frac{\partial(\overline{v_i' v_j'})}{\partial t} + V_k \frac{\partial(\overline{v_i' v_j'})}{\partial x_k} = -\left(\overline{(v_i' v_k')}\frac{\partial V_j}{\partial x_k} + \overline{(v_j' v_k')}\frac{\partial V_i}{\partial x_k}\right)$$

$$+ \frac{p'}{\rho}\left(\frac{\partial v_i'}{\partial x_j} + \frac{\partial v_j'}{\partial x_i}\right) - 2\nu\frac{\overline{\partial v_i' v_j'}}{\partial x_k \partial x_k} \qquad \text{(II.13)}$$

$$+\frac{\partial}{\partial x_k}\left(\frac{1}{\rho}\left[\delta_{jk}\overline{p' v_i'} + \delta_{ik}\overline{p' v_j'}\right] + \overline{v_i' v_j' v_k'} - \nu\frac{\partial(\overline{v_i' v_j'})}{\partial x_k}\right)$$

by letting j=i and k=j, the following transport equation for k can be obtained:

$$\frac{\partial k}{\partial t} + V_j\frac{\partial k}{\partial x_j} = -\overline{v_i' v_j'}\frac{\partial V_i}{\partial x_j} - \nu\overline{\frac{\partial v_i'}{\partial x_j}\frac{\partial v_i'}{\partial x_j}}$$

$$-\frac{\partial}{\partial x_j}\left(\frac{1}{\rho}\overline{[p' v_j']} + \overline{k v_j'} - \nu\frac{\partial k}{\partial x_j}\right) \qquad \text{(II.14)}$$

$$= P_k - \epsilon + D_k$$

Where:

$$P_k = -\overline{v_i' v_j'}\frac{\partial V_i}{\partial x_j} \qquad (\textit{Production of } k) \qquad \text{(II.15)}$$

$$D_k = -\frac{\partial}{\partial x_j}\left(\frac{1}{\rho}\overline{[p' v_j']} + \overline{k v_j'} - \nu\frac{\partial k}{\partial x_j}\right) \qquad \text{(II.16)}$$

and the diffusion terms are modelled in the following way:

$$D_k = -\frac{\partial}{\partial x_j}\left(\frac{1}{\rho}\overline{[p' v_j']} + \overline{k v_j'} - \nu\frac{\partial k}{\partial x_j}\right) = \frac{\partial}{\partial x_j}\left(\gamma_k\frac{\partial k}{\partial x_j}\right) \qquad \text{(II.16a)}$$

$$\epsilon = \nu\overline{\frac{\partial v_i'}{\partial x_j}\frac{\partial v_i'}{\partial x_j}} \qquad (\textit{Dissipation of } k) \qquad \text{(II.17)}$$

where, $\gamma_k = \nu_T/\sigma_k$ is the eddy diffusivity, and D_k is the diffusion of k due to turbulence, pressure and viscous motion.

The transport equation for the dissipation of the turbulent kinetic energy, ϵ, can be obtained in a similar way by differentiating Eq.(II.4) with respect to x_j, and then multiplying the resulted equation with $\mu(\partial v_j'/\partial x_i)$ and performing time averaging. The entire k-ϵ model is:

$$\frac{Dk}{Dt} = \frac{\partial}{\partial x_j}\left(\frac{\nu_T}{\sigma_k}\frac{\partial k}{\partial x_j}\right) + P_k - \epsilon \qquad \text{(II.18)}$$

$$\frac{D\epsilon}{Dt} = \frac{\partial}{\partial x_j}\left(\frac{\nu_T}{\sigma_\epsilon}\frac{\partial \epsilon}{\partial x_j}\right) + \frac{\epsilon}{k}(C_1 P_k - C_2\epsilon) \qquad \text{(II.19)}$$

where the constants were experimentally determined; the values listed in Table II.2 are most commonly used.

Table II.2 Constants in the k-ε Model

c_μ	c_1	c_2	σ_k	σ_ϵ
0.09	1.44	1.92	1.0	1.3

The k-ε model has been used to predict various flow problems with various degrees of success (Rodi,1984). In the modelling of various flow problems encountered in the metallurgical processes, the k-ε model has been almost exclusively used for the calculation of both single phase and multiphase flow fields. It must be noted, however, that this model is still an empirical one without universal applicability. The constants listed in Table II.2 may not be applicable even for some fairly simple flows to yield reasonable prediction, as discussed by Rodi (1984).

2.1.3 SIMPLE Algorithm

Numerous computation schemes have been developed in the past for the numerical solutions of the Navier-Stokes equations. These schemes may be divided into two categories, schemes using primitive flow variables of velocity and pressure, and

schemes using non-primitive flow variables such as vorticity and stream function. Since the vorticity and stream function are limited to two dimensional problems, it is sometimes difficult to assign boundary conditions to them; thus, the primitive schemes using velocity and pressure as the flow variables are more widely used.

To use primitive variables in the computation, the most difficult task is to calculate the pressure distribution of the flow. Since there is no transport equation for pressure, the pressure can only be calculated through the manipulation of the known variables. The procedure for the calculation of pressure in the SIMPLE algorithm (Patankar, 1980) is briefly reviewed here.

For a staggered grid, where the velocities are located at the points half way between grids for pressure and other variables as shown in Figure II.2 (Patankar, 1980), the one dimensional flow equations can be discretized into the following form:

$$\left(\rho U\phi - \Gamma_\phi \frac{\partial \phi}{\partial x}\right)_e A_e - \left(\rho U\phi - \Gamma_\phi \frac{\partial \phi}{\partial x}\right)_w A_w = \int_V S^\phi \, dV \qquad \text{(II.20)}$$

or:

$$a_P \phi_P = \sum a_{nb} \phi_{nb} + S^\phi \qquad \text{(II.21)}$$

where the subscript nb means the neighbouring grids and A is the area for the corresponding flux. To assign proper values to the above coefficients, some careful consideration is needed. With central difference, where the variables are calculated by averaging their values at the interfaces, or other schemes are used, the computation program could either diverge at large Reynolds numbers due to negative coefficients,

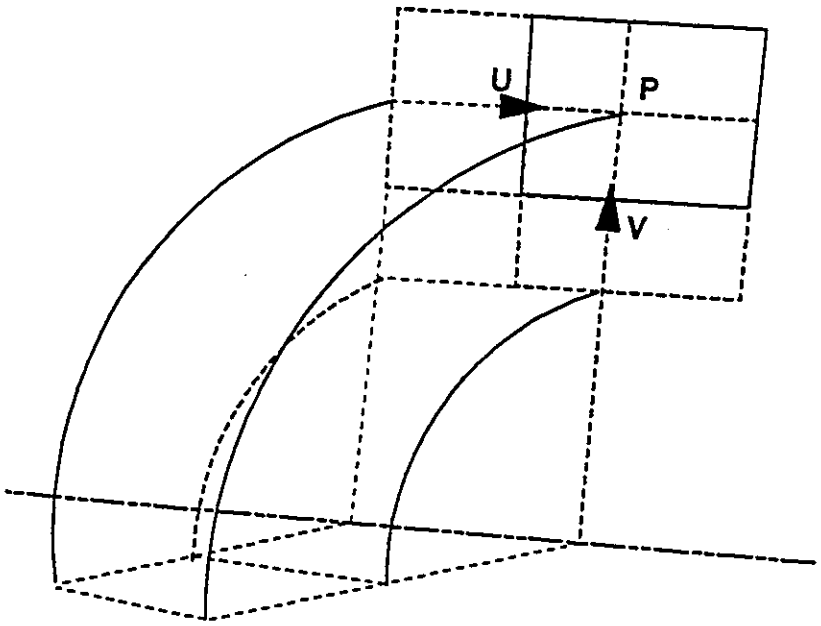

Figure II.2 Illustration of the staggered grid in cylindrical coordinates

or yield an unstable solution when Peclet number, Pe=ρUL/Γ, is larger than 2. To avoid these problems, the upwind scheme (Patankar, 1980) should be adopted, where the values of the variables at the upwind position of the flow are used:

$$\begin{aligned} \phi_e &= \phi_P \quad if\ F_e > 0 \\ \phi_e &= \phi_E \quad if\ F_e < 0 \\ F &= \rho UA \end{aligned} \tag{II.22}$$

The coefficients are then calculated in the following way:

$$\begin{aligned} a_E &= D_e + [\![-F_e, 0]\!] \\ a_W &= D_w + [\![F_w, 0]\!] \\ D &= \frac{\Gamma A}{\delta x} \end{aligned} \tag{II.23}$$

Where, [[A,B]] means the larger of A and B. The momentum equation can be then discretized into:

$$a_e U_e = \sum a_{nb} U_{nb} + b = (P_P - P_E) A_e \tag{II.24}$$

The pressure correction in the SIMPLE algorithm starts the computation with an estimated pressure distribution P^*, which in turn would produce an imperfect velocity distribution U^*. The correct pressure and velocity can then be obtained by modifying P^* and U^* with a pressure correction P' and velocity correction U' respectively as follows:

$$P = P^* + P'; \quad U = U^* + U' \tag{II.25}$$

The velocity calculated from an estimated pressure is:

$$a_e U_e^* = \sum a_{nb} U_{nb}^* + b - (P_P^* - P_E^*) A_e \tag{II.26}$$

Subtracting Eq.(II.26) from Eq.(II.24) results in the velocity correction:

$$a_e U_e' = \sum a_{nb} U_{nb}' - (P_P' - P_E') A_e \tag{II.27}$$

If the elimination of the first term on the RHS of Eq.(II.27) is considered to have no effect on the final computational results, a simpler form as Eq.(II.28) is obtained for the velocity correction:

$$U_e' = d_e (P_P' - P_E') \tag{II.28}$$

where, $d_e = A_e / a_e$. The correct velocity can now be calculated if the pressure correction is known:

$$U_e = U_e^* + d_e (P_P' - P_E') \tag{II.29}$$

The pressure correction equation can be obtained by inserting Eq.(II.29) into the continuity equation which yields:

$$a_P P_P' = a_E P_E' + a_W P_W' + b \tag{II.30}$$

where:

$$\begin{aligned} a_E &= (\rho dA)_e \\ a_W &= (\rho dA)_W \\ a_P &= \sum a_{nb} \\ b &= (\rho U^* A)_w - (\rho U^* A)_e \end{aligned} \tag{II.31}$$

To summarize, the general sequence of operation of the SIMPLE algorithm is (Patankar,1980):

1. estimate the pressure field P^*,
2. solve the momentum equations to obtain velocity field U^*.
3. solve the pressure correction equation to obtain P',
4. calculate the correct pressure field P,
5. calculate the correct velocities and then other flow variables if necessary.

2.1.4 TEACH Code

The TEACH code (Gosman and Pun, 1974; Lilley and Rhode, 1982) was originally developed for the prediction of the turbulent flow in a stirred tank based on the SIMPLE algorithm discussed in the previous section. Turbulence is modeled with the two-equation k-ε model in the bulk flow zone, and with the so-called wall functions in the vicinity of a solid wall. Since the steep variation of velocities close to the wall is modeled with the universal logarithmic profile, the wall function technique saves computer time and storage. It also allows the introduction of additional empirical information, such as the roughness of the wall (Launder and Spalding, 1974). All the transport equations are discretized and then integrated with respect to a finite set of control volumes. The resulting algebraic equations are solved with an implicit line-by-line relaxation technique using the Tri-Diagonal Matrix algorithm. The program structure is illustrated with Figure II.3 and the main features are briefly discussed in the following sections based on the work of Gosman and Pun in 1974, and of Lilley and Rhode in 1982.

2.1.4.1 The Main Subprogram

The MAIN subprogram performs the function of controlling and monitoring the entire computation sequence, which includes data input, initializing, iteration loop, updating the main variables and output control. It is divided into several chapters (Figure II.3). Chapter 1 specifies various parameters and control indices. The geometry of the problem is also given in this chapter. In chapter 2, the subroutine INIT is called to assign initial values to the variables in all the grids. Iteration starts in chapter 3 with the calling of subroutines CALCU, CALCV to update the variables for all the grids. Chapter 4 controls the output for the computation results and determines the end of the program.

2.1.4.2 Main Subroutines

The coefficients of the finite difference equations of momentum are calculated in the subroutines CALCU and CALCV. Subroutines MODU and MODV are called by CALCU and CALCV respectively to modify the boundary conditions using the wall-function (Launder & Spalding, 1974). The new values for U and V are then obtained by calling LISOLV to solve the finite difference equations.

The coupling coefficients of finite difference equations of continuity are calculated in the subroutine CALCP in a similar way to CALCU, except for using different control values. The pressure correction and velocity corrections are performed in this subroutine to give correct pressure and velocity fields.

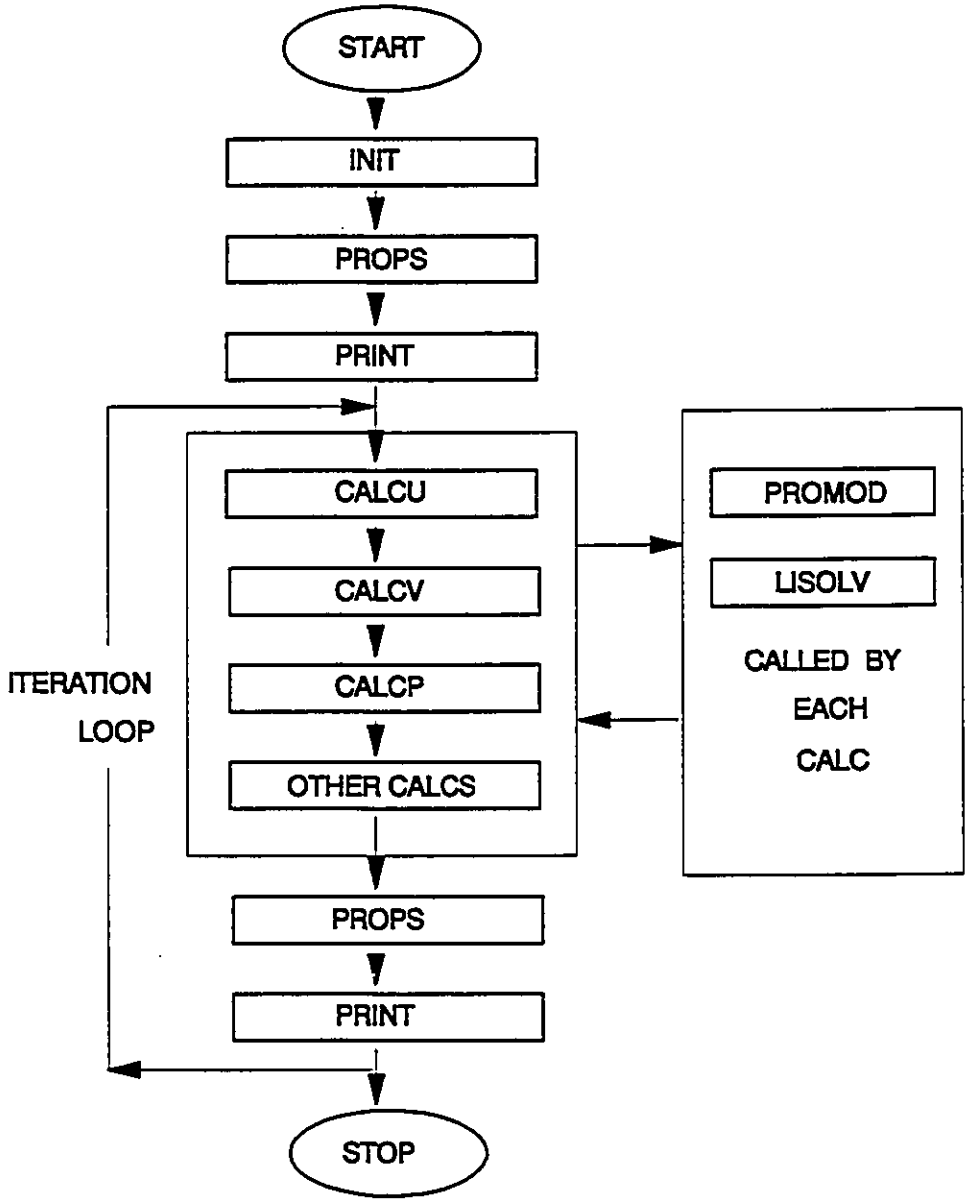

Figure II.3 Illustration of the program structure of the TEACH code

The fluid properties, such as turbulent viscosity are updated in the subroutine PROPS after new values of k and ϵ are obtained. The boundary condition modifications for all the main variables, such as MODU and MODV, are incorporated into PROMOD. Each chapter in this subroutine begins with the statement ENTRY to control the calling of a particular modification subroutine.

2.2 Theories on Bubbly Plume Modelling

There are two descriptive schemes used in the fluid dynamics, namely, the Eulerian and the Lagrangian schemes. In the former, the variation of some fluid property is considered with respect to a fixed coordinate system. In the later the variation of the property connected with a given fluid particle or fluid lump is considered during the motion of this particle or lump through the flow field (Hinze, 1975). Both of the methods have been used extensively in bubbly plume modelling or similar simulations. For the Eulerian type models, attention has been given to modelling the void fraction distribution of the gas, and its effect on the liquid flow as sources of momentum and turbulence. Once a proper model for the void distribution is at hand, the flow field may be obtained by solving the well-known turbulent Navier-Stokes equations for fluid flow. If the Lagrangian scheme is chosen, the problem would then be to find ways to model the interaction between liquid and discrete bubbles, and the effects of the shape and size of bubbles on that interaction.

2.2.1 Models of the Eulerian Type

Models developed at the early stages were of Eulerian type. The core of these models was to calculate the void fraction distribution of gas in the plume zone. The simplest model of the void fraction was first proposed by Wallis in 1969. In this model, the void fraction is assumed to be only a function of the height in the plume. It is a cross-sectional average and can be calculated with the following equation based on continuity:

$$\alpha = \frac{Q_g}{2\pi \int_0^{R_c} r(u + U_r)dr} \qquad \text{(II.32)}$$

With the omission of the slip flow velocity between bubble and liquid, U_r, an even simpler model can be obtained. This model has been used by Deb Roy et al. (1978), El-Kaddah and Szekely (1981) and Salcudean et al. (1983) for metallurgical plumes. The cross-section average, according to the experimental results (Sano and Mori, 1980a,b; Castillejos and Brimacombe, 1987a,b), is far from realistic, so that some other empirical models have been also proposed. The most commonly accepted models are based on the assumptions of either a radial Gaussian distribution of the void fraction, originally proposed by Kobus (1968), or a radial exponential distribution of the void fraction (Kawakami, et al., 1985; Mazumdar and Guthrie, 1985; He et al., 1984; Castillejos and Brimacombe, 1987b; Bankoff, 1960). Both of the distributions need some empirically determined constants. Due to the uncertainty of these empirically determined void fractions, some tried to use the measured void fraction data or velocity data at plume boundaries for the calculation of the recirculation field (Szekely et al., 1976; He et al., 1984). The plume models based on the above void fraction models are called local

homogeneous flow (LHF) models. With these models, the gaseous phase is assumed dispersed completely into the liquid phase, its dynamic behaviour is neglected except as a momentum source for the liquid flow, or only accounted in a simple turbulent viscosity model (Deb Roy et al., 1978; Sahai and Guthrie, 1982). For the computation of the recirculation of liquid in the bubbly plume flows, the dominant factor is the distribution of the void fraction which supplies the buoyant force for the liquid flow. When the void fraction distribution is known, these models can be used to obtain reasonably good predictions.

The main disadvantage of the above models is that the real behaviour of the gas phase as discrete bubbles is ignored, and the void fraction variation as a result of bubble dispersion cannot be predicted. As a result, the fluctuation of the liquid flow field, as well as mass and heat transfer inside the plume, cannot be addressed with such models. The problem was addressed by Farias and Irons (1986). They approximated the plume as a one dimensional column and assigned different motion equations for particle, bubble and liquid phases respectively. This model yielded void fraction variation along the vertical direction, however, it would be very difficult to extend the model of Farias and Irons to more than one dimension.

McKelliget et al. (1987) proposed the idea that the turbulent diffusion of mass is proportional to mass fraction gradient and calculated gas concentration contours for different ladle injection processes. The contours of gas concentration predicted by Mckelliget et al. appear narrower than in water models (Castillejos and Brimacombe, 1987).

Recently, some new methods have been developed to model two-phase dispersed flows. These models take into consideration the interaction between the fluid phase and the dispersed phase. One type of the new model proposed by Chen and Wood (1984) treated both phases in a gas and fine particle jet as two completely inter-penetrating continua with the same mean velocities. The turbulent interaction between the two phases was modeled in terms of characteristic response time of the particle and characteristic time scale of the eddy. The particle dispersion was mainly controlled by the turbulent diffusion so that the void fraction was calculated together with the turbulent flow field. In case of an unconfined jet with very fine particles (< 100 μm) and low loading ($\alpha << 1$), the response time of a particle was assumed smaller than the time scale of the mean fluid motion. The model gave good prediction of the fluid flow and showed that the existence of particles has significant influence on the distribution of turbulent kinetic energy. This kind of model is called coupled two-phase flow (CTF) model.

There are difficulties in applying the model of Chen and Wood directly to the problem of bubbly plumes. Even if it is still acceptable to assume that the bubble phase is a continuum that inter-penetrates with the liquid phase, the turbulent interaction is much different than that of a fine particle jet. Because the bubble size is much larger than that of the fine particles, dispersion of bubbles by turbulent diffusion could be also different. The most difficult problem in applying the model to bubbly plume flow is the determination of the bubble size distribution, which must be known for the calculation of various time and length scales. Due to the constant breakup and coalescence of bubbles in the plume, the distribution of bubble size is a variable of the flow which must be modeled properly before the model of Chen and Wood could be applied. As a result,

the turbulent interaction and the void dispersion should not be modeled in the same way as in the case of a fine particle jet. More appropriate models must be developed.

All the above mentioned models are of Eulerian type and the well known Navier-Stokes constitutive equations are used for the prediction of the mean liquid flow field. The dominant variable of the computation is the distribution of the void fraction. With the LHF models, the void fraction distribution is determined either with the experimentally measured data or with empirical correlations. With the CTF models, the void fraction distribution can be calculated by solving the motion equations of bubbles. The turbulence in the continuous phase is modelled with the k-ε model in most cases. The turbulent behaviour of the dispersed phase is totally neglected in the LHF models, but accounted in terms of turbulence generation in both phases in the CTF models.

2.2.2 Models of the Lagrangian Type

Another type of model commonly used for the prediction of the dispersed two-phase flow is based on a Lagrangian scheme. These models are also called particle/bubble tracking or the trajectory models. There are two kinds of Lagrangian models: deterministic separated flow (DSF) and stochastic separated flow (SSF). Both start with an equation of motion for a single discrete particle or bubble in a turbulent fluid flow field and the trajectory is calculated. In DSF, the motion of particles or bubbles is only affected by mean fluid flow field; while in SSF, turbulent influences on the motion of particles or bubbles are accounted for using the method originally proposed by Gosman and Loannides (1981). Particles or bubbles are assumed to

interact with a succession of turbulent eddies using the random walk calculations and the mean trajectory is obtained from the random trajectories of a large number of particles. The main assumptions for SSF are that the turbulence is isotropic and eddies are uniform. The basic calculation procedure is to use the turbulence model to calculate the fluid flow field assuming no second phase is present, which gives the local instantaneous velocity of the fluid after making suitable assumptions regarding turbulent time scale, length scale and isotropy. Then the equation of motion of a particle or bubble is solved to give its trajectory. The void fraction can be calculated when the bubble trajectory and size are known. Shuen et al. (1983, 1985) used this method to predict the particle motion in a turbulent jet; Weber et al. (1984) used it to calculate the particle dispersion in a confined turbulent flow; Parthasarathy and Feath (1987) used it to study the particle-laden turbulent water jets. In the case of bubbly two-phase flow with bubble size in the range of several millimetres, Sun and Feath (1986a, 1986b) and Sun et al. (1986) applied it to the study of turbulent bubbly jet; Johansen and Boysan (1988) used it to set up a model simulating the argon stirring process in a steel making ladle with bubble size as large as 6 mm in diameter. All the authors claimed good agreement between prediction and experimental observation.

The main limitations of the SSF model are its assumptions that the presence of the second phase does not affect the turbulent flow field of the fluid phase, and the bubbles are carried away by isotropic turbulent eddies. These approximations would be valid when the bubble size is small and void fraction is low. In many practical cases, especially in the case of ladle metallurgy, the situation is too complicated to apply the above models directly. Johansen and Boysan (1988) noted the problem and considered the turbulent interaction between bubbles and the fluid phase in their model while keeping the assumptions of isotropic turbulence and equal size of bubbles. This is still

far away from the real situation as will be demonstrated with the experimental results. Bubbles affect liquid flow field so much that the fluctuation of liquid velocity is much larger than what would be predicted by the above models. The assumption of isotropic turbulence is also questionable inside the bubbly plume. Furthermore, the interaction among bubbles needs consideration, and the sizes of bubbles vary significantly inside the plume zone, which adds another limitation to Johansen's model.

2.2.3 Bubble Behaviour in Plumes

2.2.3.1 Bubbling and Jetting Transition

When gas is injected into the liquid, it generally assumes the following three kinds of behaviours for different gas flowrates (Brimacombe, 1991):

1. In the case of low gas flowrates, the gas will form distinct bubbles and rise up to the bath top in the form of a chain of bubbles.

2. In the case of high gas flowrates, a continuous gas jet will form.

3. When gas flowrates are between the above two cases, a bubbly plume forms. In this case, distinct bubbles are produced at the nozzle, and undergo either breakup or coalescence during rise to form a cone-like two-phase flow zone. If the walls of the container are some distance away from the plume zone and do not affect the rising behaviour of bubbles, the plume is unconfined (Figure II.4).

The definition of high, moderate and low gas flowrates depends on the system conditions. Much work has been done to differentiate gas behaviours at low gas flowrates. At very low gas flowrates, the volume of bubble at release from the nozzle

is determined by a balance between its buoyancy force and those surface tension forces constraining it to the nozzle; the size of bubble is independent of the gas flowrate (constant volume range). As the gas flow rate increases, a force balance between the buoyancy and the force required to accelerate the liquid away from the expanding gas-liquid interface controls the bubble size. The constant volume regime of bubble is replaced by a constant frequency regime where the volume of bubble is almost directly proportional to gas flowrate, as illustrated in Figure II.5 (Irons and Guthrie, 1978). Bubble chains as formed in both constant volume and constant frequency regimes of bubble formation have gas flowrates lower than about 0.2×10^{-4} m^3/s for nozzles with an inner diameter in the range of 0.005 m in an air-water system.

The transition from bubbling to jetting at high gas flowrates has also received wide attention (Hoefele and Brimacombe, 1979). Among criteria proposed for the determination of the transition, the critical gas velocity based on the critical gas Weber Number best fit the existing experimental data (Zhao & Irons, 1990). According to this model, a chain of bubbles forms at low gas flowrates (Figure II.6a). When gas flowrates increase, the interface instability breaks up the interface of the discharging gas to form discrete bubbles (Figure II.6b). When gas flowrate further increases to a critical value, the growth of the interface instability is too slow compared to the interface movement, and any perturbation would be swept away before it breaks the interface. As a result, a gas jet forms (Figure II.6c). The critical gas flowrate calculated with this model is about 1.0×10^{-3} m^3/s when the inner diameter of the nozzle is 0.005 m for an air-water system.

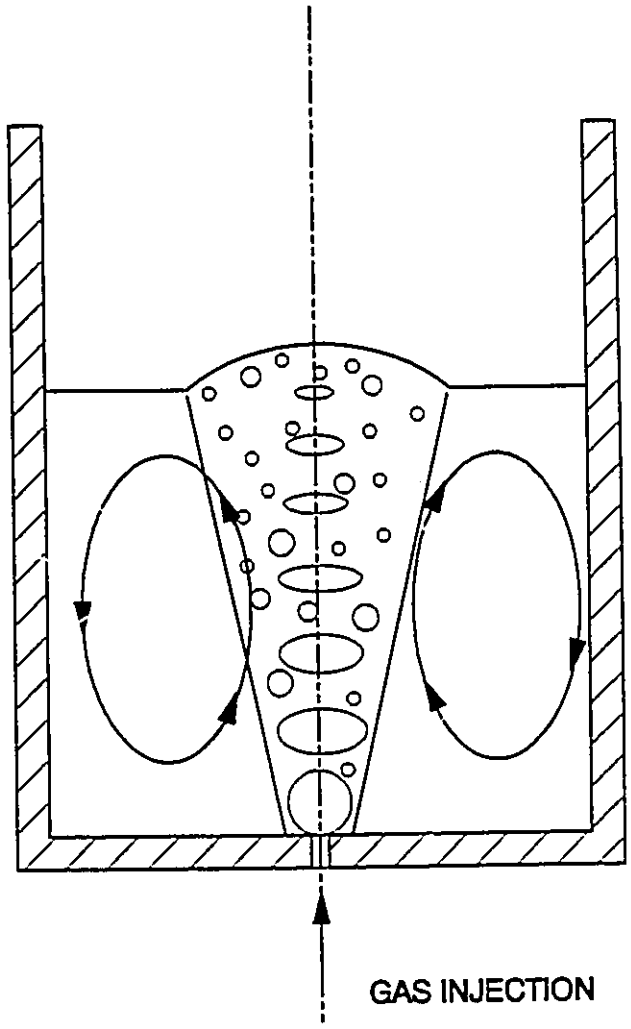

Figure II.4 Illustration of a bubbly plume flow in a steelmaking ladle Gas is injected from a nozzle located at the center of the ladle bottom, and the recirculation of the liquid is shown by the arrows.

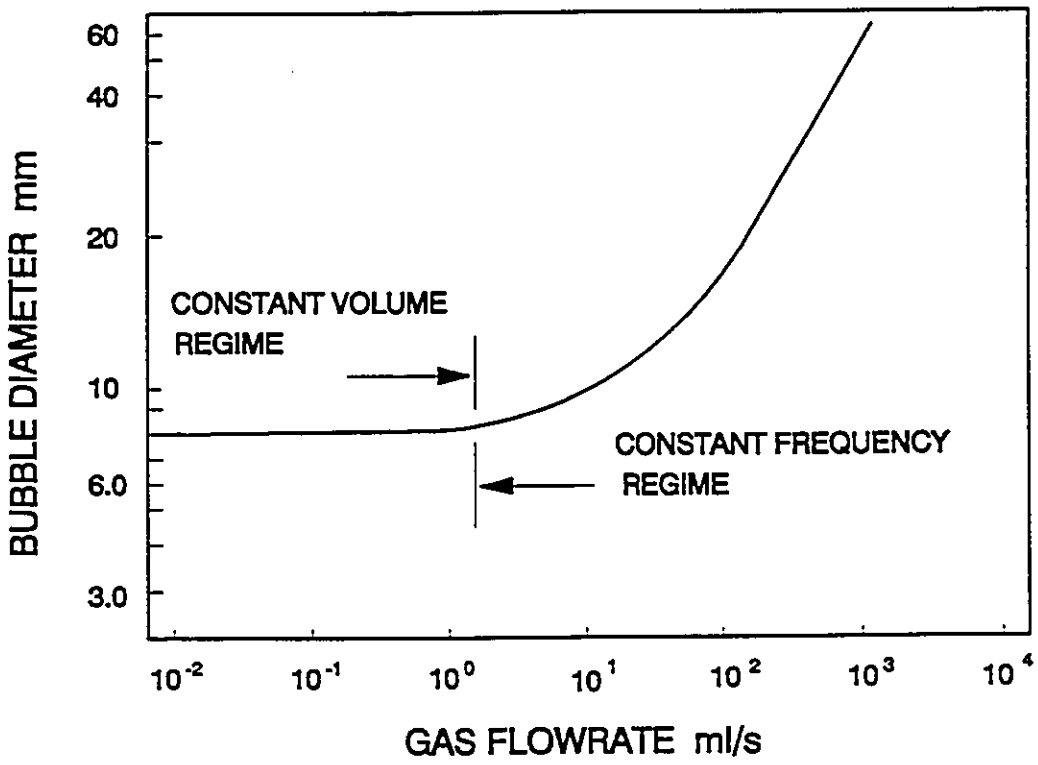

Figure II.5 Transition of the constant volume regime to constant frequency regime in bubble formation at a nozzle

2.2.3.2 General Behaviour of Bubble in Plumes

Bubble behaviour in a bubbly plume flow is characterized by spatial distributions of the bubble occurrence frequency, void fraction, bubble size and bubble velocity. There have been a significantly number of reports on the experimental measurements of the distributions of the above variables, and a good review can be found in the article by Brimacombe (1991).

The distributions of both void fraction and bubble frequency in bubbly plumes are very close to a Gaussian distribution, with the maximum values located on the centerline of the plume. The empirical relations established by Brimacombe (1991) can be used for the estimation of the void fraction distributions.

The distributions of bubble sizes and bubble rising velocity in bubbly plumes may also assume Gaussian distributions. Due to the uncertainty of the bubble size variation and the lack of proper experimental techniques for bubble velocity measurement, much less data exist than for void fraction and bubble frequency. One approach worth mentioning here has been reported by Brimacombe (1991) who characterized the breakup and dispersion behaviour of a bubble during rising with a dispersion number defined as follows:

$$N_D = \frac{x}{d_o}\left(\frac{g d_o^5}{Q_g^2 \rho_g / \rho_l}\right)^{0.3} \qquad \textbf{(II.33)}$$

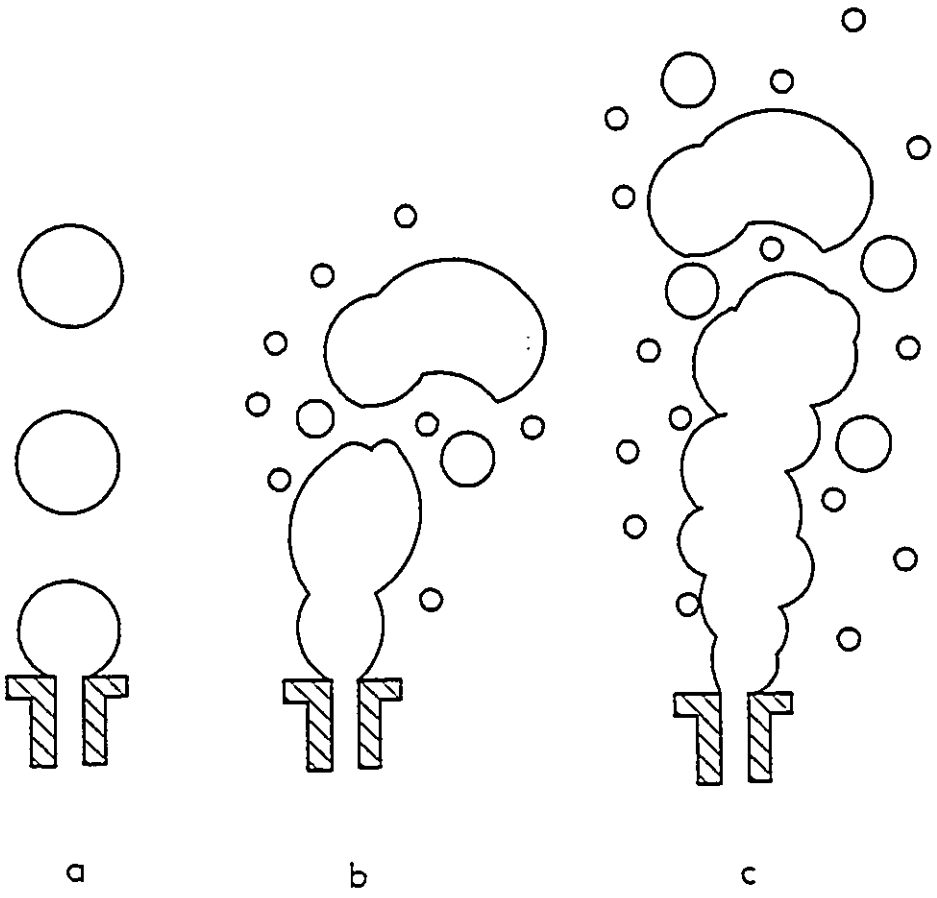

Figure II.6 Illustration of the transition from bubbling to jetting

(a) When the gas flowrate is low, a chain of bubbles is formed;

(b) At moderate gas flowrates, distinct bubbles form at the nozzle and they would breakup to form a plume during rising;

(c) When the flowrate exceeds the critical value, a jet would form.

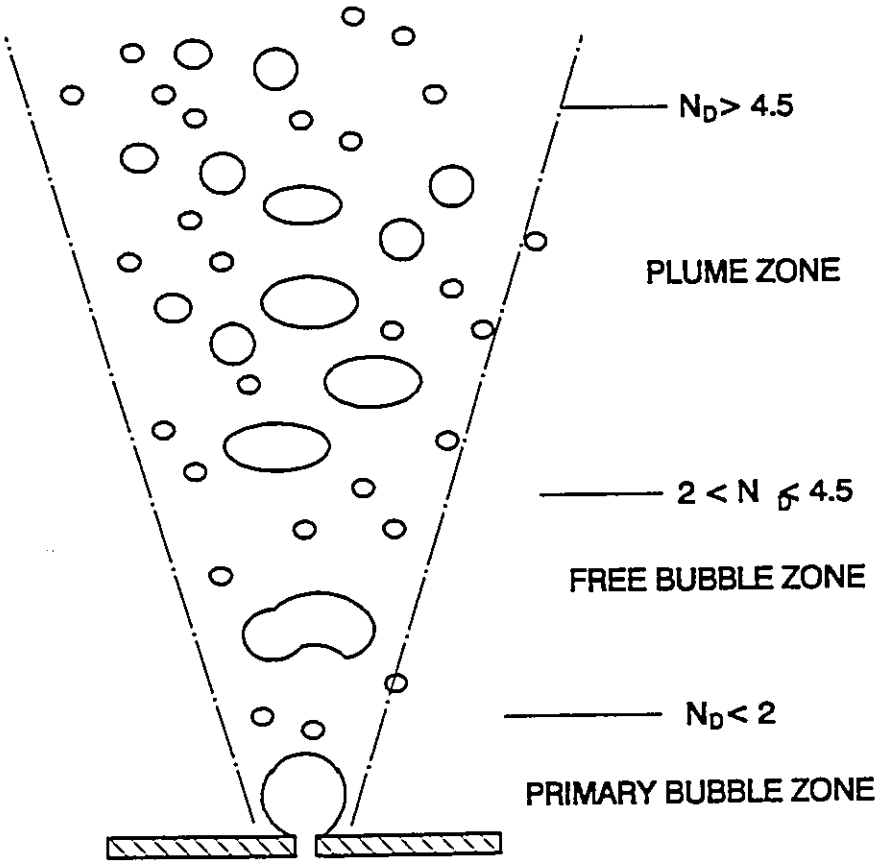

Figure II.7 Illustration of the regimes in a plume

(a) Close to the nozzle with $N_D<2$, primary bubble zone where bubbles detach the nozzle; (b) In the middle of the plume ($2<N_D<4.5$), free bubble zone; (c) When $N_D>4.5$, the breakup of bubbles forms the plume

Based on the available experimental data, the plume was considered to assume the following regimes during rising (Figure II.7):

1. When $N_D < 2$, there is a primary bubble zone, where bubbles detach the nozzle;

2. When $2 < N_D < 4.5$, there is a free bubble zone, where bubbles rise without significant breakup;

3. When $N_D > 4.5$, there is a plume zone where breakup of bubbles occurs to form the plume.

This approach may be used to draw an overall picture of the plume, however, it fails to supply more information on the detailed structure of the plume such as the sizes of bubbles resulting from the breakup of the primary bubble.

When information of bubble sizes is available, the bubble trajectories can be calculated by solving the motion equations of the bubble. Among other parameters, there are two factors which have been the main concerns for plume modelling, namely, the determination of the drag on the bubble and lateral dispersion behaviour of the bubble.

2.2.3.3 Determination of the Drag on Bubble in Plumes

There have been no convincing correlations for the estimation of the drag on a bubble in a turbulent bubbly plume where local void fraction varies considerably. The simplest treatment of the problem is to use the non slip approach, in which the velocity

difference between the bubble and the liquid is neglected (El-Kaddah and Szekely, 1981). This is obviously an over-simplification. Another treatment of the problem was to assume that the terminal rising velocity of a single bubble in stagnant liquid should be a better guess for the real rising velocity of bubbles in a plume (Deb Roy et al., 1978). This approach, however, has not received either theoretical or experimental support. Recently, some of the correlations for the bubbly pipe flows received much attention, for example, the experimental measurement done by Tsuji et al. (1982) and the drag coefficient model originally proposed by Ishii and Zuber (1979). Both predict a decrease in drag coefficient when void fraction increases. The detailed work of Tsuji et al. and Ishii and Zuber needs to be discussed more fully.

Tsuji et al. (1982) measured the drag on a solid ball behind several other balls in a channel flow. They found that when the preceding ball was closer, the drag is lower, and therefore concluded that the drag would be decreased with an increase in the void fraction. The shortcoming of the technique is that the effect of liquid flow around the ball in question is not properly considered. When the apparent drag force F_D appeared to be lower, the U_r could be also lower. The seemingly reduced C_D could be a result of the liquid flow variation caused by the preceding balls. If the C_D is calculated with its velocity relative to the liquid surrounding the ball instead of the liquid as a whole in the channel, C_D may not have been lowered so significantly.

The original derivation of Ishii and Zuber model started with the discussion of the momentum transport equation of each phase as an continuum in one dimensional bubbly pipe flow systems. The authors assumed that in the absence of the wall, and under a steady state condition without phase change, a multi-bubble system in an infinite medium essentially reduces to a gravity dominated one-dimensional flow. The

axial component of the momentum equation for k phase can be written as:

$$0 = -\alpha_k \frac{dp_m}{dz} - \alpha_k \rho_k g + M_{ik} \tag{II.34}$$

where, p_m is the pressure of the mixture, which is assumed to be equal to the pressure of both the continuous phase and the dispersed phase, and M_{ik} is the generalized drag force on the k phase. Summing over k phases:

$$\sum_{k=1}^{m} M_{ik} = 0 \tag{II.35}$$

Eq.(II.34) can be re-written into the following form:

$$\frac{dp_m}{dz} = -\rho_m g \tag{II.36}$$

where:

$$\rho_m = \alpha \rho_g + (1-\alpha)\rho_l \tag{II.37}$$

The drag force is defined as:

$$F_D = -\frac{1}{2} C_D \rho_l U_r |U_r| A_B \tag{II.38}$$

and is related to M_{ig} in the following way:

$$F_D = \frac{M_{ig}}{n_B} = M_{ig} \frac{V_B}{\alpha} \tag{II.39}$$

where V_B is the volume of the bubble, n_B is the number of bubbles in a unit volume of continuous phase.

Now if Eq.(II.34) is valid for the dispersed phase, which means that the axial pressure drop is the result of the gravity of the dispersed phase, the effect of the generalized drag on the dispersed phase, Eq.(II.34) can be rewritten as:

$$M_{ig} = \alpha\frac{dp_m}{dz}+\alpha\rho_g g = -\alpha g(\rho_m-\rho_g) = -\alpha g[(1-\alpha)\rho_l-(1-\alpha)\rho_g] \tag{II.40}$$

and the relative velocity can be calculated with the following equation when a steady state is reached:

$$U_l|U_l| = -\frac{M_{ig}V_B}{\alpha}\frac{2}{C_D\rho_l A_B} = -\frac{8}{3}\frac{r_B}{C_D\rho_l}(\rho_l-\rho_g)(1-\alpha)g \tag{II.41}$$

Compared with the relative velocity for a single bubble:

$$U_\infty|U_\infty| = \frac{8}{3}\frac{r_B}{C_D\rho_l}(\rho_l-\rho_g)g \tag{II.42}$$

the possible reduction of the apparent drag coefficient for a multiphase system is expressed by the following equation:

$$C_D = C_{D\infty}\left(\frac{U_\infty}{U_r}\right)^2(1-\alpha) \tag{II.43}$$

Ishii and Zuber went further to argue that in the case of a bubbly churn-turbulent flow, the relative velocity in Eq.(II.38) should be replaced with the drift velocity:

$$v_{dj} = v_d - j = (1-\alpha)U_r \tag{II.44}$$

where j is the mixture volumetric flux. Since the bubble sizes are fairly large in this flow, due to the overlapping of the wakes and the bubble boundary layers, the entrainment of bubbles in the wake of the preceding bubble is possible. As a result, a typical bubble moves with respect to the average volumetric flux j rather than the average velocity of the continuous phase. So that Eq.(II.38) assumes now the following form:

$$F_D = -\frac{1}{2}C_D\rho_f v_{dj}|v_{dj}|A_B \tag{II.45}$$

The drag force is correspondingly rewritten into the following form:

$$F_D = -\frac{8}{3}(1-\alpha)^2\frac{\rho_f U_r|U_r|\pi r_B^2}{2} \tag{II.46}$$

Compared with the system of a single bubble where C_D=8/3 for a spherical cap bubble according to Clift et al. (1978):

$$C_D = \frac{8}{3}(1-\alpha)^2 \tag{II.47}$$

The model of Ishii and Zuber was adopted by Johansen and Boysan (1988) in their model of the plume, however, the applicability of the model to plumes with large bubbles still needs further verification.

2.2.3.4 Lateral Migration of Bubbles in Plumes

For the lateral dispersion of a particulate phase or bubbles inside a continuous fluid, there are two important transport mechanisms other than the bulk convection, namely, by turbulent diffusion and by the lateral lift force. The effect of turbulent diffusion is a result of the random interactions among turbulent eddies, which tends to transport fluid properties such as heat from high temperature areas to low temperature areas. Turbulent diffusion in particulate jet flows has been discussed extensively in a Lagrangian frame, where the collision of the particles with eddies is assumed to be responsible for the lateral migration of the particles in the jet (Sun et al., 1986). For bubbly plume flows, the effect has been modeled in a Eulerian frame in terms of bubble diffusion (Kikuchi et al. 1986) based on the fact that the dispersion behaviour of the void fraction is similar to a molecular diffusion process. Kikuchi et al. related the rising velocity of a bubble to the ratio of the turbulent viscosity over the bubble diffusivity, and made comparison between the observed and calculated rising velocity of bubbles for three values of the ratio. They found that the bubble diffusivity is equal to the turbulent viscosity. However, the results were not well-verified, since they did not mention the accuracy of the measured bubble velocity, and the differences among the calculated rising velocities were so small that they could be within the deviations of the measured values when the ratio of the bubble diffusivity to the turbulent viscosity varied from 0.5 to 2.

The general definition of the lateral lift force may be written in the following form (Thomas et al., 1983):

$$F_{Br} = -C_L \rho V_B U_r \times \nabla \times U \qquad \text{(II.48)}$$

where C_L is the lateral force coefficient. The lateral movement of a bubble due to the force is illustrated in Figure II.8, where the upward liquid flow has a dominant velocity gradient along the radial direction and a lateral displacement away from the centerline is shown for the bubble with higher rising velocity than the liquid.

There has been quite a large amount of work done on the lift force on particles, spheres or bubbles moving in liquid, although most of them are limited to specific situations (Auton,1987; Drew, 1988; Drew and Lahey, 1987; Giddings, 1988). In the case of small bubbles, Zun et al. (1975) modified the classic solution for a rotating sphere (Schlichting, 1959) and modeled bubble transport in terms of the lateral lift force and bubble diffusion. The idea was experimentally proved by Serizawa et al. (1975) and Beyerlein et al. (1985). Based on the idea of lateral dispersion force, Beyerlein et al. were able to set up a model to predict the lateral flux of the bubbles. Other theoretical development includes studies of lift force on particles in laminar flow (Southard, 1971; Halow and Wallis, 1970; Saffman, 1965; Summer, 1984) and in turbulent flows (Govan et al. 1989 and Hall, 1988). Most of the theoretical formulations of the lift force started from the analysis of forces acting on a single sphere.

Work involving both theory and systematic experimental measurements have been reported by Eichhorn and Small (1964), Beyerlein et al. (1985) and Wang et al. (1987). Eichhorn and Small formulated an expression to relate the lift force coefficient with flow variables of the two phases such as void fraction, axial liquid velocity gradient, bubble rising velocity and bubble relative velocity. They carefully measured the lift force on a solid sphere by balancing it with the lateral component of gravity in an inclined pipe flow. Eichhorn and Small's formulation was adopted by Wang et al.

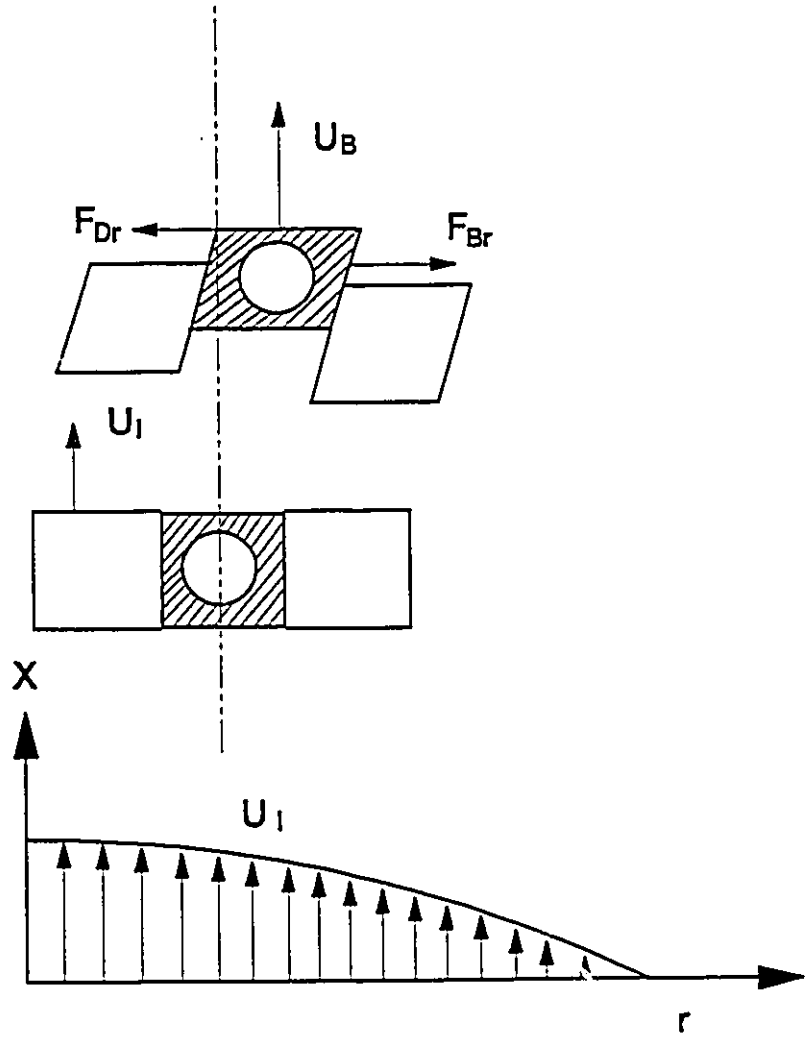

Figure II.8 Illustration of the lateral migration of a bubble due to the effect of the lift force

With their own experimental data from a bubbly pipe flow, Wang et al. developed a more comprehensive formulation, which will be further discussed in chapter V. Beyerlein et al. have performed a similar study to that of Wang et al., but they related the lift force coefficient with only the void fraction. The coefficient measured by them ranges from 0.03 to 0.3.

The above discussion reveals that, the lateral dispersion caused by the turbulent diffusion is the result of the random interaction of the bubbles with the turbulent eddies, which produces random patterns of the bubble trajectory. The apparent lateral migration is only a result of the random movement of a large number of bubbles. The lift force, on the other hand, is a result of the interaction of the bubble with the mean flow field of the continuous phase. Where the mean velocity gradient of the continuous phase is significant, it constantly drives the bubble toward the outer region of the plume. Some of the calculated void concentration contour is narrower than expected from experiments, such as the one reported by McKelliget et al. (1987) who considered only bubble diffusion effect; the reason may be due to the neglect of the lift force effect on the dispersion of these small bubbles.

2.2.4 Turbulence Modelling in Bubbly Plumes

Since most bubbly plume flows are of a turbulent nature, the turbulent k-ε model proposed by (Launder and Spalding, 1974) for single phase flow has been adopted in most studies for single-phase recirculating flow zones. Some attempts have also been made to apply the model to some simple multiphase flows, however, for the bubbly two-phase flows, the original k-ε model obviously lacks the ability to account

for the effect of the gaseous phase. To overcome this shortcoming of the k-ε model, the empirical relation of effective viscosity, which had been originally proposed by Pun and Spalding (1967) for a single phase combustion model, was adopted by Deb Roy et al. (1978) to bubbly plume study. The effective viscosity was formulated based on the mixing length theory:

$$\mu_{eff} = KD^{2/3}L^{-1/3}\rho_L^{2/3}(mU_o^2)^{1/3} \qquad \textbf{(II.49)}$$

where, K is an empirical constant, D and L are ladle dimensions, and **m** is the mass flow rate of the air. This equation is virtually the same as the form of Pun and Spalding, and implies the following phenomenological relations:

(1) μ_{eff} increases with local density,

(2) μ_{eff} increases with increase in the amount of fluid kinetic energy, and

(3) μ_{eff} increases with increase in diameter, but diminishes with increase in length.

The above formulation was modified by Sahai and Guthrie (1982). They take into consideration the gaseous phase effect by deriving a new formulation with mean void fraction as one of the main variables as follows:

$$\mu_{eff} = C\rho_L[Q(1-\alpha)g/D]^{1/3} \qquad \textbf{(II.50)}$$

where C is an empirical constant with a value of 5.5×10^{-3}. Since dimensional arguments were made in the derivation of this formulation, its authors claims that it is physically more plausible. Recently modifications were made by (Mazumdar, 1989), and a new value of 2.7×10^{-3} for C was derived for this model.

The above models are principally the same, they were derived on the basis of a macroscopic energy balance while neglecting all the origins of turbulence in the two fluids. Consequently the local turbulent characteristics of the two fluids in the plume zone cannot be investigated. The two-phase plume zone in these models is then almost a black box zone. Only mean values of the turbulent variables over the whole plume zone can be obtained.

More recently, a modified k-ε formulation was proposed for buoyant two-fluid models. The concerns about the application of the k-ε model to the multiphase flows have been two fold. The first is how to account for the generation and dissipation of the turbulent kinetic energy resulting from the interaction among the different phases at their interfaces, and the second is about the additional contribution to the turbulence due to the flow pattern changes, caused by the passage of the second phase.

Malin and Spalding (1984) proposed an additional source term for the transport equations for both k and ε when studying the process of injecting hot air into a stagnant cool air environment. They found that the spreading of the hot air jet was underestimated with the conventional k-ε model (Malin, 1983), and argued that this was a result of the neglect of the additional generation and dissipation of turbulence at the turbulent hot air and non-turbulent cool air interface. The extra source terms for k and ε in the following forms were then proposed to take into consideration these effects:

$$S_{Kl} = C_{kl}\,\alpha(1-\alpha)G \qquad \text{(II.51)}$$

$$S_{\epsilon 1} = C_{\epsilon 1}\,\alpha(1-\alpha)G\frac{\epsilon}{k} \qquad \text{(II.52)}$$

where, G is the usual generation term and C_{k1} and $C_{\epsilon 2}$ are empirical constants assuming values of 2.5 based on the experimental data of hot air jets.

The considerations made in the derivation of above equations are similar to those for Equations (II.49) and (II.50). It was simply assumed that this extra generation or dissipation of the turbulence is directly proportional to the usual generation of turbulence due to the turbulent shear, and also proportional to the volumetric fraction of the two phases, α and (1-α), respectively. The two empirical constants were experimentally determined and may not be universally applicable. Another point worth mentioning is that the hot air jet configuration is still a single phase flow, so that the existence of a clear interface between the hot turbulent jet and the cool non-turbulent surrounding air is uncertain. Proper consideration should be made before applying this model to bubbly two-phase plume flows.

To account for the effects on turbulence by the flow pattern change caused by the movement of bubbles, Simonin and Viollet (1988) proposed additional source terms for k and ϵ. The forms of them are similar to the terms proposed by Malin and Spalding:

$$S_{k2} = C_{k2}\,\alpha\,\rho_l C_f k \qquad \text{(II.53)}$$

$$S_{\epsilon 2} = C_{\epsilon 2}\,\alpha\,\rho_l C_f \epsilon \qquad \text{(II.54)}$$

Where, C_{k2} and $C_{\epsilon 2}$ are two empirical constants. For bubbles smaller than 5 millimetres rising in water, they assume a value of 0.3 as proposed by the authors. C_f is the friction factor defined by the following equation:

$$C_f = \frac{3}{4D_B} C_D |U_r| \qquad \text{(II.55)}$$

where, C_D, D_B and U_r are drag coefficient on bubble, bubble volume equivalent diameter and the relative bubble velocity.

The extra source terms made the conventional k-ϵ model applicable to the various two-phase flows, and the local turbulence can now be estimated. Although the actual functioning processes of the extra sources were not elaborated in detail, this phenomenological treatment of turbulence in the two-phase zone is still an improvement compared to the previous models. The main shortcoming of the extra source models is the difficulty in the determination of the new constants. The constants used in the conventional k-ϵ model were calculated based on the measurement of the variables in simplified k and ϵ equations with specially designed experiment, thus are considered to have universal applicability. The new constants, as proposed by their original authors, have not received any experimental verification, so that careful choice of these constants must be made when applying the model to various two-phase flows such as the bubbly plume flows. The extra turbulence sources should be stronger in bubbly plumes than in the case of two gaseous fluids, and consequently the constants may assume different values. The model with the original constants have been recently adopted to the bubbly plume flow study by Ilegbusi and Szekely (1990) and Burty et al. (1990) without any modification. Their predictions should not be as convincing as claimed by the authors due to the reasons discussed above.

The complete set of sources terms used in the modified k-ϵ model can be now summarized as follows:

$$S^k = G - C_D \rho \epsilon + C_{k1} \alpha (1-\alpha) G + C_{k2} \alpha \rho C_f k \tag{II.56}$$

and:

$$S^\epsilon = -\frac{C_1 C_\mu \rho k^2 G}{\mu k} - \frac{C_2 \rho \epsilon^2}{k} + \frac{C_{e1} \alpha (1-\alpha) G \epsilon}{k} + C_{e2} \alpha \rho C_f \epsilon \tag{II.57}$$

where G is related to P_k defined in Eq.(II.14) as follows:

$$G = \rho P_k \tag{II.58}$$

If a Lagrangian scheme is used, the modelling of the turbulence in the plumes is totally different, as proposed by Johansen and Boysan, (1988). In this model, the trajectory of each bubble is calculated, and the local void fraction is calculated by summing the contributions from many bubbles passing the same location. The effect of the passage of these bubbles on the turbulence is taken into account by assuming that, the shear work performed on the liquid by bubbles contributes to the production of the turbulence, and the work is equal to the product of the drag force on the bubble and the relative velocity. The total production of the turbulence in a unit volume due to the effects of bubbles, P_B, can be then estimated by summing contributions from all the bubbles passing the given control volume as follows:

$$P_B = \frac{Q_g}{N_B V_B} C_b \sum_{i=1}^{N_B} \int_0^{t_{ri}} \frac{3}{4} \frac{\mu_l}{D_B^2} C_D Re_B (U_B - U)^2 dt \tag{II.59}$$

where, C_b is an empirical constant within the range between 0 and 1, t_{ri} is the residence time of the ith bubble in the grid cell with a volume of V_B, and Re_B is the bubble Reynolds number.

The prediction of the turbulent velocities with this model was shown to be in rather good agreement with the measured ones. Questions remain, however, such as the accuracy of the local turbulence production calculation, and how much of the bubble work can be assumed to turn into the turbulent kinetic energy.

2.3 Experimental Study of Bubbly Plume Phenomenon

There are many experimental techniques for the study of various two-phase flow parameters as summarized by Banerjee and Lahey, (1981). For the purpose of this project, only Laser Doppler Anemometer (LDA) and Electric Resistance Probe (EP) techniques will be briefly reviewed here.

2.3.1 LDA Techniques for Two-Phase Flow Study

The basic principle of LDA is that the Doppler frequency shift caused by a body moving relative to the light source and the observer is linearly related to the velocity of the moving body. The frequency shift can be easily recorded with the LDA system. In the area of single-phase flow, LDA has been successfully used to measure both the mean flow field and the turbulent intensity of the flow for various fluids containing proper seeding.

The simplest way to demonstrate the operation principle of LDA is to use the fringe model as shown in Figure II.9. Two monochromatic laser beams intersect to form a focus which is called the measuring volume (MV). Typical MV size is listed in Table II.3.

Table II.3 Typical Data of a LDA Measuring Volume

λ nm	l_f mm	l_b mm	θ°	l_m mm	h_m mm	N_f	d_f μm
633	300	26	5	6	0.22	30	7.3

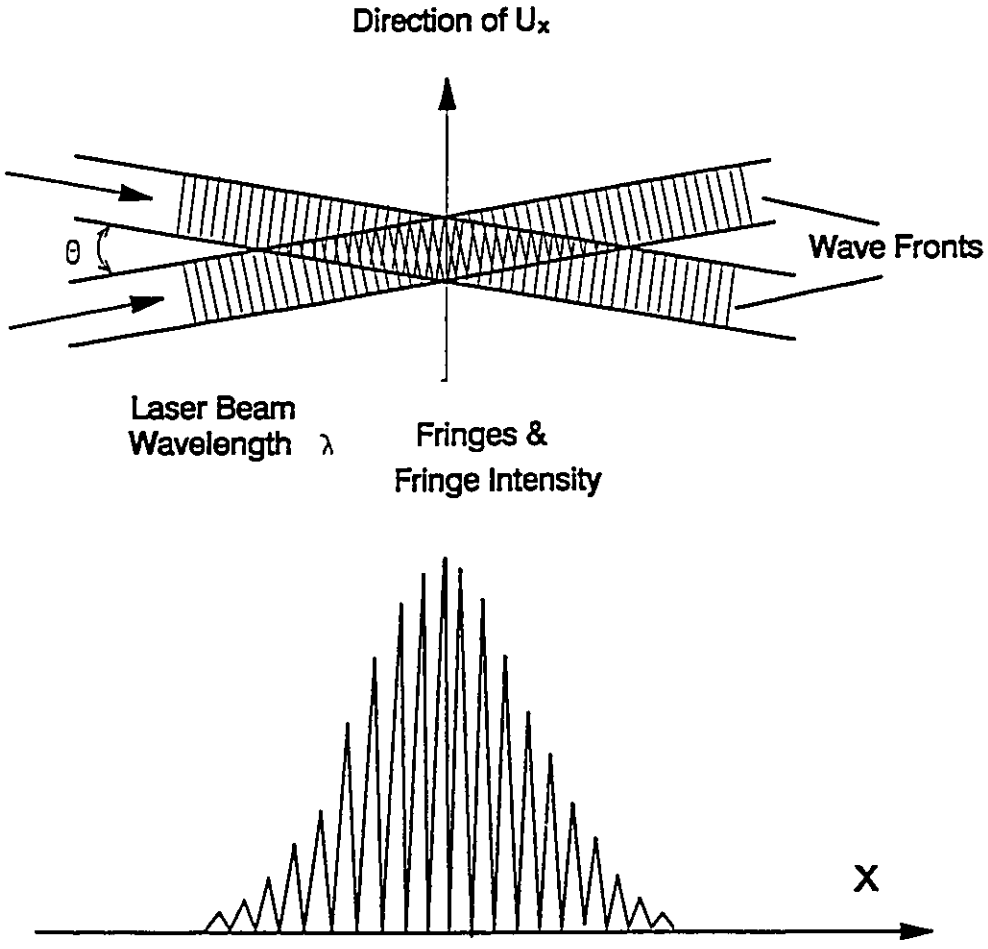

Figure II.9 Illustration of the formation of fringes within a LDA focus The upper diagram shows a particle moving through the focus with velocity U_x, and the lower diagram shows the intensity of light reflected from the particle

where, λ is the wavelength of the laser beam, l_f the focal length, l_b separation between two laser beams, θ intersection angle of laser beams, l_m length of the measuring volume; h_m height of the measuring volume, N_f number of the fringes in the measuring volume and d_f fringe spacing.

Due to the interference of the two beams, alternating dark and bright fringes form inside the measuring volume. The spacing between two neighbouring bright and dark fringes can be calculated with the following equation:

$$\delta_f = \lambda/(2\sin\frac{\theta}{2}) \qquad \textbf{(II.60)}$$

When a moving particle with velocity U passes through the measuring volume, it scatters light from the bright fringes at a frequency equal to the doppler frequency shift, which can be calculated with:

$$f_D = \frac{U_x}{\delta_f} = \frac{2U_x}{\lambda}\sin\frac{\theta}{2} \qquad \textbf{(II.61)}$$

When this frequency is recorded with a photomultiplier (PMT) and analyzed with a LDA signal processor, e.g. a counter or frequency tracker, the velocity U_x can be obtained (Drain, 1980).

For two-phase flows, special difficulties arise. First, since most of the two-phase flows contain particles or bubbles with sizes much larger than the measuring volume of the LDA, their surface shape may affect doppler signals. Secondly, since there exist two sources of velocity from the two phases which are recorded by the LDA at the same time, the discrimination of the mixed velocities is a very difficult problem.

It was Durst and Zare (1975) who first tried to tackle the problem both theoretically and experimentally. They derived the relations between Doppler frequency shift and velocity for reflecting or refracting surfaces, and recorded and analyzed signal shapes from different objects. They measured the particle or bubble velocity with a multichannel signal analyzer to discriminate the bubble's velocity from that of the fluid. Ohba et al. (1976, 1977, 1986) proposed a clearer relation between the Doppler shift and the velocity of large objects. They used a spectrum analyzer to discriminate the bubble's signals from those of the liquid. They also used the laser attenuation technique to measure the void fraction in the two-phase area. Martin et al. (1981) later proposed another technique to discriminate the velocities of different phases. They experimentally proved that the amplitude of the pedestal, which is the low frequency component of the intensity variation of the Doppler signal, increases with particle size and the recorded pedestal amplitude is proportional to the pinhole size. With this discovery, they were able to design an adjustable pinhole aperture to record only bubble signals. This method was later used by Durst et al. (1986) with two LDA systems and four extra photodiodes to measure bubble rising velocity, bubble size, bubble frequency and liquid velocity at the same time. The extra diodes were put opposite to the laser beams; when large objects pass through the laser focus, the beams were blocked which causes an interruption of signals from the diodes. The blocking time, together with the moving velocity of the object, is used to calculate the size of the object. A similar technique was also used by Lee and Srinivasan (1978) to measure the velocity variation in a particulate two-phase flow. By using two photomultipliers and one photodiode, Lee and Durst (1982) and Lee and Cho (1983) measured the blocking and velocity of particles at the same time and obtained instantaneous particle size measurement.

Although application of LDA techniques to two-phase flow study has a history of less than 20 years, many attempts have already been tried and encouraging results obtained. Most of the applications use similar techniques as those discussed above. Table II.4 summarizes the operating conditions and results of some researchers' work in this field. The following conclusions may be drawn from this body of work:

(1) LDA is capable of measuring the velocity of objects with sizes larger than the measuring volume of the LDA. Signals from larger objects are different from those from much seeding particles in both doppler amplitude and pedestal amplitude. The difference can be used to discriminate the two velocities.

(2) The discrimination based on amplitude or other signal properties needs specially designed electronic equipment, which makes the application of LDA to two-phase flow problems much more expensive than to a single phase flow.

(3) The discrimination can be also achieved by specially designed LDA optical settings, e.g. use of two PMT to measure velocities of the two phases and use photodiodes to record the blocking of the laser beam as an indication of the passage of bubbles. This also requires expensive extra equipment.

It must be pointed out now, that all the above mentioned techniques only work in limited circumstances, i.e. in a chain of small bubbles with fairly smooth interfaces or in a particulate flow where signals from the two phases are really much different from each other. Another shortcoming of the amplitude discrimination technique is that the measuring time is too long; sometimes it takes more than half an hour to measure the velocity from one point inside a chain of bubbles (Boerner et al.

Table II.4 LDA for the Two-Phase Flow Measurement

Reference	Laser & Optics	Data Taken	Data Analyzer	Discrimination Technique
Boerner et al. (1984)	15 mW He-Ne	U	Counter	Amplitude analysis
Durst & Zare (1975)	15 mW,He-Ne, 2 PMT, or 2 PD	U_p, U_B	Multi-channel analyzer	characteristic analysis of signal (amplitude and wave shape)
Durst et al. (1986)	15 mW, He-Ne, 2 LDA, 2 PMT, 4 PD	U_B, U_l D_B, f_B	Frequency tracker	Amplitude and blockage of light to photo diodes
Lee & Srinivasan (1978)	15 mW He-Ne	PDF of U_p	Tracker & counter	Amplitude & time discrimination
Lee & Durst (1982)	15 mW 1 PMT 2 PD	U_p, U_B	Unknown	Amplitude and frequency discrimi nation with special filterbanks
Lee & Srinivasan (1982)	15 mW, He-Ne, 1 PMT, 1 PD	U_p, D_p	Counter	Amplitude gating & blocking
Lee & Cho (1983)	15 mW, He-Ne, 2 PMT, 1 PD	U_p, D_p	Two counters	Amplitude gating & blocking
Marie & Lance (1983)	Unknown	U_B, U_l	Frequency tracker	Two distinct peaks on the velocity PDF
Martin et al. (1981)	5 mW, He-Ne, 2 PMT	U_B, D_B	Unknown	Pinhole aperture for amplitude analysis
Momii et al. (1986)	Unknown	U_l, U_p	Unknown	Forward scattering for U_l, backward for U_p
Ohba et al. (1976a,b)	15 mW, He-Ne	U_l, α	Spectrum analyzer, etc.	Light attenuation for void fraction
Ohba et al. (1986)	15 mW, He-Ne, 2 PMT	U_B, U_l	Spectrum analyzer, etc.	Light blocking of one PMT for U_B
Tsuji et al. (1984)	15 mW, He-Ne	U_p, U_B	Tracker and Special signal analyzer	Amplitude analysis of both the Doppler & the pedestal
Ueda et al. (1986a,b)	Unknown	U_l, U_p	Unknown	Setting optimum threshold values for the Doppler signal amplitude

1984). The most inconvenient aspect is that all the above mentioned techniques are not directly applicable to the bubbly plume study. Because of the very irregular interface of the wobbling bubbles, signals from bubbles in plumes are not always stronger than those from the liquid, and the noise is much stronger. Gating and blocking is not useful either, due to the fact that many bubbles are present at the same time inside the bubbly plume. To meet the demand of the experimental study of the bubbly plume flows, a new technique must be developed.

2.3.2 EP Technique for Two-Phase Study

Electric probes have been used to study flow phenomena for a long time (Hinze, 1975). The principle for the measurement of bubble behaviour in a bubble/water two-phase flow using an electric resistance probe is that the conductivity of any gas is much lower than that of water, so that when the probe tip is enclosed by a bubble, there would be a large change of voltage in the measuring circuit compared to when the tip is in water. With an EP and a good signal processor, it is possible to measure the bubble frequency, the void fraction and the bubble sizes if the rising velocity of the bubble is also known. With a double EP technique, it is also possible to measure the rising velocity of bubbles when two tips of the probes are arranged along the bubble's path with known separation (Hardy and Hylton, 1984; Castillejos and Brimacombe, 1987).

Extensive measurements of bubbly two-phase flow were first done by Seriwara et al. in 1975 when they systematically measured bubble behaviour in a bubbly pipe flow. Welle (1985) also used the technique to measure the rising velocity, size and

void fraction of bubbles in a bubbly pipe two-phase flow. For the purpose of metallurgical study, Sano and Mori (1980a,b,1983) have applied the technique to the study of the bubbly plume in injection metallurgy; they measured the spatial distribution of bubble frequency and void fraction in a water model ladle and in a mercury bath. Similar studies were also carried out by He et al. (1984) in a water model ladle and Kawakami et al. (1985) in molten iron. Recently, Castillejos and Brimacombe (1987a,b) used a specially designed double EP system and carefully measured the spatial distributions of bubble frequency, void fraction and bubble rising velocity. All these works provided a fairly clear understanding of the bubbly plume phenomena in metallurgical processes.

The disadvantages of the electric probe are its intrusive effect on the flow field, and its effects on bubbles' rising velocity measurement when it contacts the bubble. It is not possible to measure the liquid velocity with electric probe techniques. To better understand the bubbly two-phase flow, it is necessary to develop a technique which combines the EP with a powerful velocity measuring technique, such as LDA.

CHAPTER III

A COMBINED LASER DOPPLER ANEMOMETER AND ELECTRICAL PROBE TECHNIQUE FOR BUBBLY FLOW DIAGNOSTICS

3.1 Conception of the Combined LDA and EP Technique

To understand the dynamic process of a bubbly plume flow, it is essential for one to be able to measure both the velocities of each phase and the characteristic parameters of the gaseous phase, such as the local values of the bubble frequency and the void fraction. As discussed in the previous chapter, equipment such as a Laser Doppler Anemometer (LDA) can be used for the measurement of a single phase velocity, or velocity of the discrete phase in a two-phase flow under very limited conditions. The Electrical Probe (EP) can be used for the measurement of bubble frequency and void fraction. However, for the measurement of a bubbly plume flow, the application of LDA and EP individually are very limited. Due to the very irregular behaviour of bubbles in the plume zone, it is very difficult to use LDA to measure velocities of the two phases at the same time, and to measure bubble frequency and void fraction. On the other hand, an electrical probe is not able to measure the velocity of the liquid phase. It is then logical for one to think of the combination of the two types of equipment, i.e., using LDA for velocity measurement while using EP for bubble frequency and void fraction measurement. If the signals from EP can be recorded

simultaneously with that from LDA, it is also possible to use the EP signal for the purpose of phase identification.

The main feature of the combined Laser Doppler Anemometer and Electrical Probe technique developed in this project is as follows. At the point in the two-phase flow zone where measurement is to be made, the LDA measuring volume is first focused, and then the electrical probe is carefully put to a position about 1 mm below and 1 mm beside the measuring volume, where it causes least interference of the flow. If the electrical probe is put above the measuring volume, the probe may not be able to detect a bubble which just reaches the measuring volume. With the present arrangement of the equipment, when a bubble is at the measuring volume of the LDA and generates a velocity signals, the bubble is also sensed by the electrical probe in most cases. There are some exceptions, such as when the bubble is about to leave the measuring volume while the EP tip is already out of the bubble. With the EP signal, values of bubble frequency and void fraction can be obtained, and the LDA velocity signal from the bubble can be identified so that all the velocity data of the bubble can be separated from the mixed signals. With the help of the simultaneous response from the electrical probe, it is not necessary to use any other modifications to the LDA for the purpose of discriminating signals from the gas or liquid phase. This technique is also described in a recent publication (Sheng and Irons, 1991).

3.2 Characteristics of LDA

The LDA system used in this project consists of one He-Ne laser (DANTEC model 127) with a power of 60 mW, one DISA Type LDA counter processor, one

photomultiplier and one oscilloscope. The LDA system and the experimental set-up are shown in Figure III.1, and Figure III.2 respectively. The LDA can be operated in both backward and forward scattering for two-phase velocity measurement.

The original Doppler signal burst consists of fringes as those shown in Figure II.9. The signals are then transformed into square waves as shown in Figure III.3 before being sent to the counter for further processing to yield velocity data.

The counter has two time registers. The high count register records the time of 8 fringes, t_H, and the low count register records the time of 5 fringes, t_L, as shown in Figure III.3. With the time for the given number of fringes known, the doppler frequency can be obtained. The quality of the measurement is controlled by the validation circuit used in the counter, which performs the following operation:

$$100 \cdot \left| \frac{5}{8} \cdot t_H - t_L \right| \leq e \frac{5}{8} t_H \qquad \textbf{(III.1)}$$

where, e is the tolerance in % of the result of the comparison, and can be adjusted. A typical value of e used in the present experiment is 1.5%. If the fringes are not from a Doppler burst caused by the passage of a particle through the measuring volume, the time intervals between them would not be regular. As a result, the LHS of Eq.(III.1) would be larger than when the fringes have the same time interval. When the LHS of Eq.(III.1) is bigger than the given tolerance level, the burst would be treated as a noise. If Eq.(III.1) is satisfied, validated velocity data would be obtained.

There are several operational modes for the counter (Tropea and Struthers, 1987), two of which were used in the experiment, namely, Fixed Mode and Combined

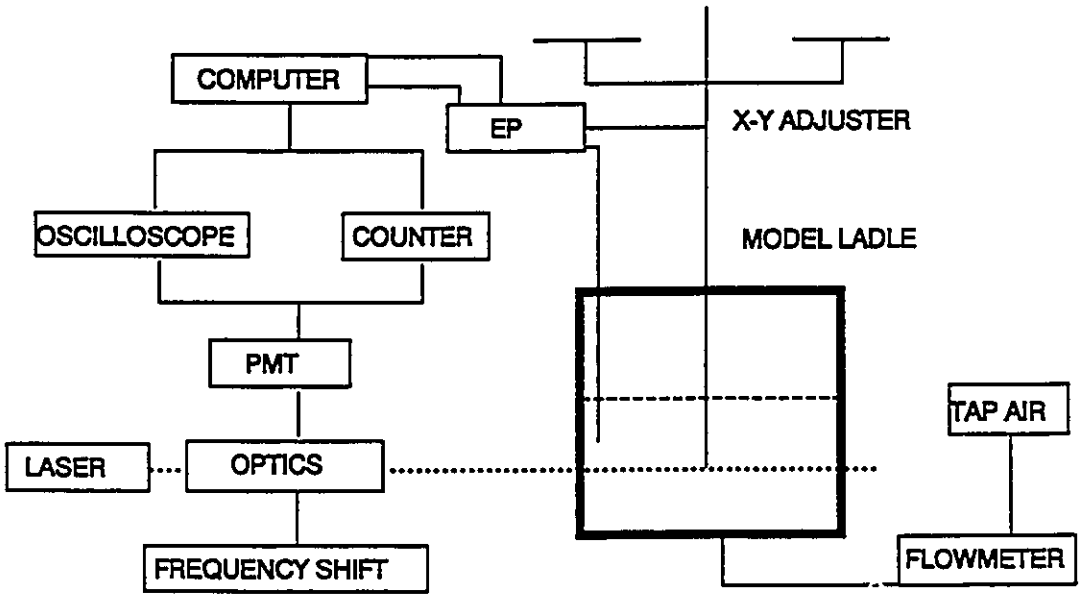

Figure III.1 Illustration of the LDA/EP experiment set up

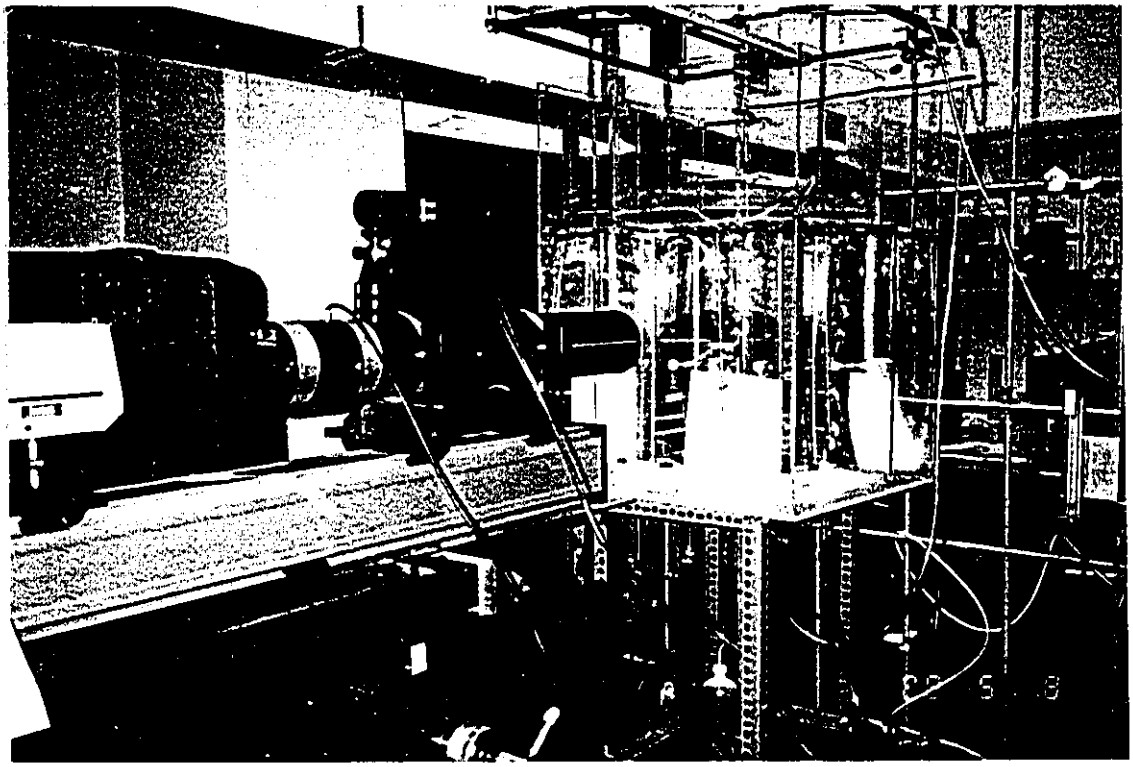

Figure III.2 Photograph of the LDA/EP experiment set up

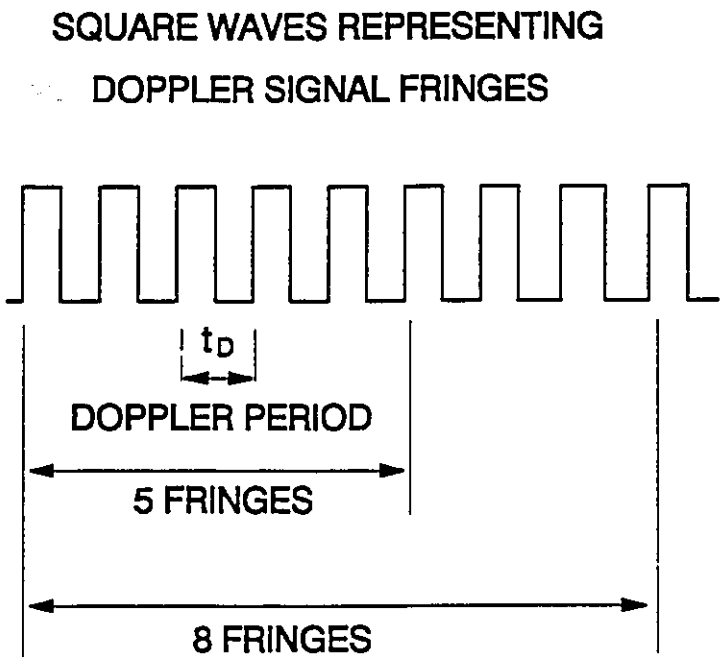

Figure III.3 Illustration of the square waves representing the Doppler signal fringes

Mode. With the Fixed Mode, the counter performs the validation for all the fringes, and all the validated data are recorded. As a result, a signal burst can yield several velocity data, when the number of fringes in the burst is much larger than 8, which is the number of fringes needed for one velocity validation. With the Combined Mode, all the fringes contained in a burst are counted, but only the first 8 fringes are used for the 5/8 comparison. As a result, only one velocity datum can be recorded for a burst, no matter how many fringes it contains. The Fixed Mode is suitable for the flow pattern measurement which requires data continuity in the measurement, such as measuring the velocity variation in the interval between two bubbles. The Combined Mode is better for the measurement of mean velocity with less data fluctuation, such as in a single phase flow. In this case, the same number of data were taken from more signal bursts, and the sampling time is longer.

The LDA system has also an analog data acquisition channel which can be operated simultaneously with the digital data acquisition, and the analog data acquisition can be carried out under either the Timer Mode or LDA Mode. When the Timer Mode is chosen, the data are acquired at a pre-set time interval. In this case, the velocity data would be obtained in the following way. If a velocity datum is validated at the same time as the analog datum, this velocity datum would be recorded, however, if there is no validated velocity datum at the moment an analog datum is to be taken, the previous velocity datum would be taken over as the velocity at this moment. When LDA Mode is chosen, the analog data are enabled by validated velocity data. For the purpose of two-phase velocity measurement, the LDA Mode is more suitable, while for the measurement of gas parameters, such as the bubble frequency and void fraction, with EP analog input, the Timer Mode is better. In case of high LDA data rate, it is also possible to obtain good flow pattern measurement.

3.3 Characteristics of the Electrical Probe

The structure of the electrical resistance probe and the measuring circuit used in this experiment are shown in Fig.III.4 and Fig.III.5 respectively. To increase the sensitivity, a bridge circuit was used. The EP signals were collected by the same A/D interface (Tropea and Struthers, 1987) as the LDA signals and controlled by the same computer program so that simultaneous EP and LDA data acquisition was achieved. For different purposes as discussed in the previous section, either Timer Mode or LDA Mode can be chosen for the measurement.

3.4 Data Acquisition and Processing

The procedures of acquisition and processing of both LDA and EP data are shown in Figure III.6. The raw data of both LDA and EP are collected and stored with the help of computer program LDAMP. The LDAMP is a general measurement program for use with the LDA data acquisition interface (Tropea, 1986; Tropea and Struthers, 1987). It acquires data from the LDA interface and stores them in unformatted files on a disc. These raw data are then processed with different programs to obtain the following variables.

(1) Local time averaged void fraction and bubble frequency from the EP raw data. The mean values of void fraction and bubble frequency are calculated with the following equations:

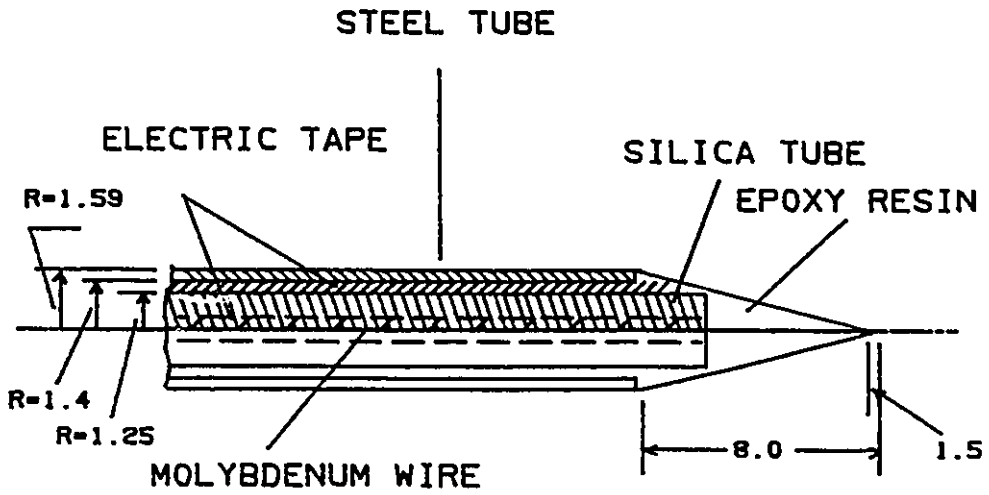

Figure III.4 Illustration of the details of the electrical probe tip. The dimensions are in mm.

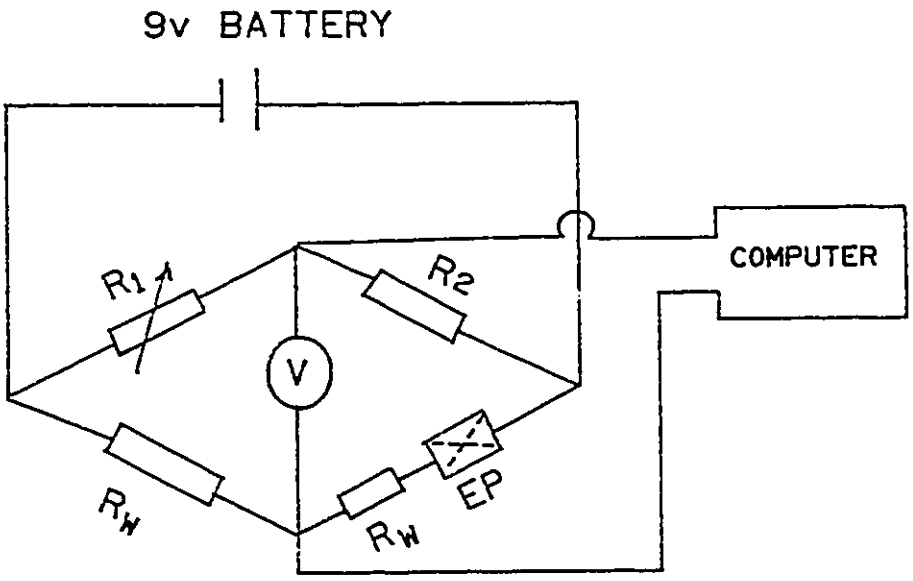

ELECTRIC PROBE CIRCUIT

Figure III.5 Illustration of electrical probe circuit to improve sensitivity

$$\alpha = \frac{N_B}{N_B + N_l} \tag{III.2}$$

$$f_B = \frac{N_{Bp}}{T} \tag{III.3}$$

where, N_B is the number of EP data with the voltage higher than the threshold separating signals of bubble from signals of liquid, and N_l is the number of liquid signals, whose voltage are lower than the threshold. N_{Bp} is the number of EP voltage pulses over the threshold, and T is the measuring time.

(2) Mean velocities of both liquid phase and gas phase along both vertical and radial directions from the raw data of LDA and EP using the following equations:

$$U = \frac{1}{N_l} \sum_{i=1}^{N_l} u_i \tag{III.4}$$

and:

$$U_B = \frac{1}{N_B} \sum_{i=1}^{N_B} u_{Bi} \tag{III.5}$$

(3) Turbulent components of velocities are obtained with the following equations:

$$u' = \sqrt{\frac{1}{N_l - 1} \sum_{i=1}^{N_l} (u_i - U)^2} \tag{III.6}$$

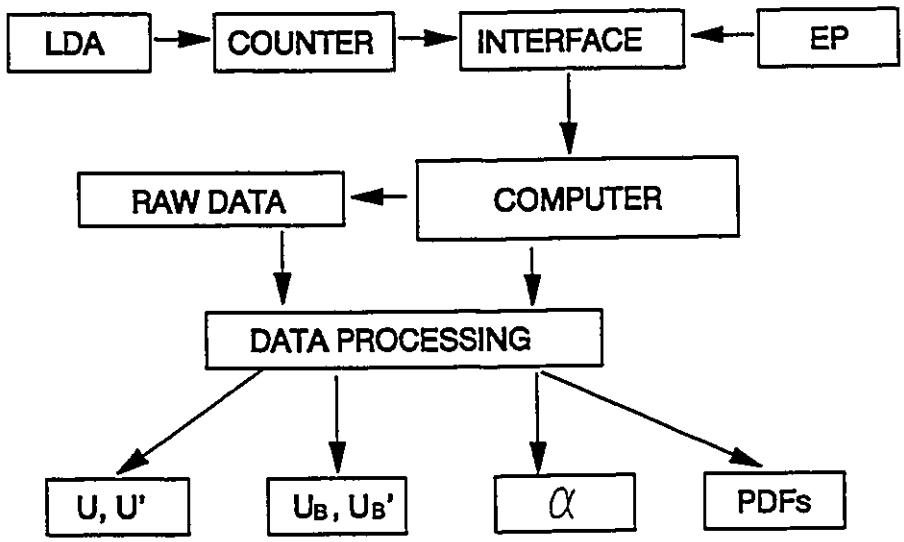

Figure III.6 Illustration of the data acquisition and processing

$$u_B' = \sqrt{\frac{1}{N_B - 1}\sum_{i=1}^{N_B}(u_{Bi} - U_B)^2} \qquad \text{(III.7)}$$

(4) The time series of liquid phase velocity which can be utilized for the analysis of turbulent characteristics of the flow.

3.5 Results of Preliminary Experiments

3.5.1 Calibration of the Technique

For preliminary evaluation of the combined LDA and EP technique, a small plexiglass box (100 x 100 mm^2 x 150 mm high) was used at low gas flow rates in which individual bubbles followed each other in single file (bubble chains). The box was filled with distilled water to 125 mm in depth. A 4 mm inside diameter copper tube was placed 25 mm above the bottom. The EP was positioned 45 mm above the nozzle. The gas flow rate was varied between 0.58 ml/s and 20.2 ml/s. In order to improve the liquid velocity signals, small quantities of market rice powder were used for seeding. With proper seeding, acceptable data rates could be achieved (0.1 kHz to 0.2 kHz).

To calibrate the combined LDA/EP technique for bubble frequency, void fraction and bubble velocity, still photographs were taken with strobelight illumination. The movement of bubbles during the time interval between two flashes is shown in Figure III.7. The simultaneous variation of the EP voltage and LDA velocity with time are shown in Figures III.8 and III.9, for forward and backward scattering, respectively.

In Figure III.8, LDA was operating under TIMER mode, so that both LDA and EP data were obtained at a pre-set frequency of 0.1 kHz. All the EP voltage data are true values, but not all the LDA velocity data are. At the time when data are to be taken, if there is a validated velocity datum, then this datum would be recorded as a true value, if there is none, then the previous velocity datum would be taken as the present value. Attention should be paid to the bubble velocity data too. Since forward scattering was used, most bubble velocity data could not be recorded because of the blockage to the PMT by the bubble at the focus itself. In Figure III.9, the LDA was working under LDA mode and backward scattering was used, the velocity variation caused by bubble passage was well recorded and indicated by the EP voltage response. Even without the information from the EP on the presence of bubbles, the liquid and gas velocities can be clearly distinguished, when there is only a low frequency chain of bubbles.

When bubble velocities are separated from the liquid velocities on the basis of the probe measurement, they compare favourably with those measured from the strobe photographs as shown in Figure III.10. The difference between them is negligible at 95% significance level, using Student's t-test.

Bubble frequency can be measured by either the EP or by visual inspection of the LDA velocity time series, such as in Figures III.8 and III.9, however, the latter method can only produce good bubble frequency measurements when the void fraction is low and the passage of the bubble is clearly indicated by the peak velocity variation. In such situations there is good agreement with frequencies from the strobe photographs; the difference is less than 5% (Figure III.11).

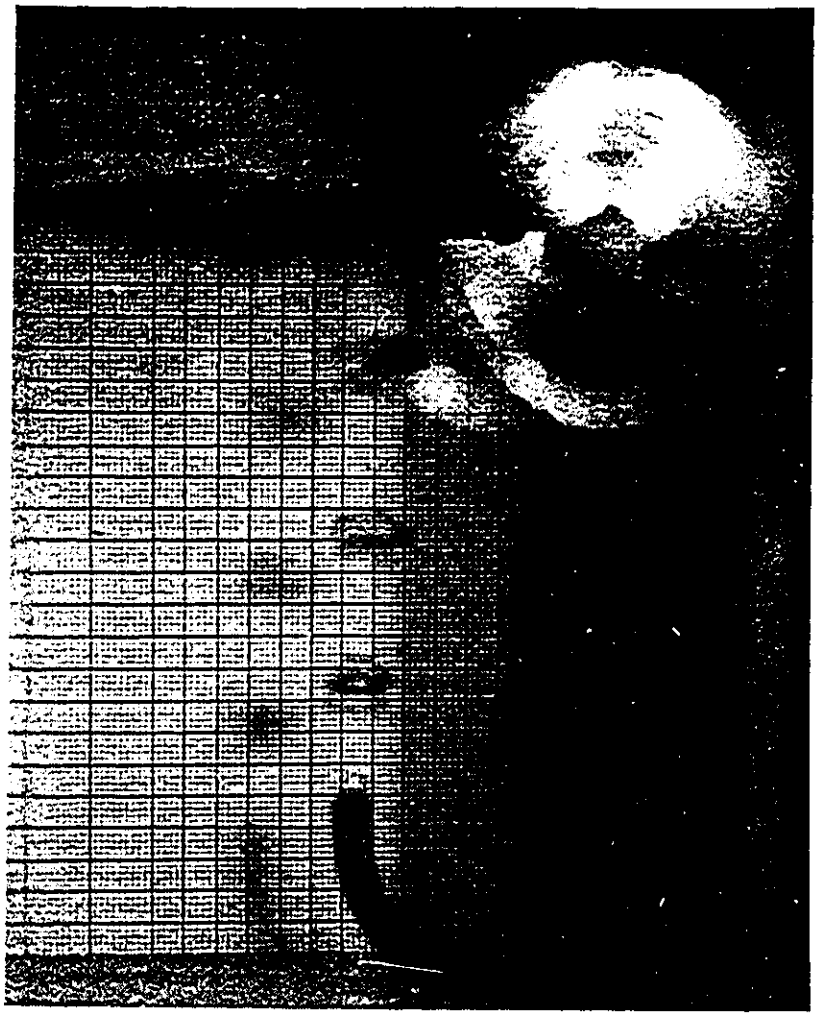

Figure III.7 Photograph of the movement of the bubble chain in the small tank during two flashes of the strobe light. The bright spot at the upper right corner is the reflection of the strobe light. The injector used has an inner diameter of 4 mm and outer diameter 6 mm. The strobe light frequency was 105 Hz, the gas flowrate was 5×10^{-6} Nm^3/s, U_B=0.40 m/s, α=0.31, f_B=14.5/s, and D_B=8.8 mm.

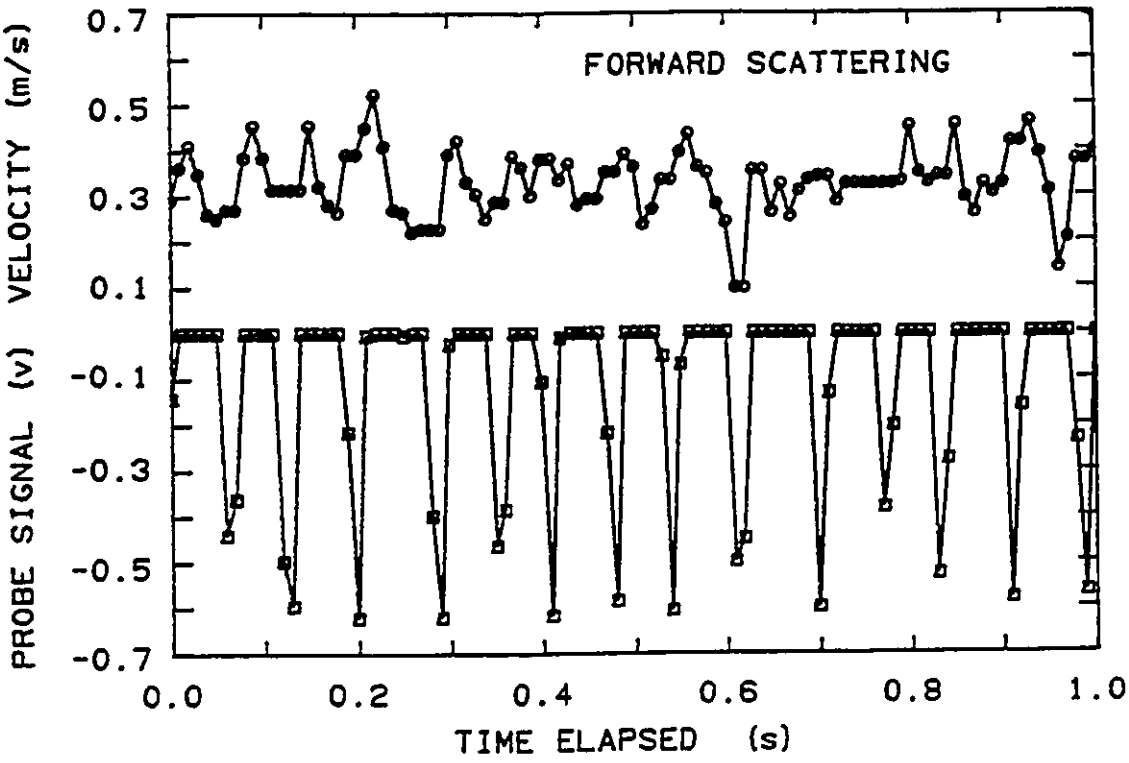

Figure III.8 Time series of velocity (upper) and probe voltage (lower) produced in the forward scattering configuration. This was performed in the small box with a nozzle of 4 mm in diameter. The LDA was operated under mode of Fixed/Timer. Q_g=5.0x10^{-6}Nm^3/s, U_B=0.40 m/s, α=0.31, f_B=14.5/s, and D_b=8.8 mm.

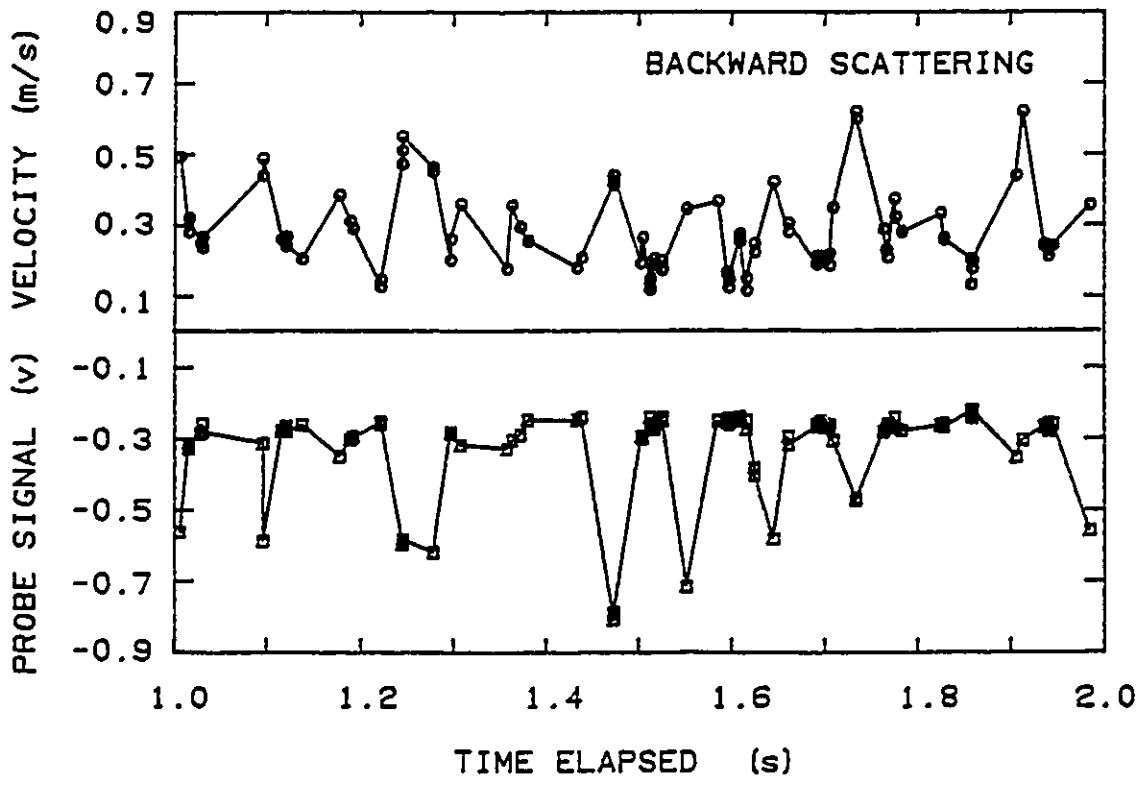

Figure III.9 Time series of velocity (upper) and probe voltage (lower) produced in the backward scattering configuration. This was performed in the small box with a nozzle of 4 mm in diameter. The LDA was operated under mode of Combined/LDA. Q_g=7.75x10^{-6}Nm^3/s, U_B=0.44 m/s, α=0.38, f_B=15/s, and D_b=9.96 mm.

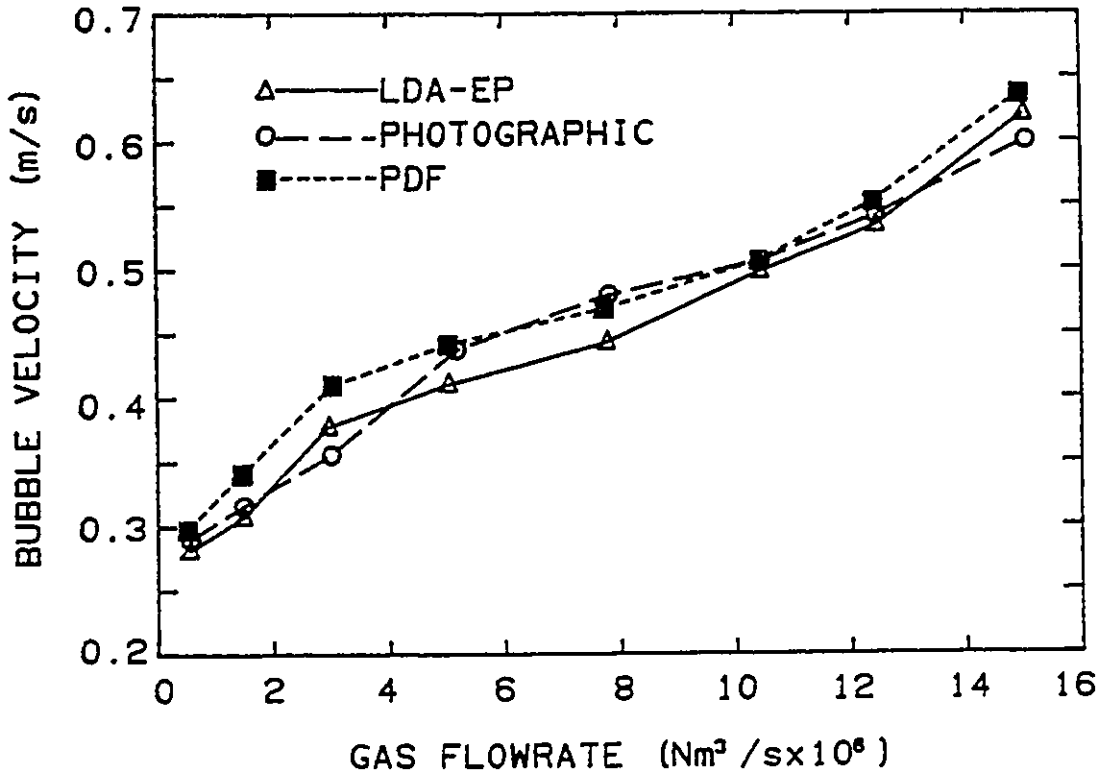

Figure II.10 Bubble velocity measured by three different methods in a bubble chain. In the photographic technique the distance travelled between strobe flashes was used. The LDA/EP technique simply involved inspection of the probe voltage time series for U_B. The PDF technique is described in the text. The agreement between the methods is very good. For these experiments the small box was used with a 4 mm diameter nozzle. LDA was operated under Combined/LDA mode with backward scattering.

The present LDA velocity time series, by itself, cannot be used to obtain the void fraction, because the data rate is too low to produce several signals during the passage of a bubble, thus the time resolution is poor. On the other hand, the electrical probe data are reliable measures of the time-averaged void fraction, as discussed in the Review of the Literature. The time-averaged void fraction at the measuring point was independently calculated from the bubble height in the rising direction, D_{Bh}, bubble frequency, f_B, and bubble velocity, U_B, which were measured from the photographs:

$$\alpha = f_B D_{Bh} / U_B \qquad \textbf{(III.8)}$$

As Figure III.12 shows, there is good agreement for the void fraction from the photographic and EP techniques; the differences are negligible at the 95% significance level.

3.5.2 Techniques for the Discrimination of Gas and Liquid Velocities

3.5.2.1 Discrimination Based on the Probability Distribution Function of Two-Phase Velocity

Very small bubbles, with sizes from less than 1 mm to 4 mm, are produced when gas is injected through the fritted glass, and in these cases it is easy to see the velocity distributions for the gas and liquid because there is little overlap (Figure III.13). However, for bottom injection the bubbles are considerably larger and there is more overlap in the probability distribution function (PDF). For example, in Figure III.14, the bubble velocities appear at the knee at approximately 0.3 m/s, as a result, visual

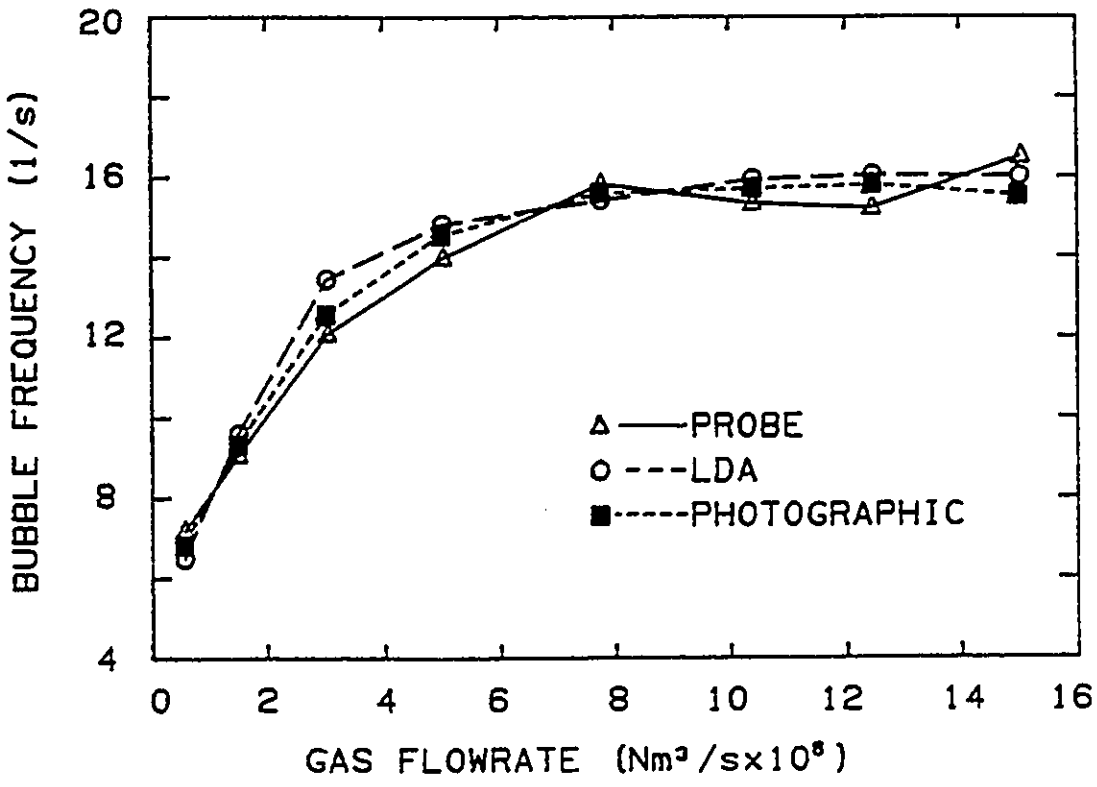

Figure III.11 Bubble frequency measured by three different methods in a bubble chain. The LDA method involved inspection of the velocity time series. The photographic technique is described in the text. For these experiments, the small box was used with a 4 mm diameter nozzle. LDA was operated under Combined/LDA mode with backward scattering.

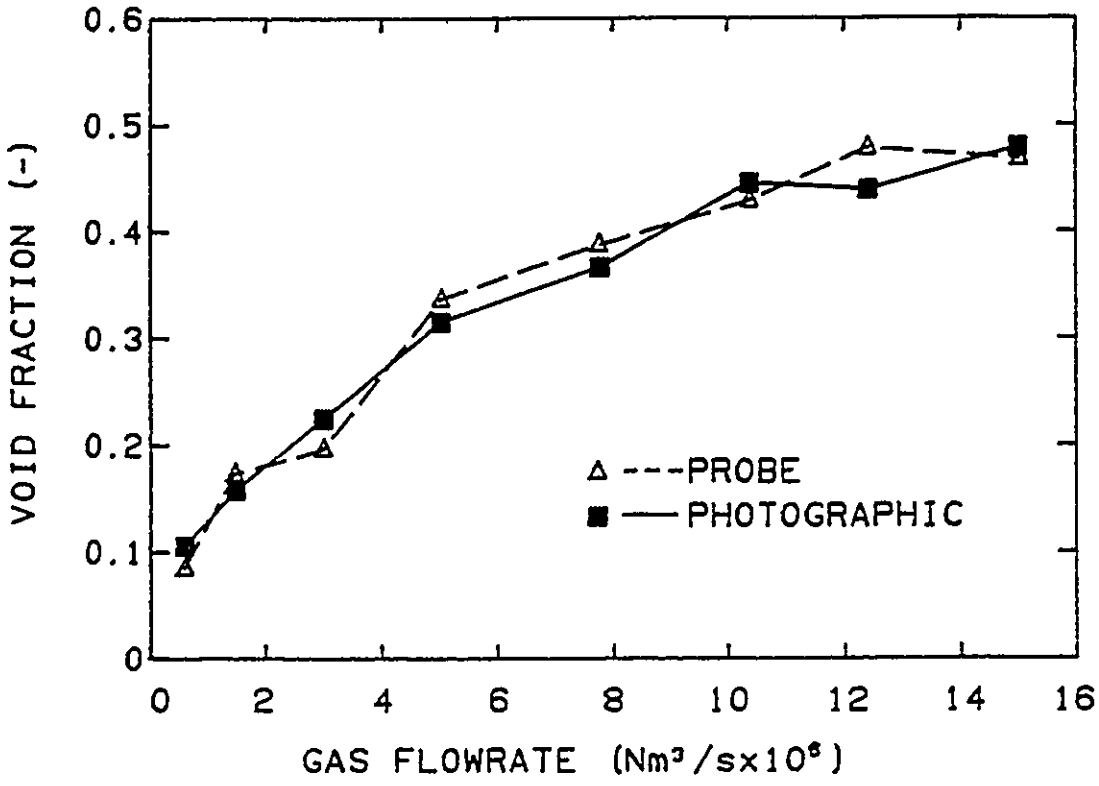

Figure III.12 Void fraction measured by the electrical probe and photographic techniques. Bubble chain produced in small box with a 4 mm diameter nozzle. The LDA was operated under Fixed/Timer mode with data acquisition rate of 100 Hz for f_B and α.

inspection cannot be used to separate the distributions. A statistical technique was investigated to solve this problem.

3.5.2.2 Discrimination by Mixture PDF

The statistical technique is best described graphically. Independent normal distributions of the gas and liquid velocities will appear as straight lines in normal probability plots, as shown in Figure III.15. Mixtures of these two distributions according to:

$$U_m = \alpha U_g + (1-\alpha) U_l \qquad \textbf{(III.9)}$$

with various void fractions, α, will not be straight except at the tails of the distribution as shown in Figure III.15. Tangents to the tails represent the superficial velocity distributions of the gas, αU_g, and liquid, $(1-\alpha)U_l$. These relationships were used in the following procedure to separate the gas and liquid velocities:

(1) Plot the mixture velocity distribution on normal probability paper, as illustrated in Figures III.16 and III.17, for the data in Figures III.13 and III.14, respectively.

(2) Construct tangents to the tails to obtain the superficial velocity distributions for gas and liquid.

(3) Make an initial guess of the void fraction, α.

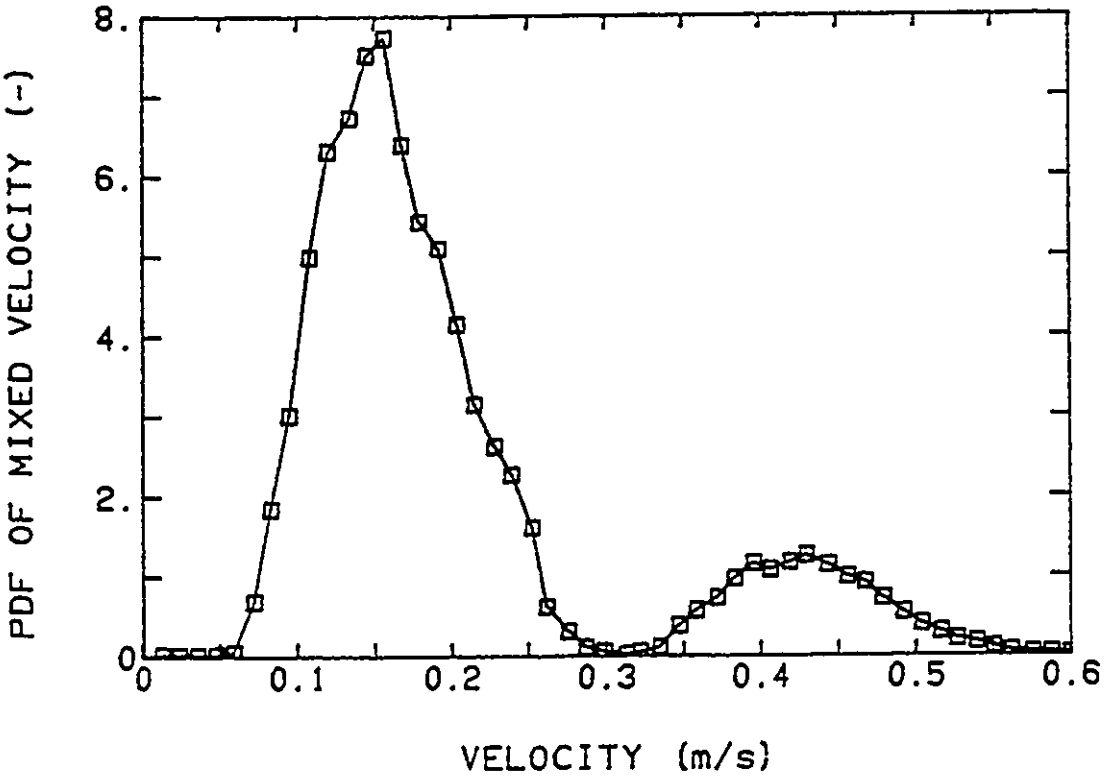

Figure III.13 Velocity Probability function for the gas and liquid velocities. The plume consisted of small bubbles (approximately 2 mm diameter) produced with a fritted glass injector inside the model. The data were taken at a position 30 mm above the injector and 10 mm away from the plume centerline. The LDA was operated under Combined/LDA mode with backward scattering. Q_g=5.0x10^{-6} Nm^3/s, and α was estimated to be approximately 0.01 at this position.

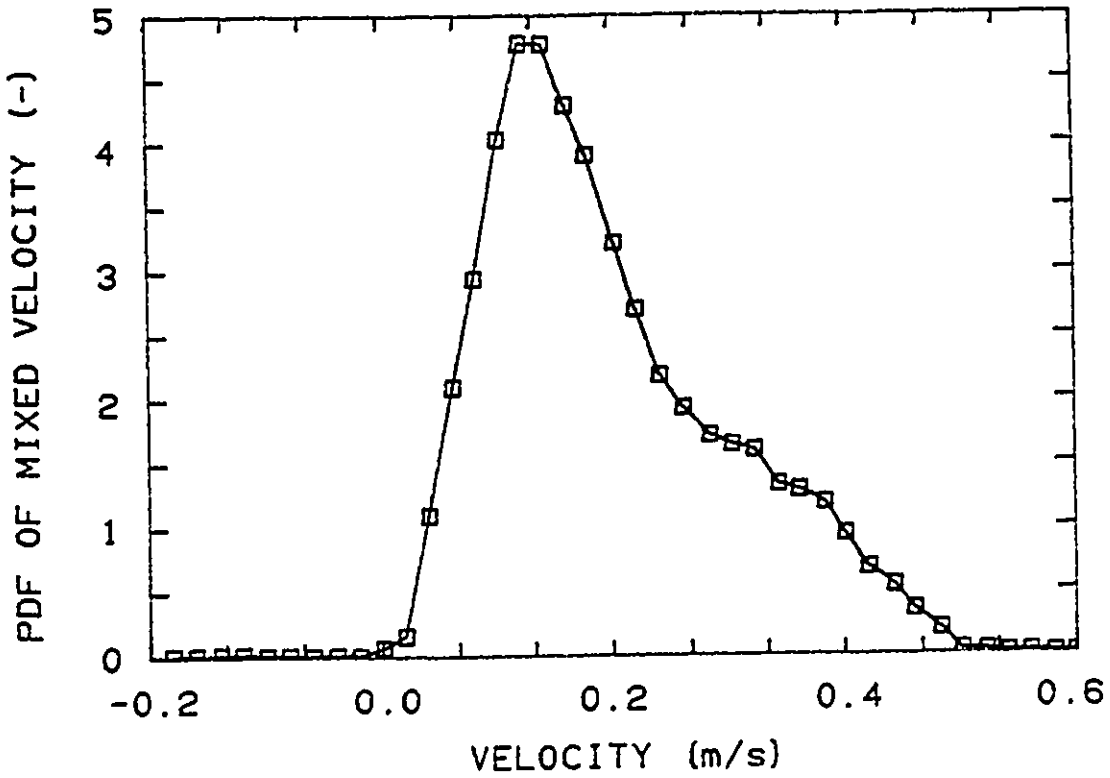

Figure III.14 Velocity Probability function in a chain of bubbles. The chain was produced in the small box with a 4 mm diameter injector. The LDA was operated under Combined/LDA mode with backward scattering. Q_g=1.5x10^{-6} Nm^3/s, U_B=0.32 m/s, f_B=9.2/s, D_B=6.8 mm, and α=0.18.

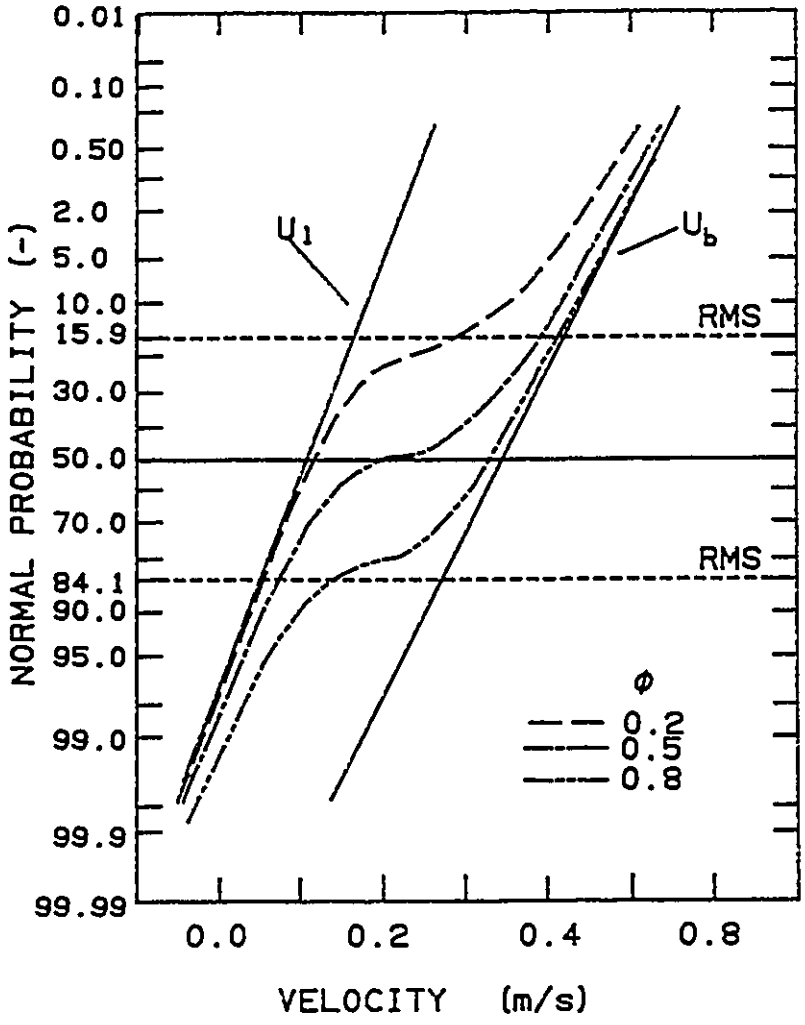

Figure III.15 Graphic representation of combined gas and liquid probability distribution functions. The dotted lines represent the summation of two independent distributions for U_l and U_B for various volume fraction weightings.

(4) From the estimate of α, the guessed U_g and U_l distributions corresponding to this estimated α can be obtained by considering those portions of U_g or U_l as independent distributions and recalculating their PDF respectively.

(5) With these estimates of α, U_g, and U_l, calculate U_m of the distribution for this mixture using Equation III.7.

(6) Compare the calculated U_m distribution with the actual one, and adjust α to minimize the sum of squares between the two by looping through steps 4 and 5.

(7) Plot U_g and U_l distributions, along with the raw data, as seen in Figures III.16 and III.17. The mean velocities and RMS values can be immediately determined.

Velocities determined in this way agree very well with those measured from photographs, and with velocity discrimination on the basis of the probe (Figure III.10). With larger bubbles and higher void fractions it is not possible to separate the two distributions with this technique. This problem led to the development of the combined LDA/EP technique.

3.5.2.3 Discrimination by the Combined LDA/EP Technique

The combined LDA/EP technique can be used for bubbly two-phase flow measurement, where the bubble sizes are large and turbulence is strong. Both of the discrimination techniques discussed in the previous sections are not suitable. Results are presented in Figure III.18 for the mean and RMS values of gas and liquid velocity

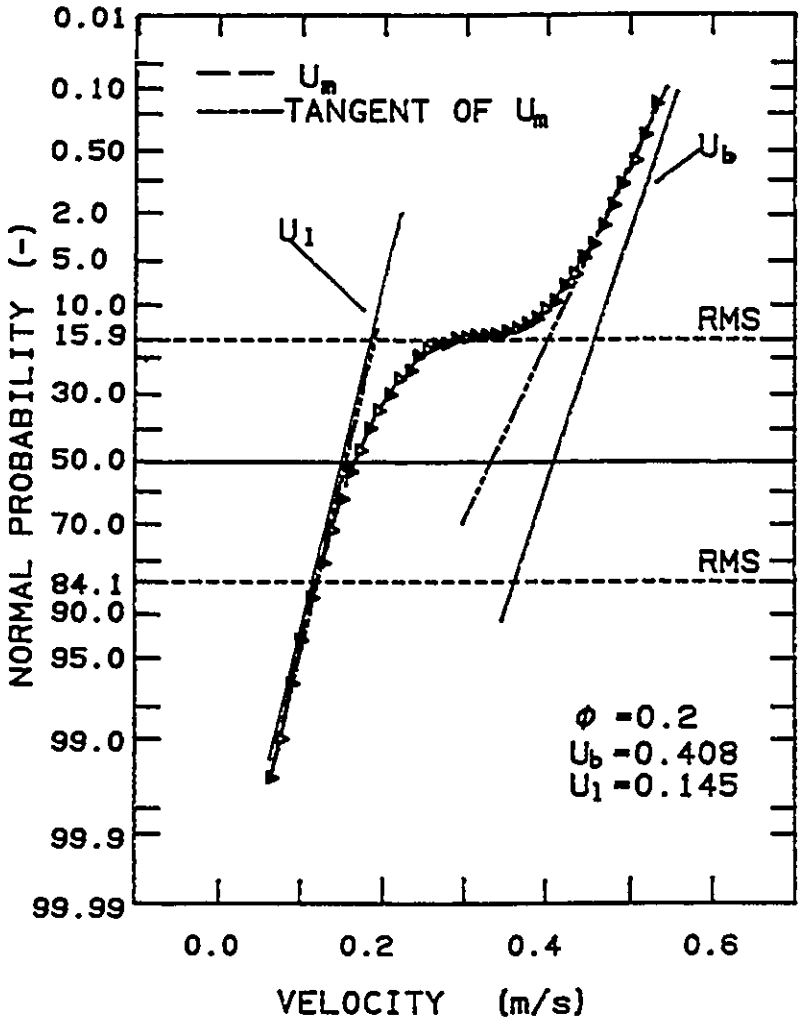

Figure III.16 Probability distribution function of the mixed velocity for the data in Figure III.13. The constructions for the tangents (superficial velocity distributions) and gas and liquid velocities are superimposed.

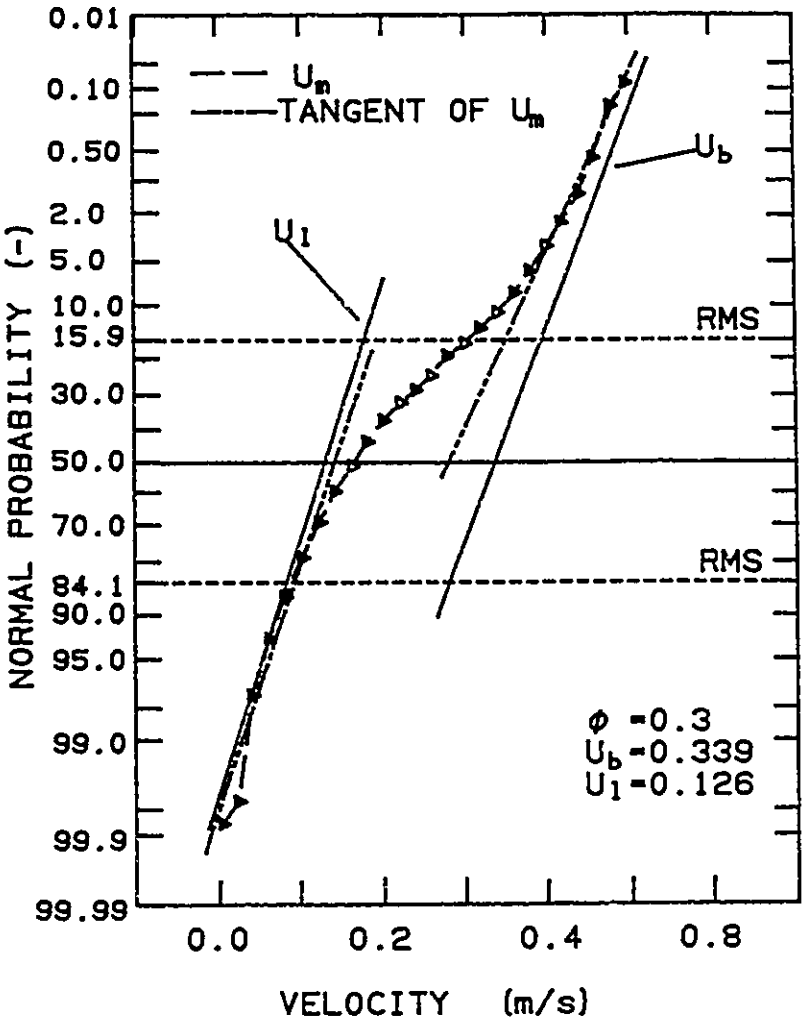

Figure III.17 Probability distribution function of the mixed velocity for the data in Figure III.14. The constructions for the tangents (superficial velocity distributions) and gas and liquid velocities are superimposed.

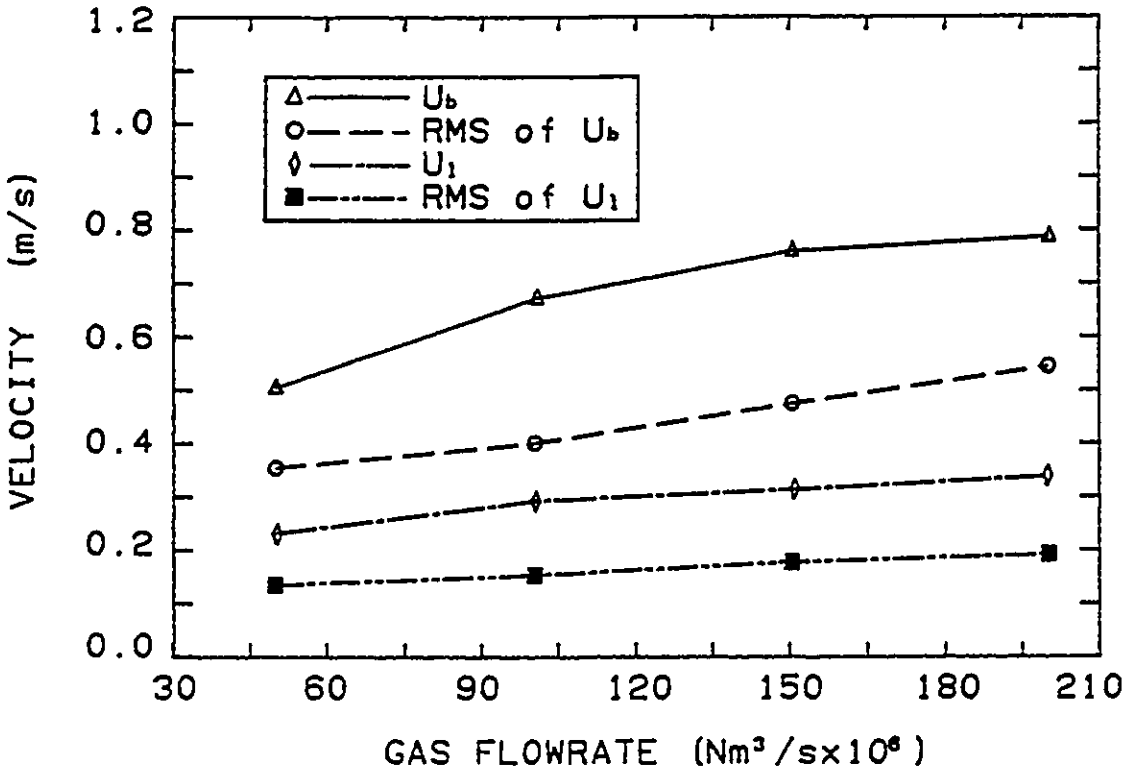

Figure III.18 Bubble and liquid velocities in a bubbly plume determined with the combined LDA/EP technique. Large bubbles (5 to 50 mm) were produced by a flush-mounted orifice (4 mm diameter) at the center of the large model. The LDA was operated under Combined/LDA mode with backward scattering. U_B=0.51 to 0.79 m/s, α=0.06 to 0.12, f_B=2.8 to 6.1/s.

for large bubbles (10 to 40 mm diameter) at void fractions of 0.06 to 0.12. Note that in these plumes, the RMS values for gas and liquid are generally greater than 50% of the mean.

3.6 Discussion

3.6.1 Discrimination by Mixture PDF

In Figure III.16, the gas and liquid velocities±RMS are 0.408±0.05 and 0.145±0.034, respectively, and in Figure III.17 the corresponding values are 0.359±0.058 and 0.126±0.048 m/s. As the means become closer, and the RMS values increase, the distributions overlap. There are two major limitations of the PDF technique when the distributions overlap.

(1) The observed mixture distribution becomes more of a straight line (more normal), making separation more difficult; one is not sure that data at the tails are due to either gas or liquid alone.

(2) The assumption that the individual gas and liquid distributions are normal and independent is not justifiable.

According to the present experimental results, it is not recommended to apply this technique to bubbles larger than 15 mm and void fractions higher than 0.4. This, of course, is only a general guideline because the useful upper limit will depend on the accuracy required, the distribution of bubble size, and the level of turbulence.

3.6.2 Discrimination by the LDA/EP Technique

This technique yields time series for gas and liquid velocities at a particular point, therefore it is useful for correlating these mean and RMS components. Other potential applications would include the measurement of drag coefficients, and the measurement of mass transfer coefficients as a function of interfacial fluctuations.

There are several variables which affect the quality of data which are discussed in the following subsections.

3.6.2.1 LDA Configuration

Forward scattering cannot be used to measure bubble velocity because the bubbles are larger than the control volume. Very good signals can be obtained from the bubbles in the back-scattering mode, however the liquid signals are relatively weak, resulting in a low data rate. This problem is largely alleviated by adjusting the seeding correctly so that the data rate for the back-scattered radiation from bubbles and liquid is comparable. Another possible solution to the problem is to measure the bubbles by back-scattering, and the liquid by forward scattering using two photomultiplier tubes.

3.6.2.2 Electrical Probe Position

Several different positions for the probe relative to the control volume were evaluated; the best was less than 1 mm below the control volume. The time-scale

resolution of this technique is of the order of the probe/LDA control volume separation (less than 1 mm) divided by the velocity which is approximately 2 ms. The EP voltage reading is enabled by the LDA data-ready signal. When the probe signal is from a bubble, the LDA data will also be from the bubble, most of the time. The exceptions are the instances in which the bubble interface is between the probe and the control volume or when the bubble is about to leave the measuring volume while the tip of the electrical probe is already out of the bubble. The number of these velocity signals without the correct accompanying EP signal is believed to be small, since in most of these cases, the doppler signals are usually not good enough to be validated due to the relative position of the measuring volume and the bubble, and the irregular bottom shape of the bubble. The fraction of incorrectly attributed velocities will be the ratio of the probe/control volume separation distance to the bubble height which was always less than 0.1 and decreased to 0.01 for the larger bubbles.

3.6.3 Limitations of the Technique

While the combined LDA/EP technique has been shown to be suitable for large bubbles at large void fractions, it is difficult to apply it to small bubbles at low void fraction because there are so few bubble signals compared to the liquid signals, and because small bubbles do not produce as large a change in probe response. Thus, the LDA/EP and PDF Discrimination Techniques are complementary.

CHAPTER IV
RESULTS OF DIAGNOSTICS OF THE BUBBLY PLUME WITH LDA-EP TECHNIQUE

4.1 Experimental Apparatus

The LDA and EP experimental set up is the same as described in the previous chapter, however, the vessel used in this part of experiment was a 1/10 scale model of a steelmaking ladle of 150 ton. The model consisted of a 500 mm diameter cylinder 760 mm high, inside an outer box 560 x 560 mm^2 x 760 mm high, as shown in Figure IV.1. The outer box was filled also with water to minimize distortion due to curvature. Five horizontal slots were cut on the inner cylinder wall to eliminate the curvature effect for lateral velocity measurements; the slots were 3 mm high and one quarter of the cylinder circumference long. Two types of injectors were used. A glass lance with fritted glass (FG) at the end was used to produce small bubbles, 0.5 to 4 mm diameter. Larger bubbles (approximately 5 to 40 mm diameter) were produced by a flush-mounted orifice (4 mm inner diameter) placed at the centre of the bottom.

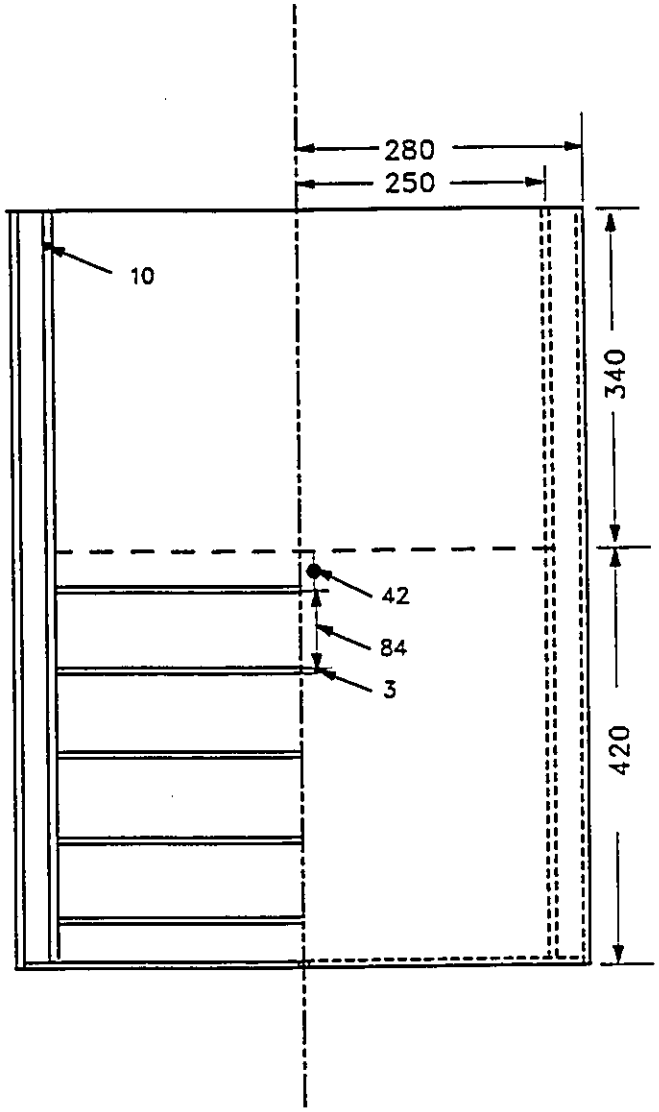

Figure IV.1 Illustration of the water model used in the experiment. The model ladle is made of the plexiglass with a thickness of 10 mm, the positions of the slots cut for the LDA measurement are also shown.

4.2 Experimental Design

The water model size and the gas flowrates employed in the experiments were designed based on the Similarity theory with a scale-down ratio of 1/10. The similarity theory is based on the fact that many physical processes are governed by similar laws, and can consequently be represented with similar mathematical formulations. The similarity numbers representing different force balances can be derived from these mathematical formulations. In fluid flows, for instance, the Navier-Stokes equations discussed in Chapter II can be used to represent most flow problems. The most important similarity numbers are the Reynolds number, Re, which is the ratio of inertial forces to viscous forces, and the Froude number, Fr, which is the ratio of inertial forces to buoyancy forces. Similarity theory indicates that, it is possible to deduce the most satisfactory information for an original facility from experimental work with a model, which maintains geometrical, kinematic and dynamic similarity, as well as maintaining similar boundary conditions to the original facility (Coulson and Richardson, 1955). It is usually very difficult to establish complete similarity between models and originals, and in many cases, only the most important factor is chosen for the similarity consideration. In the case of the bubbly plume flow encountered in this project, bubble behaviour is governed by similarity numbers such as the Eotvos number, Reynolds Number and Morton number. Morton number is the most important similarity number which determines the shape of bubbles:

$$Mo = \frac{g\mu^4\Delta\rho}{\rho^2\sigma^3} \qquad \text{(IV.1)}$$

For gas bubbles in molten steel, Mo is in the range of 10^{-12} to 10^{-13}, while in the water model, Mo is in the order of 10^{-11}. Both are in the regime of spherical cap bubbles (Clift et al. 1978). The liquid flow resulting from the plume, however, is mainly governed by the inertial force, gravitational force and viscous force with the first two playing more important roles (Mazumdar and Guthrie, 1990). The resulting similarity number is the Froude Number. For the selection of the gas flowrates in this experiment, the similarity based on Fr number between the water model and the steelmaking ladle can be obtained by using the same stirring energy input into the liquid (Mazumdar and Guthrie, 1990). In the case of gas-only injection, the energy input into the liquid bath can be calculated with the following equation (Nakanishi et al., 1975; Sano and Mori, 1982b):

$$W = \frac{P_o Q_g T_2}{T_o}\left(\left[1 - \frac{T_1}{T_2}\right] + \ln\left[\frac{P_1}{P_2}\right]\right) \quad (W) \qquad \textbf{(IV.2)}$$

where, T_o = 273 K and P_o = 1 atm. When Q_g is in m^3/s, the above equation becomes:

$$W = 371.22\, Q_g T_2\left(\left[1 - \frac{T_1}{T_2}\right] + \ln\left[\frac{P_1}{P_2}\right]\right) \quad (W) \qquad \textbf{(IV.3)}$$

where, T_1 and T_2 are temperatures of gas before being injected into the bath and of liquid, respectively. P_1 and P_2 are pressures at the free surface and nozzle exit, respectively. The gas flowrates selected and the corresponding energy inputs are listed in Table IV.1 where the industrial data are also listed for reference (Irons, 1986; Mazumdar & Guthrie, 1985).

To investigate the behaviour of small bubbles in the plume, LDA measurements were also carried out for the bubbly plume produced with the fritted glass where the sizes of bubble were smaller than 4 mm. The gas flowrates used in this part of the measurement range from 0.6 to 5.0×10^{-6} m^3/s.

Table IV.1 Experimental Parameters

Liquid	$Q_g x10^{-6}$ (m^3/s)	Energy input, W (W/ton)	M (ton)
Steel	950-7100	8 - 40	150
Water	50,100,150,200	5 - 20	0.083

4.3 Characteristics of LDA and EP Data from Bubbly Plumes

The LDA can be arranged in either forward scattering or backward scattering position. When LDA signals are strong enough, it is better to use the backward scattering operation for acquiring bubble velocities with little seeding. However, for the purpose of flow pattern measurement, it is better to use the forward operation for much higher data rate. The simultaneous measurement of the flow pattern and void fraction was carried out with the forward scattering, while for the simultaneous measurement of the bubble and liquid velocities, backward scattering was used.

The characteristics of the LDA and EP signals from a bubbly plume are shown in Figures IV.2 and IV.3. In Figure IV.2, the LDA was operating under the Timer-Combined mode. In Figure IV.3, the operating LDA mode was Timer-Fixed. The operation modes have been discussed in Chapter III. In both cases, the data were acquired at a fixed time interval of 10 ms. However, when Combined mode is used, the number of the true velocity data is less than when the Fixed mode is used, since only one validated datum is acquired during a signal burst in the case of Combined mode. As a result, the number of the true velocity data in Figure IV.3 is about 2 to 3 times higher, and the flow pattern is therefore better recorded than that shown in Figure IV.2.

The passages of the bubbles were clearly recorded in both Figures IV.2 and IV.3 with the EP voltage variation, together with the corresponding velocity variation recorded by LDA. Compared with Figures III.8 and III.9, the occurrence of bubbles along the centerline of the plume is not as regular as in the case of a chain of bubbles, because of the bubble movement away from the center and bubble breakup. Furthermore, the bubbles rise slightly off the centerline, and therefore missed by the electrical probe, can still cause an abrupt variation of the liquid velocity along the centerline as shown in Figures IV.2 and IV.3, where more bubble data are seemingly held by the EP than in the case of a chain of bubbles. The velocity variation is much larger in the case of a bubbly plume, which reflects stronger liquid turbulence and more violent bubble surface movement.

This is the first time that the bubble velocities in such a bubbly plume flow have been measured with the LDA/EP technique developed in this project. The separated velocities of the bubble and the liquid based on the simultaneously measured data of LDA\EP are very important for the further investigation of the bubble behaviour, such as the calculation of the transit time of bubbles, drag coefficient for bubbles and the turbulent features of the liquid flow in the plume.

4.4 Void Fraction Distribution in Bubbly Plumes

The contour maps plotted with the measured void fraction data in bubbly plumes are shown in Figures IV.4 and IV.5 for gas flowrates of 0.5 and 1.5×10^{-4} m^3/s, respectively. The maps revealed the typical distributions of the void fraction in a vertical plane passing through the centerline of the bubbly plume. The highest

concentration is located a short distance above the nozzle, and decays rapidly in both vertical and radial directions. The general shape of the bubbly plume is like a inverted cone, as observed by other researchers such as Castillejos and Brimacombe (1987), with larger expansion angle for larger gas flowrates.

4.5 Variation of Bubble Size and Shape in Bubbly Plumes

The measurement of the bubble size and shape were carried out with a video camera which is capable of generating 30 frames per second. Three photographs taken from the video pictures are shown in Figure IV.6. Information on bubble sizes and shape variation can be obtained from these photographs. The vertical size variations of bubbles rising along the centerline for four different gas flowrates are shown in Figure IV.7 in terms of volumetric equivalent diameter of bubble. The volume of the bubble is calculated with the measured chord length and height of the bubble based on the assumption that the bubble is a spherical cap with a circular bottom. The bubble frequency at the nozzle is about 10 1/s in these cases. The shape variations of the bubbles are shown in Figure IV.8 in terms of E, the ratio of the bubble height, H_B, to its chord length, L_B. In the above two figures, data from small bubbles produced from the break up of big bubbles are not included, in order to show more clearly the behaviour of the big bubbles. These big bubbles contribute most to the void fraction, and are the main concern in the development of a mathematical model for the prediction of the local void fraction. In Figure IV.7, a steady decline of the size was observed for two lower gas flowrates. For the two higher gas flowrates, the bubble size increases right after detaching from the nozzle as a result of coalescence of the bubbles occurring above the nozzle, and then decline more rapidly as a result of stronger break

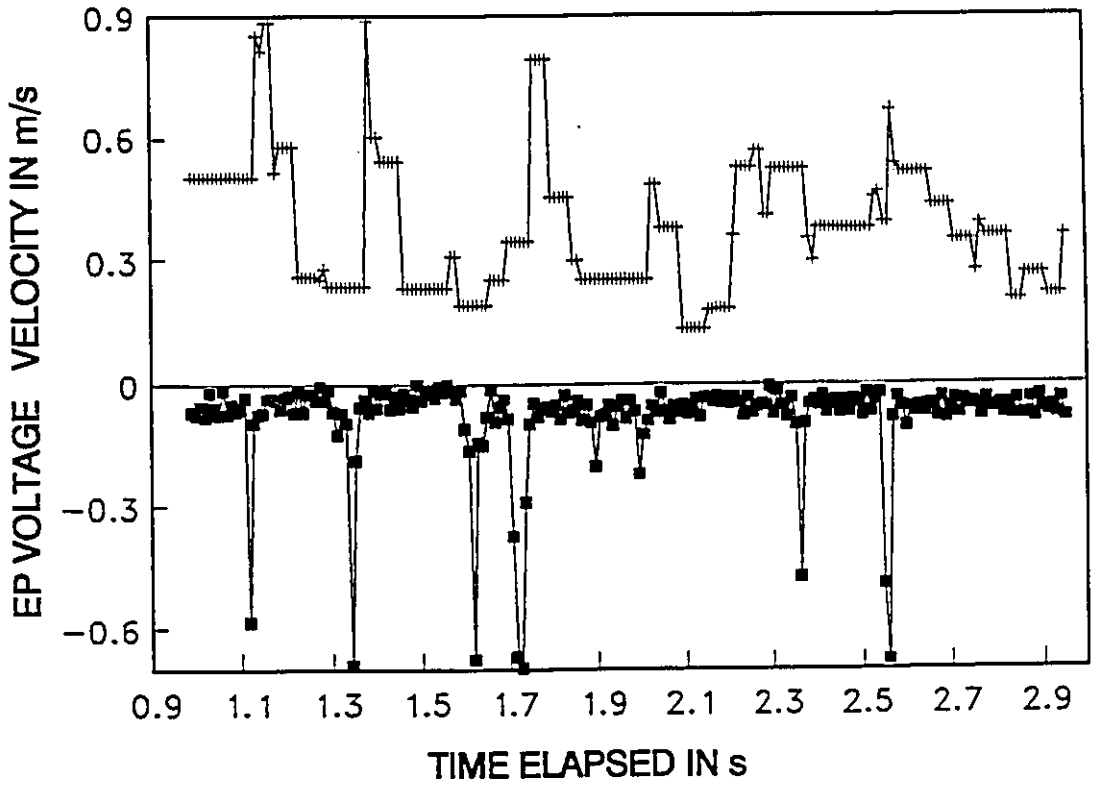

Figure IV.2 Time series of velocity (upper) and probe voltage (lower) from the bubbly plume produced in the water model. The LDA was operating under the Timer/Combined mode, the data acquisition frequency is 100 Hz, Q_g=1.0x10^{-4} Nm^3/s, x=0.21 m, r=0.02 m.

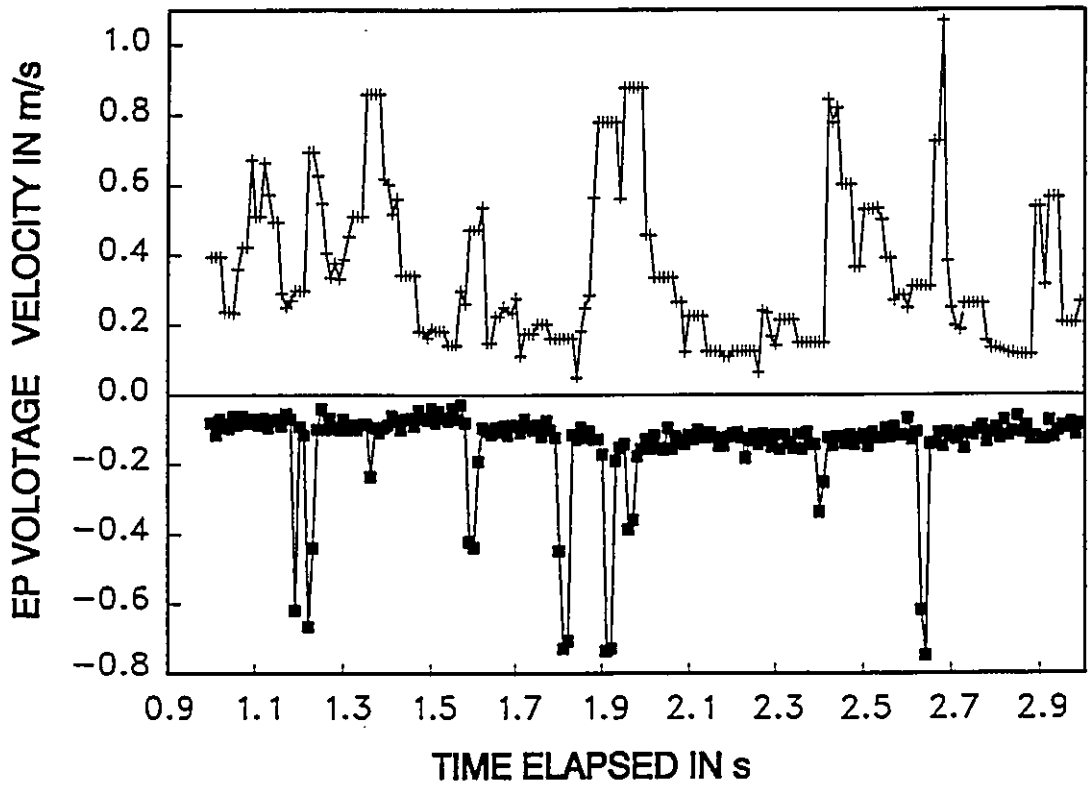

Figure IV.3 Time series of velocity (upper) and probe voltage (lower) from the bubbly plume produced in the water model. The LDA was operating under the Timer/Fixed mode, the data acquisition frequency is 100 Hz, Q_g=1.0x10^{-4} Nm^3/s, x=0.21 m, r=0.012 m.

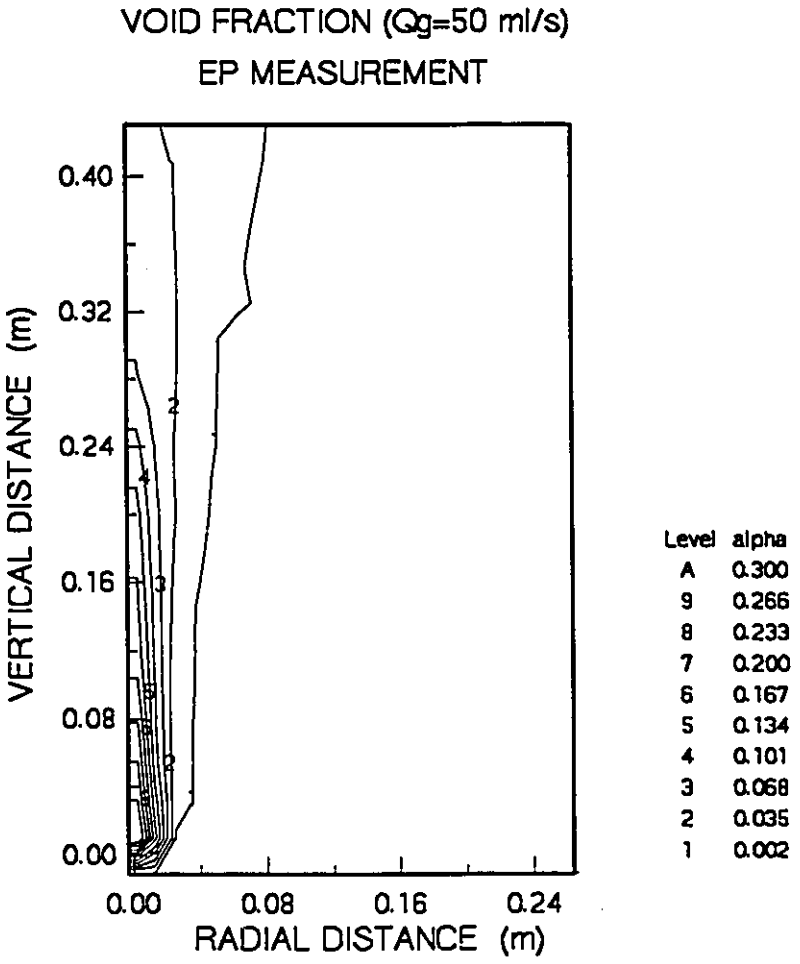

Figure IV.4 Void fraction contour map measured with EP in the water model ladle, Q_g=5.0x10^{-5} Nm^3/s.

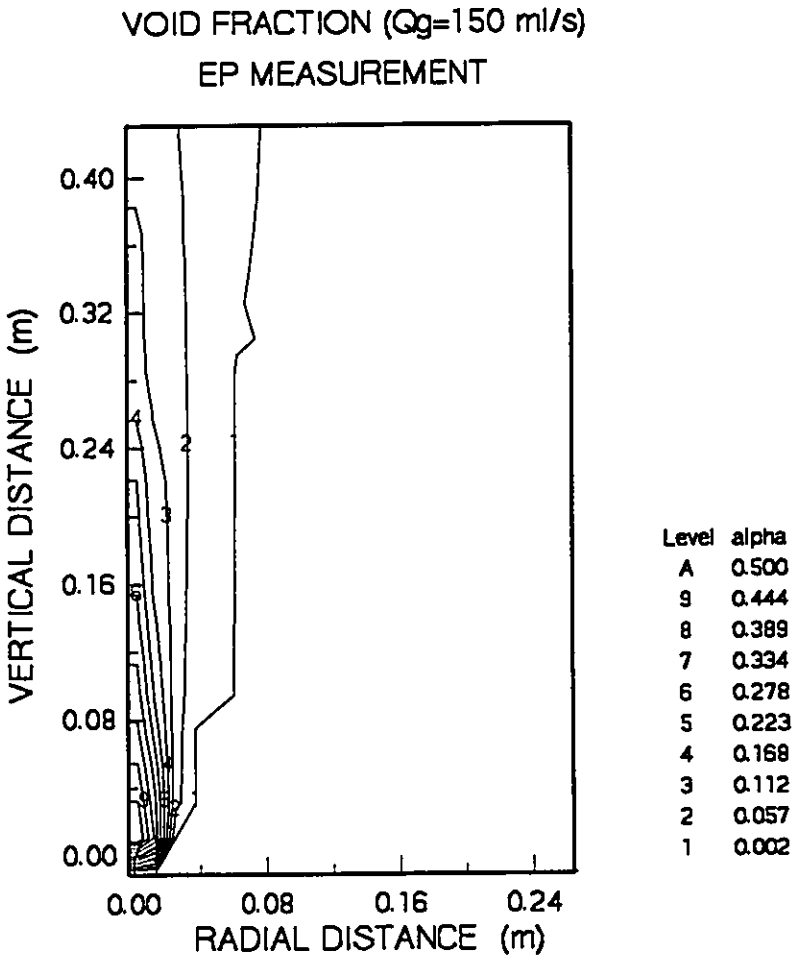

Figure IV.5 Void fraction contour map measured with EP in the water model ladle, Q_g=15.0x10^{-5} Nm^3/s

up. In Figure IV.8, the horizontal elongation processes were similar for all the gas flowrates. The shape ratio of the bubble is larger than unity right after detaching from the nozzle, and then declines steadily during rise.

4.6 Bubble Velocity Distribution in Bubbly Plumes

The mean bubble velocities and their RMS values were obtained with Equations (III.5) and (III.7), once bubble velocities were separated from the mixed velocity sample with the LDA/EP technique described in Chapter III. Typical variations of the bubble velocities and its RMS values along both the radial and the vertical directions are shown in Figures IV.9 and IV.10, respectively. In Figure IV.9, a steady radial decay of bubble velocity was observed. In Figure IV.10, the vertical variation of bubble velocity and its RMS value is not as straightforward. The present model study indicates that there is an accelerating period in which bubbles achieve their maximum velocity, and soon after that, the velocity would decay probably because of bubble breakup. It further decreases when the bubble is approaching the free surface, where the liquid velocity is decelerating. It is also found that, the RMS value of bubble velocities in the center area of the plume can be higher than the mean velocity. It decreases rapidly as the bubble sizes decrease during the breakup process. This reflects the fact that the bubble interface wobbles violently with interface vibration during rise in the plume (see Figure IV.6).

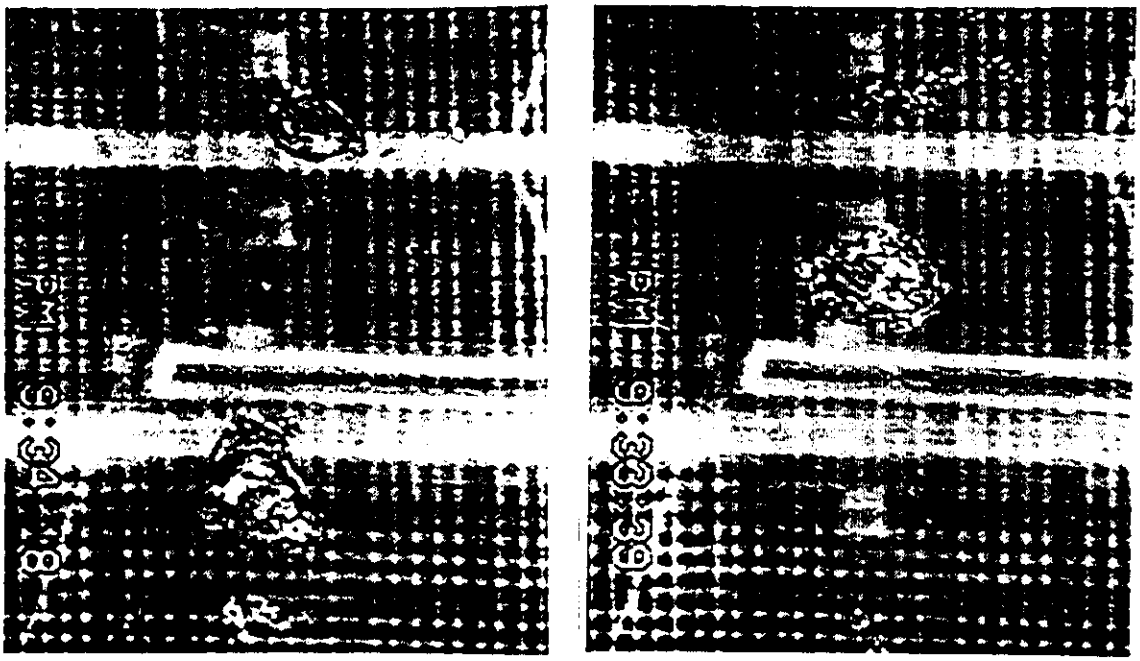

a b

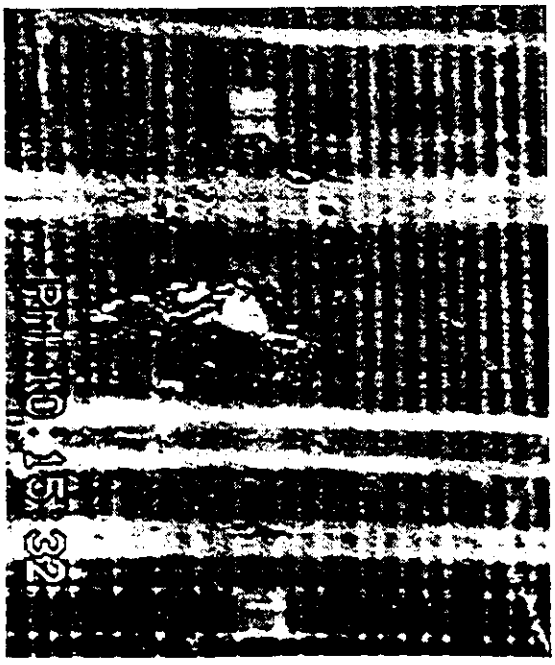

c

Figure IV.6 Photographs of the shape and size of bubbles rising in plumes in the large water model, the grid size is 5 mm. (a) Q_g=5.0x10^{-5}/Nm^3/s, x=0.21 m, r=0.0 m, (b) Q_g=5.0x10^{-5}/Nm^3/s, x=0.29 m, r=0.1 m, (c) Q_g=5.0x10^{-5}/Nm^3/s, x=0.29 m, r=0.0 m

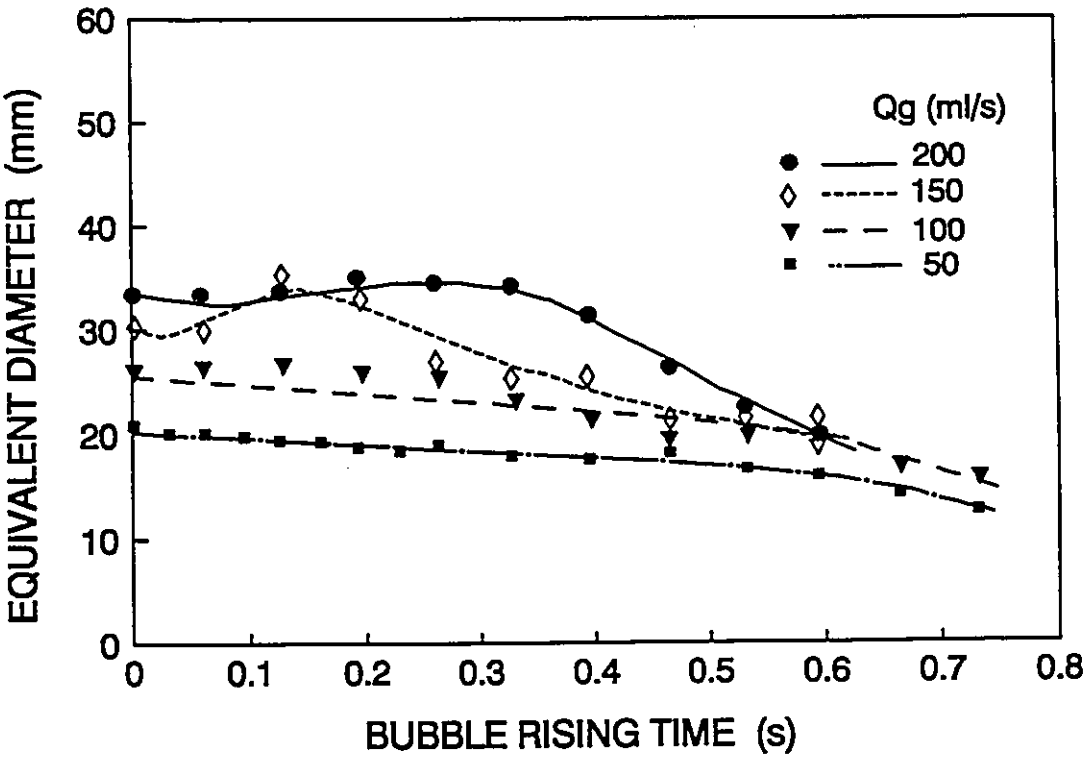

Figure IV.7 Variation of equivalent bubble diameter along the centerline of plumes. This was performed in the large water model and the data were obtained with a video camera.

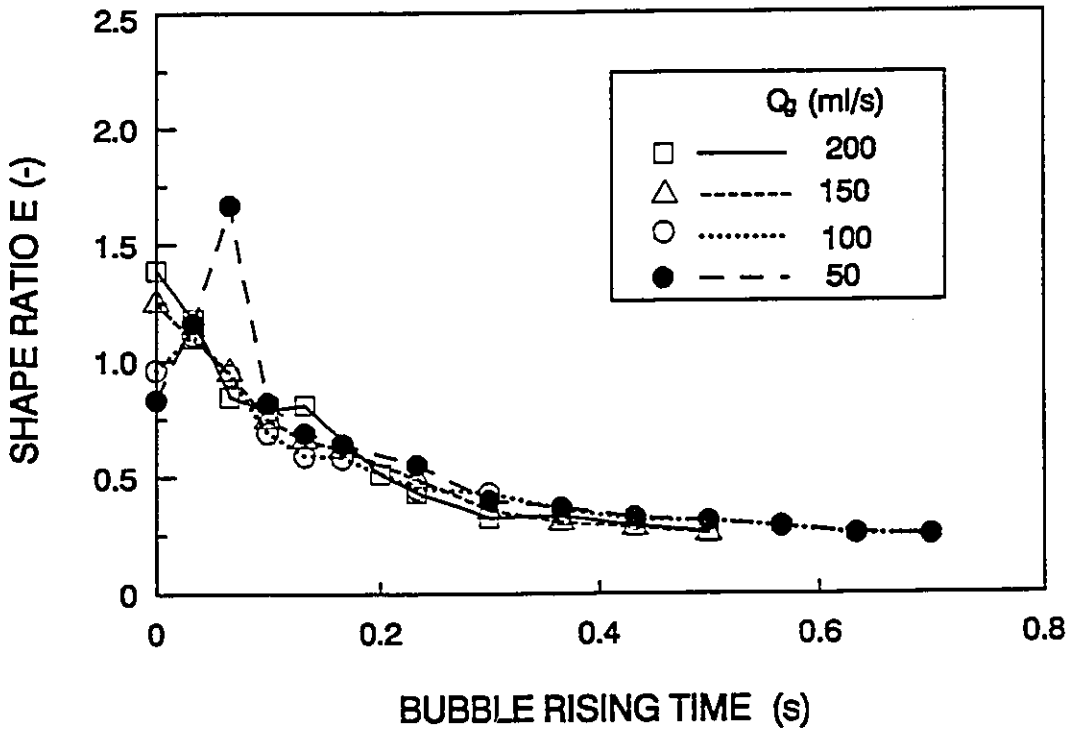

Figure IV.8 Variation of the shape of big bubbles along the centerline of plumes. This was performed in the large water model and the data were obtained with a video camera in terms of the ratio of bubble chord length to its height.

4.7 Liquid Flow in Bubbly Plumes

The characteristic variation of both mean and RMS value of the liquid velocity along the centerline line are shown in Figure IV.11 for a gas flowrate of 1.0×10^{-4} m^3/s. A slight decline was observed for both the mean and the RMS value, and the turbulent intensity, which is defined as the ratio of the RMS value over the mean liquid velocity, is in the range of 0.5-0.7, which is much higher than in the region outside of the plume.

The mean liquid flow fields are shown in Figure IV.12 through IV.15 for gas flowrates of 0.5, 1.0, 1.5 and 2.0×10^{-4} m^3/s respectively. The figures reveal that the flow inside the two-phase plume zone is much faster than the flow in the single phase region. The velocity decays significantly along the radial direction due to the fast decay of the void fraction along the radial direction. Along the side walls, the downward flow is still strong. In the region close to the bottom wall, however, the flow is slow.

4.8 Turbulence Characteristics in Bubbly Plumes

In most single phase flows, the turbulence intensity is usually smaller than 0.2. However, in the two-phase region of a bubbly plume flow, the turbulence intensity of the liquid flow is much stronger. The measured distribution pattern of the RMS values of the liquid velocity are shown in Figures IV.16 through IV.19 for gas flowrates of 0.5, 1.0, 1.5 and 2.0×10^{-4} m^3/s respectively. The movement of bubbles contributes a great deal to the generation of the turbulence in the two-phase region though the interaction with the liquid at the interfaces, such as the wake shedding, wobbling movement and the

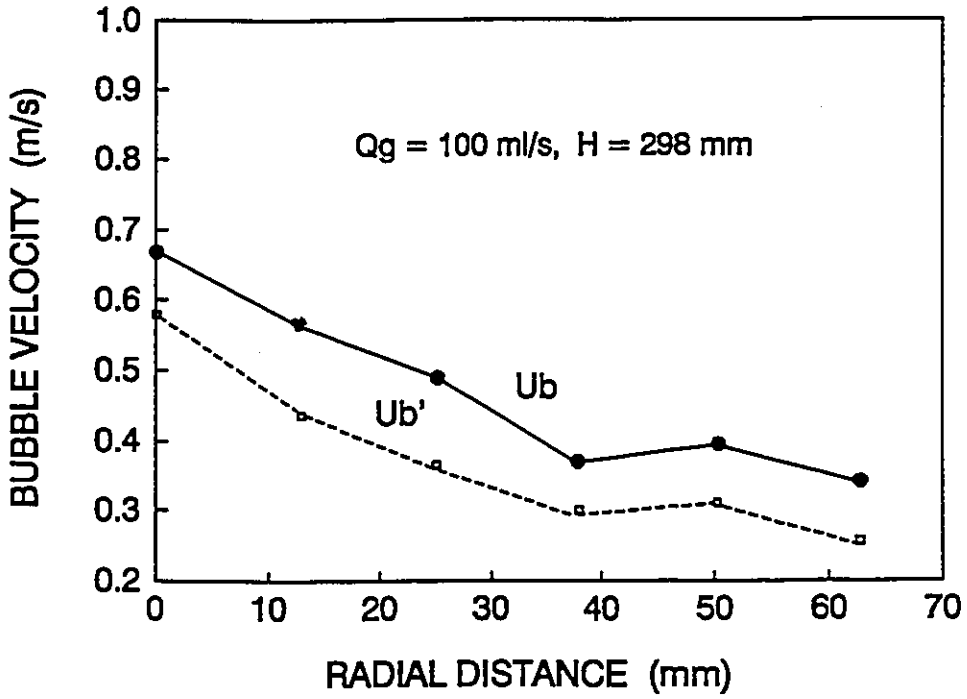

Figure IV.9 Radial variation of bubble rising velocity. This was performed in the large water model and the bubble velocity was measured with LDA/EP technique

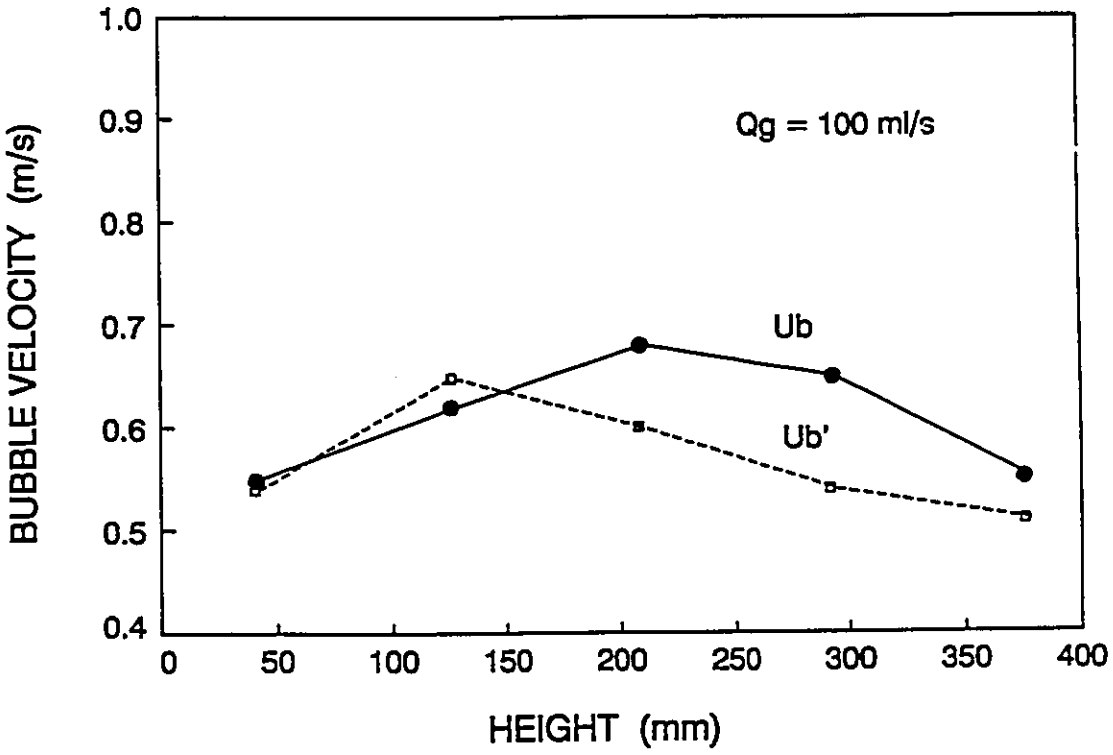

Figure IV.10 Vertical variation of bubble rising velocity. This was performed in the large water model and the bubble velocity was measured with LDA/EP technique.

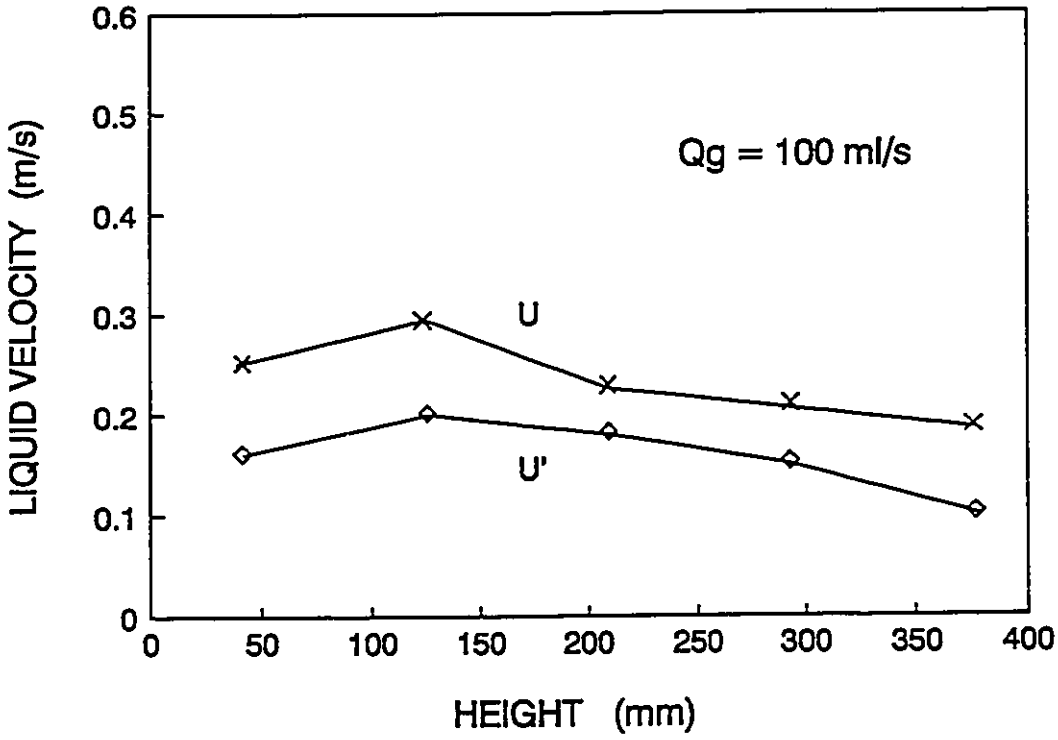

Figure IV.11 Vertical variation of the liquid velocity. This was performed in the large water model and the velocity data were measured with LDA/EP technique

break up of big bubbles. Since larger bubbles have more momentum, and more violent interface vibration and wobbling, they tend to generate more turbulence than smaller bubbles. The void fraction affects turbulence in a similar way. When the void fraction is high, it means that there is more buoyant energy available to generate more turbulence. The above discussion is qualitatively consistent with the experimental results shown in Figures IV.16 through IV.19, which indicate that, along the centre line of the plume, the turbulence intensity can be as high as 0.5, much higher than turbulence intensity in the region outside the plume.

It has never been determined whether the turbulence within a two-phase plume is isotropic. One of the most important features of an isotropic turbulence is that all the turbulent components of velocity are the same, and the angle of the turbulent velocity vector defined with the following equation:

$$\theta = arctg(u'/v') \qquad \textbf{(IV.4)}$$

should be 45°. Similar angles formed by either u' and w' or v' and w' should also be 45° in isotropic turbulence. The angular component of turbulent velocity, w', is not available in this project due to equipment limitations and therefore assumed to be equal to the corresponding radial component of the turbulent velocity. In Figures IV.16 through IV.19, the experimental results clearly demonstrate that, turbulence in the recirculating single phase flow region is close to isotropic. Turbulence inside the two-phase region, with slightly stronger fluctuating velocity component along the vertical direction, however, is not an isotropic one. In the later case, θ is about 55° for u' and v'. The average value of the measured θ_t inside the plume for four different gas flowrates are shown in Figure IV.20.

If w' is assumed to be equal to v', it is then possible to calculate the distributions of turbulent kinetic energy, k, based on measured values of the u' and v'. The contours of the k obtained are shown in Figure IV.21 to IV.24. These experimental results are also described in two recent publications (Sheng and Irons, 1992a; 1992b).

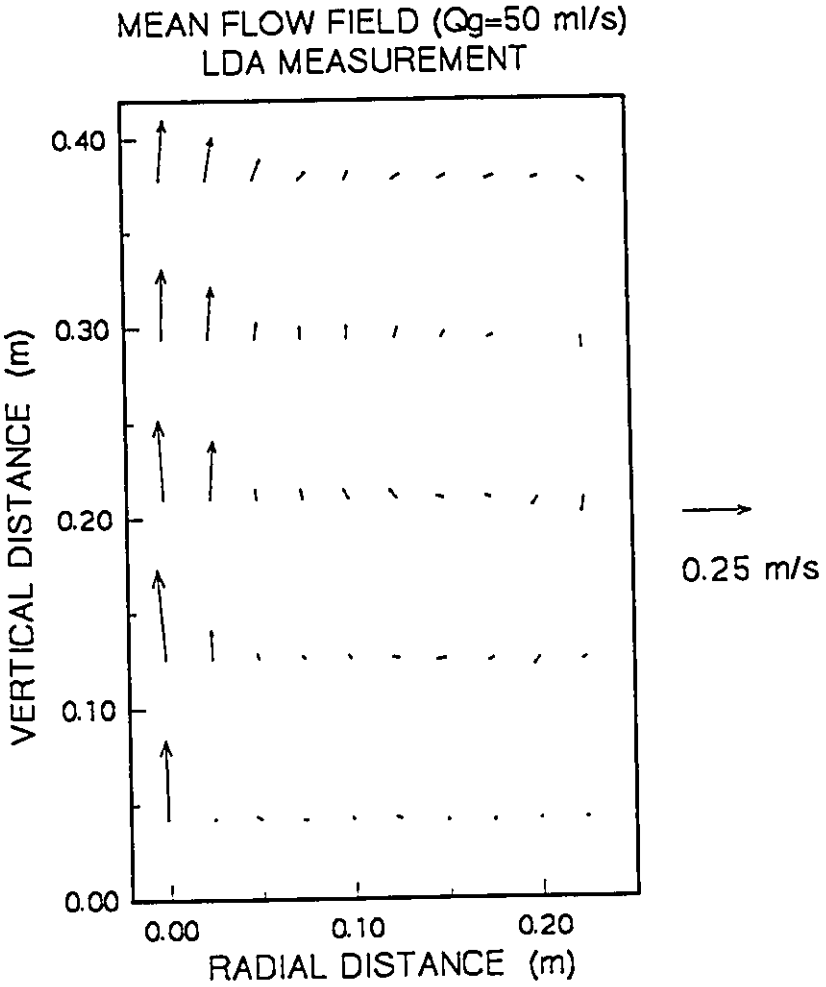

Figure IV.12 The mean liquid flow field in the large water model ladle measured with LDA/EP technique, Q_g=50 ml/s.

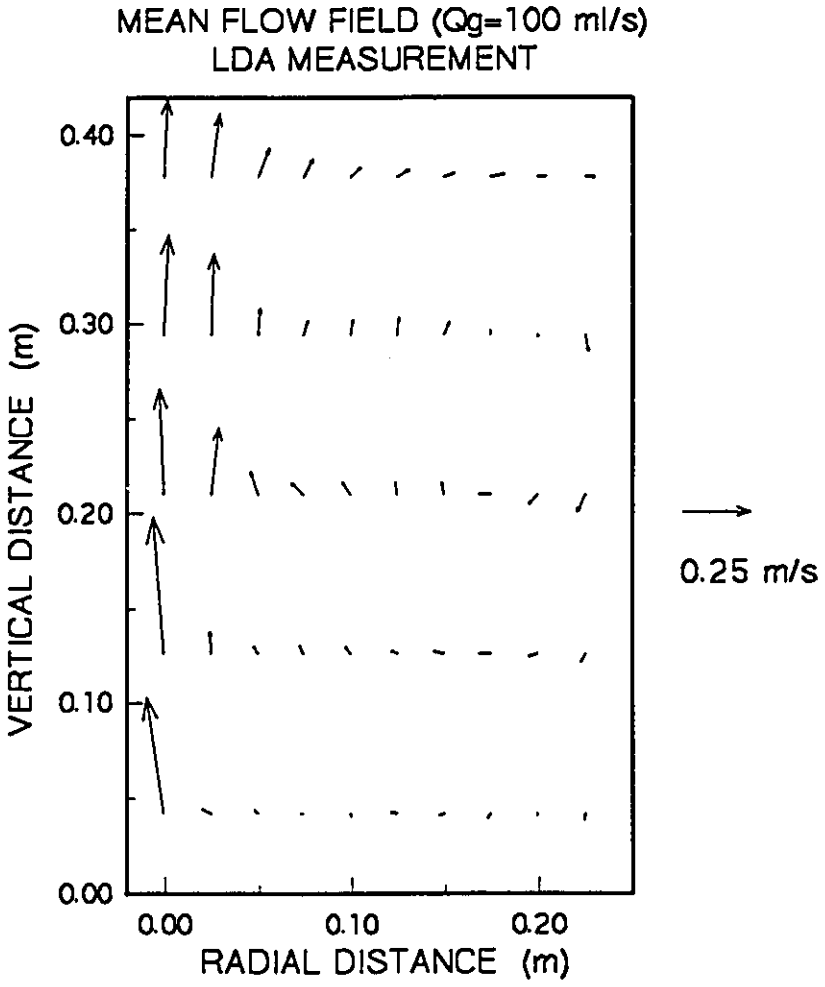

Figure IV.13 The mean liquid flow field in the large water model ladle measured with LDA/EP technique, Q_g=100 ml/s

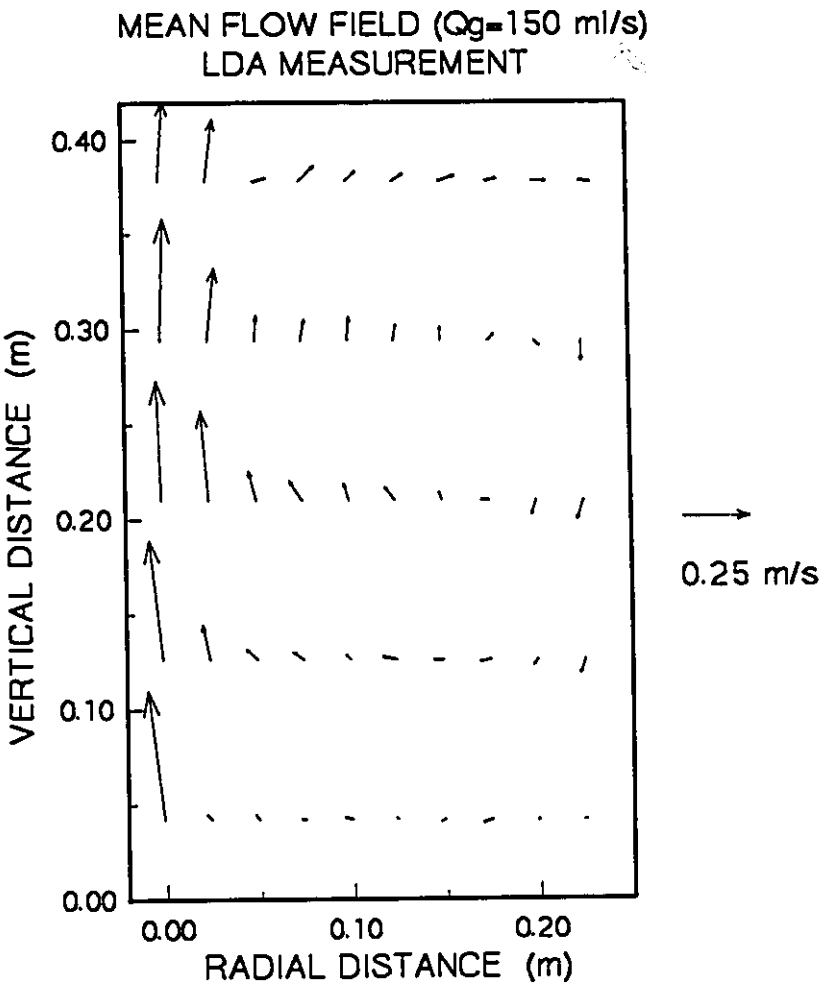

Figure IV.14 The mean liquid flow field in the large water model ladle measured with LDA/EP technique, Q_g=150 ml/s

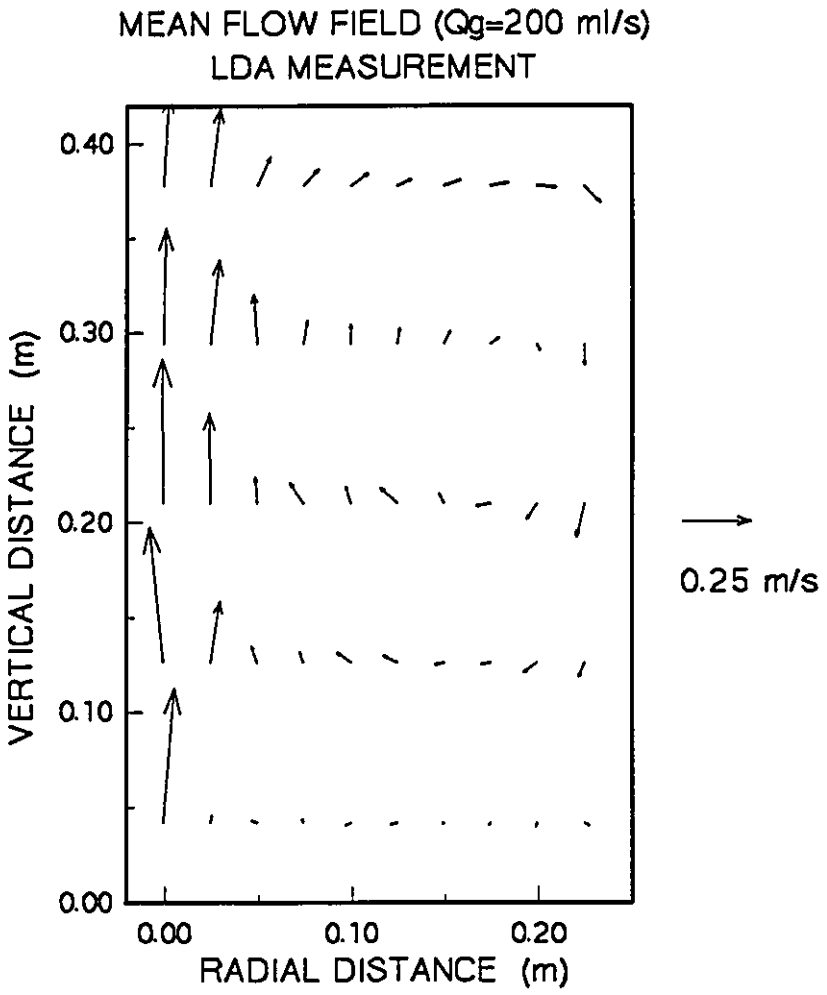

Figure IV.15 The mean liquid flow field in the large water model ladle measured with LDA/EP technique, Q_g=200 ml/s

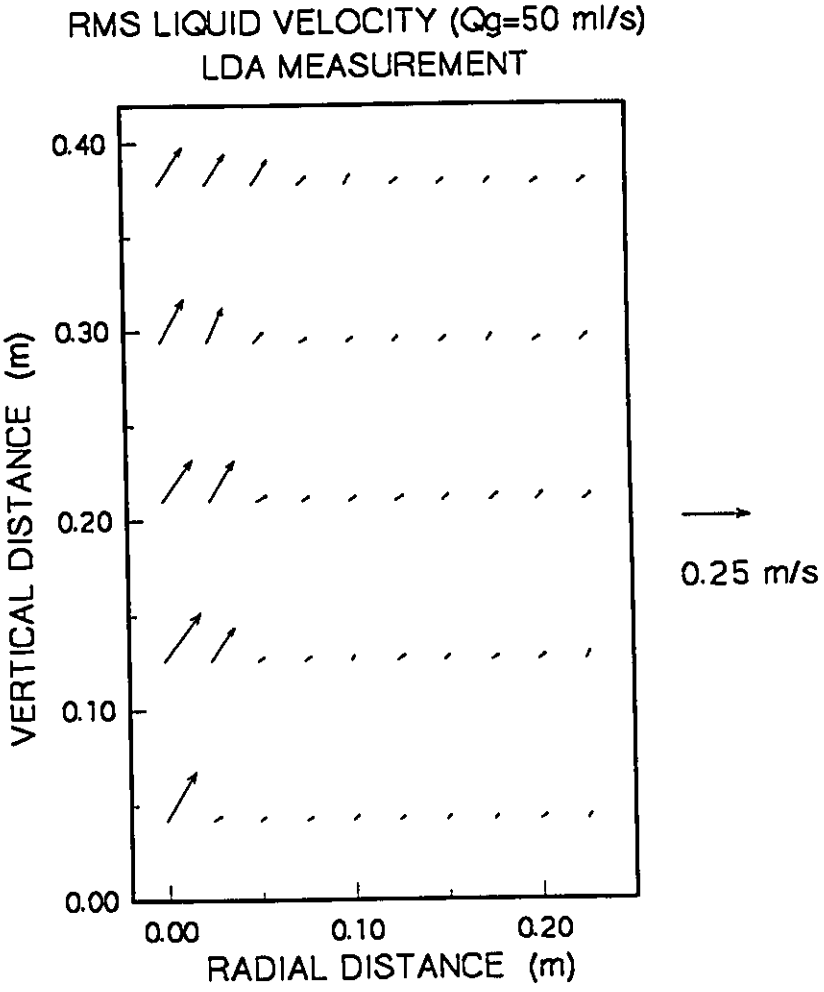

Figure IV.16 The RMS liquid flow field in the large water model ladle measured with LDA/EP technique, Q_g=50 ml/s.

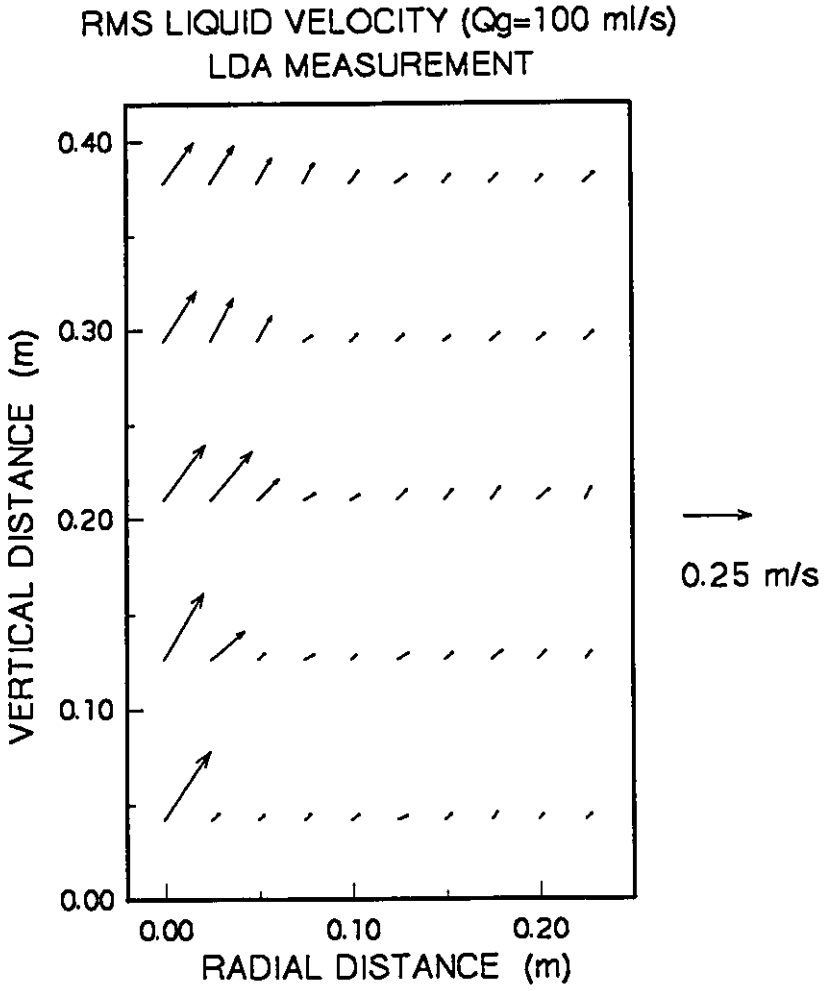

Figure IV.17 The RMS liquid flow field in the large water model ladle measured with LDA/EP technique, Q_g=100 ml/s.

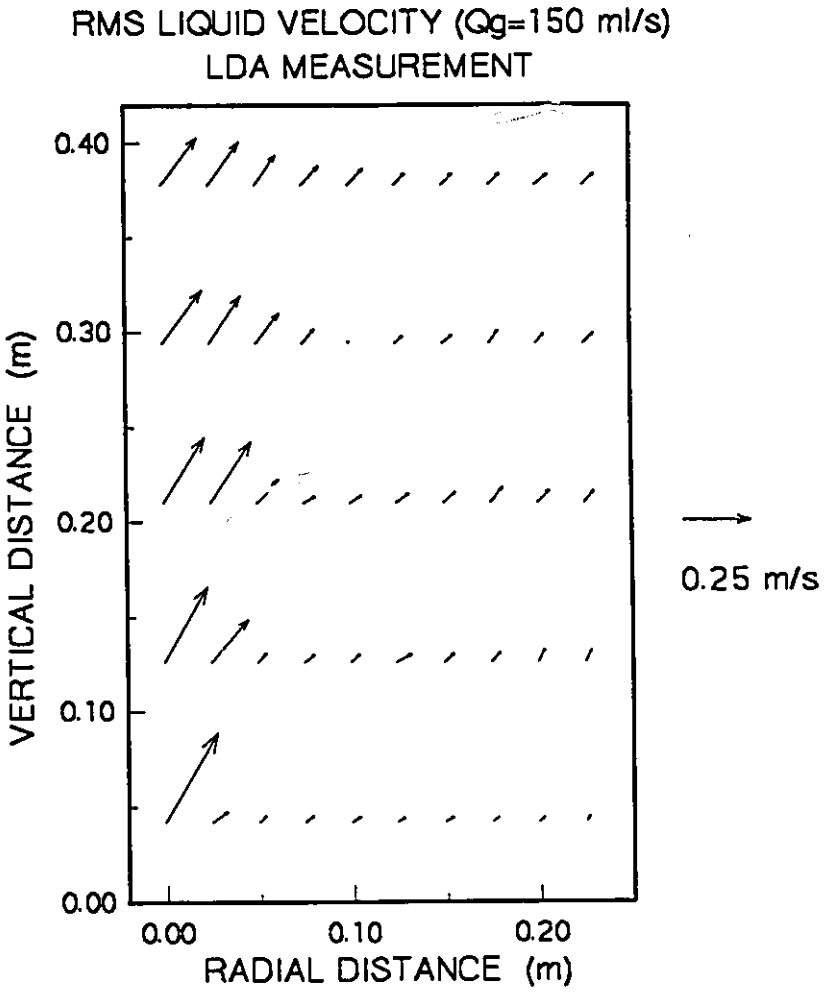

Figure IV.18 The RMS liquid flow field in the large water model ladle measured with LDA/EP technique, Q_g=150 ml/s.

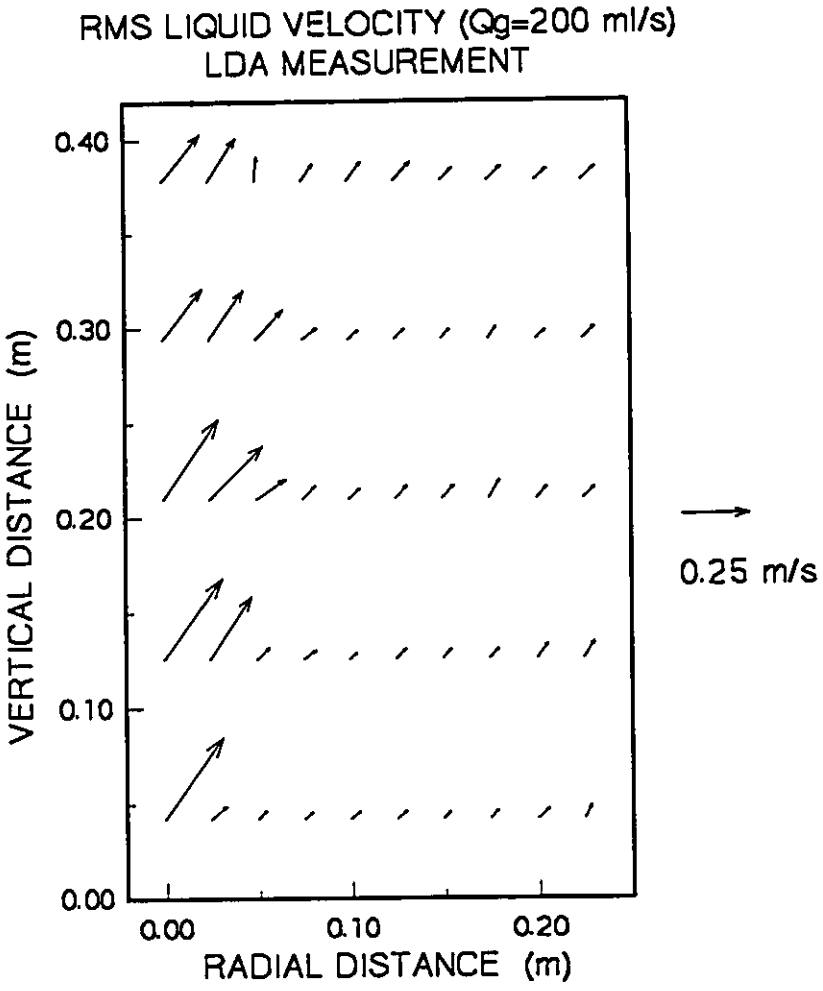

Figure IV.19 The RMS liquid flow field in the large water model ladle measured with LDA/EP technique, Q_g=200 ml/s.

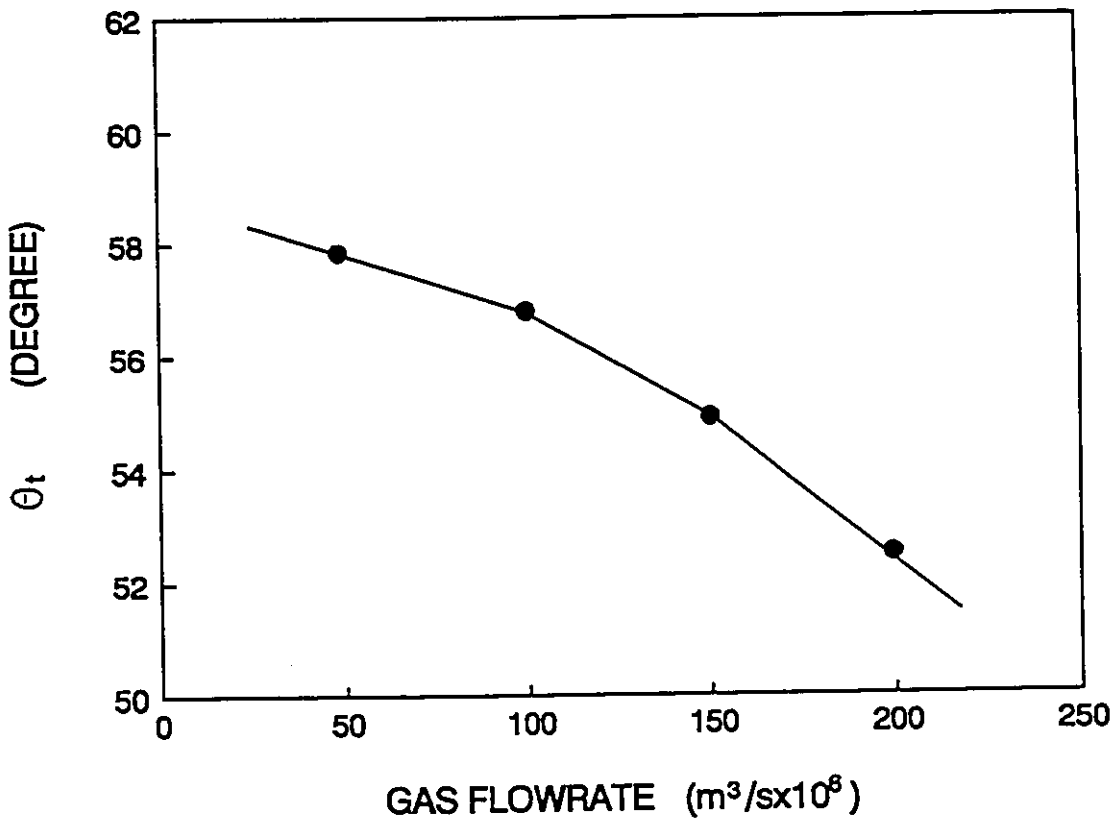

Figure IV.20 Variation of the angle of non-isotropy with gas flowrates

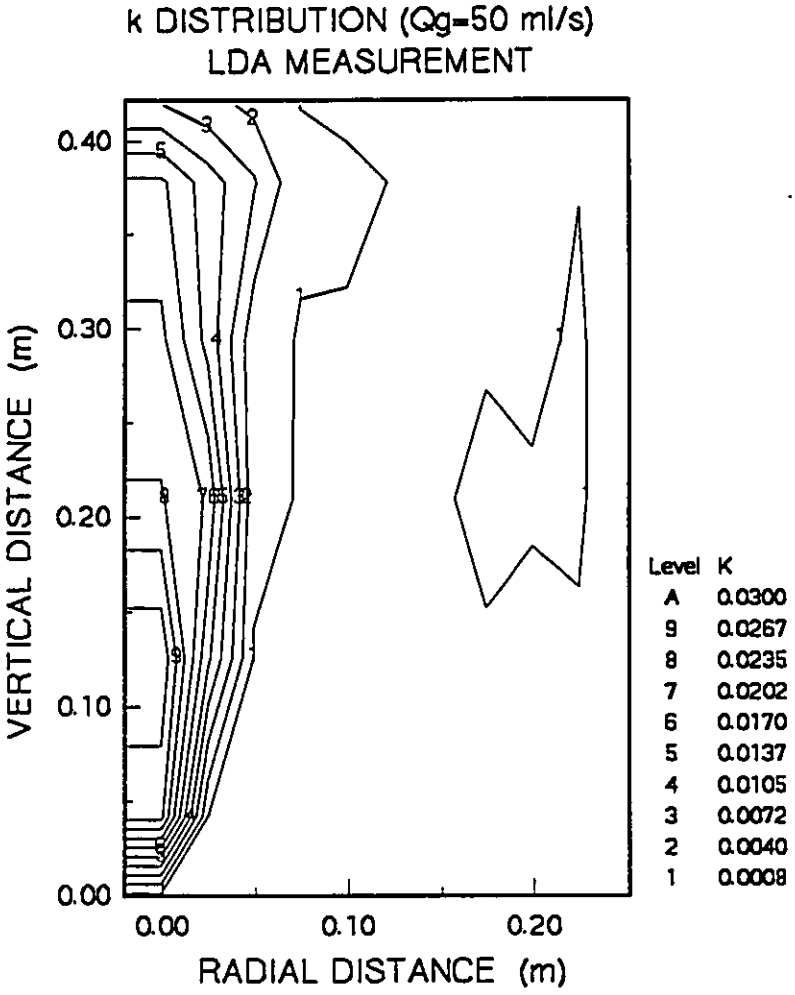

Figure IV.21 Contour map of the turbulent kinetic energy in the large water model ladle measured with LDA/EP technique, the unit for k is m^2/s^2, Q_g=50 ml/s.

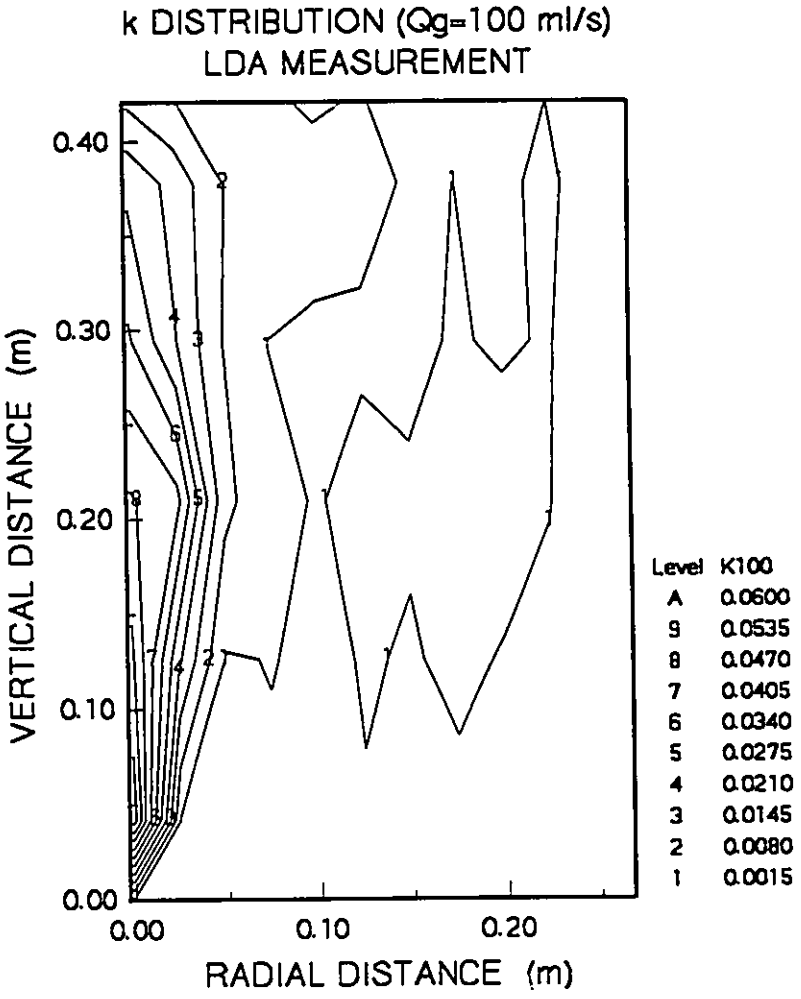

Figure IV.22 Contour map of the turbulent kinetic energy in the large water model ladle measured with LDA/EP technique, the unit for k is m^2/s^2, Q_g=100 ml/s.

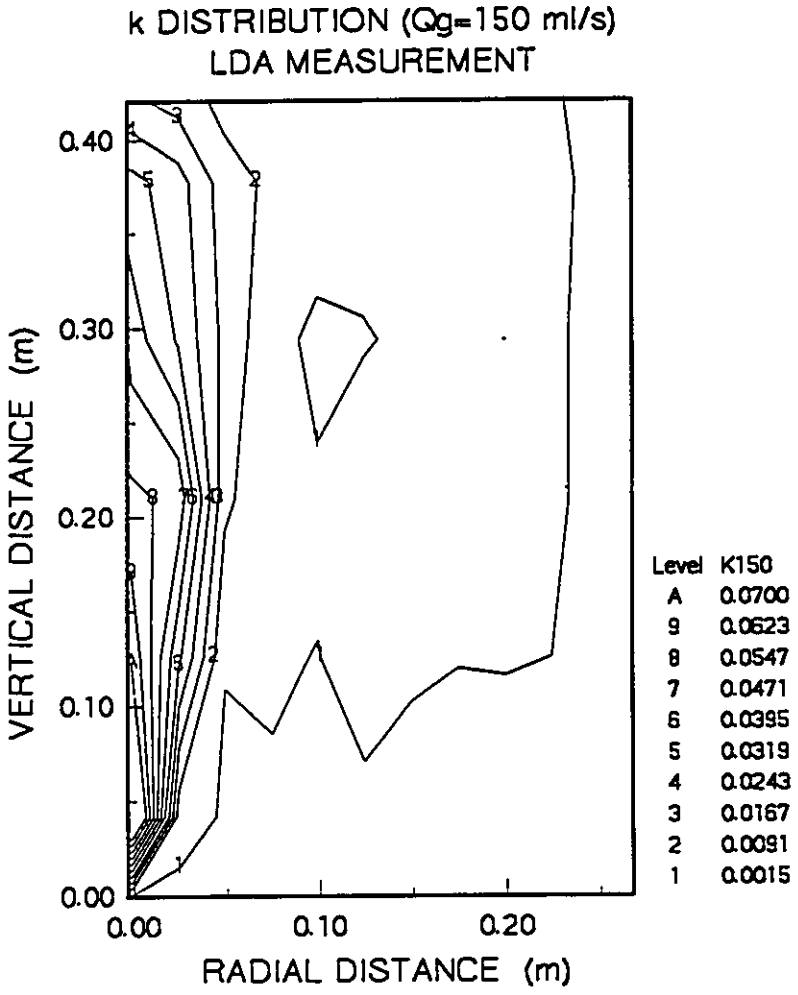

Figure IV.23 Contour map of the turbulent kinetic energy in the large water model ladle measured with LDA/EP technique. the unit for k is m^2/s^2. Q_g=150 ml/s.

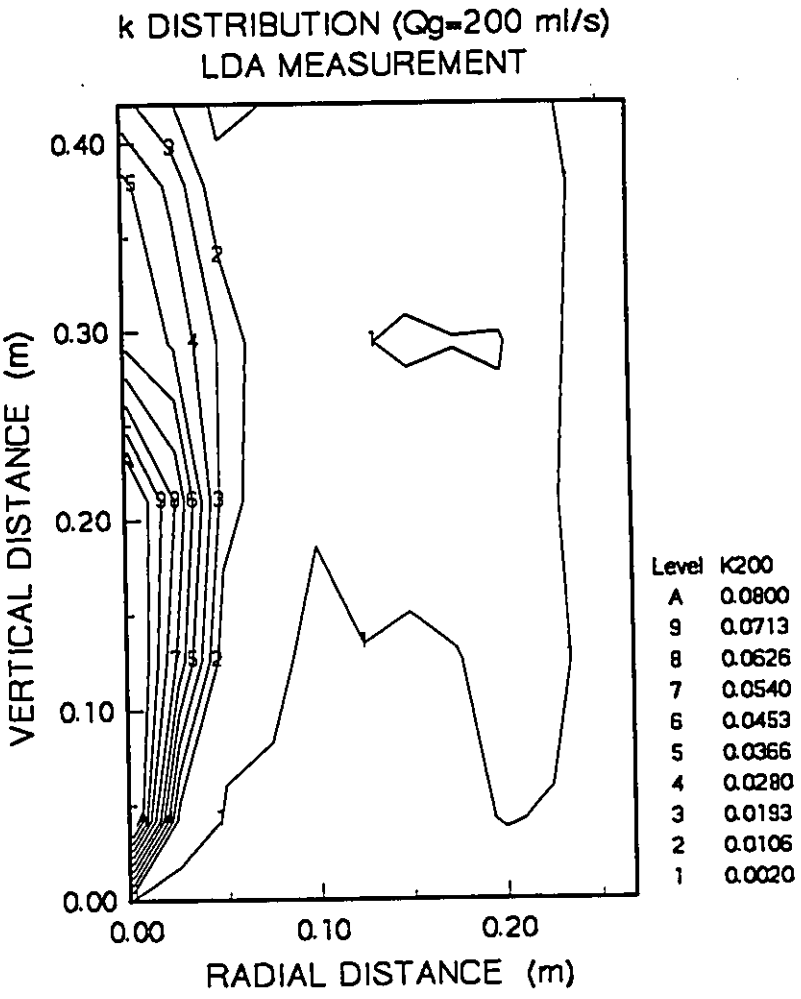

Figure IV.24 Contour map of the turbulent kinetic energy in the large water model ladle measured with LDA/EP technique, the unit for k is m^2/s^2, Q_g=200 ml/s.

CHAPTER V

SOME DYNAMIC ASPECTS IN BUBBLY TWO-PHASE FLOWS

In a bubbly plume flow, the interaction between the liquid and bubbles is one of the important factors that is not well understood. In this chapter, the experimental measurement of the behaviour of bubbles in the bubbly plume, obtained with the combined LDA/EP technique and discussed in the previous chapters, will be used to provide an improved understanding of the following dynamic aspects in a bubbly plume flow:

(1) Determination of the slip velocity of a bubble;
(2) Lateral migration of bubbles due to lateral lift force;
(3) Breakup of bubbles during rising;
(4) Turbulence characteristics in plumes.

5.1 Determination of Drag and Slip Velocity of Bubble

The slip velocity between a bubble and the liquid or the relative velocity of a bubble will be defined as the difference between time averaged velocities of the bubble and the liquid at the same point inside the two-phase flow zone. This definition is not

the same as the conventional definition for a single bubble, where liquid is virtually stagnant. However, since the bubble movement relative to the liquid is most important in affecting the force balance on the bubble, the two definitions should reflect similar bubble behaviour during rising.

The drag force exerted by the liquid is one of the most important, and consequently one of the most studied. Unfortunately, nearly all the studies on this subject have been based on a single bubble rising in stagnant liquid (Clift et al., 1978) or in bubble column flows. As a result, the application of the results of these studies to bubbly plume flows has been always in doubt. The most uncertain factor is the influence of the void fraction distribution.

A brief literature review on the drag determination in bubbly plume or pipe flow situations has been presented in chapter II, where both theoretical and experimental work of several people have been discussed. Further discussion is presented in this section based on the experimental data obtained with the combined LDA/EP technique and discussed in chapter III and chapter IV.

The data used in the following discussion include data from three experiments as listed in Table V.1 and shown in Figure V.1. The two-phase velocity discrimination techniques discussed in Chapter III are used for the separation of gas and liquid velocities. The velocity PDF analysis technique was used in the case of the fritted-glass-produced plume, and for the other two cases, the combined LDA and EP technique were used. The U_l used is the time averaged liquid velocity measured with the LDA, while U_B is obtained with LDA for the last two cases and with video photograph for the plume produced with the flush mounted nozzle (first case). For large bubbles in the

plume, data from small bubbles passing the same measuring point were omitted. All the bubble sizes were measured with the video photograph. The void fraction in the fritted-glass-produced plumes was estimated to range from 0.001 to 0.015. The void fractions in the bubble chain and in the flush-mounted-nozzle produced plume were measured with EP at the position where the velocities are measured. The void fractions ranged from 0.1 to 0.45 for the bubble chain, and from 0.06 to 0.12 for the plume.

Table V.1 Experimental conditions for C_D measurement

	Vessel	Nozzle	D_B, mm	Technique	Seeding
I	Big tank	flush-mounted	0 - 40	LDA/EP & Video Camera	D.W.,no seeding
II	Big tank	Fritted glass	1 - 4	LDA & Video camera	D.W. seeding
III	Small tank	copper tube	5 - 15	Same as I	D.W. seeding

(D.W.---distilled water)

The drag coefficient of the bubble can be determined with Eq.(V.1):

$$C_D = \frac{2F_B}{\rho U_r^2 A_B} \qquad \textbf{(V.1)}$$

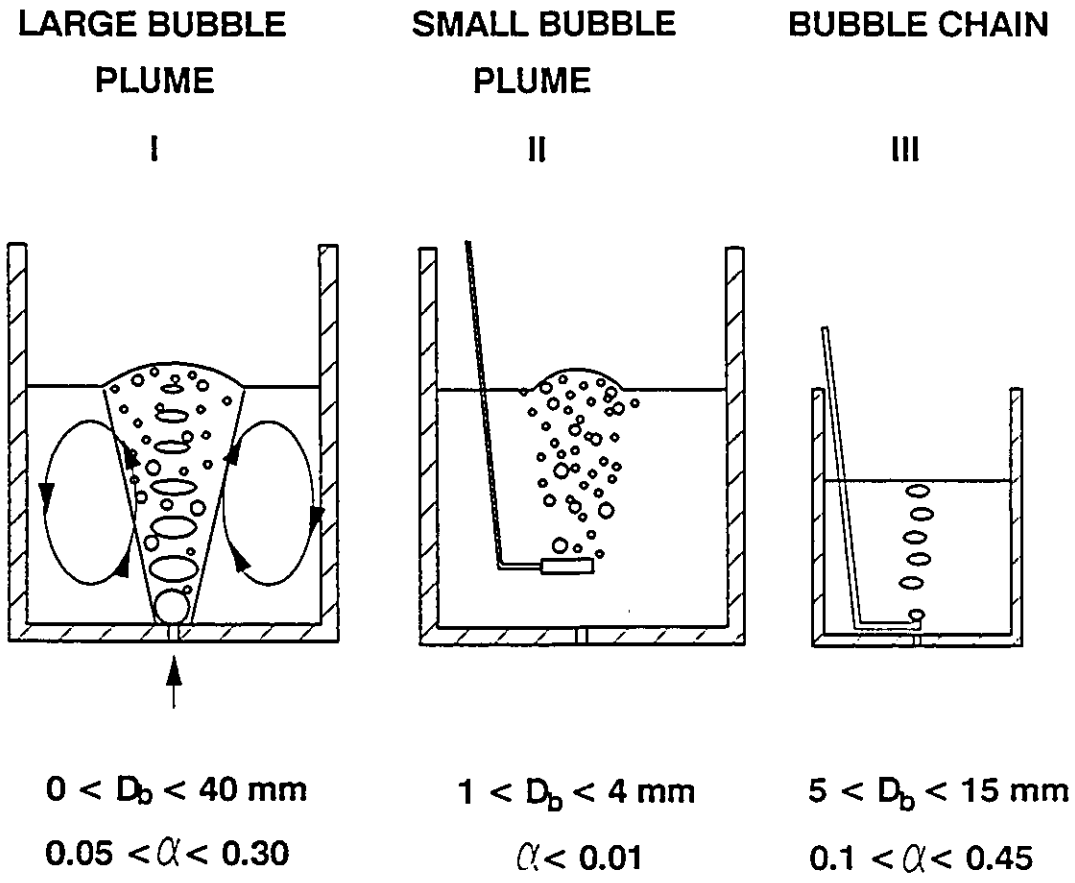

Figure V.1 Illustration of the experimental conditions for the determination of drag coefficient.

where A_B is the maximum horizontal cross sectional area of the bubble, U_r is the relative velocity and the body force F_B is taken as bubble buoyancy:

$$F_B = V_B(\rho_l - \rho_g)g \qquad \text{(V.2)}$$

Other forces due to the acceleration of the bubble, added mass and history terms are small compared to the buoyancy. The acceleration of bubbles in the plume is typically less than 0.1 m/s^2, consequently added mass terms are less than 1% of the buoyancy due to gravitational acceleration (9.81 m/s^2). The drag coefficients are plotted as a function of Reynolds Number in Figure.V.2. The standard drag curve for spheres and drag coefficients for bubbles in pure and contaminated water are also shown for comparison. In the present apparatus, bubble size and void fraction depend on flow rate and also on position in the vessel. These relationships are shown in Figure V.3 for both the small and large vessels. Comparison of Figure V.2 and V.3 shows that the drag coefficient is only weakly dependent on void fraction. It is very surprising that there is such good agreement between the single bubble drag coefficients and those in the two experimental systems at high void fractions and high levels of turbulence. It should be noted that distilled water was used for the small bubble plume (FG) in the small vessel, while seeding was used in the larger vessel. For the bubbles produced with the fritted glass at low void fraction (< 0.02) the data (circles in Figure V.2 and V.3) are almost identical to the single bubble data. The bubbles in the bubble chain (triangles in Figure V.2 and V.3) had drag coefficients higher than for bubbles in pure water. This may be due to the high void fraction and short distance between the measuring position and the nozzle which limited the full acceleration of the bubble. The largest bubbles (solid points in Figure V.2 and V.3) had drag coefficients close to the single bubble values, but there was more scatter in the data. The mean values of the drag coefficient are in good agreement with those of a single bubble.

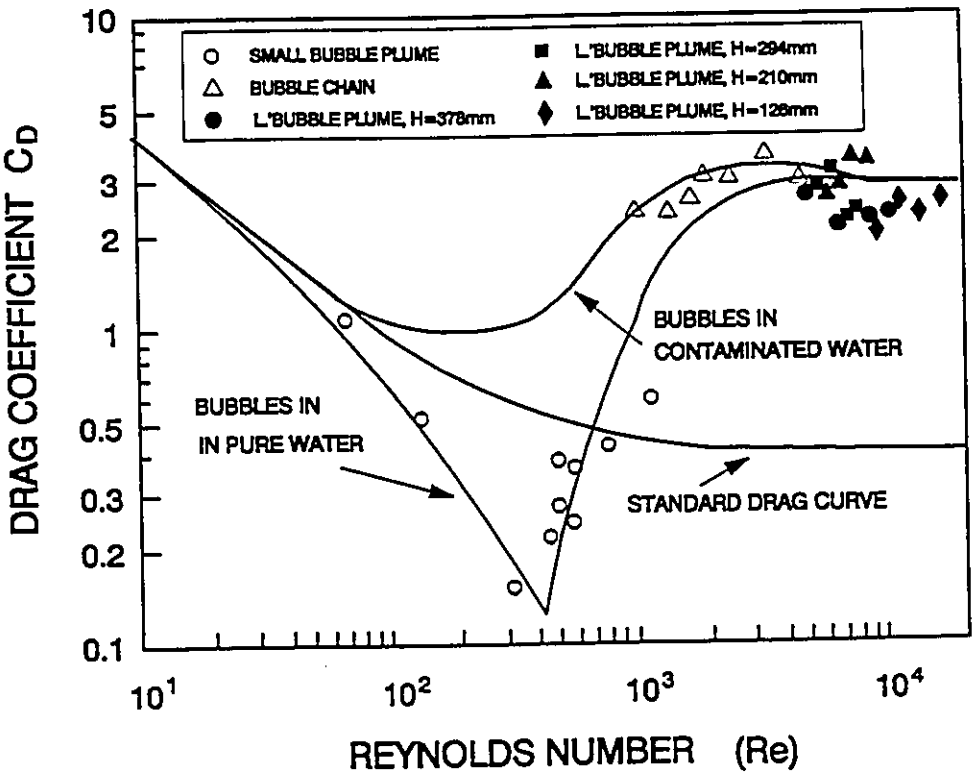

Figure V.2 Variation of the drag coefficient with Reynolds number. The experiments were performed in the small box for a chain of bubbles, and in the large water model for the plumes.

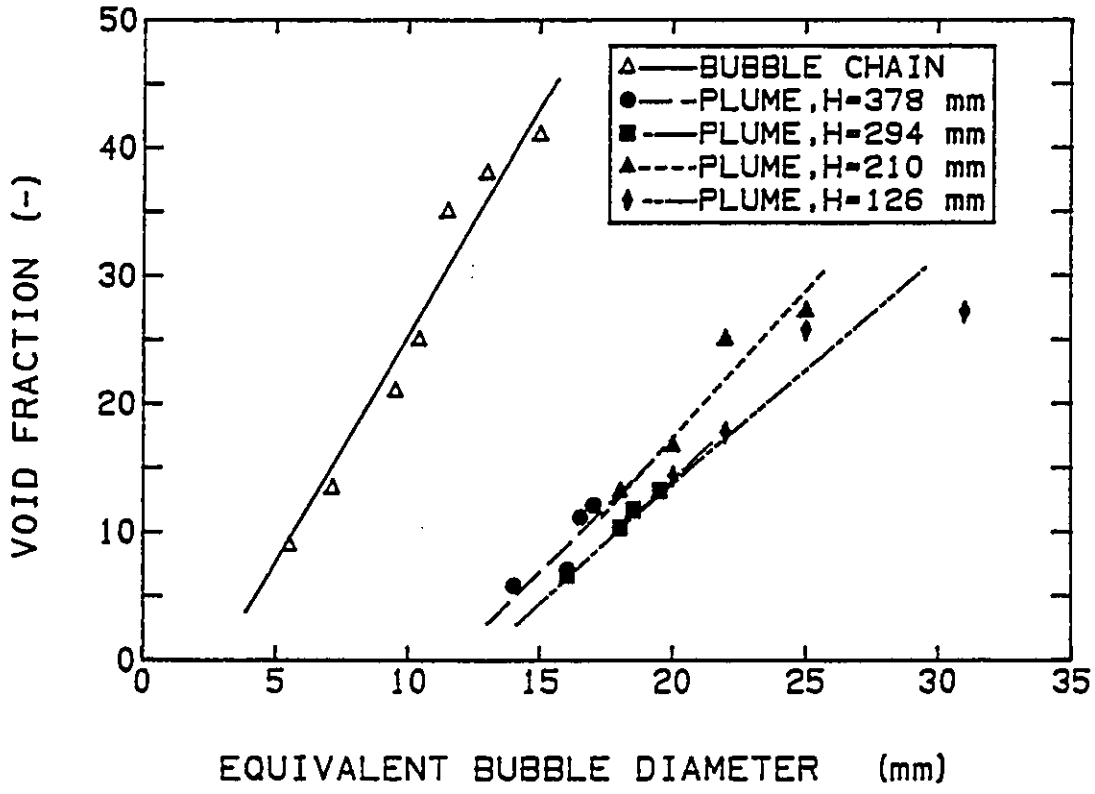

Figure V.3 Void fractions corresponding to velocity data in Figure V.1. The void factions in a chain of bubbles and in bubbly plumes were measured with LDA/EP technique, and estimated in the case of small bubble plumes.

The data is re-plotted in Figure V.4 to show the relationship between the relative velocity and equivalent diameter, and to compare it with the curves from Clift et al.(1978) which summarize the terminal rising velocities of single bubbles in stagnant water. The range of void fractions can be taken from the companion diagram, Figure V.3. The above experimental results suggest that the relative velocity of bubbles in a bubbly plume can be well represented by the terminal velocity of a single bubble.

This is the first time that the slip velocities of bubbles in plumes relevant to ladle metallurgy have been measured (Sheng and Irons, 1992a, 1992b). A variety of simplifying assumptions have been used for plume velocities. The earliest approach was also the simplest: no slip between the two phases (Szekely et al. 1978). The terminal velocity for a single bubble of one size has been used most often to represent the relative velocity of the entire bubble phase, (Deb Roy et al., 1978; Salcudean et al, 1985; Farias and Irons, 1986). The present experimental results suggest that this assumption is valid.

More recently, Johansen et al. (1989) have adopted a Lagrangian frame of reference to track individual bubbles through the turbulent flow. In this model, the relative velocities of bubbles were calculated based on the drag coefficient model originally proposed by Ishii and Zuber (1979) as discussed in Chapter II, which takes the following form:

$$C_{D\alpha} = C_D (1-\alpha)^b \qquad \text{(V.3)}$$

where $C_{D\alpha}$ is the drag coefficient on bubble in the two-phase flow with an average void fraction of α, C_D is the standard drag coefficient for single bubbles in stagnant fluid, and b is a coefficient assuming a value of 1 for bubbly pipe flow and 2 for bubbly churn

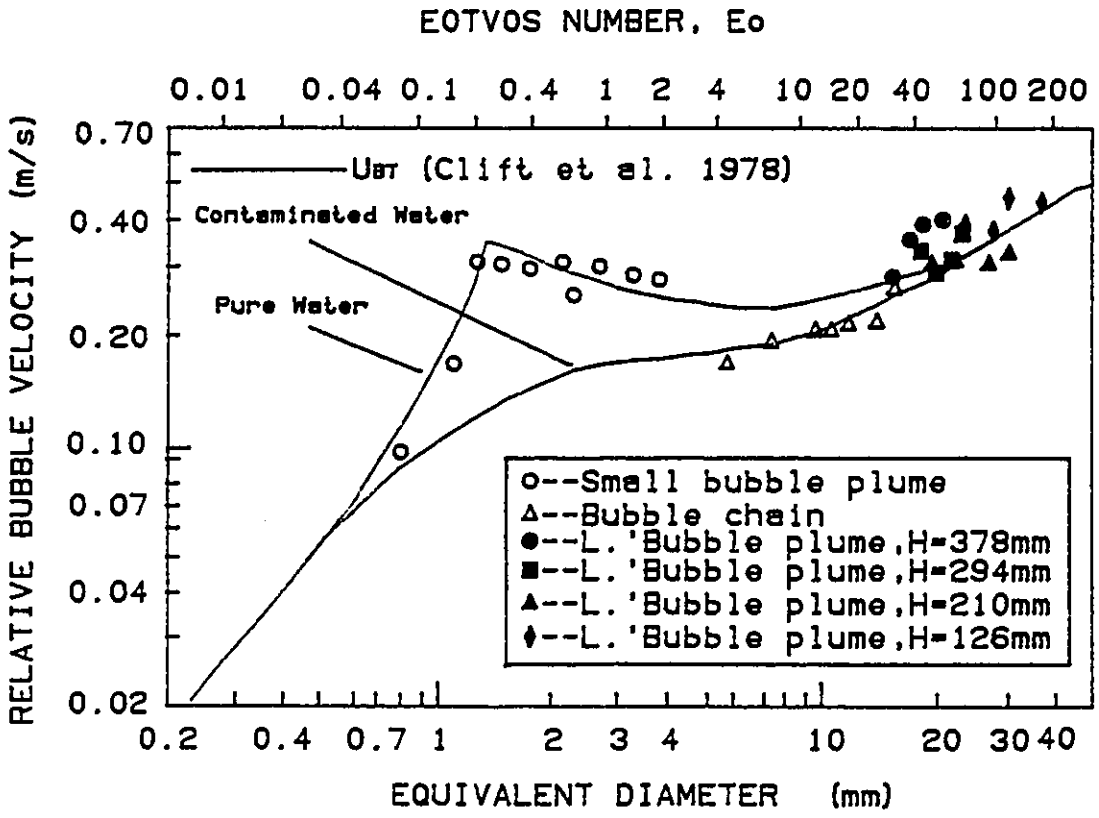

Figure V.4 Slip velocity measured with combined LDA/EP technique. The experiments were performed in the small box for a chain of bubbles, and in the large water model for the plumes.

flow. For a void fraction of 0.25, the drag coefficient is reduced by between 25 and 44 percent, depending on the value of b. Clearly, this is not the case as shown in Figure V.4.

Ishii and Zuber developed Equation V.3 for a gas-liquid pipe flow. All the variables in their study were time and area averaged ones rather than the local time averaged values used in this project. It was assumed that the pressures in the liquid and the gas phases are the same so that the mixture pressure drop could be calculated with a momentum balance of only the gas phase while the other momentum losses in the liquid phase could be neglected. The drag between the gas and liquid was calculated by simply adding up the drag forces on all of the bubbles inside the control volume. When bubble density is high in a pipe flow and the boundary layers of these bubbles are overlapping, both phases may be approximated as continua, and the above assumptions may hold. In an unconfined plume, the vertical pressure drop is more appropriately given by the hydrostatic head in the liquid; thus, the calculation of pressure drop in the gas phase with momentum balance only in the gas phase is not applicable. Therefore, bubbles should be treated individually with respect to the liquid flow around them.

The above discussion implies that the model of Ishii and Zuber may only be applied to bubbly flows with rather small bubbles and dense bubble population. For the bubbly plume flows encountered in the present study, the bubbles should be treated as individual bubbles, and the relative velocity with respect to the liquid flow around the bubble can be better predicted using the terminal velocity rather than using the model of Ishii and Zuber.

5.2 Determination of Lateral lift coefficient for Small Bubble

There has been less work performed on this topic than on the determination of the drag coefficient of a bubble. Theoretical determination of the lateral lift coefficient of a bubble, C_L, in a bubbly plume is almost impossible due to the complexity of the flow. The practical way to evaluate this factor for specific cases, is to measure C_L. In the following sections, the results from small bubble plumes produced with a fritted-glass injector are presented.

The lateral force coefficient defined by Eq.(II.48) in Chapter II can be expressed:

$$C_L = \left[\frac{V_B - V}{U_{BT}}\right]^2 \frac{g}{(U_B - U)(-\partial U/\partial r)} \qquad \textbf{(V.4)}$$

for a bubble undergoing the lateral migration as illustrated in Figure II.8.

The following assumptions are made for the derivation of the above equation:

(1) The lateral lift force is balanced only by the lateral drag force when steady motion in the radial direction is achieved.

(2) The flow in the radial direction is a steady flow and much smaller than in the vertical direction, and its effect is therefore neglected. The vertical velocity gradient in the r direction is the lateral driving force.

(3) The turbulence intensity is low due to extremely low void fraction, and its effect on the lateral movement of a bubble is neglected. As a result, the lateral migration of a bubble is mainly the result of the lateral lift force.

(4) The shape of bubbles in this case is spherical or elliptical, so that the lateral drag acting on the bubble is similar to that of the vertical drag. The lateral drag coefficient is therefore assumed to be the same as the vertical drag coefficient.

To measure C_L as defined by Eq.(V.4) and meet the requirements defined in the above assumptions, plumes with small bubbles were produced with the fritted glass as described in chapter IV. The bubble size is between 0.5 to 4 mm, which was measured with the video camera. The results of the velocity measurement with LDA in the two-phase plume zone are characterized in Figures V.5 and V.6. Figure V.5 shows the vertical velocity variations with Q_g of both liquid and bubbles in the plume center, and Figure V.6 shows the vertical velocity variations in the radial direction of both liquid and bubbles for $Q_g = 4x10^{-6}$ m^3/s. The lateral velocities of bubble and liquid in bubbly plumes are obtained based on the analysis of the PDF of the mixed lateral velocity as discussed in chapter III. Two typical PDFs of the mixed lateral velocity are shown in Figures V.7 and V.8, respectively which were obtained with LDA. The lateral slip velocity of bubbles, V_r, is defined as the difference between the lateral velocity of a bubble and the lateral velocity of the liquid, represented by the adjacent peaks in Figures V.7 and V.8. The other information needed for the calculation of C_L with Eq.(V.4) were obtained from LDA velocity measurements such as those shown in Figures V.5 and V.6, and from video camera measurement of bubble sizes. The results of the measurement and the calculated results of C_L are listed in Table V.2.

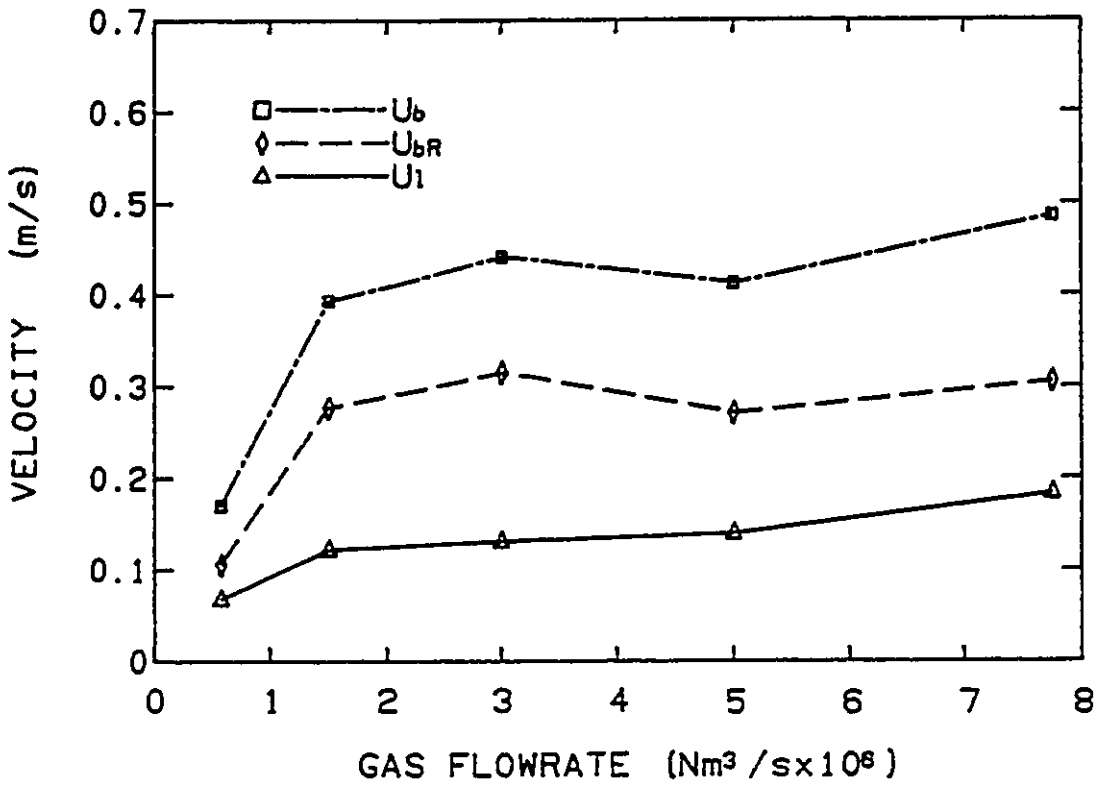

Figure V.5 Variation of vertical velocities with gas flowrate at the centerline of the plume. This was performed in the large water model, and the plume was produced with the fritted glass. The liquid velocity was measured with LDA in forward scattering, the bubble velocity was measured with a video camera at the plume center. x=0.29 m.

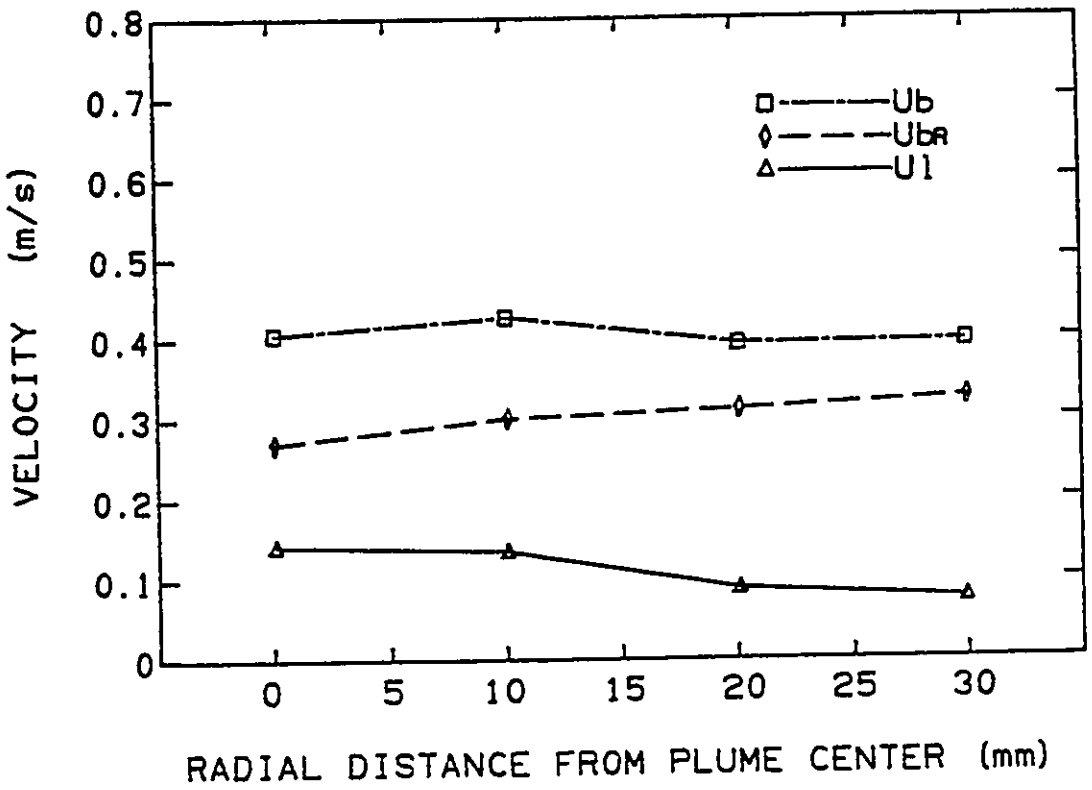

Figure V.6 Radial variation of vertical velocities for Q_g=4.0x10^{-6} Nm^3/s. This was performed in the large water model, and the plume was produced with the fritted glass. The liquid velocity was measured with LDA in forward scattering, the bubble velocity was measured with a video camera, x=0.29 m.

Table V.2 Measured Lateral Lift Coefficient

D_B cm	V_r cm/s	U_B cm/s	U_l cm/s	$\partial U_l/\partial r$ 1/s	U_r cm/s	$\xi x10^{10}$ -	C_L -
0.10	1.61	27.2	7.1	2.5	20.1	1.744	0.127
0.20	3.62	37.9	8.2	3.0	29.7	1.092	0.160
0.25	2.41	41.5	15.4	3.5	25.9	4.170	0.093
0.25	2.22	38.1	11.8	2.5	26.3	2.22	0.109
0.30	2.67	36.0	3.5	3.0	32.5	1.001	0.115
0.30	2.94	44.7	14.8	3.5	29.9	2.96	0.12
0.35	2.44	40.1	5.0	2.1	35.1	1.536	0.117
0.35	3.39	44.8	10.7	3.5	34.1	1.933	0.14
0.37	2.42	33.0	8.8	3.4	24.2	5.15	0.112
0.38	2.29	39.8	8.0	3.75	31.8	2.764	0.064

Some discussion is needed to interpret the results listed in Table V.2 in terms of the relations among V_r, C_L, D_B and U_r. Figures V.9 shows the dependence of V_r on the size of bubbles, and Figures V.10 shows the dependence of V_r on the vertical slip velocity U_r. V_r generally increased with increases of both D_B and U_r, and the data are more scattered as the two variables become larger. There is one irregular data point for D_B = 2 mm in Figure V.9, which corresponds to the bubble velocity peak in Figure V.4. It is obvious that the relation between V_r and U_r is more straightforward. The relation between V_r and $\partial U/\partial r$ is shown in Figure V.11, where with an increase of the velocity gradient, the lateral relative velocity of bubble also increases slightly. The variation of C_L with U_r is shown in Figure V.12. The solid lines were drawn in the above diagrams to show data variation tendency. The measured values of C_L are in the range of 0.1 to

0.15; they increase only slightly with an increase of the vertical slip velocity. The above simple correlations revealed some important features of the C_L. More complicated ones are still needed to give a clearer understanding of the combined effect of the experimental parameters.

One such example was given by Wang et al. as mentioned in Chapter II, who used the following combination of variables to interpret their experimental data:

$$\xi = e^{-\alpha}\frac{D_B}{U_r}\frac{\partial U}{\partial r}\left(\frac{D_B}{D}\frac{1}{Re_B}\right)^2\left(\frac{U_B}{U_{BT}}\right)^2 \qquad \textbf{(V.5)}$$

where D = 5.715×10^{-2} m, is the diameter of the pipe used in the experiment of Wang et al. and taken as a constant in this study. The effect of the size of the vessel is considered already included in the parameters such as the mean liquid velocity and its radial gradient. Wang et al. established the following relation between C_L and ξ to fit their experimental data (Figure V.13):

$$C_L = 0.010 + \frac{0.490}{\pi}\cot^{-1}\left(\frac{\log\xi + 9.3168}{0.1963}\right) \qquad \textbf{(V.6)}$$

The calculated values of C_L and ξ are listed in Table V.2 and shown in Figure V.13, where the data from Wang et al. are also plotted for comparison.

There does not exist a clear relation between Eq.(V.4) and equations developed by Wang et al., which are essentially empirical correlations. However, the main features in Eq.(V.4) are qualitatively revealed by the correlations. For instance, the effect of the velocity gradient, $\partial U/\partial r$, on C_L. In both equations, an increase of $\partial U/\partial r$ produces a decrease in C_L. The effect of bubble sizes on C_L is reflected by the effect of their rising velocities. In Eq.(V.4), the larger rising velocity of a larger bubble

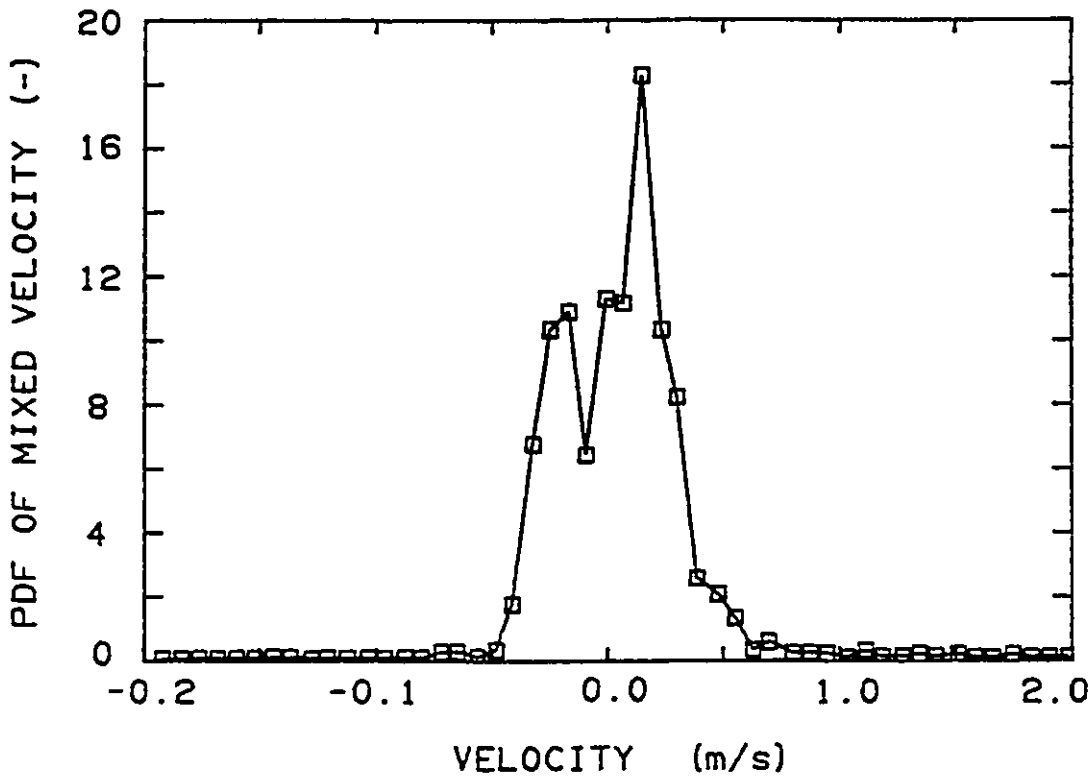

Figure V.7 Probability Distribution Function of mixed lateral velocity This was performed in the large water model, and the plume was produced with the fritted glass. The velocity was measured with LDA in backward scattering, $Q_g=4x10^{-6}$ Nm^3/s, x=0.29 m, r=0.02 m.

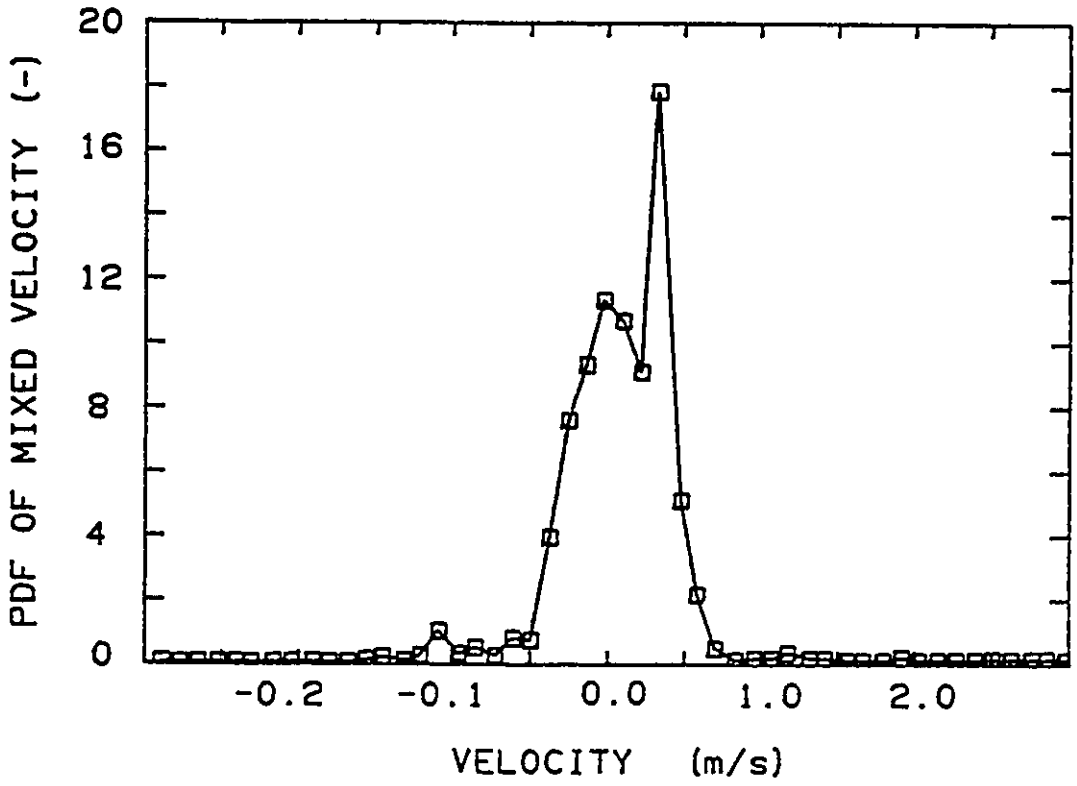

Figure V.8 Probability Distribution Function of mixed lateral velocity. This was performed in the large water model, and the plume was produced with the fritted glass. The velocity was measured with LDA in backward scattering, $Q_g=5x10^{-6}$ Nm^3/s, x=0.21 m, r=0.03 m.

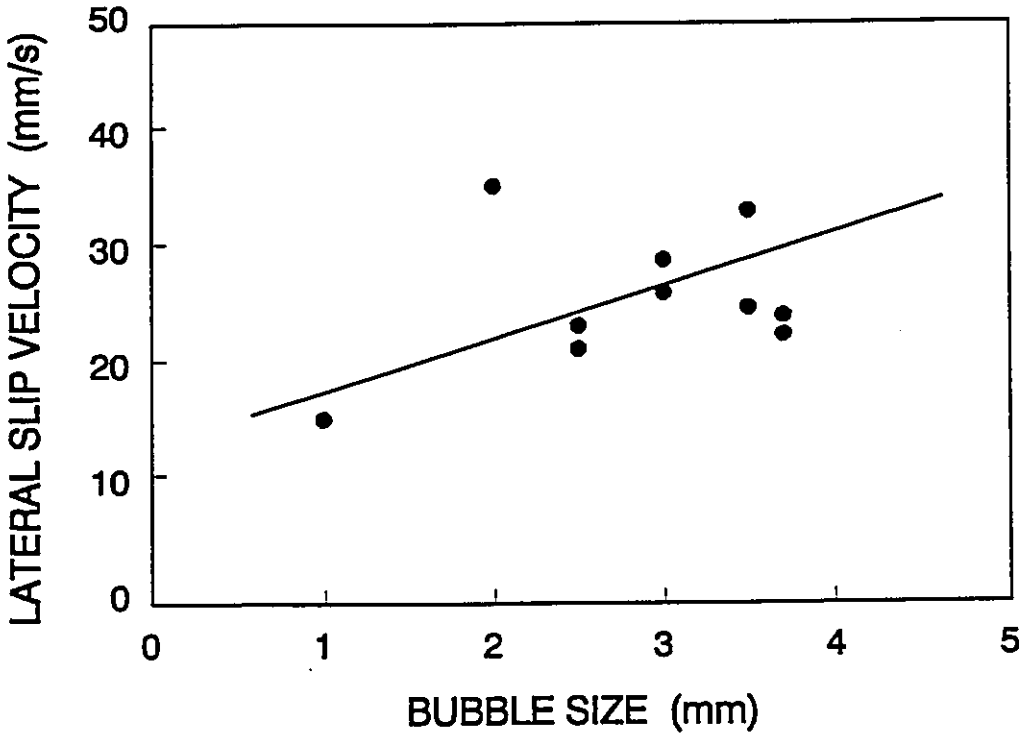

Figure V.9 Variation of the lateral slip velocity with the bubble size. This was performed in the large water model, and the plume was produced with the fritted glass. The velocity was measured with LDA in backward scattering, $Q_g=5x10^{-6}$ Nm^3/s, x=0.21 m, r=0.03 m.

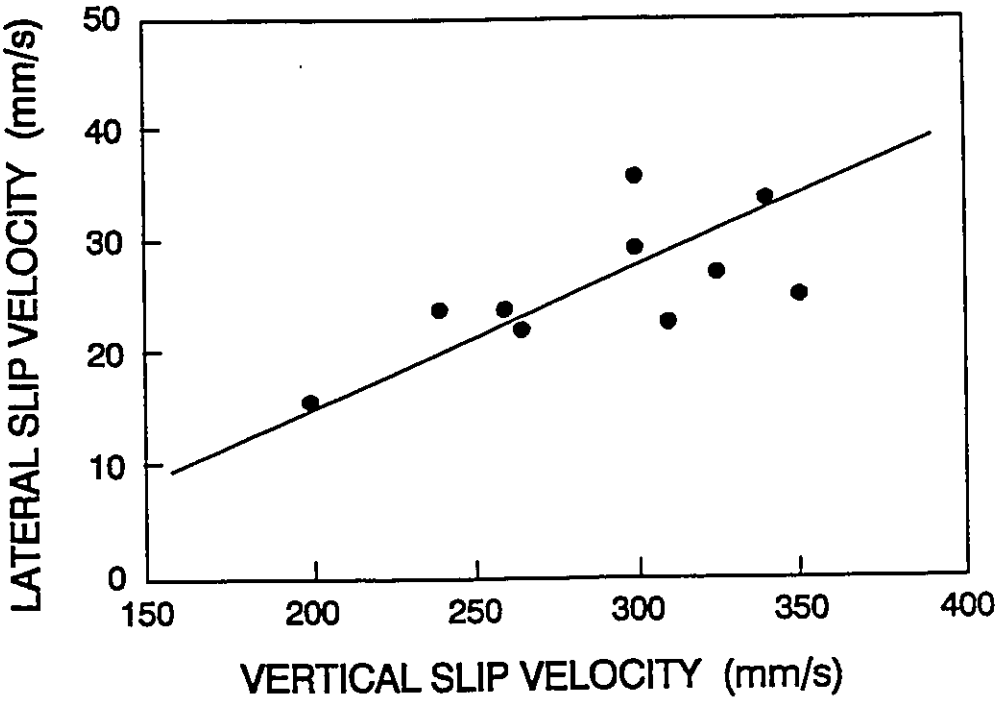

Figure V.10 Variation of the lateral slip velocity with the vertical slip velocity. This was performed in the large water model, and the plume was produced with the fritted glass. The velocity was measured with LDA in backward scattering, $Q_g=5x10^{-6}$ Nm^3/s, x=0.21 m, r=0.03 m.

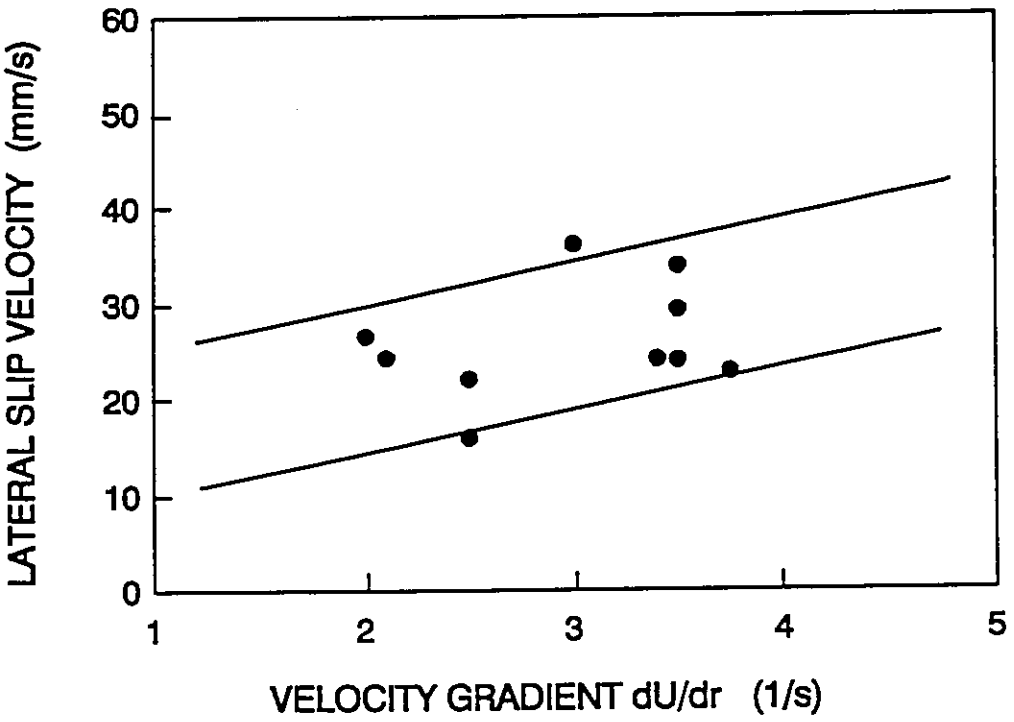

Figure V.11 Variation of the lateral slip velocity with the vertical velocity gradient. This was performed in the large water model, and the plume was produced with the fritted glass. The velocity was measured with LDA in backward scattering, $Q_g=5x10^{-6}$ Nm^3/s, x=0.21 m, r=0.03 m.

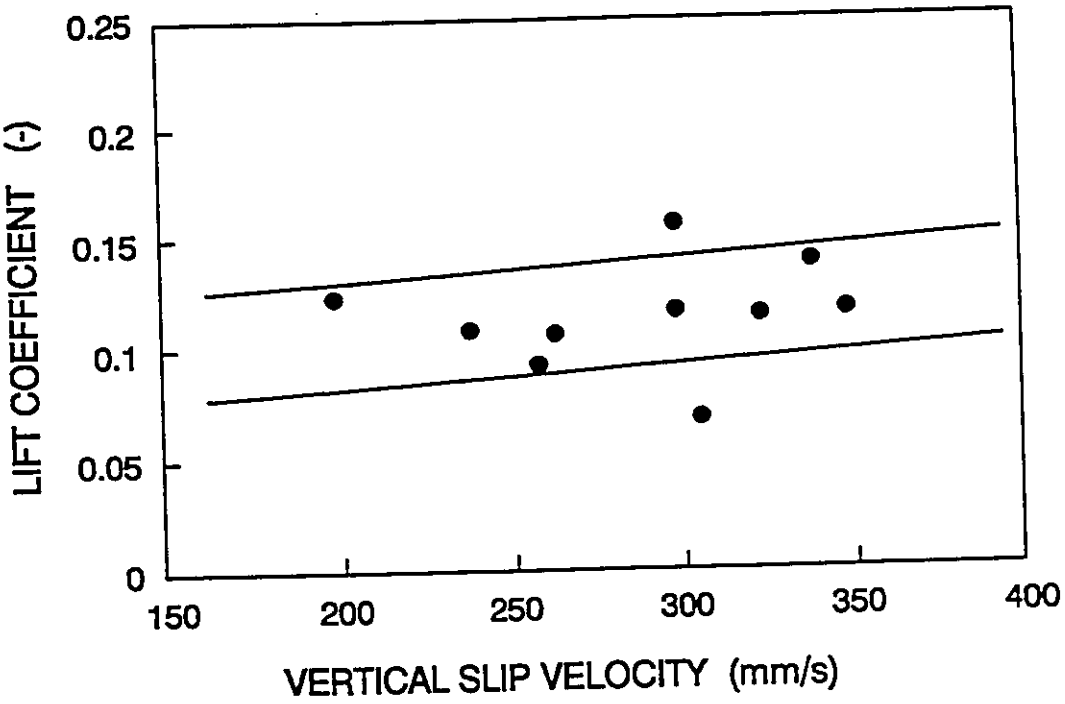

Figure V.12 Variation of the lateral lift coefficient with the vertical slip velocity. This was performed in the large water model, and the plume was produced with the fritted glass. The velocity was measured withLDA in backward scattering, Q_g=5x10^{-6} Nm^3/s, x=0.21 m, r=0.03 m.

indicates a lower value of C_L. In Eq.(V.5), a similar conclusion may be drawn. Since U_{BT} is usually proportional to $D_B^{0.5}$, when D_B is larger, Eq.(V.5) would yield larger value of ξ, which in turn indicates lower value of C_L.

The measured data of C_L shown in Figure V.13 fall in the range of 0.07 to 0.16. The results of the present study extended the results of Wang et al. in the lower ξ range as shown in Figure V.13. The present results are also in good agreement with the measurement of Beyerlein et al (1985), who reported C_L in the range of 0.03 to 0.3 as shown in Figure V.14, where data range of present study is also marked for comparison.

The experimental results discussed above indicate that, for small bubbles, the lift force plays important role in the lateral migration of bubbles. This argument, however, may not be true for large bubbles in the plume. In large bubble plumes, the intensity of turbulence is high, and the interaction of bubbles with the turbulent eddies may also play an important role in the lateral migration of bubbles.

5.3 Breakup of Bubbles in Bubbly Plumes

The breakup of bubbles in a turbulent bubbly plume may result from several reasons, such as bubble shape oscillation resonance, shear stresses (Clift et al. 1978), turbulent dynamic pressure forces (Hinze, 1955) and the instability at the gas/liquid interface (Kitscha and Kocamustafaogullari, 1989). Figure V.15 shows the basic forces involved in the splitting of bubbles in a plume. The shear stresses and the inertial force are splitting forces, and are balanced by bubble surface tension force, which sustains the

existing shape of the bubble. The relative significance of these forces may vary in different flow situations (Clift et al., 1978). In turbulent bubbly plumes, the mechanism of bubble breakup has not received adequate attention, and little experimental study of the breakup processes has been reported. In the following section, some of the preliminary experimental results obtained with video camera photography are presented and discussed.

The bubbly plume was produced in the large 1/10 scale model of a ladle under the experimental conditions described in chapter IV with a flush-mounted orifice. The break-up processes of bubbles rising in the center region of the plumes were followed with a video camera at a speed of 30 frames per second. The different break-up processes may be summarized into the following two types based on the experimental observation:

(1) When the gas flowrate is low, most bubbles first elongate, which is caused by the viscous shear stresses (Clift et al. 1978); the disturbances are then found to appear in the gas/liquid interface, and some of these disturbance grow rapidly to break up the bubble in less than 0.05 s (Figures V.16a to V.16c and V.17a to V.17d). This mode of break up as a result of the gradual growth of the instability disturbance in the gas/liquid interface seem to be the dominant mechanism when gas flowrate is lower than 1.0×10^{-4} m^3/s.

(2) Break-up of bubble could be a result of the combined effects of the stripping by shearing liquid flow around the bubble and the growth of the instability disturbances. With increases of Q_g, the bubble size also increases and the liquid flow becomes much stronger, which means much stronger stripping on the bubble surface.

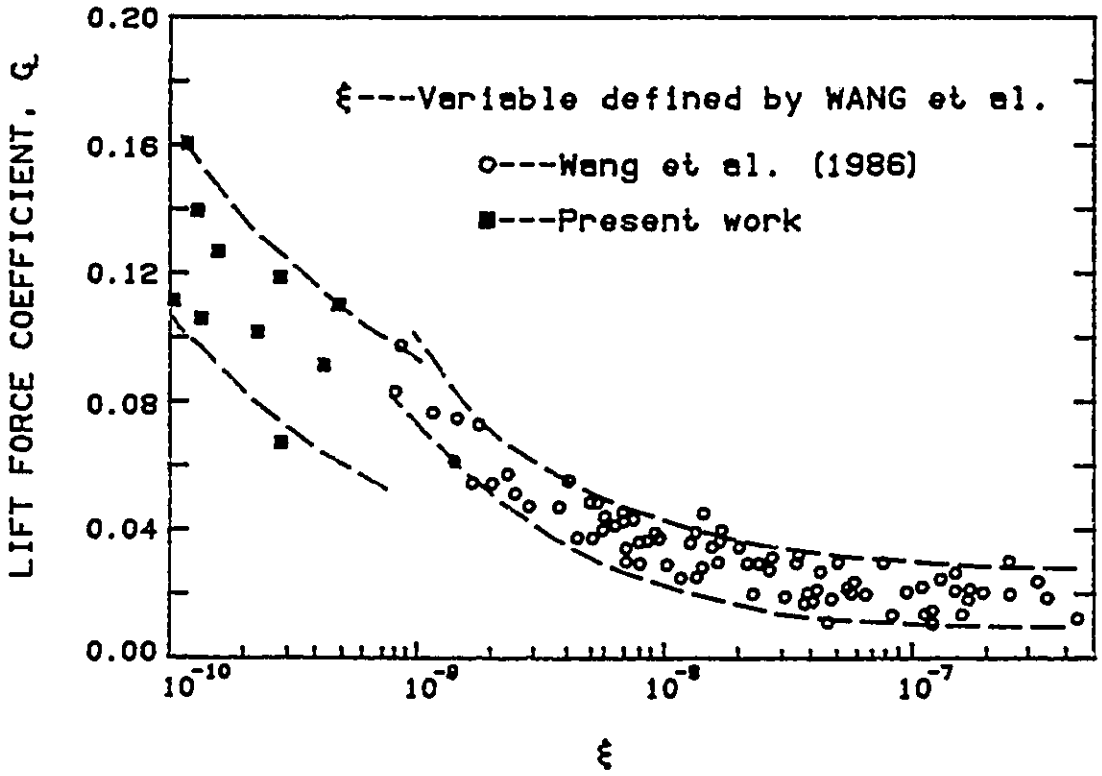

Figure V.13 Comparison of the measured C_L with the results of Wang et al. This was performed in the large water model, and the plume was produced with the fritted glass. The velocities were measured with LDA in backward scattering, other experimental conditions are listed in Table V.1

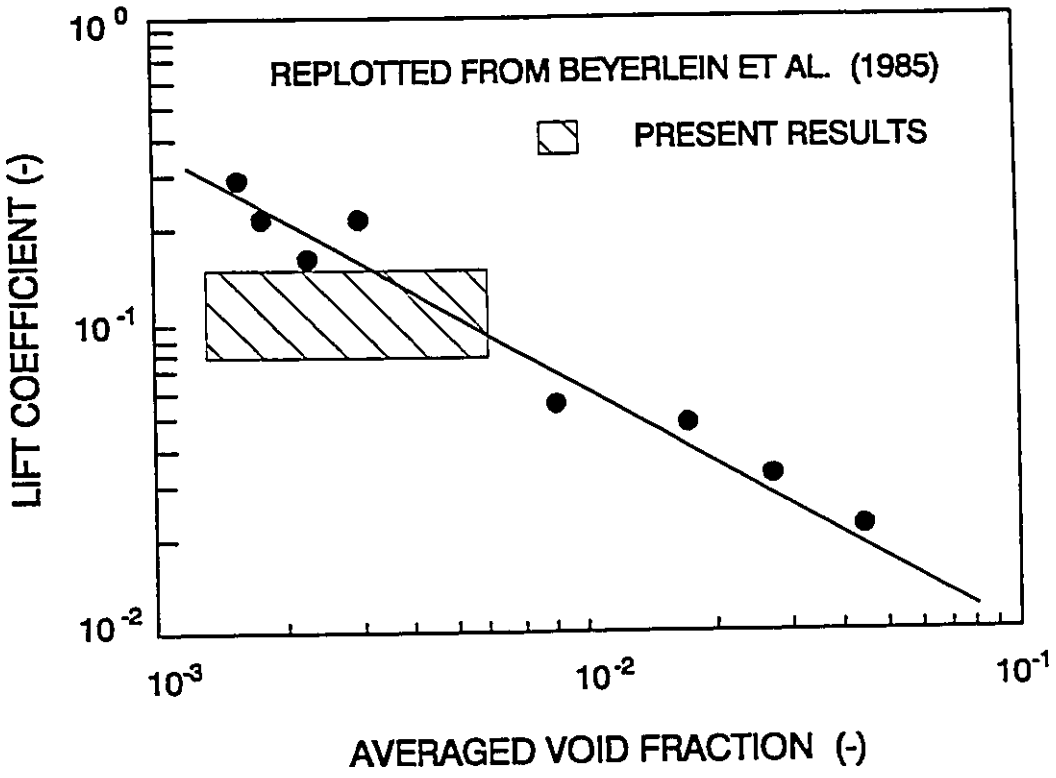

Figure V.14 Lift force coefficient, C_L, measured by Beyerlein et al. (1985)

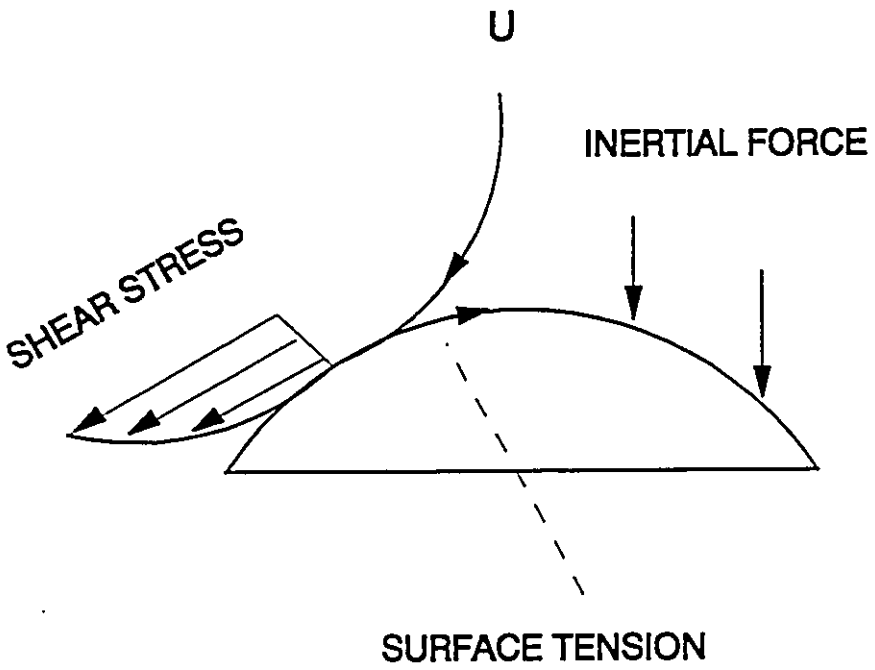

Figure V.15 Illustration of the forces acting on the surface of a bubble

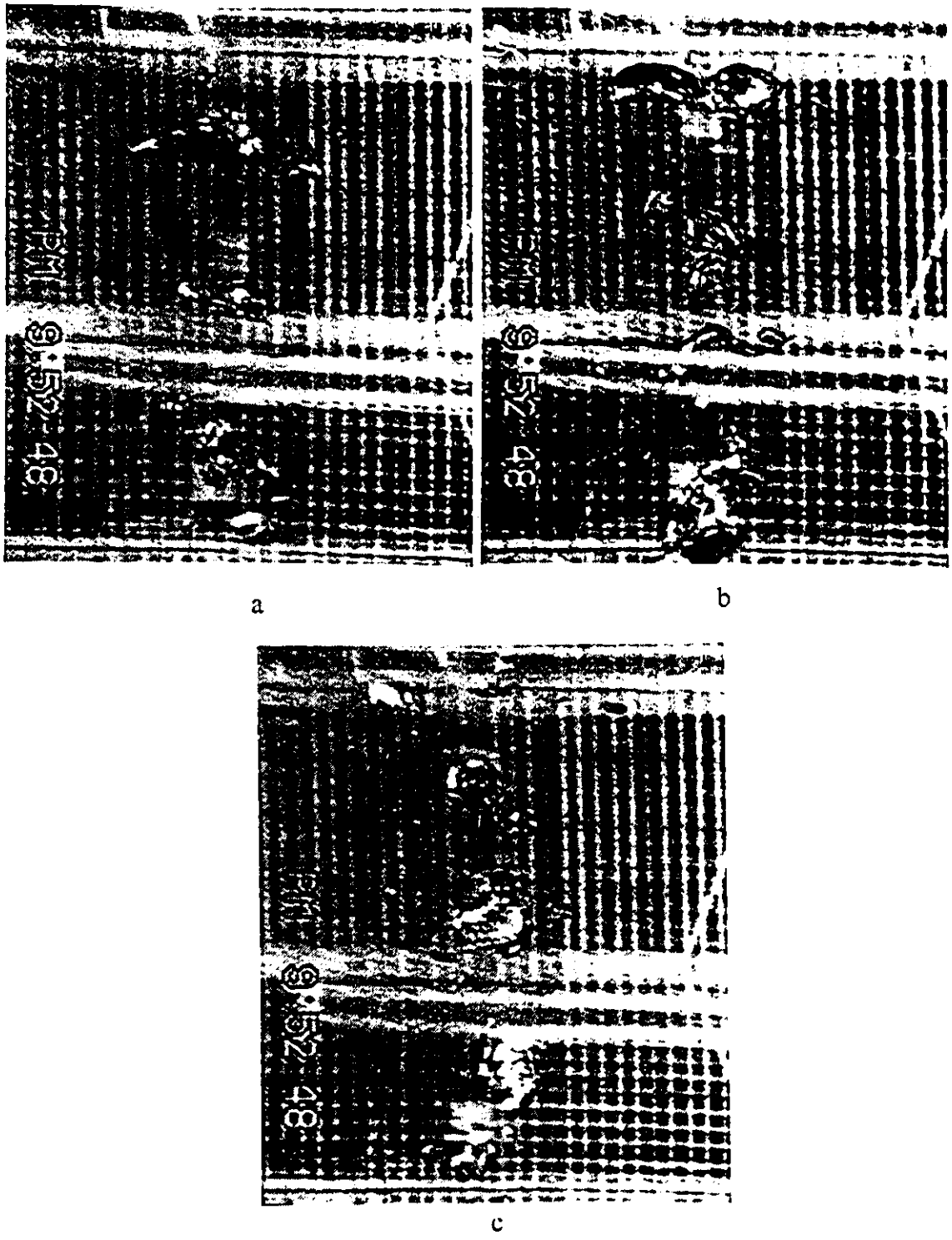

a b c

Figure V.16 Photographs Showing a bubble (Top of the photo) undergoing breakup in the center of the plume. (a) t=0.0 s, (b) t=0.033 s, (c) t=0.066 s. Q_g=5x10^{-5} Nm^3/s, x=0.21 m.

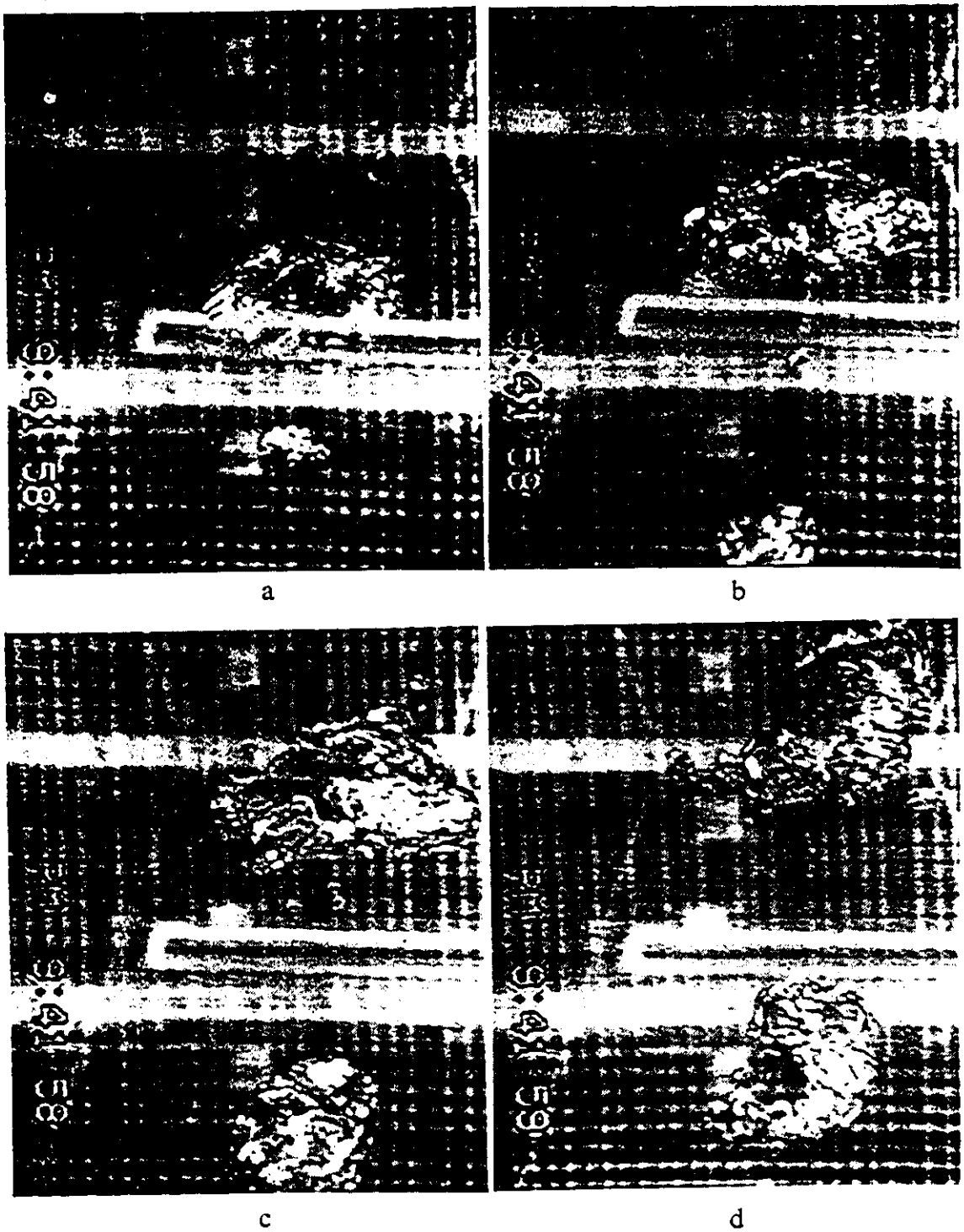

a b

c d

Figure V.17 Photographs Showing a bubble undergoing breakup in the center of the plume. (a) t=0.0 s, (b) t=0.033 s, (c) t=0.066 s, (d) t=0.1 s. $Q_g=1x10^{-4}$ Nm^3/s, x=0.29 m.

As a result, the elongation of the bubble is more violent, and more disturbances are found at the bubble surface with faster growth rate. The breakup assumes a different mode than the previous case, where it usually happens at center-top of a bubble and produce only a few small bubbles. The bubble starts to breakup as its rim is being torn apart to produce a large number of small bubbles, and finally explodes as several disturbances become big enough at the same time (Figures 18a to 18d and 19a to 19d).

The above experimental observation suggests that, under the present experimental conditions, the break-up of bubbles in a bubbly plume is fairly strong, and results in a steadily decreasing bubble size distribution in vertical direction as discussed in Chapter IV. This experimental information is very important to the modelling of the process. More work, however, is needed to improve the present understanding of the process.

5.4 Turbulence Characteristics in Two-Phase Plumes

In Chapter IV, the experimental results indicated that, turbulence inside the two-phase plume is not isotropic. Some insight into this non-isotropy can be gained with turbulence theory. Turbulence in single phase flow is generated by the viscous shear forces, which in turn are the results of the mean velocity gradient. Using the Einstein convention, the time averaged turbulent energy budget assumes the following form (Tennekes and Lumley, 1972):

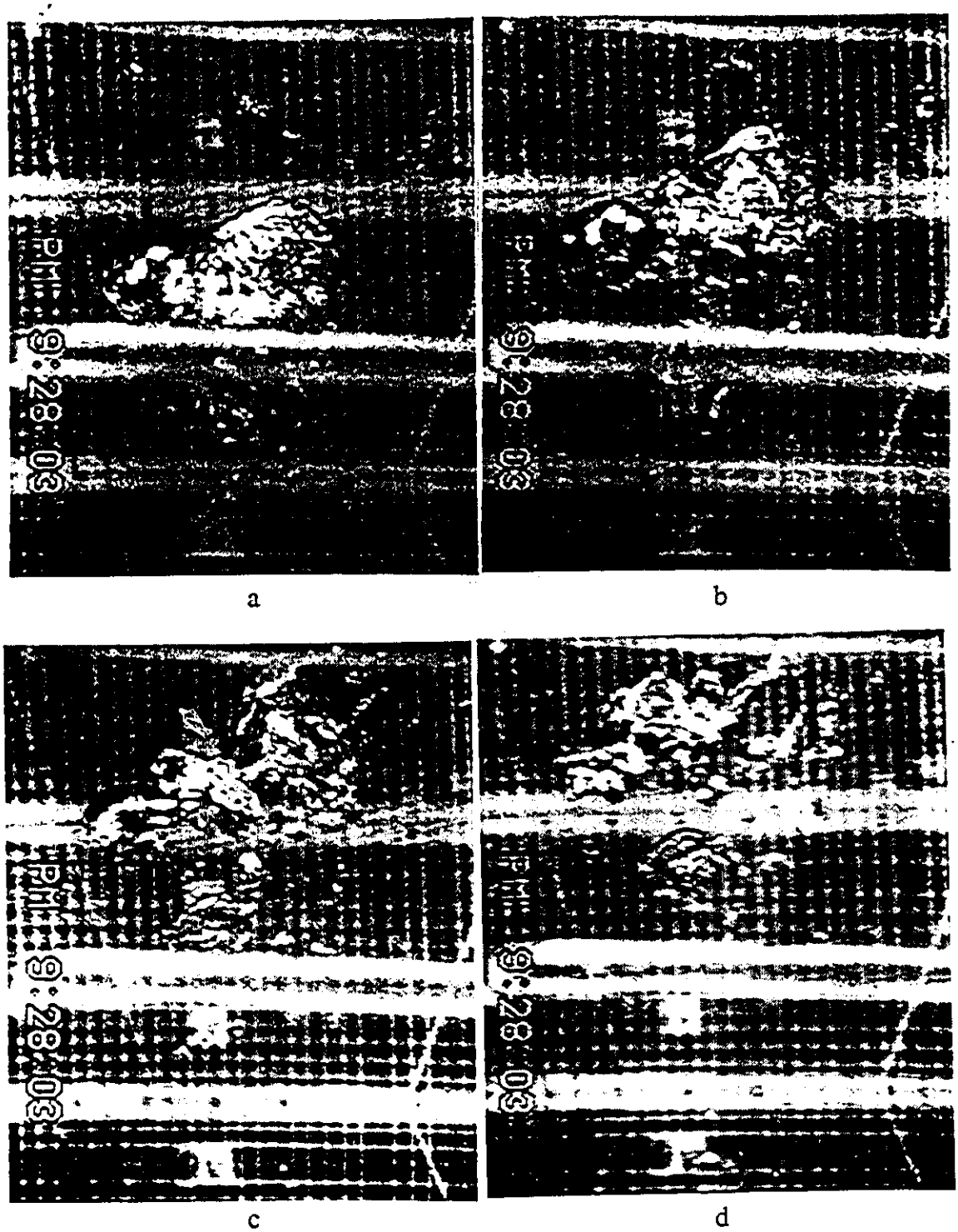

Figure V.18 Photographs Showing a bubble undergoing breakup in the center of the plume. (a) t=0.0 s, (b) t=0.033 s, (c) t=0.066 s, (d) t=0.1 s. Q_g=1.5x10^{-4} Nm^3/s, x=0.29 m.

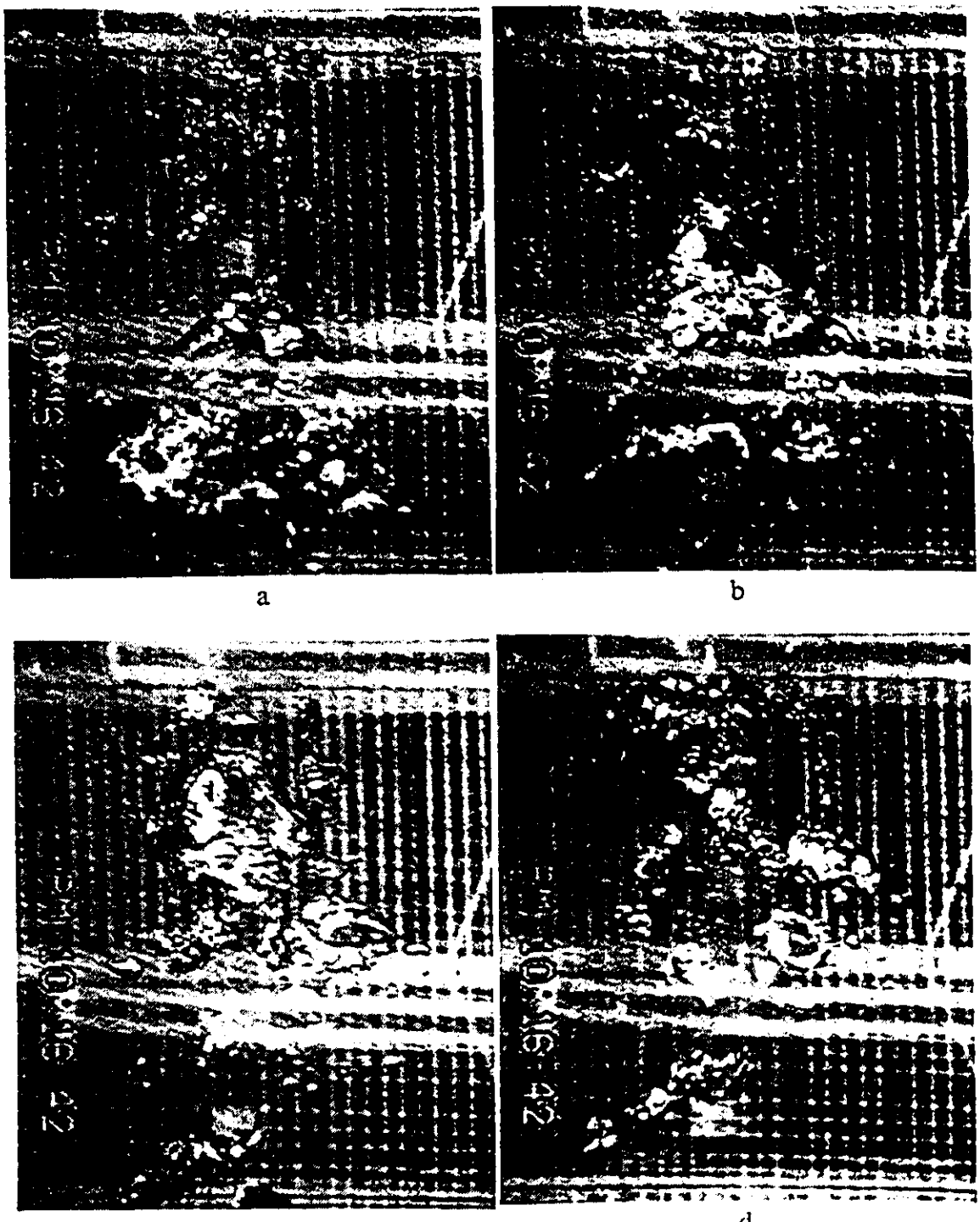

a b

c d

Figure V.19 Photographs Showing a bubble undergoing breakup in the center of the plume. (a) t=0.0 s, (b) t=0.033 s, (c) t=0.066 s, (d) t=0.1 s. $Q_g=1.5x10^{-4}$ Nm^3/s, x=0.37 m.

$$U_j \frac{\partial}{\partial x_j}\left(\frac{1}{2}\overline{u_i u_i}\right) = -\frac{\partial}{\partial x_j}\left(\frac{1}{\rho}\overline{u_j p} + \frac{1}{2}\overline{u_i u_i u_j} - 2\nu\,\overline{u_i s_j}\right) \qquad \textbf{(V.7)}$$

$$- \overline{u_i u_j} S_{ij} - 2\nu \overline{s_{ij} s_{ij}}$$

where:

$$s_{ij} = \frac{1}{2}\left(\frac{\partial u_i}{\partial x_j} + \frac{\partial u_j}{\partial x_i}\right) \qquad \textbf{(V.8)}$$

and:

$$S_{ij} = \frac{1}{2}\left(\frac{\partial U_i}{\partial x_j} + \frac{\partial U_j}{\partial x_i}\right) \qquad \textbf{(V.9)}$$

The subscripts 1, 2 and 3 indicate x, r and θ directions, respectively. If one assumes that the flow is dominated by flow in the axial, x, direction, then one can ignore U_j and $\partial U_i/\partial x_j$ except for U and $\partial U/\partial r$. Taking the velocities in the x, r and θ directions as U, V and W, respectively, the equations for $\frac{1}{2}\overline{u^2}$, $\frac{1}{2}\overline{v^2}$, $\frac{1}{2}\overline{w^2}$ can be simplified respectively to:

$$0 = -\overline{u'v'}\frac{\partial U}{\partial r} + \frac{1}{\rho}\overline{p\frac{\partial u'}{\partial x}} - \frac{\partial}{\partial r}\frac{1}{2}\overline{u'^2 v'} - \frac{1}{3}\epsilon \qquad \textbf{(V.10)}$$

$$0 = 0 + \frac{1}{\rho}\overline{p\frac{\partial v'}{\partial r}} - \frac{\partial}{\partial r}\overline{\left(p'/\rho + \frac{1}{2}v'^2\right)v'} - \frac{1}{3}\epsilon \qquad \textbf{(V.11)}$$

$$0 = 0 + \frac{1}{\rho}\overline{p\frac{\partial w'}{\partial \theta}} - \frac{\partial}{\partial r}\left(\overline{\frac{1}{2}w'^2 v'}\right) - \frac{1}{3}\epsilon \qquad \text{(V.12)}$$

The only turbulent production term is the first one on the right hand side of Equation 11; there is no generation of turbulence in the r and θ directions. They can only acquire kinetic energy from the non-linear pressure-velocity interactions (Tennekes and Lumley, 1972). This argument also implies that larger velocity gradients along a particular direction would produce more turbulence and skew it towards that direction. However, it should also be noted that turbulent kinetic energy tends to break up large eddies which are more likely to cause the non-isotropy, so that isotropy would be improved by pressure-velocity interactions. The measured θ for four different gas flowrates are shown in Figure IV.20, where the degree of non-isotropy decreases with increasing gas flowrate, and the relation can be represented with the following regressional equation for the present data:

$$\theta = 55 - 0.02522\, Q_g \qquad \text{(V.13)}$$

This observation qualitatively supports the above argument (Sheng and Irons, 1992b).

The above equations may also be used to estimate the turbulence level in the two horizontal directions. Since in both directions, turbulence is developed in a similar way through the pressure-velocity interaction, it is likely that v' and w' are at the same level. Some experimental measurement of turbulence in developed pipe flow (Lawn, 1971) and in a self-preserving jet (Wygnanski & Fiedler, 1969) seem to support this argument. As a result, it should be reasonable to assume that the turbulence intensity is the same in the horizontal directions for the calculation of k as presented in Chapter IV.

CHAPTER VI

MATHEMATICAL MODELLING OF BUBBLY PLUME FLOWS

6.1 General Considerations

Bubbly plume flows encountered in a ladle metallurgical process have been experimentally studied with the physical model described in chapters III and IV. Since the principal mechanism of the flow in the molten metal is the same as the flow in the water, and the behaviour of bubbles is similar in the two liquids according to Morton similarity as discussed in Chapter IV, except for the thermal expansion of the gas at the exit, the physics of the flow as revealed by the experimental results improved the understanding of the plume behaviour in a steelmaking ladle. Based on this understanding, a detailed flow simulation can be performed with a mathematical model, which solve both the liquid flow equations and the motion equations of the bubble.

The flow is a buoyancy-driven two-phase flow in the bubbly plume zone. The flow in the liquid phase is assumed to have the following properties:

(1) it is a Newtonian incompressible flow,

(2) it is a turbulent recirculating flow,

(3) it is a steady and two-dimensional axisymmetrical flow.

These assumptions are appropriate since both water and molten steel are Newtonian fluids with negligible compressibility. The flow is generated by the bubbles rising in the center of the cylindrical vessel and then recirculates from the plume centre towards the side walls. The magnitude of the liquid flow is in the range of 0.1 to 0.4 m/s, as a result, the Reynolds number in terms of this velocity and the dimension of the vessel is in the order of 10^4 which is well above the value required for the transition from laminar flow to turbulent flow.

The computation is divided into the following two parts:

(1) In the first part, only the liquid flow is computed. The liquid phase is treated as a pseudo-continuum with the void fraction resulting from the existence of bubbles assumed to be completely inter-penetrating with the liquid. Consequently, the liquid flow can be predicted with the computation code TEACH and the modified k-ϵ model in an Eulerian frame as discussed in chapter II, using the experimentally measured void fraction distributions. The predictions of both the mean flow field and the turbulent kinetic energy obtained with different groups of the extra source constants are compared with the experimental results obtained in the previous chapters for the determination of the most appropriate values for the extra source constants of the modified k-ϵ model. The results of the first part computation is presented in Section 6.6.1: Part I---Determination of extra source term coefficients.

(2) In the second part of the computation, the behaviour of bubbles in the plume is modeled in a Lagrangian frame to yield the void fraction distribution, which is then used to predict the liquid flow in the same way as in the first part of the computation with the modified k-ϵ model and the newly determined coefficients of the extra source

terms. The large bubbles rising in the centre of the plume are called mother bubbles, and the small bubbles produced from the break up of the mother bubbles are called daughter bubbles. The bubble motion equations are to be solved for the trajectories of both mother and daughter bubbles to yield the void fraction distribution. The results of the second part computation is presented in section 6.6.2: Part II---Predictions of the plume flow (Sheng and Irons, 1992d).

The dimensions and the grid design for the computation is shown in Figure VI.1. A 14x22 grid system is chosen for half of the flow field inside the model ladle. The locations of the narrow window on the cylindrical wall of the model for the LDA measurement are marked in Figure VI.1.

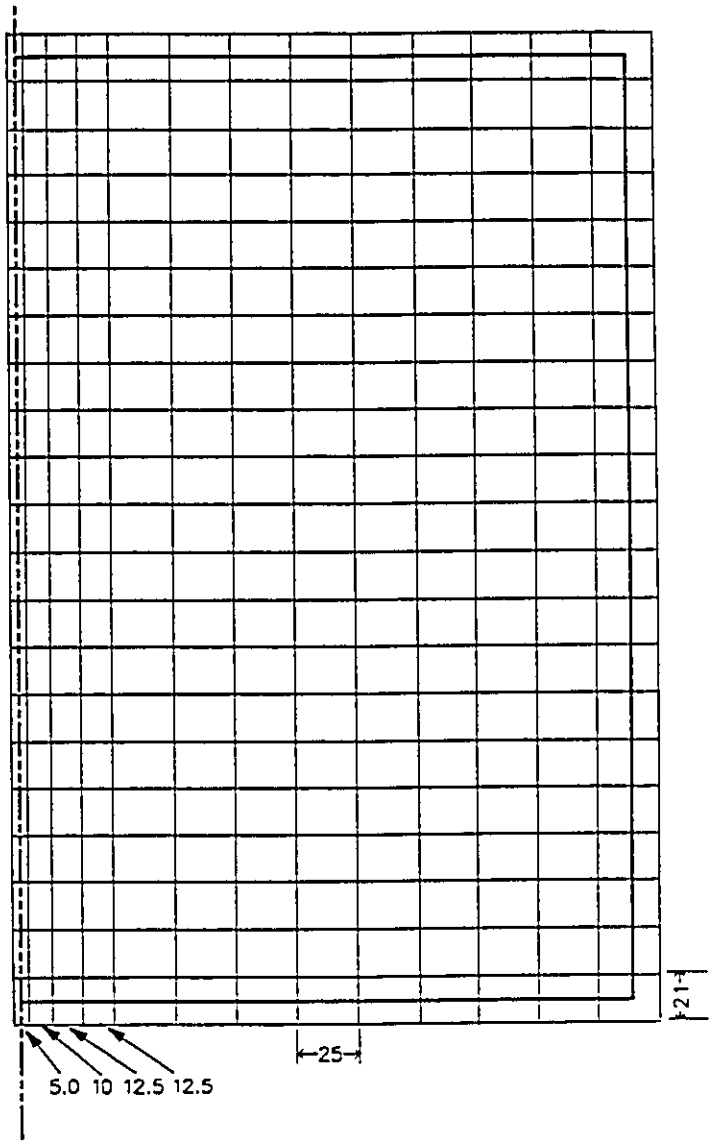

Figure VI.1 Illustration of the grid design for the computation

The boundary is shown with the thicker solid line, the symmetrical axis is shown with the dashed line and the slots for LDA measurement are marked with dashed lines with arrows.

6.2 General Algorithm of the Mathematical Model

The overall structure of the computer program PLUME for the calculation of the both liquid flow field and the void fraction distribution is shown in Figure VI.2. The algorithm of the main program is virtually the same as the TEACH code discussed in Chapter II. The only difference is that, in the part II computation, when the convergence of the liquid flow is achieved, a subroutine BUBBLE is called in to track the motion of the bubbles and calculate the resulting void fraction distribution. The renewed void fraction is then brought back into the main program to update the liquid flow field. The program stops when convergency for both the liquid flow field and the void distribution is achieved. In the first part of the computation, where the measured void fractions are used for the determination of the extra source term coefficients, subroutine BUBBLE is turned off in the computation process.

6.3 Modelling of the Bubble Behaviour in Plumes

Based on the experimental observations presented in the previous Chapters and previous work on similar processes discussed in Chapter II, the following considerations and assumptions are considered appropriate for the mathematical modelling of the plume flow in the part II computation:

6.3.1 General Considerations and Assumptions

(1) The liquid flow field can be first obtained with an initial estimate of void fraction distribution by solving the turbulent Navier-Stokes equation in an Eulerian

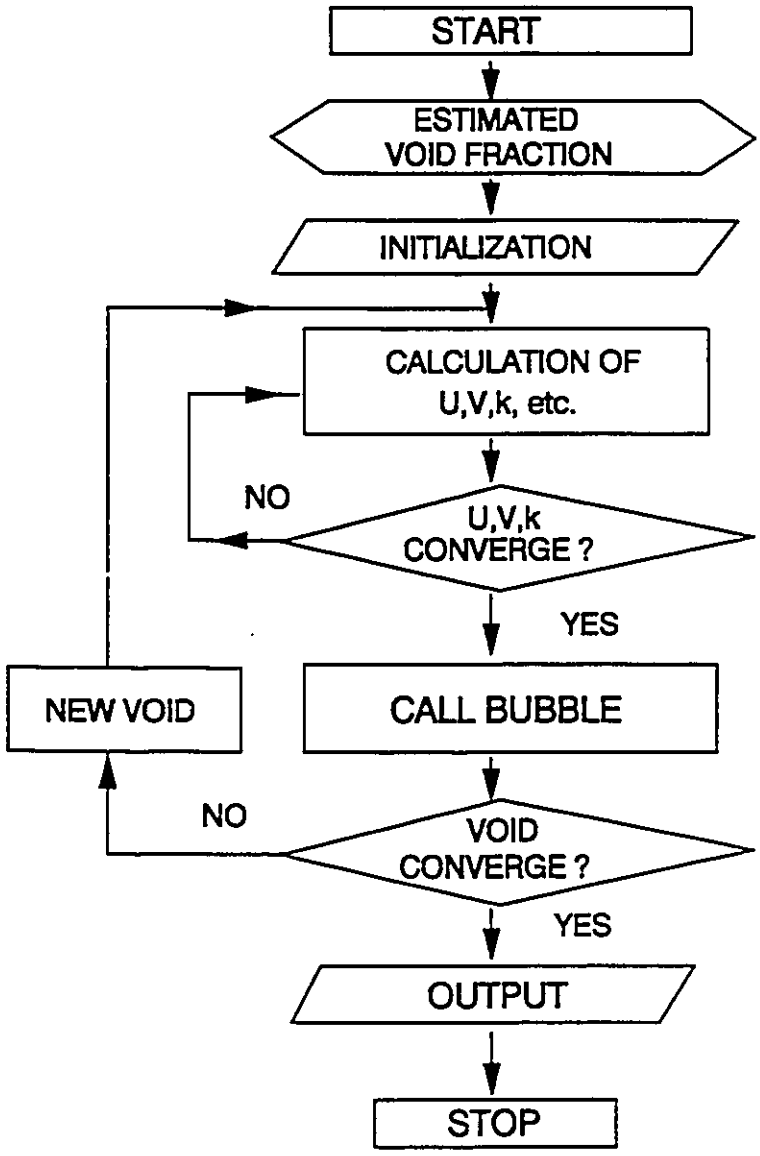

Figure VI.2 Illustration of the structure of the program PLUME

scheme, where turbulence is modeled with the modified k-ε model discussed in Chapter II. With this estimate for liquid flow field, the bubble motion equations can be solved in a Lagrangian frame to give such variables as the bubble rising velocity, which would then be used to make a new estimate of the void fraction distribution. The updated void fraction is used for a new round of computation of the liquid flow field. The iteration ends when both the liquid flow field and the void fraction distribution converge.

(2) The bubble rising process consists of an initial rising period during which no bubble break up occurs, and a free rising period in which break up of bubbles happens randomly. This assumption is based on the facts observed in the experimental work of Brimacombe (1991) and this project as discussed in Chapters II and IV. Brimacombe identified the following three regimes during bubble rise in plumes:

(1) Primary zone where a bubble detaches the nozzle,
(2) Free Bubble zone where no breakup occurs, and,
(3) Breakup zone where a plume forms.

In the present model, the detachment of bubble from the nozzle is simplified as a smooth rising period and treated as a part of the initial rising period.

(3) For the purpose of local void fraction distribution calculation, the shape of bubbles must be known to determine such parameters as transit time of a bubble in a given cell and the volume of the cell occupied by the bubble during its passage through the cell. The shape of the bubble at the nozzle is assumed to be a sphere and gradually elongates in the horizontal direction during rising. The shape variation of the bubble is approximated with the variation of its shape ratio E which is the ratio of the bubble

height to its chord length. It was assumed that, during the rising process E declines linearly from 1, which is the shape ratio of a spherical bubble, to the minimum value of 0.24 which a bubble can maintain before break up (Clift et al. 1978). The minimum value of E is reached in about 0.3 to 0.5 s after detachment from the nozzle for the present experimental conditions, based on the experimental observation performed in this project (Figure IV.8) and reported in the literature. The minimum value of E of 0.24 for a single bubble (Clift et al., 1978) is assumed valid also for bubbles in the plume.

(4) The principal mechanism causing the break up of bubbles in the plume is assumed to be the interface instability, which is intensified by the liquid turbulence and shear force. The break up criteria based on the combined Kelvin-Helmholtz and Rayleigh-Taylor instability theory is used to determine the breakup of bubbles in the process (Kitscha and Kocamustafaogullari, 1989). For a bubble bigger than the critical size of break up, it will break up during rising, and the breakup position is determined randomly. The number and size of the daughter bubbles produced from the break up is also determined randomly. In the model, these random processes are controlled by generating several series of random numbers independently from a standard normal distribution.

(5) The mechanism of the lateral motion of bubbles in the plume is not completely understood at the present time, however the following assumptions are considered necessary and appropriate based on the previous work and experimental observation of this project. The lateral motion of the mother bubbles rising in the center of the plume is assumed mainly caused by the interaction with the turbulent eddies and the spiral movement related to the wake shedding. For small daughter

bubbles, the lateral migration is caused by the interaction with turbulent eddies and the lateral lift force resulting from the axial liquid velocity gradient in the radial direction. The lateral migration of bubbles is also a result of the mean liquid flow in the radial direction which carries bubbles with it due to the drag effect.

(6) The bubbles are followed one by one in the computer simulation. When one bubble is being followed, the influence from other bubbles existing in the plume at the same time is neglected. Coalescence is considered not to have a significant effect since few cases of coalescence were observed during the free rising period of a bubble in the experiments.

(7) The void fraction is calculated in the following way. The grids covered by kth bubble (both mother and daughter bubbles) during its rising are recorded. For a given grid cell with coordinates (i,j), if the cell is occupied by a part of the bubble for a transient time $t_k(i,j)$, the contribution to the void fraction in the cell by the bubble is calculated in the following way:

$$\alpha_k = t_k(i,j)\frac{V_{Bp}}{V_G} \qquad \text{(VI.1)}$$

where V_G is the volume of the grid cell, and V_{Bp} is the volume of the part of the bubble in the cell. The time averaged void fraction over a period of T and N_B bubbles is then:

$$\alpha(i,j) = \frac{1}{T}\sum_{k=1}^{N_B}\alpha_k = \frac{1}{T}\sum_{k=1}^{N_B} t_k(i,j)\frac{V_{Bp}}{V_G} \qquad \text{(VI.2)}$$

6.3.2 Flow Sheet of Subroutine BUBBLE

The flow chart is shown in Figure VI.3a and VI.3b. The subroutine is composed of the following parts.

6.3.2.1 The Initial Conditions

The gas flowrate, Q_g, is determined with the input of one of the monitoring parameters of the program, NQG, which assumes values of 1, 2, 3 and 4, corresponding to the gas flowrates of 50, 100, 150 and 200 ml/s used in the water model experiments. For each Q_g, the bubble size and frequency at the exit were determined based on the experimental measurements and previous work. Bubbles are assumed to start rising with $U_B = 0$ at the nozzle. The effect of coalescence and the mushroom shape of the bubble is neglected.

The transition from the period of the initial rising of the bubble to the free rising is affected by many factors and there has not been a clear criterion to determine it. However, based on the experimental observation in this project and those reported by Brimacombe (1991), it is reasonable to assume that the initial rising period is within a distance of approximately $1.5D_B$ from the nozzle. During this period, to simplify the computation, the shape variation of a bubble is neglected and the bubble is assumed to be a sphere.

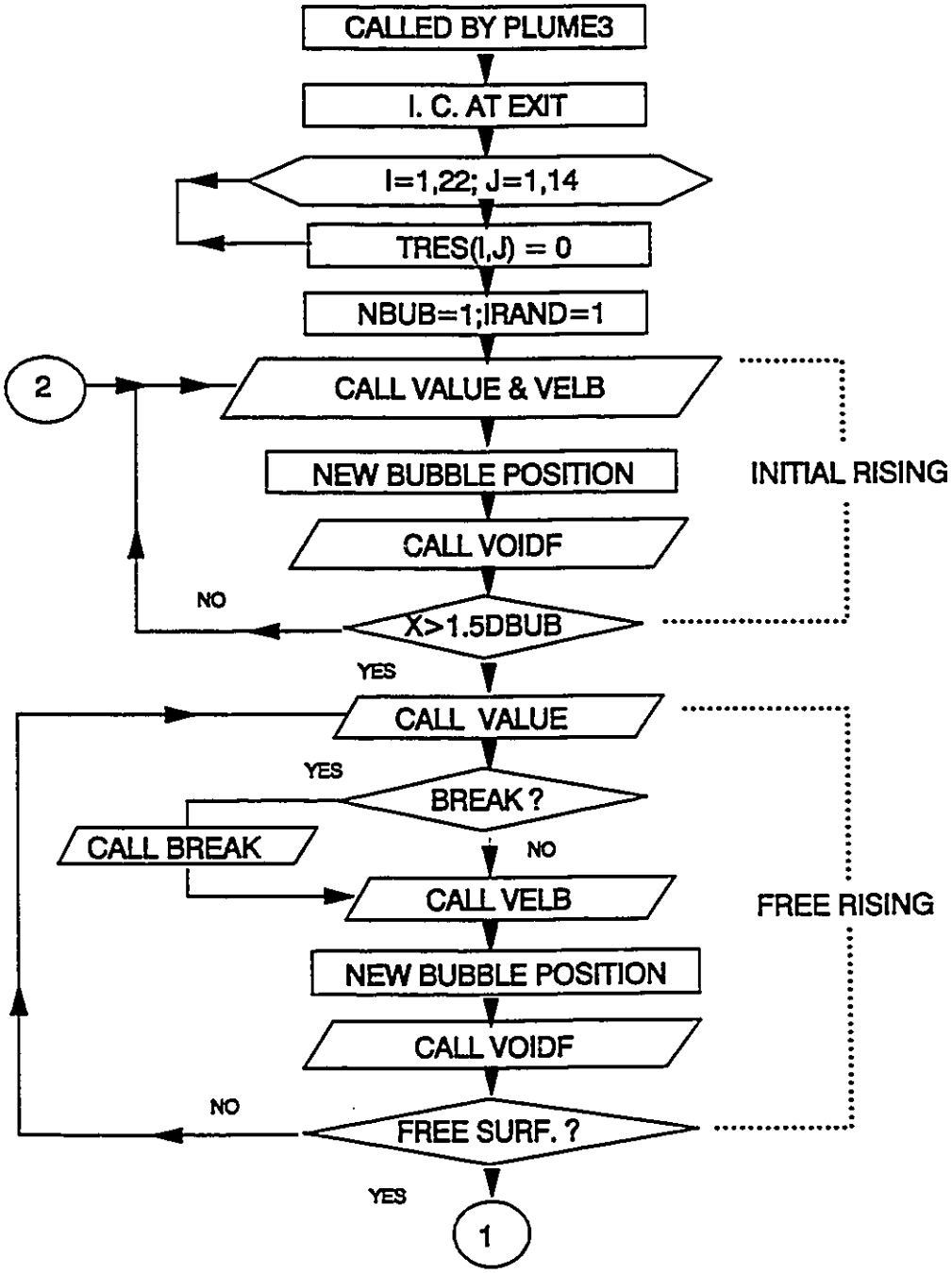

Figure VI.3a The illustration of the flow sheet of subroutine BUBBLE

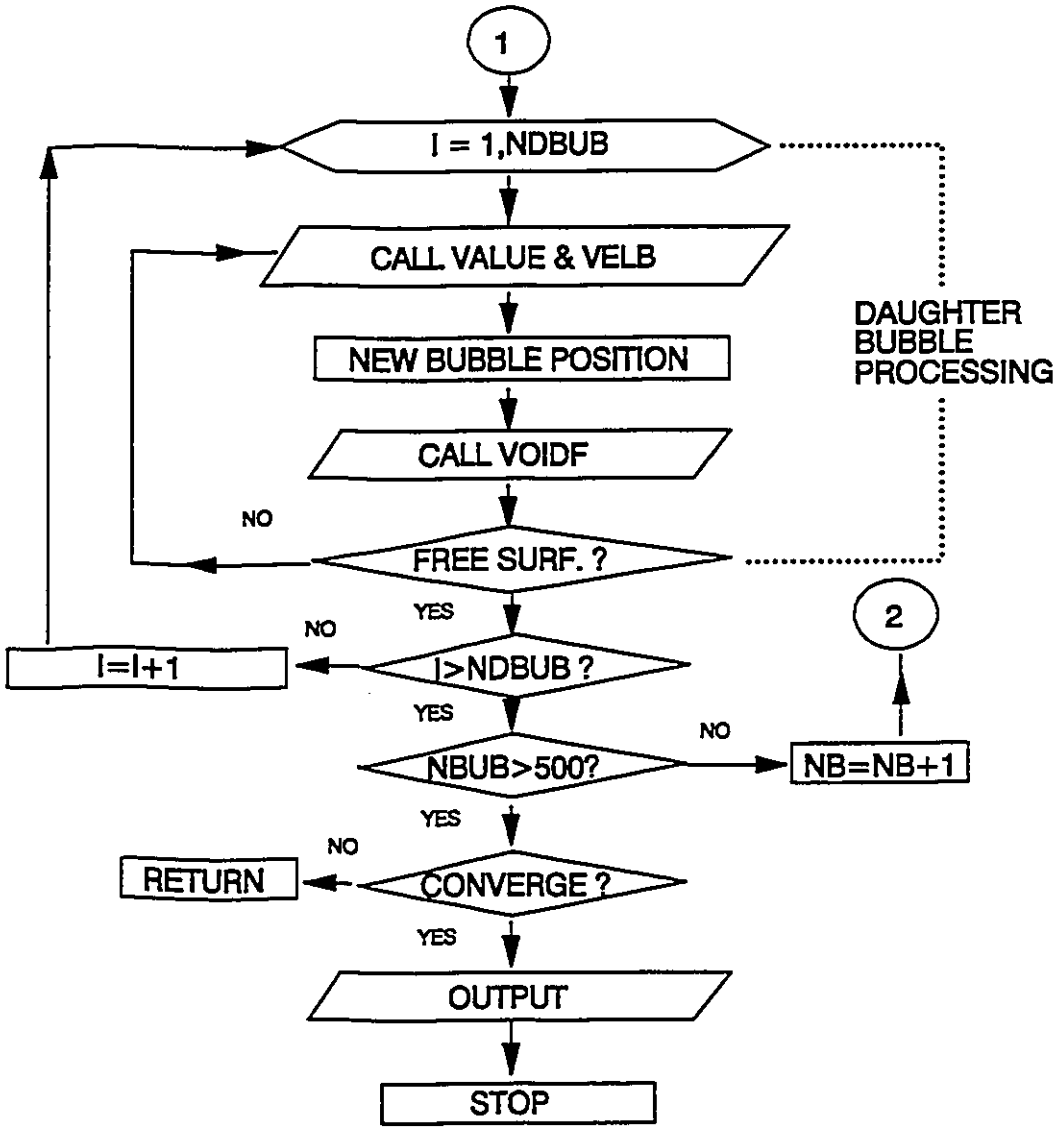

Figure VI.3b The illustration of the flow sheet of subroutine BUBBLE (Continued)

6.3.2.2 Determination of the Liquid Flow Conditions

Since the grid points do not always fall on the same place as the trajectories of bubbles, the necessary information of the liquid flow field at the point where the bubble passes is determined with linear interpolation of known values at the grids surrounding the point. Subroutine VALUE is designed for this purpose. It calculates the values of U, V, k, ε and other flow variables at the point, which are to be used for the solution of the bubble motion equations.

6.3.2.3 Modelling of Breakup Process of Bubbles

The treatment of the bubble breakup process is based on the experimental results of the size and shape variation of bubbles during rising presented in Chapters IV and V (Figures IV.7 and IV.8). The simulation of the breakup process is done in the subroutine BREAK. After the initial rising period has ended, the bubble with a size larger than the critical breakup size is assumed to undergo a random breakup process. The critical breakup size is estimated with (Kitscha and Kocamustafaogullari, 1989; Sheng, 1992):

$$0.25\frac{D_B}{U_r} \geq 1.612\left(\frac{\sigma}{\rho_f g^3}\right)^{0.25} \qquad \textbf{(VI.3)}$$

where, D_B is the bubble size and U_r is the local slip velocity. In an air-water system, the critical bubble size can be then determined with the following equation:

$$\frac{D_B}{U_r} \geq 0.1064 \qquad \textbf{(VI.4)}$$

That is, the bubble would breakup at a random position and produce a random number of daughter bubbles with random sizes. The process is controlled in the program by generating a series of random numbers. When a random number falls in the range of possible break up, the bubble is considered to break up at the point. The range of possible breakup is represented by the random numbers greater than R_{N_+} and smaller than R_{N-} from a standard normal distribution. The determination of this breakup range is based on the breakup rate of bubbles, which is the ratio of number of broken bubbles to total bubbles counted and determined empirically with the help of the video camera study of the bubbly plume. The experimentally observed mean breakup rates were 0.159, 0.197, 0.236 and 0.274 for gas flowrates of 50, 100, 150 and 200 ml/s, respectively. Consequently, the breakup ranges of the random numbers at each time step used in the model are (-0.2, 0.2), (-0.24, 0.24), (-0.30, 0.30) and (-0.35, 0.35) for the gas flowrates of 50, 100, 150 and 200 ml/s, respectively. The occurrence of the random numbers within these ranges are equal to the breakup rates of bubble for the corresponding gas flowrates at each time step. The largest bubble after the break up would be treated as the new mother bubble and be tracked accordingly. The new mother bubbles are assumed to breakup only once, and their breakup rates have the values of 0.064, 0.096, 0.143 and 0.19 for the gas flowrates of 50, 100, 150 and 200 ml/s, respectively. The corresponding breakup ranges are (-0.08, 0.08), (-0.11, 0.11), (-0.18, 0.18) and (-0.25, 0.25) for the gas flowrates of 50, 100, 150 and 200 ml/s, respectively. The information of the daughter bubbles is first stored and, after the tracking of the mother bubble has ended, it is used to follow each daughter bubble. The daughter bubble is considered not to break up and the interaction among them is also neglected.

6.3.2.4 Calculation of the Bubble Trajectory and the Void Fraction

The new positions of bubbles are obtained by solving the bubble motion equations, which are discussed in detail in section 6.4.3. Since the randomly determined turbulent components of the liquid velocity are used in the calculation, the bubble trajectories are also of a random nature. When a bubble has reached a new position, the void fraction it created during its passage from last position to the new one is calculated in the following way.

The grid cells covered by a bubble during its rising in the last time step are determined based on the information of the bubble trajectory by scanning all the grids. The transit time of the bubble through these grids is calculated, and the void fraction in these grid cells are then calculated by summing the transit time contributed by all the bubbles previously followed.

6.4 Mathematical Formulation of the Model

6.4.1 Modified Reynolds Averaged Equations

Cylindrical coordinates are chosen for the mathematical model. The notation used to depict the velocity field are listed in Table VI.1 and expressed with the following equations:

Table VI.1 Velocity Notations

DIRECTIONS	VECTOR	x	r
Unit Vector		**i**	**j**
Scalar Coord.		x	r
Liquid Velocity	**U**	U	V
Bubble Velocity	$\mathbf{U_B}$	U_B	V_B
Slip Velocity	$\mathbf{U_r}$	U_r	V_r
Instant. Vel.	**u**	u	v
R.M.S Component	**u'**	u'	v'

for the liquid velocity:

$$U = Ui + Vj \tag{VI.5}$$

The bubble velocity is expressed with the following equation:

$$U_B = U_B i + V_B j \tag{VI.6}$$

and the relative (slip) velocity assumes the form as follows:

$$\begin{aligned} U_r = U_B - U &= (U_B - U)i + (V_B - V)j \\ &= U_r i + V_r j \end{aligned} \tag{VI.7}$$

The two dimensional conservation equations for mass, momentum and other transportable variables are listed as follows.

The mass conservation is written in the form of Eq.(VI.8), where the slip velocity between the two phases is ignored as it has negligible effect on the total mass balance due to the large density difference between the liquid and air:

$$\frac{\partial(\rho U)}{\partial x} + \frac{1}{r}\frac{\partial(r\rho V)}{\partial r} = 0 \qquad \textbf{(VI.8)}$$

where:

$$\rho = \alpha\rho_g + (1-\alpha)\rho_l \qquad \textbf{(VI.9)}$$

The general conservation equation for a transportable variable ϕ is:

$$\frac{1}{r}\frac{\partial(r\phi V)}{\partial r} + \frac{\partial(\phi U)}{\partial x} - \frac{\partial}{\partial x}\left(\Gamma_\phi\frac{\partial\phi}{\partial x}\right) - \frac{1}{r\partial r}\left(r\Gamma_\phi\frac{\partial\phi}{\partial r}\right) - S_\phi = 0 \qquad \textbf{(VI.10)}$$

The conservation equation for momentum in the x-direction:

$$\frac{\partial(\rho U^2)}{\partial x} + \frac{1}{r}\frac{\partial(\rho rUV)}{\partial r} = -\frac{\partial p}{\partial x} + \frac{\partial}{\partial x}(r\mu_l\frac{\partial V}{\partial x}) + S_U \qquad \textbf{(VI.11)}$$

where S_U is the source term.

$$S_U = \frac{\partial}{\partial x}\left[\mu_l\frac{\partial U}{\partial x}\right] + \frac{1}{r\partial r}\left[r\mu_l\frac{\partial V}{\partial x}\right] + \alpha g \qquad \textbf{(VI.12)}$$

in the r-direction:

$$\frac{\partial(\rho UV)}{\partial x} + \frac{1}{r}\frac{\partial(\rho rV^2)}{\partial r} = -\frac{\partial p}{\partial r} + \frac{\partial}{\partial x}\left(\mu_T \frac{\partial V}{\partial x}\right) + \frac{1}{r\partial r}\left(r\mu_T \frac{\partial V}{\partial r}\right) + S_V \qquad \textbf{(VI.13)}$$

where S_V is the source term.

$$S_V = \frac{\partial}{\partial x}\left[\mu_T \frac{\partial U}{\partial r}\right] + \frac{1}{r\partial r}\left[r\mu_T \frac{\partial V}{\partial r}\right] - \mu_T \frac{2V}{r^2} \qquad \textbf{(VI.14)}$$

6.4.2 Modified k-e Model

In the case of axisymmetrical cylindrical coordinates, the k-ϵ model modified for two phase flow assumes the following form (Malin and Spalding, 1984):

$$\mu_T = C_\mu \frac{k^2}{\epsilon} \qquad \textbf{(VI.15)}$$

$$\frac{Dk}{Dt} = \frac{\partial}{\partial x_j}\left(\frac{\nu_T}{\sigma_k}\frac{\partial k}{\partial x_j}\right) + S_k \qquad \textbf{(VI.16)}$$

$$\frac{D\epsilon}{Dt} = \frac{\partial}{\partial x_j}\left(\frac{\nu_T}{\sigma_\epsilon}\frac{\partial \epsilon}{\partial x_j}\right) + S_\epsilon \qquad \textbf{(VI.17)}$$

where:

$$p_k = 2\mu_T\left[\left(\frac{\partial U}{\partial x}\right)^2 + \left(\frac{\partial V}{\partial r}\right)^2 + \left(\frac{V}{r}\right)^2\right] + \mu_T\left(\frac{\partial U}{\partial r} + \frac{\partial V}{\partial x}\right)^2 \qquad \textbf{(VI.18)}$$

is the production term.

The source terms are written in the following forms as already discussed in Chapter II:

$$S_k = P_k - C_D\rho\epsilon + C_{k1}\alpha(1-\alpha)P_k + C_{k2}C_f\alpha\rho_f k \qquad \textbf{(VI.19)}$$

$$S_\epsilon = \frac{C_1\epsilon P_k}{k} - \frac{C_2\rho\epsilon^2}{k} + C_{e1}\alpha(1-\alpha)P_k\frac{\epsilon}{k} + C_{e2}\alpha\rho_f C_f\epsilon \qquad \textbf{(VI.20)}$$

In the computation program, the above sources are written into linear and non-linear terms in the following way:

$$S_u^k = P_k + C_{k1}\alpha(1-\alpha)P_k + C_{k2}C_f\alpha\rho_f k \qquad \textbf{(VI.21)}$$

$$S_p^k = -\frac{C_D\rho\epsilon}{k} = \frac{C_D C_\mu \rho^2 k}{\mu_T} \qquad \textbf{(VI.22)}$$

$$S_u^\epsilon = \frac{C_1\epsilon P_k}{k} + C_{e1}\alpha(1-\alpha)P_k\frac{\epsilon}{k} + C_{e2}\alpha\rho_f C_f\epsilon \qquad \textbf{(VI.23)}$$

$$S_p^g = -\frac{C_2 \rho \varepsilon}{k} \qquad \text{(VI.24)}$$

6.4.3 Bubble Motion Equations and Their Solutions

In the derivation of the bubble motion equations, the force terms for drag, pressure, added mass, buoyancy and lateral lift are considered while the history term is assumed small and neglected due to high turbulence and large bubble size under the present experimental conditions.

The bubble motion equations used here assume the following forms (Thomas et al., 1983). In the vertical direction:

$$\frac{dU_B}{dt} = -\frac{1}{2}\frac{C_D A_B}{V_B}(U_B - u)\left|U_B - u\right| + \frac{\rho_l}{\rho_g} V \frac{\partial U}{\partial r} - \frac{1}{2}\frac{\rho_l}{\rho_g}\left(\frac{dU_B}{dt} - V\frac{\partial U}{\partial r}\right) - (1 - \frac{\rho_l}{\rho_g})g \qquad \text{(VI.25)}$$

where A_B and V_B are cross sectional area and volume of the bubble. In the radial direction:

$$\frac{dV_B}{dt} = -\frac{1}{2}\frac{C_D A_B}{V_B}(V_B - v)\left|V_B - v\right| + \frac{\rho_l}{\rho_g} U \frac{\partial V}{\partial x} - \frac{1}{2}\frac{\rho_l}{\rho_g}\left(\frac{dV_B}{dt} - U\frac{\partial V}{\partial x}\right) - \frac{\rho_l}{\rho_g} c_L U_r \frac{\partial U}{\partial r} \qquad \text{(VI.26)}$$

In the above two equations, the first term is the drag term, the second is the pressure term and the third is the added mass term. The last term in Eq.(VI.25) is the buoyancy while in Eq.(VI.26) represents the lift force.

The drag coefficient, C_D, can be written into the following form:

$$C_D = -2\frac{\rho_g g V_B}{\rho_g U_{BT}^2 A_B} \tag{VI.27}$$

Inserting Eq.(VI.27) into Eq.(VI.25) and (VI.26) results in Eq.(VI.28) and (VI.29), where U_{BT} is the terminal rising velocity of a bubble in stagnant liquid. The drag coefficient can be obtained with an empirical relation, Eq.(VI.30), which is in good agreement with the experimental results presented in Chapter V, (Clift, et al., 1978).

$$\frac{dU_B}{dt} = -\frac{\rho_g g}{\rho_g U_{BT}^2}(U_B - u)\left|U_B - u\right| + \frac{\rho_l}{\rho_g} V\frac{\partial U}{\partial r} - \frac{1}{2}\frac{\rho_l}{\rho_g}\left(\frac{dU_B}{dt} - V\frac{\partial U}{\partial r}\right) - \left(1 - \frac{\rho_l}{\rho_g}\right)g \tag{VI.28}$$

$$\frac{dV_B}{dt} = -\frac{\rho_g g}{\rho_g U_{BT}^2}(V_B - v)\left|V_B - v\right| + \frac{\rho_l}{\rho_g} U\frac{\partial V}{\partial x} - \frac{1}{2}\frac{\rho_l}{\rho_g}\left(\frac{dV_B}{dt} - U\frac{\partial V}{\partial x}\right) - \frac{\rho_l}{\rho_g} c_L U_r \frac{\partial U}{\partial r} \tag{VI.29}$$

$$U_{BT} = \left(\frac{2.14\sigma}{\rho_l D_B} + 0.505 g D_B \right)^{0.5} \qquad \textbf{(VI.30)}$$

For air-water systems (the surface tension, σ=0.072 N/s, ρ=1000 kg/m^3), Eq.(VI.30) can be written as:

$$U_{BT} = \left(\frac{1.541 x 10^{-4}}{D_B} + 4.954 D_B \right)^{0.5} \qquad \textbf{(VI.31)}$$

If the velocity variables of the liquid flow can be assumed constant during the short time step of iteration, Eq.(V.28) and (V.29) become ordinary differential equations and can be then easily integrated for a time step, $\Delta t = t - t_o$, where t_o is initial time and assigned to 0, to yield the following equations for the calculation of bubble velocities :

$$U_B = U + \frac{\sqrt{B_1}\,(e^{T_1} - 1)}{\sqrt{-A}\,(e^{T_1} + 1)} \qquad \textbf{(VI.32)}$$

and:

$$V_B = V + \frac{\sqrt{B_2}\,(e^{T_2} - 1)}{\sqrt{-A}\,(e^{T_2} + 1)} \qquad \textbf{(VI.33)}$$

where:

$$T_i = 2\sqrt{(-AB_i)}\,\left(\frac{1}{C} t - \zeta_i\right), \quad i = 1,2 \qquad \textbf{(VI.34)}$$

$$\zeta_1 = -\frac{1}{\sqrt{-AB_1}} \ln\left(\frac{(\sqrt{B_1} + U_{ro}\sqrt{-A})}{(\sqrt{B_1} - U_{ro}\sqrt{-A})}\right) \qquad \textbf{(VI.35)}$$

$$\zeta_2 = -\frac{1}{\sqrt{-AB_2}} \ln\left(\frac{(\sqrt{B_2} + V_{ro}\sqrt{-A})}{(\sqrt{B_2} - V_{ro}\sqrt{-A})}\right) \qquad \textbf{(VI.36)}$$

$$A = -\frac{\rho_g g}{\rho_g U_{BT}^2} \qquad \textbf{(VI.37)}$$

$$B_1 = 1.5\frac{\rho_l}{\rho_g} V\frac{\partial U}{\partial r} - (1 - \frac{\rho_l}{\rho_g})g \qquad \textbf{(VI.38)}$$

$$B_2 = 1.5\frac{\rho_l}{\rho_g} U\frac{\partial V}{\partial x} - \frac{\rho_l}{\rho_g} C_L U_r \frac{\partial U}{\partial r} g \qquad \textbf{(VI.39)}$$

$$C = 0.5\frac{\rho_l}{\rho_g} \qquad \textbf{(VI.40)}$$

In the iteration process, the values of the previous iteration of the flow field are used for the calculation of B_1 and B_2, and the experimentally measured lateral coefficient C_L for bubbles in a plume has been presented in Chapter V (Figure V.12, Table V.2). Based on these experimental measurements, in the computer simulation, a value of 0.1 for C_L is considered a reasonable estimate for bubbles in a plume generated with a flush-mounted nozzle at the bottom of the model ladle.

The usual technique used to determine the time step for the integration of motion equations of fine solid particles in an air jet is to compare the dissipation eddy life time with the transit time of the particle through the eddy; the smaller one is taken as the time step (Gosman and Loannides, 1981). This technique would result in too straight a rising trajectory for the large bubbles as observed in this work, and consequently a narrow distribution of the void fraction around the centerline. The reason is that the variations in the direction of a bubble is not mainly a result of its random interaction with dissipation eddies, in contrast to fine solid particles. The wake shedding activity and the interaction with large energy containing eddies contribute much more to the spiral motion of the large bubbles. The wake shedding frequency can be determined with the Strouhal Number $Sr = 2af/U_r$, where a is the horizontal dimension of the bubble and f is the wake shedding frequency. For a spherical cap air bubble in water, Sr is approximately constant, 0.3 (Clift et al., 1978). If the spiral of a bubble is mainly controlled by the wake shedding, the time during which the bubble moves in the same direction is then in the range of 0.1 to 1.5 s. On the other hand, if the interaction with the large energy containing eddies is mainly responsible for the bubble spiral, then the transit time of the bubble through these large eddies should be used as the integration time step. The sizes of the energy containing eddies may be characterized with the macro length scale of the turbulence and is estimated with the following equation (Hinze, 1975):

$$l_c = 0.544\frac{k^{1.5}}{\epsilon} \qquad \textbf{(VI.41)}$$

The calculated l_e using the computed values of k and ϵ discussed in section 6.3.3 is in the range of 0.06 to 0.1 m, and the resulting transit time of bubbles through these eddies in the range of 0.1 to 0.15 s for bubble velocity in the range of 0.6 to 0.8 m/s. Based on the above discussion, a reasonable estimate of the time step should be between 0.1 and 0.15 s for the present experimental conditions. For simplicity, the time step used in the present program is 0.1 s. With time step properly chosen and liquid flow information obtained from VALUE, the bubble motion equations are then solved in the subroutine VELB.

6.4.4 Boundary Conditions

The boundary conditions at the free surface and at the centreline of the plume as well as at the side and bottom walls of the model ladle assume the conventional form (Mazumdar and Guthrie, 1985).

The free surface is treated as a moving solid wall and the boundary conditions are:

$$U = 0$$

$$\frac{\partial V}{\partial x} = 0 \qquad \text{(VI.42)}$$

$$\frac{\partial k}{\partial x} = \frac{\partial \epsilon}{\partial x} = 0$$

At the centreline of the plume:

$$\frac{\partial U}{\partial r} = 0$$

$$V = 0 \qquad \textbf{(VI.43)}$$

$$\frac{\partial k}{\partial r} = \frac{\partial \epsilon}{\partial r} = 0$$

At the side wall and the bottom wall:

$$U = V = 0$$

$$k = \epsilon = 0 \qquad \textbf{(VI.44)}$$

The well known wall function embodied in the original TEACH code is employed for the calculation of the velocity profile in the vicinity of the walls (Launder and Spalding, 1974) as already discussed in Chapter II.

6.5 Convergency Criterion

The calculation of the void fraction distribution is carried out after 500 bubbles have been processed. Computation with more than 500 bubbles were also carried out, however, the average difference between the predicted liquid velocity with 1000 bubbles and the predicted liquid velocity with 500 bubbles is less than 5%.

Convergency of the liquid flow field and the void fraction is assumed to be reached when the maximum relative difference of void fractions and other flow variables at each node as expressed by the following equation is lower than a certain value:

$$\phi_{Diff} = Max\left(\frac{\phi(i,j)_{new} - \phi(i,j)_{old}}{\phi(i,j)_{old}}\right) \qquad \textbf{(VI.45)}$$

where ϕ stands for α, U, V, k and ϵ. The value used for U, V, k and ϵ was 0.002, while for void fraction 0.02 was used.

6.6 Computational Results

6.6.1 Part I---Determination of extra source term coefficients

The modified k-ε model as discussed in Chapter II and section 6.4.2 was developed for the gas/gas mixing. The model takes into consideration of the extra generation and dissipation of turbulence due to the interaction between the two phases at their "interface" and due to the passage of the second phase, by adding extra source terms to the conventional k-ε models. In the present case of gas/liquid flow, however, the extra generation and dissipation due to the existence of the second phase is much stronger than in the case of gas/gas flows. As a result, the original values of the extra source coefficients must be modified based on the experimental measurements.

The measured void fraction data were used in all the runs in this part of computation and only the liquid flow field is computed to avoid complicating the comparison with differences in the calculation of the void fraction. The testing procedure is as follows. Firstly, the original coefficients were used to run the program PLUME without the subroutine BUBBLE. When the predicted turbulence was underestimated compared to the measurements, groups of coefficients with larger values were tested. The appropriate values of the constants were found after testing a number of groups of constants. The evaluation of the constants was based on the comparison between predicted and measured values of both the mean liquid velocity and the turbulent kinetic energy along the centerline of the plume. The difference is less than 10% for the four gas flowrates, 50, 100, 150 and 200 ml/s, when the following values are used:

$$C_{k1}, C_{k2}, C_{\varepsilon 1}, C_{\varepsilon 2} = 6.0, 0.75, 4.0, 0.6 \quad \text{(VI.46)}$$

The predicted mean flow and turbulence fields for the gas flowrates of 50 and 150 ml/s are shown in Figure VI.4, VI.5, VI.6 and VI.7, where the measured results are also shown for comparison. The predictions with the tested coefficients obviously agree well with the experimental measurement. This demonstrated that the turbulence in the plume is indeed stronger than the cases studied by the original authors of the modified k-e model. The sensitivity of these coefficients to various experimental parameters will be discussed in section 6.7.1.

6.6.2 Part II---Predictions of the plume flow with PLUME

6.6.2.1 Void Fraction Distributions

The computed distributions of the void fraction for the gas flowrates of 50 and 150 ml/s together with the measured results are shown in Figures VI.8 and VI.9, respectively. Compared with the measured void fraction distributions for the same operating conditions, which have been shown as Figures IV.4 and IV.5 in Chapter IV, reasonably good agreement have been obtained. The void fraction in the center region of the plume is still slightly higher than the measured one, implying that the swirling movement of big bubbles in the real situations is still stronger than predicted with the present technique. The void fraction distribution away from the center line of the plume is better predicted in the model.

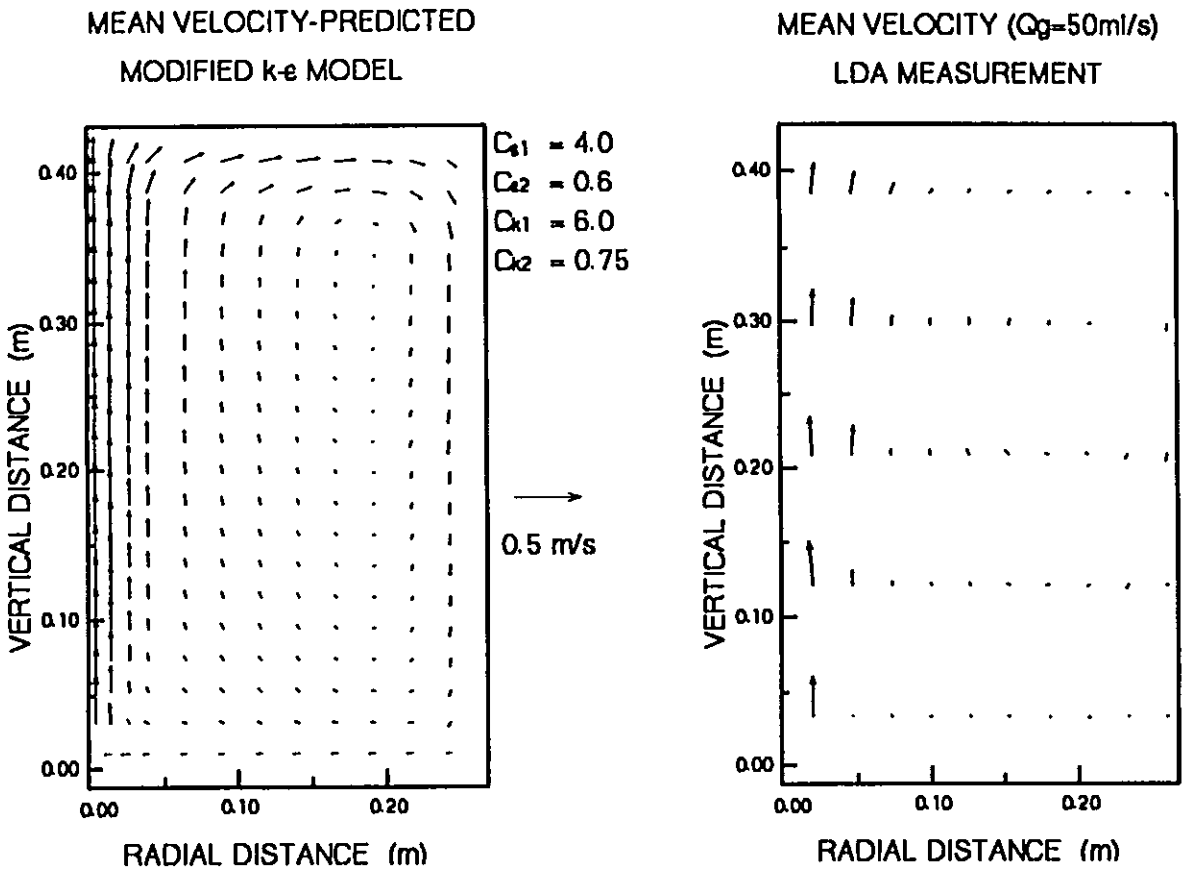

a b

Figure VI.4 (a) Mean flow field predicted with modified k-ε model and optimized constants for extra source terms. The maximum U in the centre is about 30 cm/s. This was obtained with the input of the measured α to the program described in Section 6.2. and (b) as Figure IV.12, experimental results, Q_g=50 ml/s.

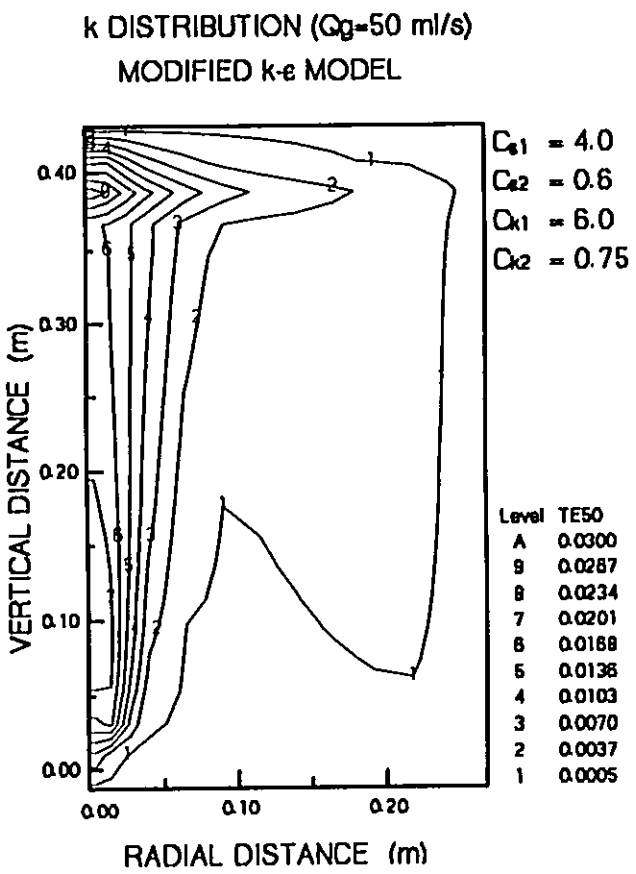

a

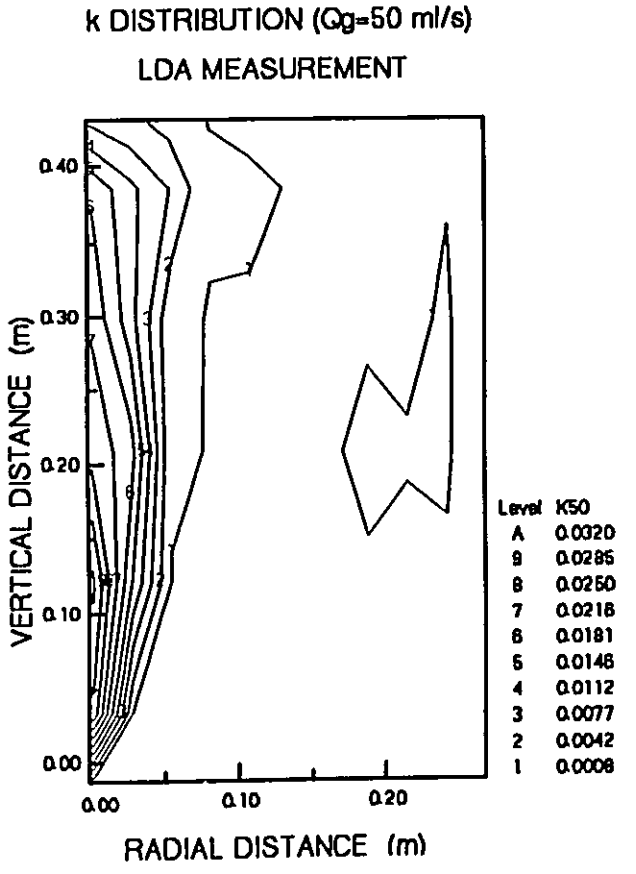

b

Figure VI.5 (a) Turbulent kinetic energy predicted with modified k-ε model and optimized constants for extra source terms. This was obtained with the input of the measured α to the program described in Section 6.2. and (b) as Figure IV.21. experimental results, the unit of k is m^2/s^2, Q_g=50 ml/s.

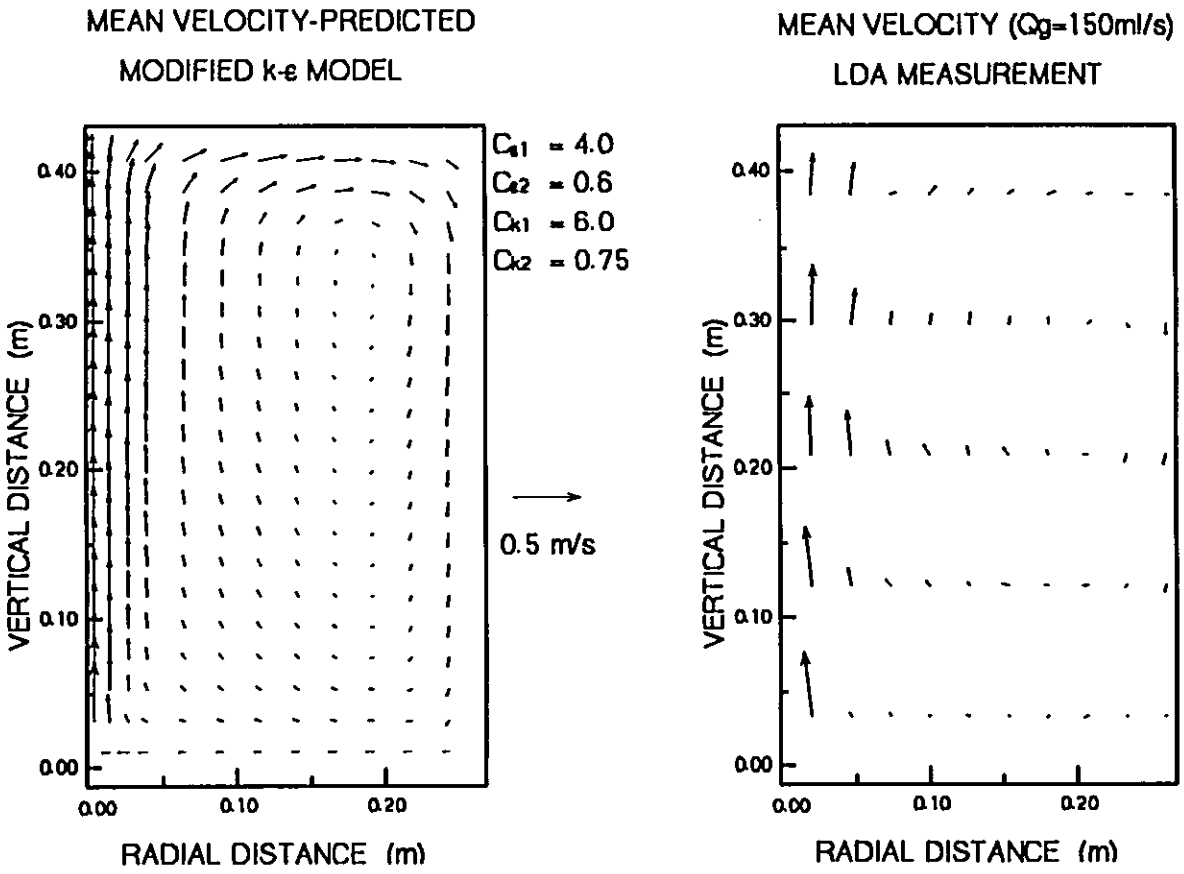

a b

Figure VI.6 (a) Mean flow field predicted with modified k-ε model and optimized constants for extra source terms. The maximum U in the centre is about 45 cm/s. This was obtained with the input of the measured α to the program described in Section 6.2. and (b) as Figure IV.14, experimental results, Q_g=150 ml/s.

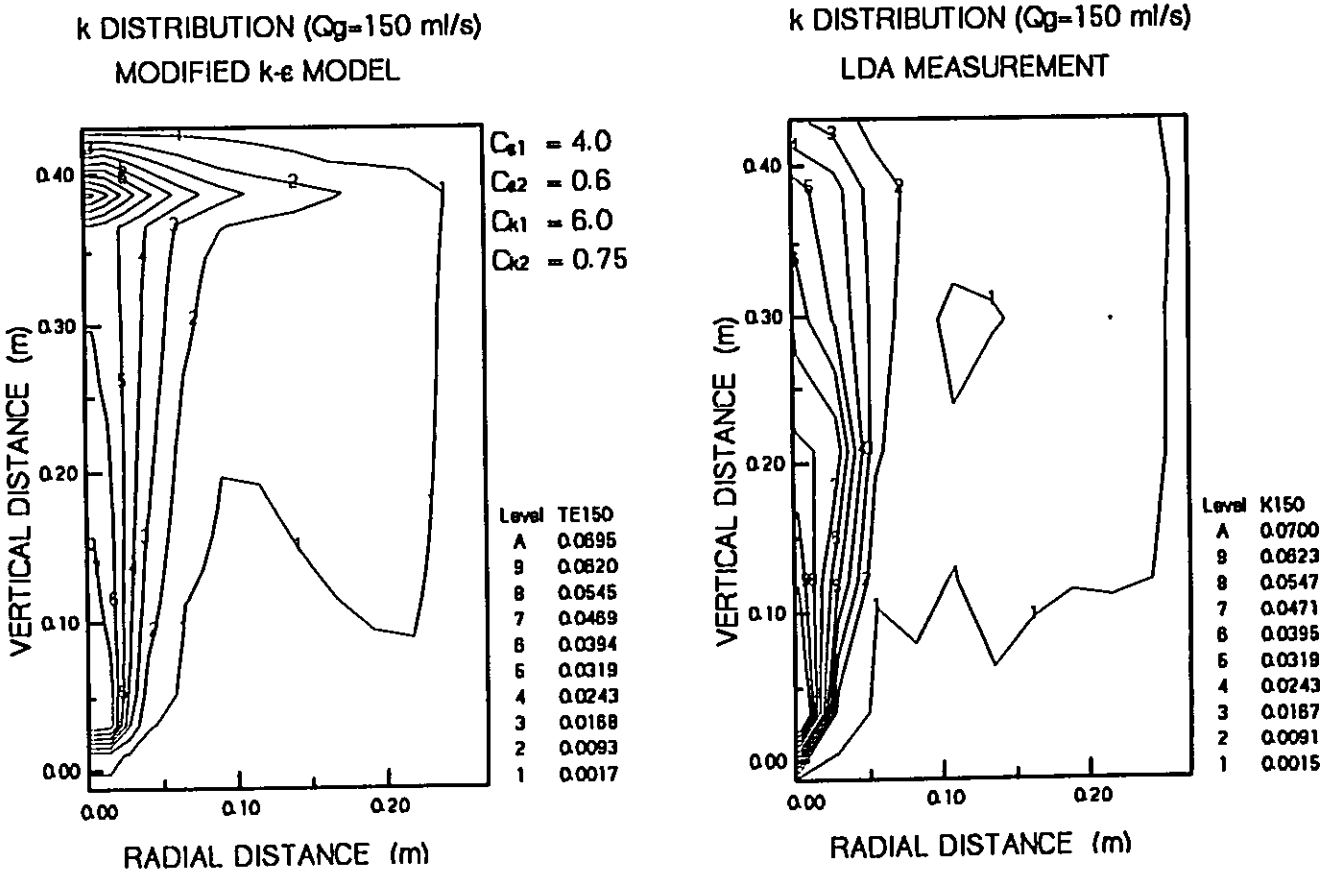

a b

Figure VI.7 (a) Turbulent kinetic energy predicted with modified k-ε model and optimized constants for extra source terms. This was obtained with the input of the measured α to the program described in Section 6.2. and (b) as Figure IV.23, experimental results, the unit of k is m^2/s^2, Q_g=150 ml/s.

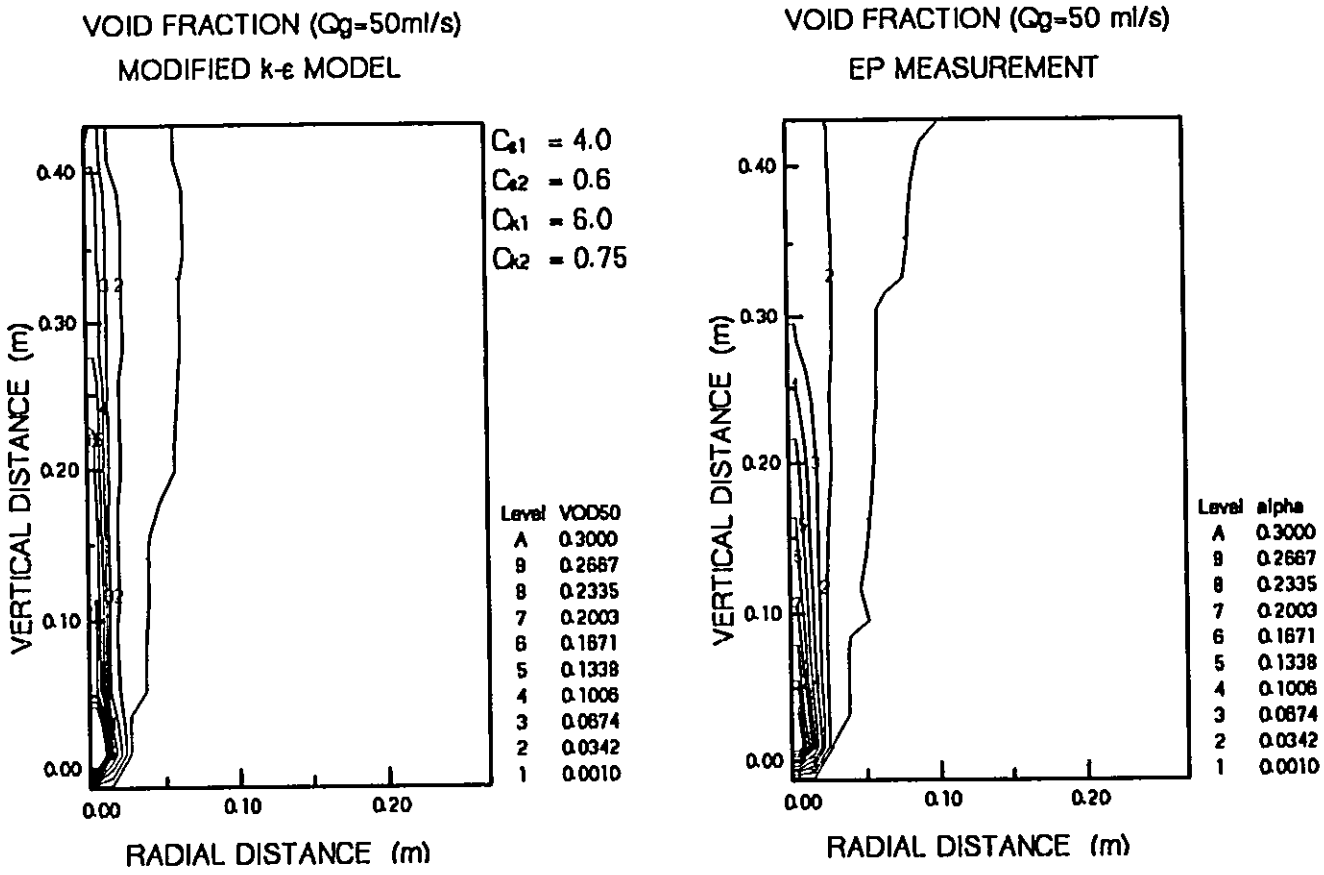

a b

Figure VI.8 (a) Predicted void fraction distribution. This was obtained with the solution of the bubble motion equations and the liquid flow field with modified k-ε model and optimized constants. (b) as Figure IV.4, experimental results. Q_g=50 ml/s.

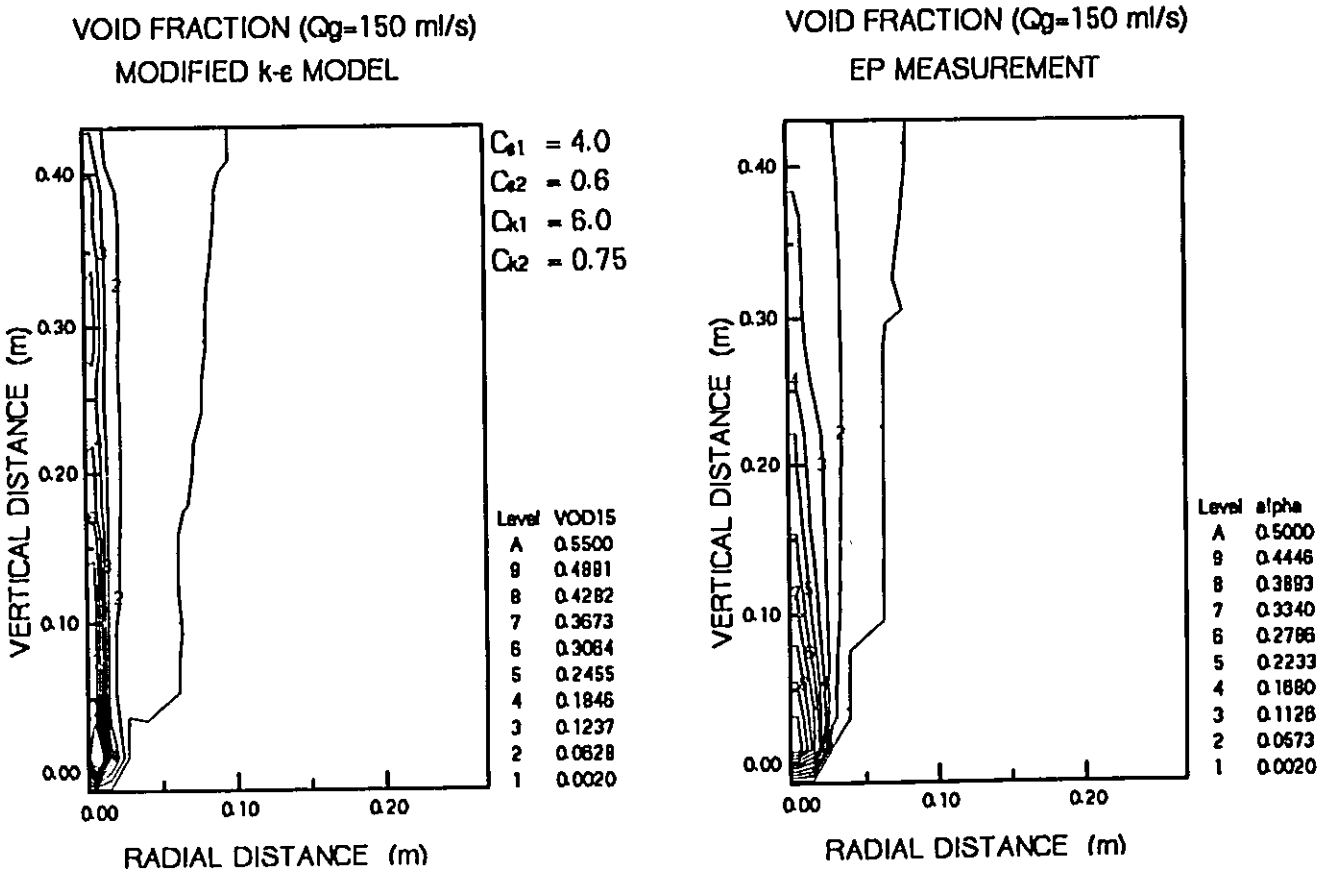

Figure VI.9 (a) Predicted void fraction distribution. This was obtained with the solution of the bubble motion equations and the liquid flow field with modified k-ε model and optimized constants. (b) as Figure IV.5, experimental results. Q_g=150 ml/s.

6.6.2.2 Mean Liquid Flow Fields

The predicted mean flow fields for the same experimental conditions in the previous section are shown in the Figures VI.10 and VI.11, together with the experimental measurements (Figures IV.11 and IV.13), respectively. It is interesting to note that the predictions are in good agreement with experimental results.

6.6.2.3 Turbulent Properties of the Liquid Flow

For two gas flowrates, 50 and 150 ml/s, the computed results of the turbulent kinetic energy are shown with the contour maps shown in Figures VI.12 and VI.13, together with the experimental results (from Figures IV.20 and IV.22), respectively. The contour maps for the computed dissipation of the turbulent kinetic energy, and for the computed distribution of the turbulent viscosity are shown in Figures VI.14 through VI.17, respectively. Compared with the measured distributions of the turbulent kinetic energy for the same gas flowrates, and the prediction of k based on the measured void fraction distributions (Figures VI.7), reasonably good agreements have been achieved. It is the first time that such comparison of the predicted turbulent kinetic energy is made with the experimental measurements.

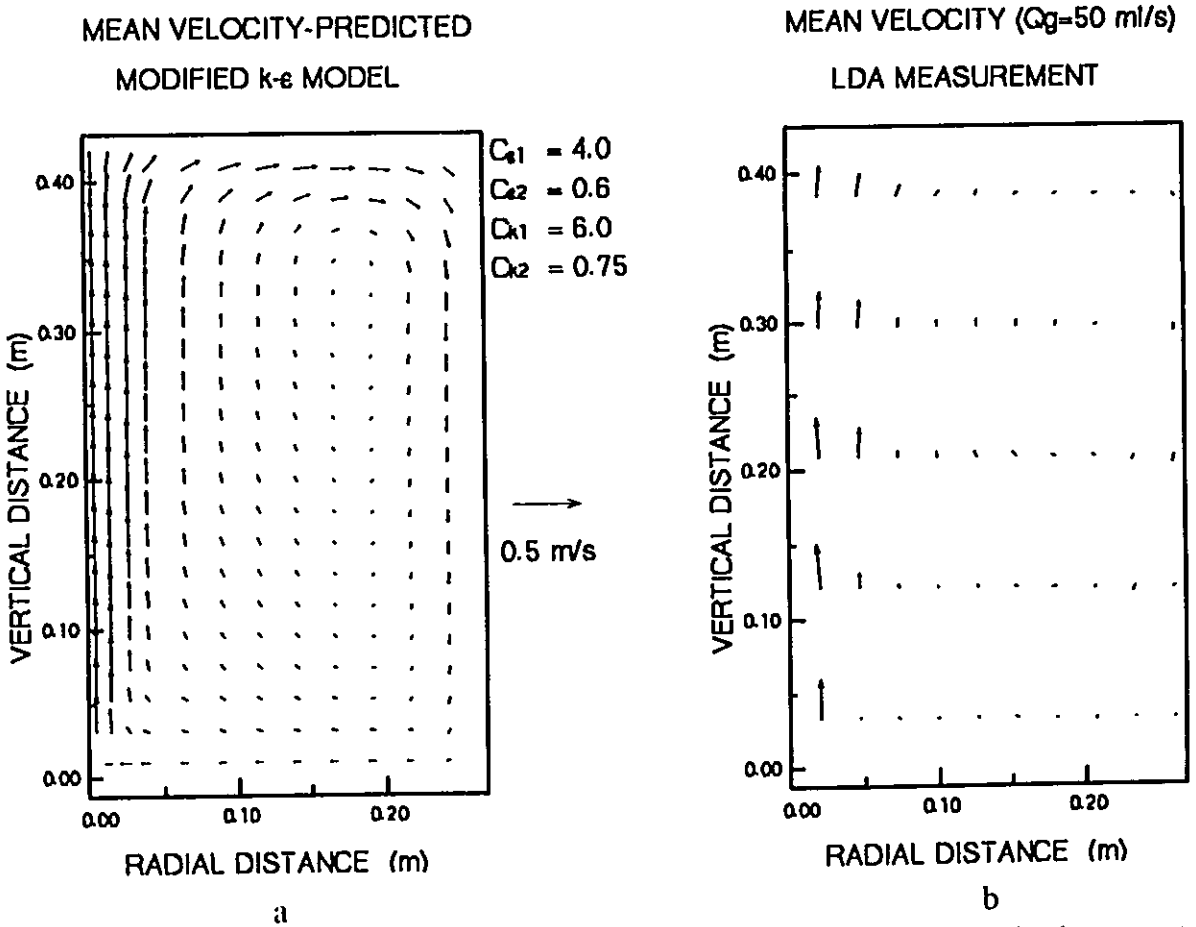

Figure VI.10 (a) Mean flow field predicted with modified k-ε model and optimized constants for extra source terms. The maximum U in the centre is about 30 cm/s. This was obtained with the predicted void fraction distribution. (b) as Figure IV.12, experimental results, Q_g=50 ml/s.

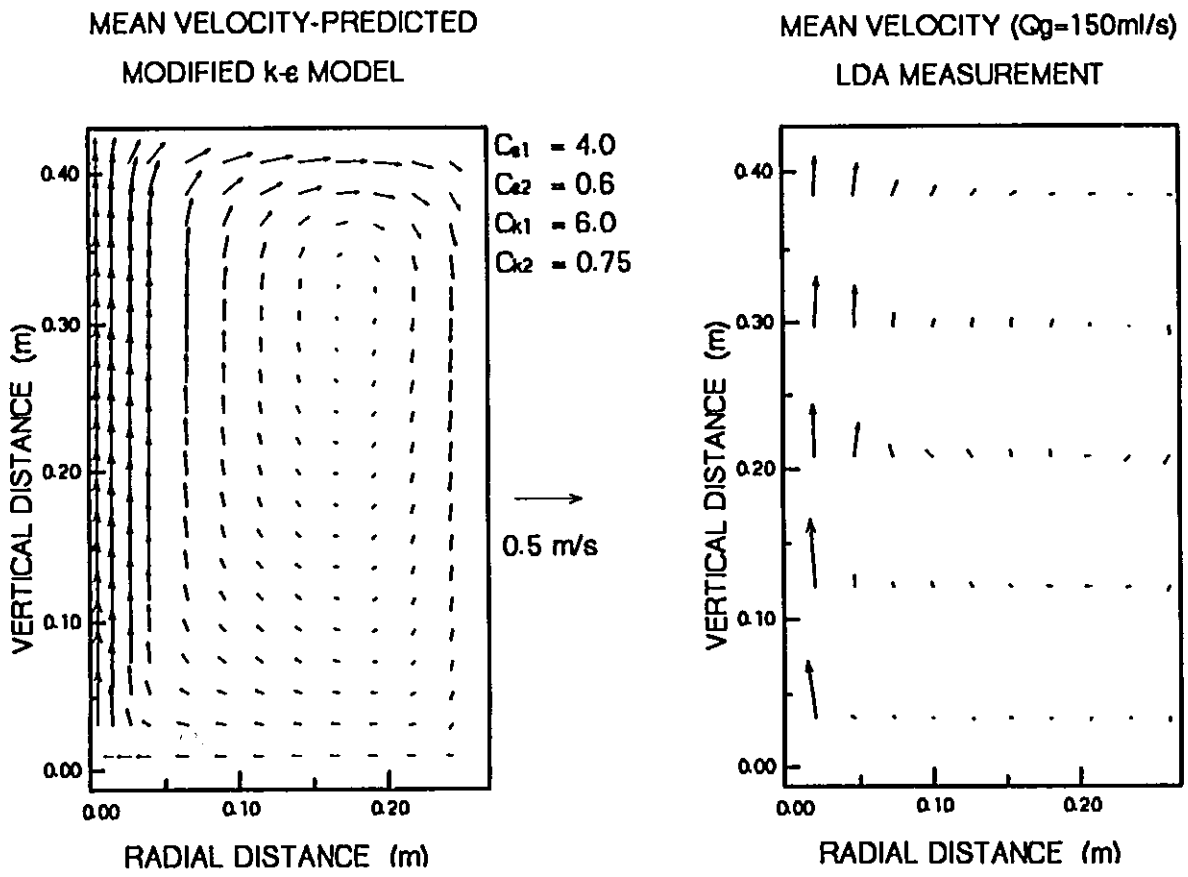

a b

Figure VI.11 (a) Mean flow field predicted with modified k-ε model and optimized constants for extra source terms This was obtained with the pree is about 45 cm/s. (b) as Figure IV.14, experimental results, Q_g=150 ml/s.

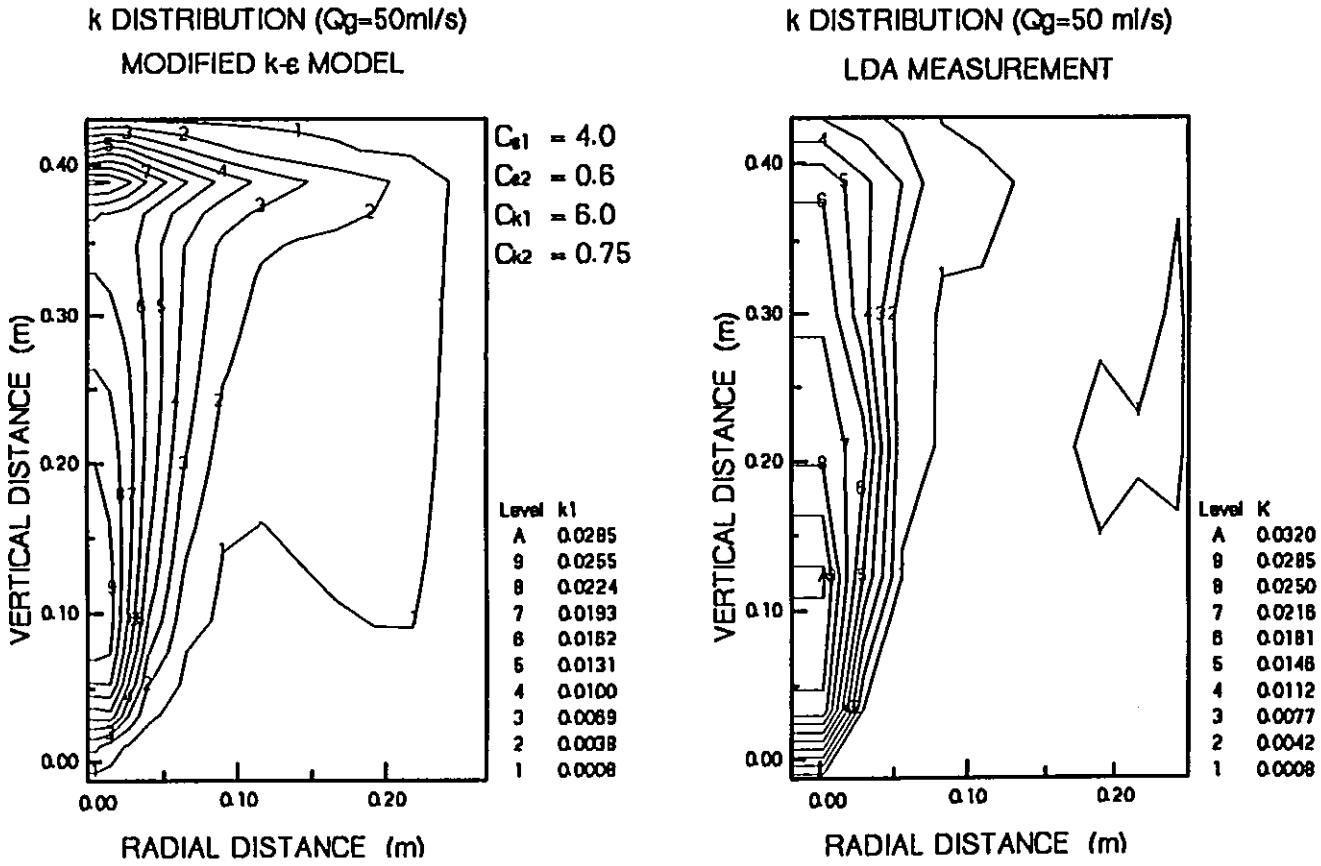

a b

Figure VI.12 (a) Predicted turbulent kinetic energy with predicted void fraction distribution. This was obtained with the solution of the bubble motion equations and the liquid flow field with optimized k-*e* model and optimized constants. (b) as Figure IV.21, experimental results. k unit is m^2/s^2. Q_g=50 ml/s.

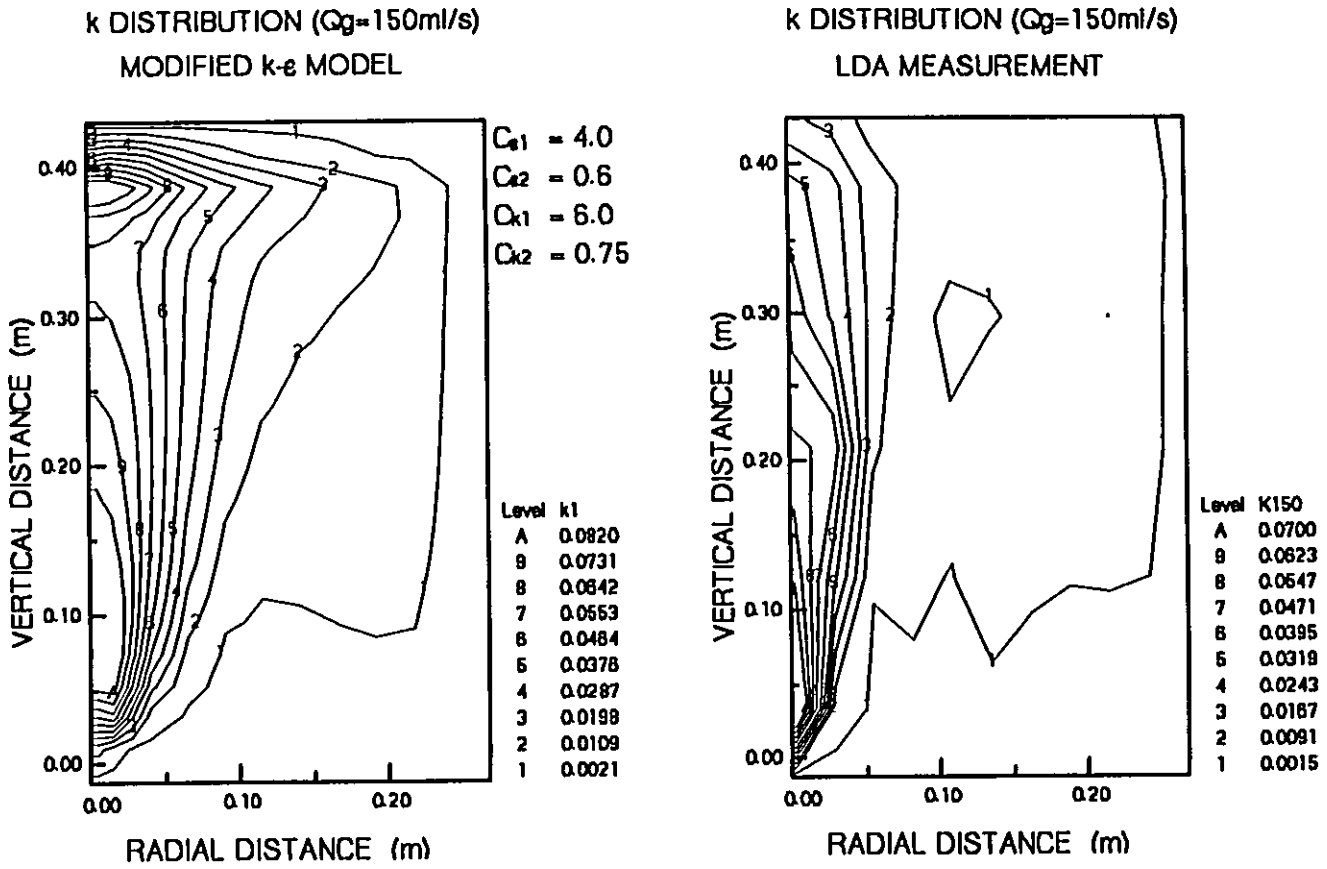

a b

Figure VI.13 (a) Predicted turbulent kinetic energy with predicted void fraction distribution. This was obtained with the solution of the bubble motion equations and the liquid flow field with optimized k-ε model and optimized constants. (b) as Figure IV.23, experimental results. k unit is m^2/s^2. Q_g=150 ml/s.

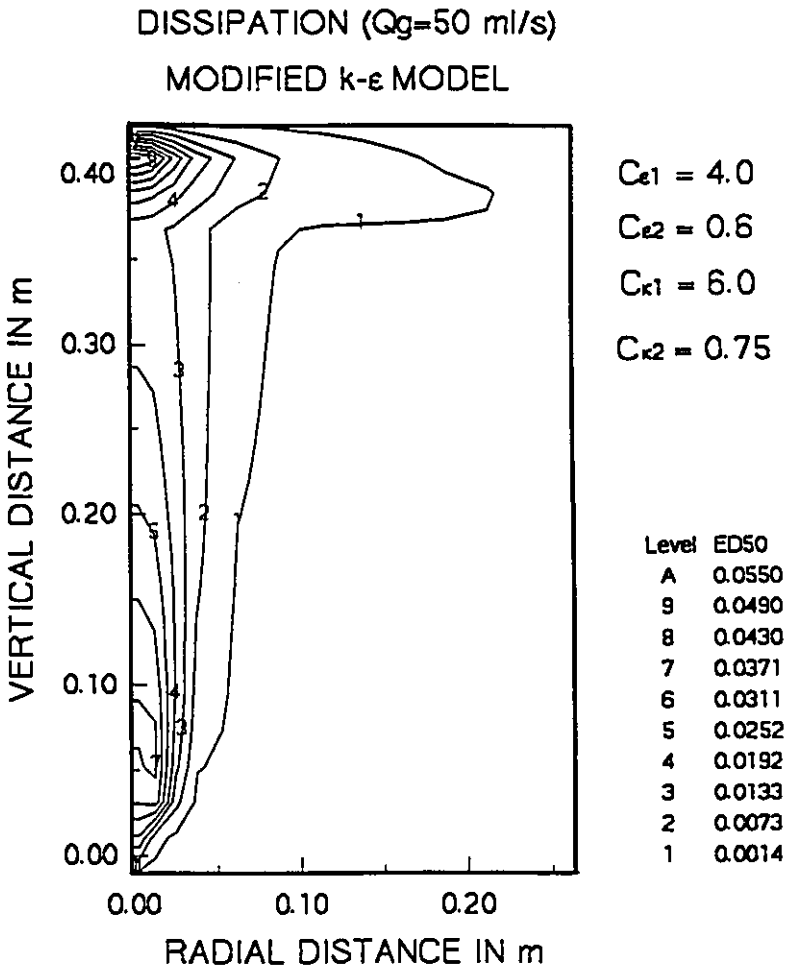

Figure VI.14 Turbulent dissipation rate predicted with modified k-ε model and optimized constants for extra source terms. This was obtained with the predicted void fraction distribution, unit of ε is m^2/s^3. Q_g=50 ml/s.

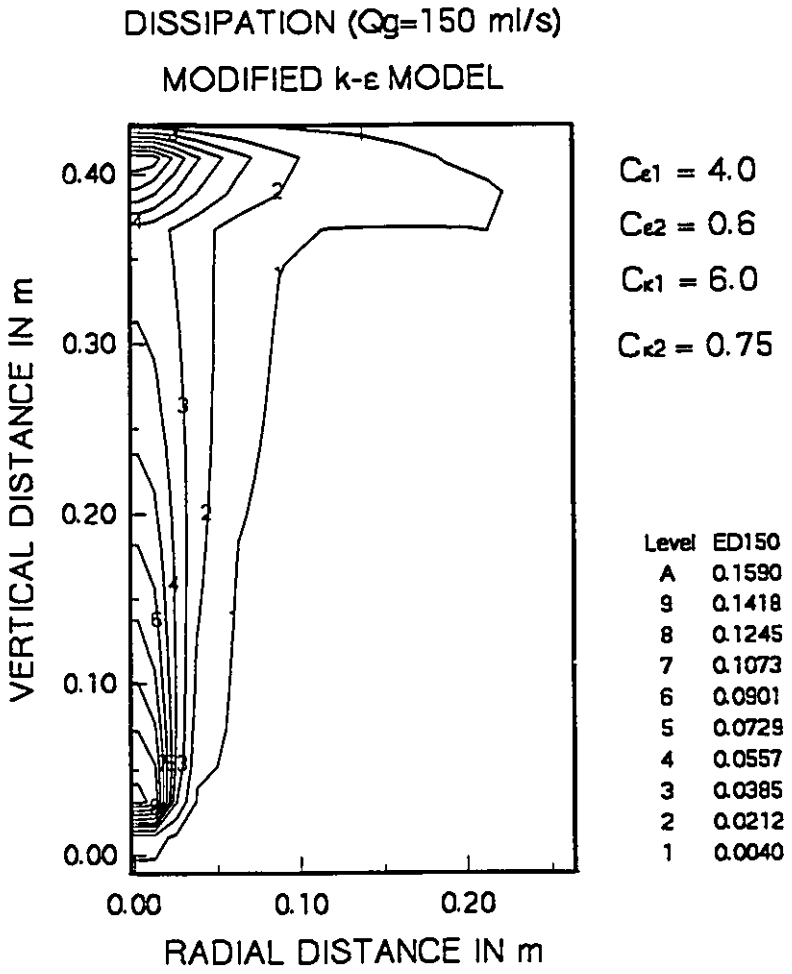

Figure VI.15 Turbulent dissipation rate predicted with modified k-ε model and optimized constants for extra source terms. This was obtained with the predicted void fraction distribution. Unit of ε is m^2/s^3. Q_g=150 ml/s.

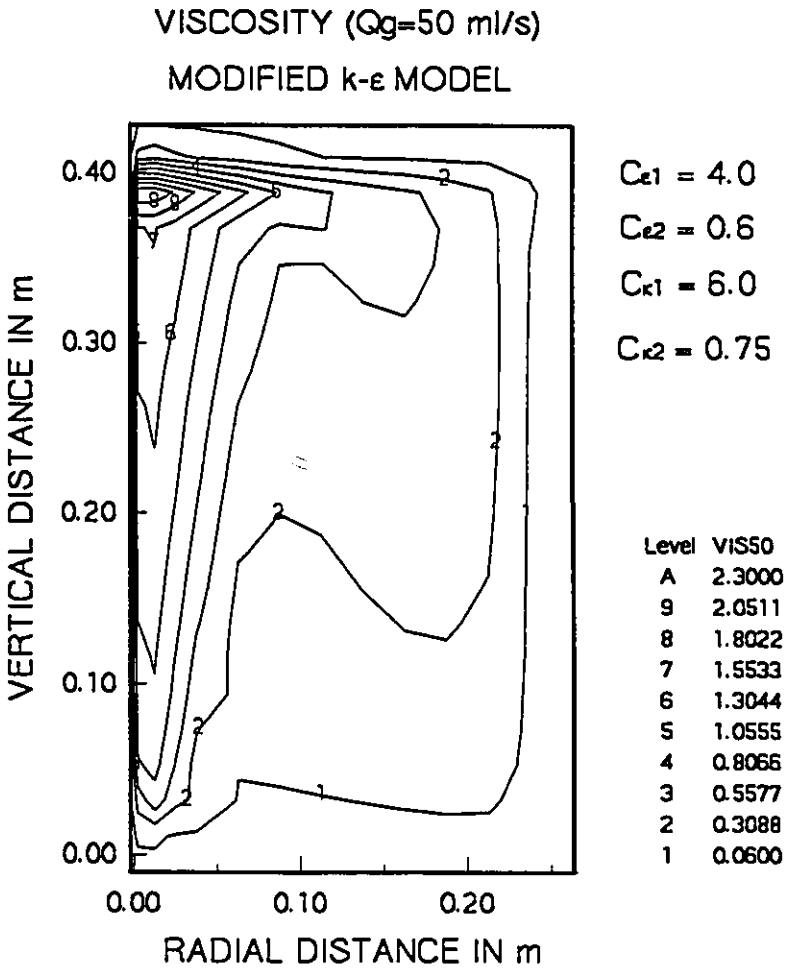

Figure VI.16 Turbulent viscosity predicted with modified k-ε model and optimized constants for extra source terms. This was obtained with the predicted void fraction distribution. Unit of viscosity is m^2/s. Q_g=50 ml/s.

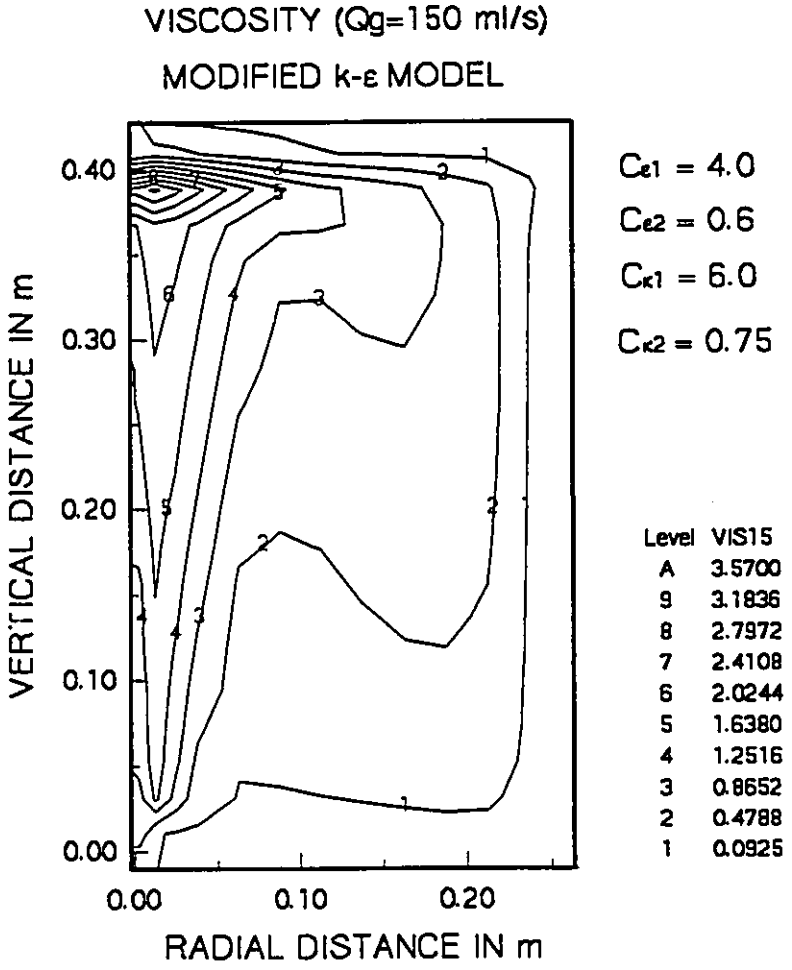

Figure VI.17 Turbulent viscosity predicted with modified k-ε model and optimized constants for extra source terms. This was obtained with the predicted void fraction distribution. Unit of viscosity is m^2/s. Q_g=150 ml/s.

6.7 Discussion

6.7.1 Turbulence Modelling in Two-Phase Plume Zone

Although the modelling of turbulence in various single phase flows has achieved considerable progress, the application of these models to the multiphase flow situation is still facing many difficulties. In Chapter II, different approaches taken to model the turbulence generation and dissipation inside the two-phase bubbly plume zone have been discussed. Among the models, the modified k-ε model would be the most convenient one, if the constants of the extra turbulence source terms applicable to the bubbly plume situation can be determined, as demonstrated in the previous sections. In this section, the predicted turbulent fields with various turbulence models are presented and compared with the measured turbulence fields as already discussed in Chapter IV. The models discussed in the following sections includes the modified k-ε model with original extra source coefficients, the bulk viscosity model (Mazumdar and Guthrie, 1985), which has been the most applied model for bubbly plume modelling and the conventional k-ε model. The program PLUME with subroutine BUBBLE turned off was employed for the computation. Experimentally measured void fraction data used to avoid complicating the comparison with differences in the calculation of void fraction distributions.

6.7.1.1 MODIFIED k-ε MODEL

Results of predictions using the modified k-ε model with three groups of constants are discussed in the following paragraphs. In the Figures VI.18 through

VI.21, the constants suggested by the original authors of the model were used:

$$C_{k1}, C_{k2}, C_{\epsilon 1}, C_{\epsilon 2} = 2.5, 0.3, 2.5, 0.30 \qquad \text{(VI.47)}$$

The computed results underestimate the turbulence level in the two-phase zone, which was expected since turbulence generation in bubbly plumes due to the existence of large bubbles is much stronger than in the case of mixing hot and cold gases. As a result, the centerline velocity of the liquid is higher than the experimental data while turbulent kinetic energy along the centerline is lower than the measured values. The flow pattern and the contour maps of the turbulent variables, nevertheless, match well with the measured ones below the free surface. The highest values of k and ϵ appeared to be in the zone right below the free surface as predicted by the model, other than in the lower center part of the plume as demonstrated by the measured results. This discrepancy is probably caused by the treatment of the free surface in the model as a moving solid wall so that the excessive strong turbulence is produced when the upward plume hits the imaginary wall which converts the mean flow into turbulence.

Since the predictions of the model with the original constants failed to agree with the experimental results, groups of constants with different values were tested. The predicted results of one of the groups with the constants assuming the following values:

$$C_{k1}, C_{k2}, C_{\epsilon 1}, C_{\epsilon 2} = 10.0, 1.5, 10.0, 1.5 \qquad \text{(VI.48)}$$

are shown in Figures VI.22 through VI.25. The values of constants in this group are obviously too high, so that the predicted turbulence is overestimated, while the predicted centerline velocity is lower than that measured.

The appropriate values of the constants were found after testing a number of groups of constants which are larger than the original constants and smaller than the values in Eq.(VI.48). The evaluation of the constants was based on the comparison between predicted and measured values of both the mean liquid velocity and the turbulent kinetic energy along the centerline of the plume. The difference is less than about 10% when the following values of the constants were used:

$$C_{k1}, C_{k2}, C_{\epsilon 1}, C_{\epsilon 2} = 6.0, 0.75, 4.0, 0.6 \qquad \text{(VI.49)}$$

The predictions have different sensitivity to these constants. They are more sensitive to C_{k1} and $C_{\epsilon 1}$, e.g., when $C_{\epsilon 1}$ decreases from 6 to 5, the mean liquid upward velocity along the centre line would increase from 0.35 to 0.45 m/s. An 10% change in C_{k2} and $C_{\epsilon 2}$ would yield less than 10% change in the same velocity. The values shown in Eq.(VI.49) are recommended for the modelling of the bubbly plume flows produced with experimental conditions similar to those used in this project. Further work, however, is still needed to determine if these constants are universally applicable to different gas flowrates and gas/liquid systems than those used in this project.

Both the velocity field and the distribution of the turbulent kinetic energy for the gas flowrates of 50 and 150 ml/s, predicted with the above model, are in good agreement with the experimental measurements as already shown in Figures VI.4, VI.5, VI.6, and VI.7, respectively, where the experimental results are also shown for comparison. The

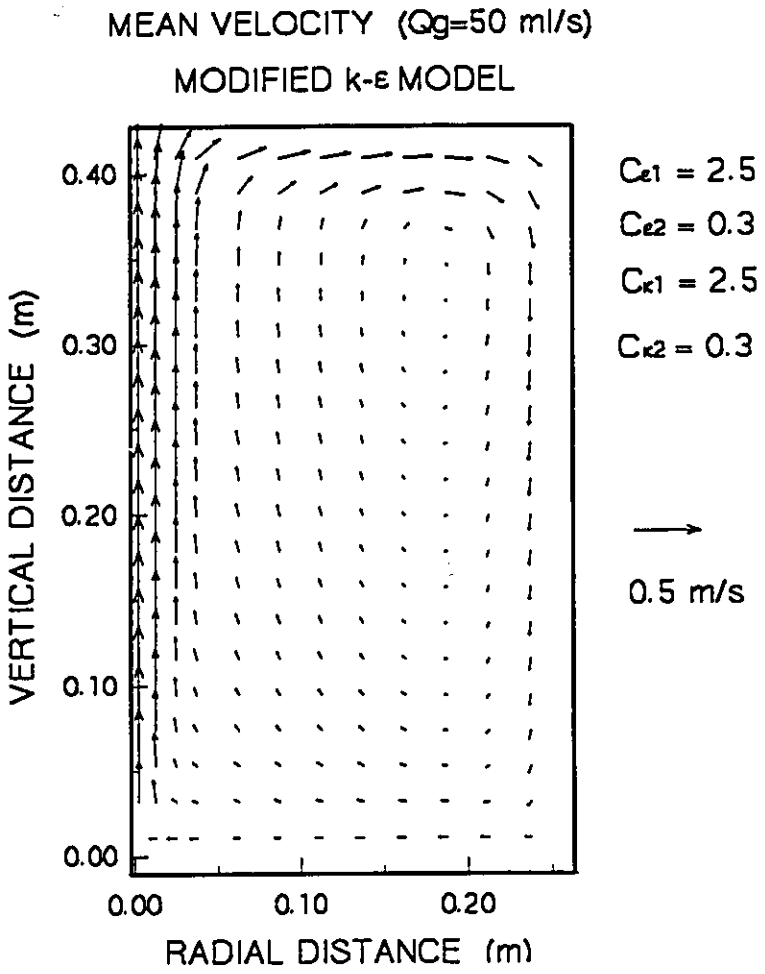

Figure VI.18 Mean flow field predicted with modified k-ε model and original constants for extra source terms. The maximum U in the centre is over 0.5 m/s. This was obtained with the input of the measured α to the program described in Section 6.2. Q_g=50 ml/s.

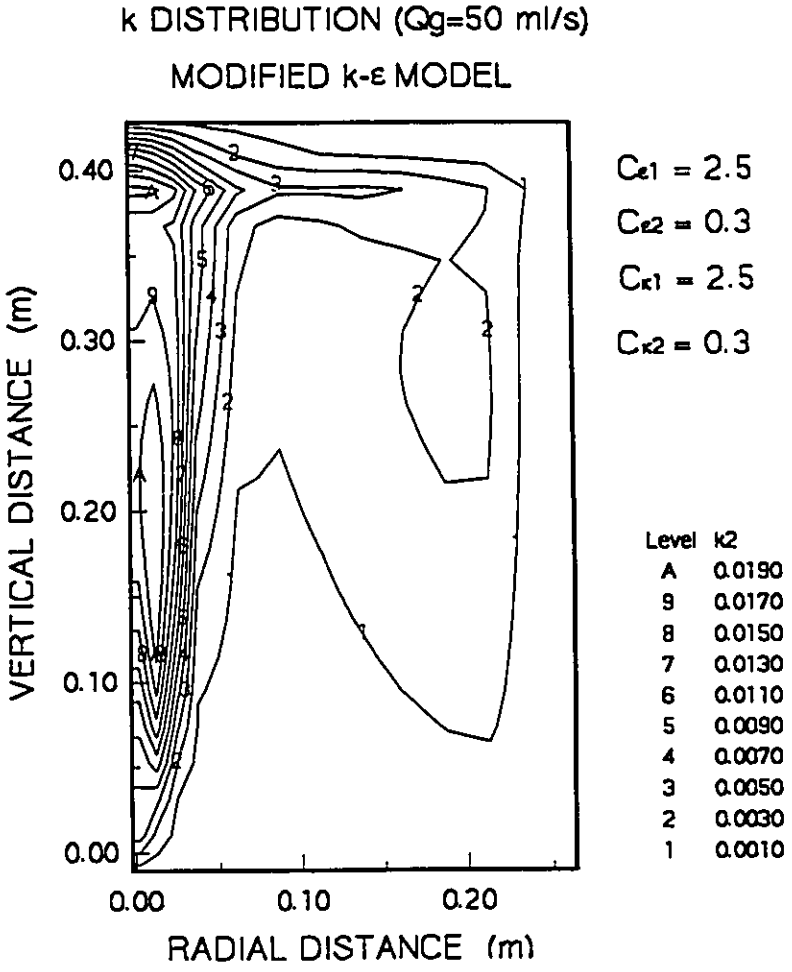

Figure VI.19 Turbulent kinetic energy predicted with modified k- model and original constants for extra source terms. This was obtained with the input of the measured to the program described in Section 6.2. Unit of k is m^2/s^2. Q_g=50 ml/s.

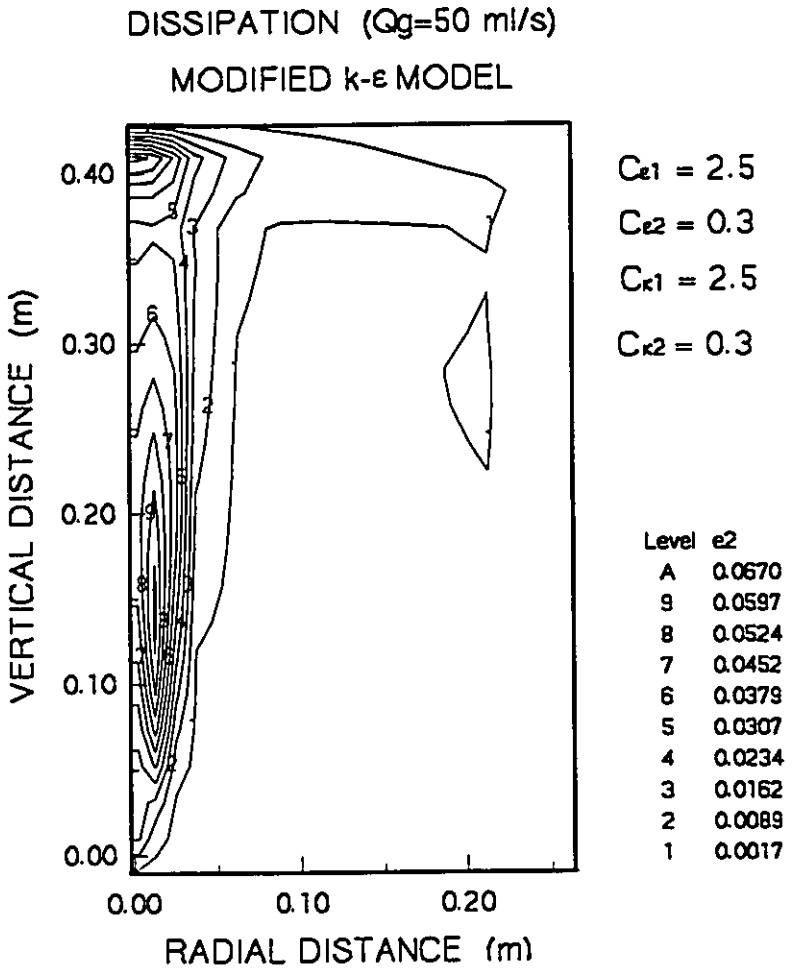

Figure VI.20 Turbulent dissipation predicted with modified k- model and original constants for extra source terms. This was obtained with the input of the measured α to the program described in Section 6.2. Unit of ε is m^2/s^3. Q_g=50 ml/s.

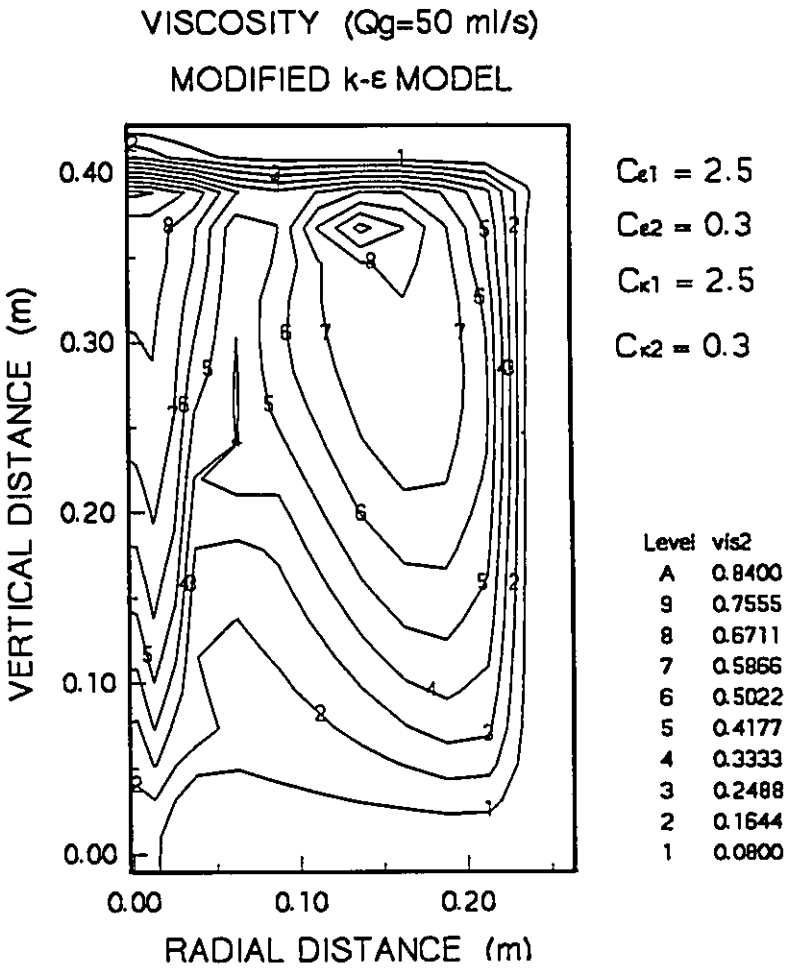

Figure VI.21 Turbulent viscosity predicted with modified k-ε model and original constants for extra source terms. This was obtained with the input of the measured α to the program described in Section 6.2. Unit of viscosity is m^2/s. Q_g=50 ml/s.

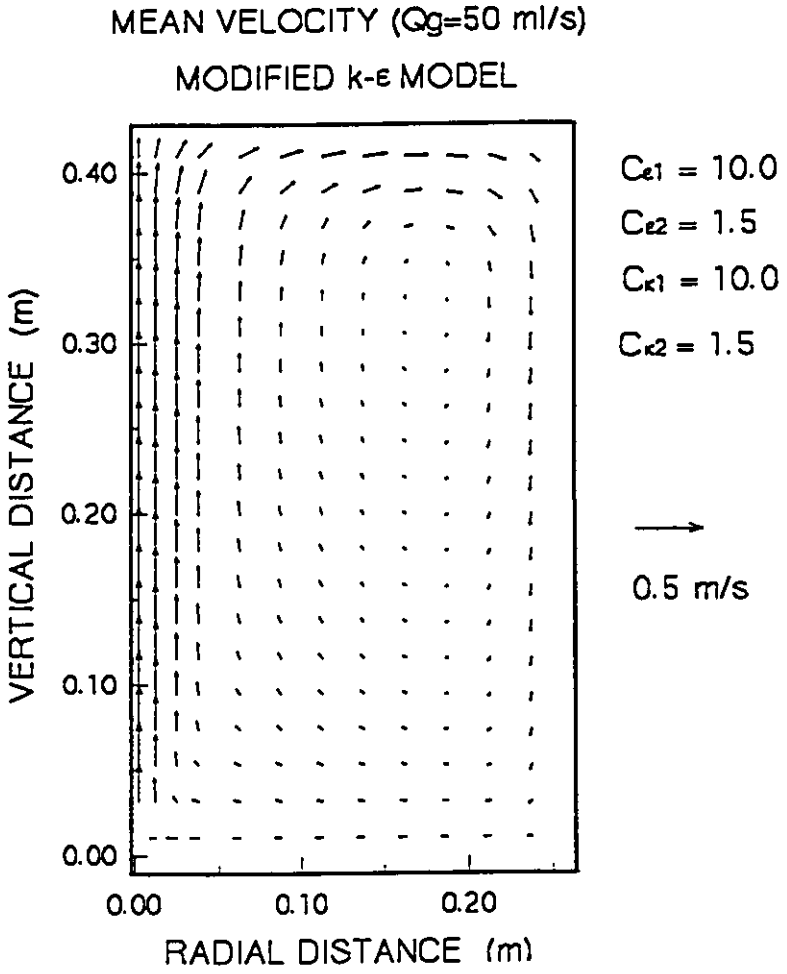

Figure VI.22 Mean flow field predicted with modified k-ε model and large constants for extra source terms. The maximum U in the centre is about 0.25 m/s. This was obtained with the input of the measured α to the program described in Section 6.2. Q_g=50 ml/s.

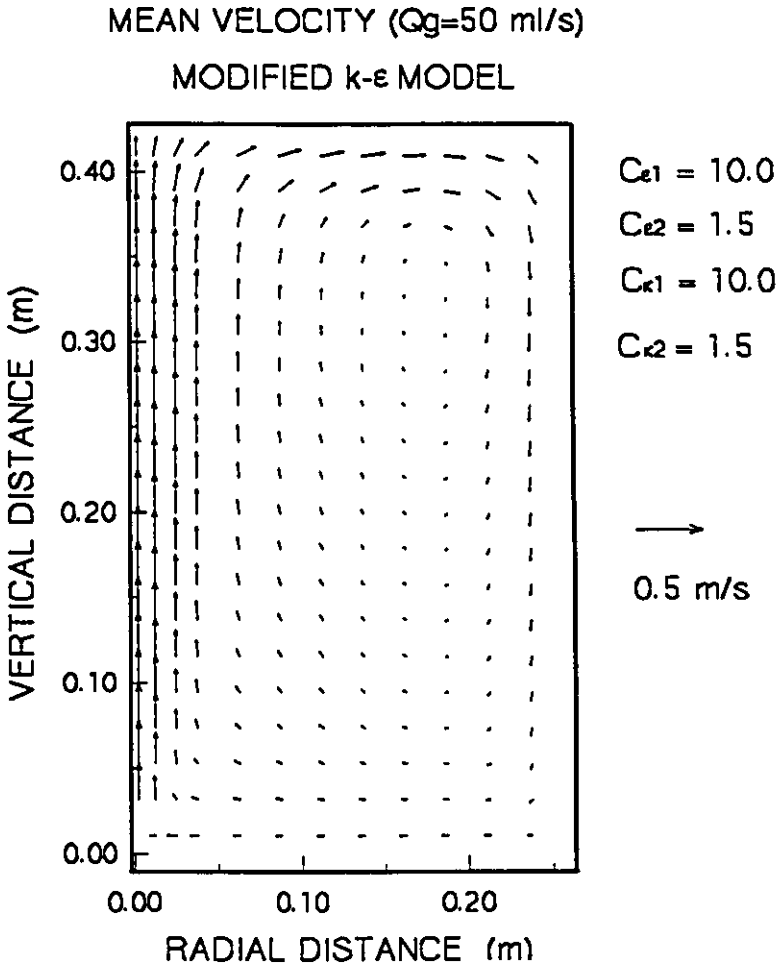

Figure VI.23 Turbulent kinetic energy predicted with modified k-ε model and large constants for extra source terms. This was obtained with the input of the measured α to the program described in Section 6.2. Unit of k is m^2/s^2. Q_g=50 ml/s.

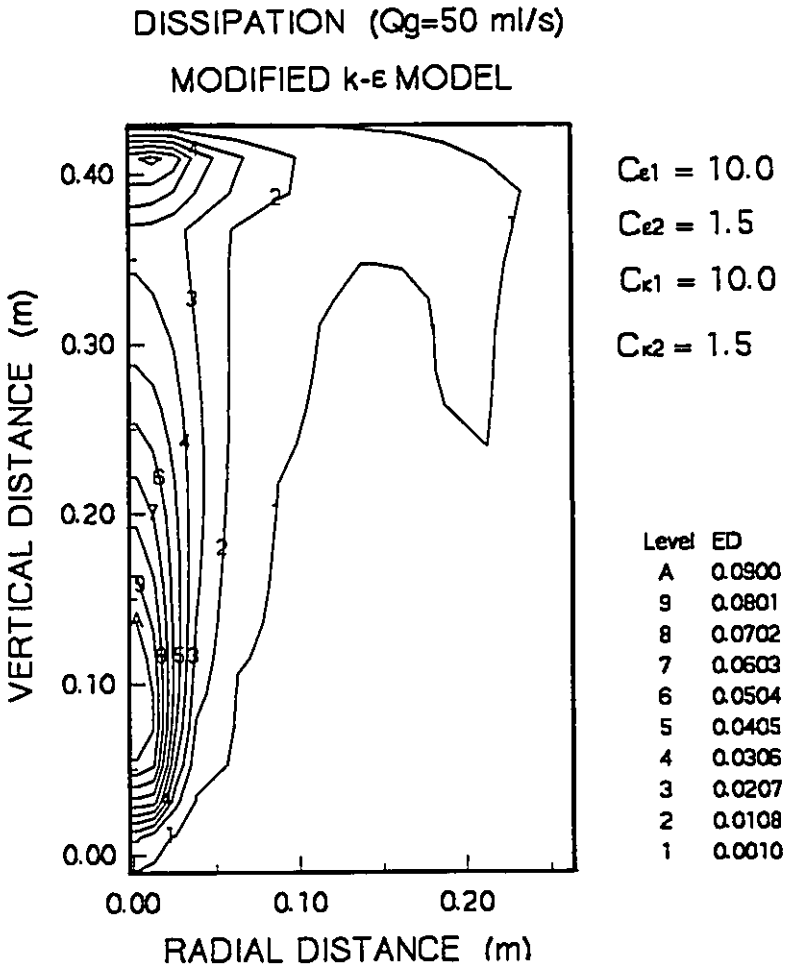

Figure VI.24 Turbulent dissipation predicted with modified k-ε model and large constants for extra source terms. This was obtained with the input of the measured α to the program described in Section 6.2. Unit of ε is m^2/s^3. Q_g=50 ml/s.

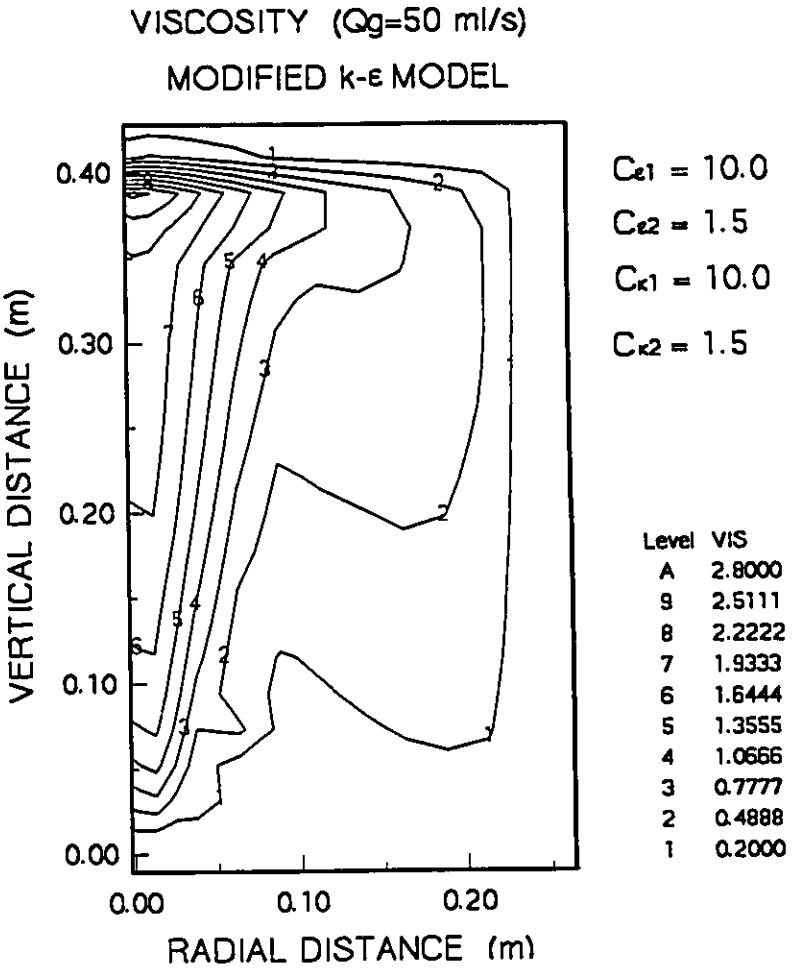

Figure VI.25 Turbulent viscosity predicted with modified k-ε model and large constants for extra source terms. This was obtained with the input of the measured α to the program described in Section 6.2. Unit of viscosity is m/s^2. Q_g=50 ml/s.

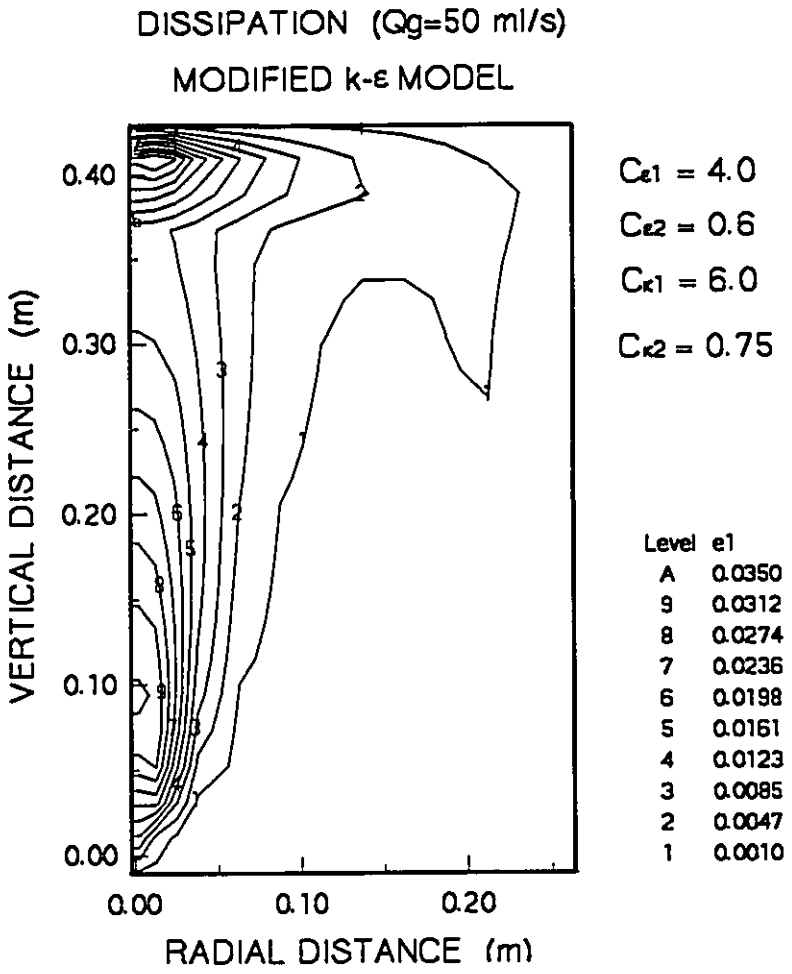

Figure VI.26 Turbulent dissipation predicted with modified k-ε model and optimized constants for extra source terms. This was obtained with the input of the measured α to the program described in Section 6.2. Unit of ε is m^2/s^3. Q_g=50 ml/s.

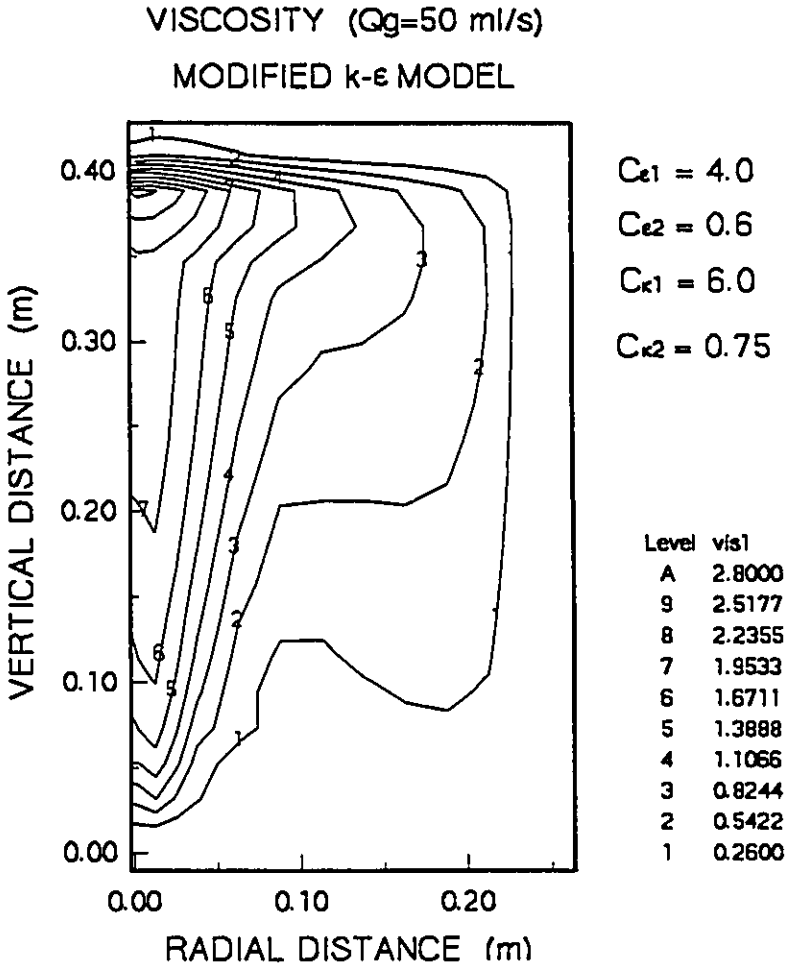

Figure VI.27 Turbulent viscosity predicted with modified k-ε model and optimized constants for extra source terms. This was obtained with the input of the measured α to the program described in Section 6.2. Unit of viscosity is m^2/s. Q_g=50 ml/s.

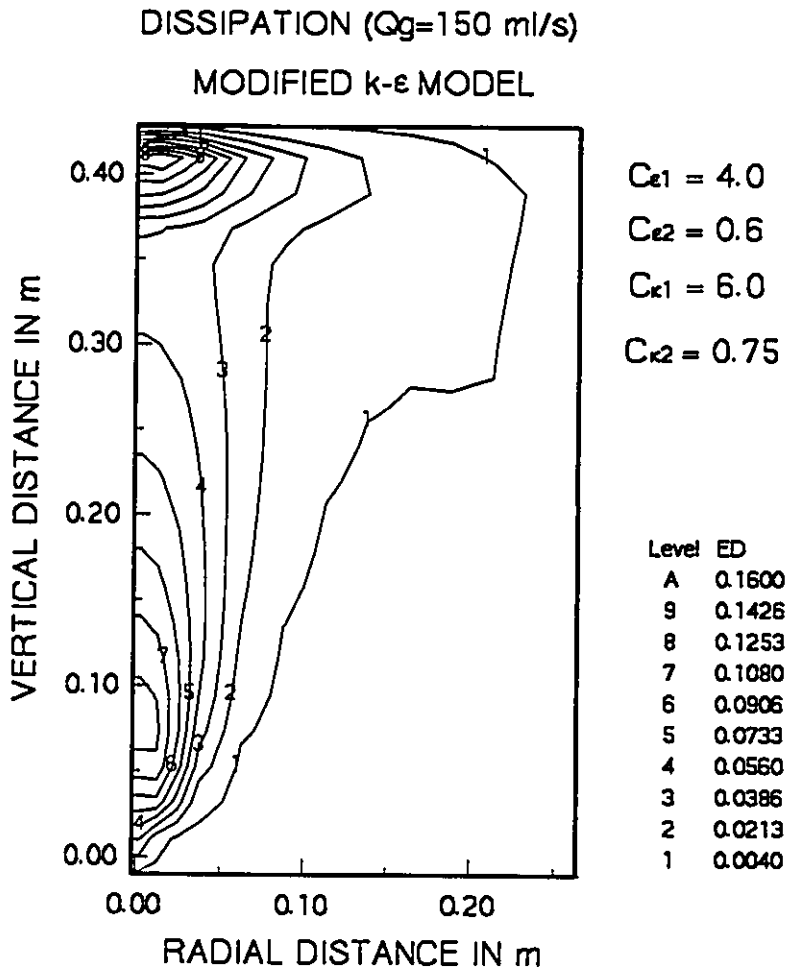

Figure VI.28 Turbulent dissipation predicted with modified k-ε model and optimized constants for extra source terms. This was obtained with the input of the measured α to the program described in Section 6.2. Unit of ϵ is m^2/s^3. Q_g=150 ml/s.

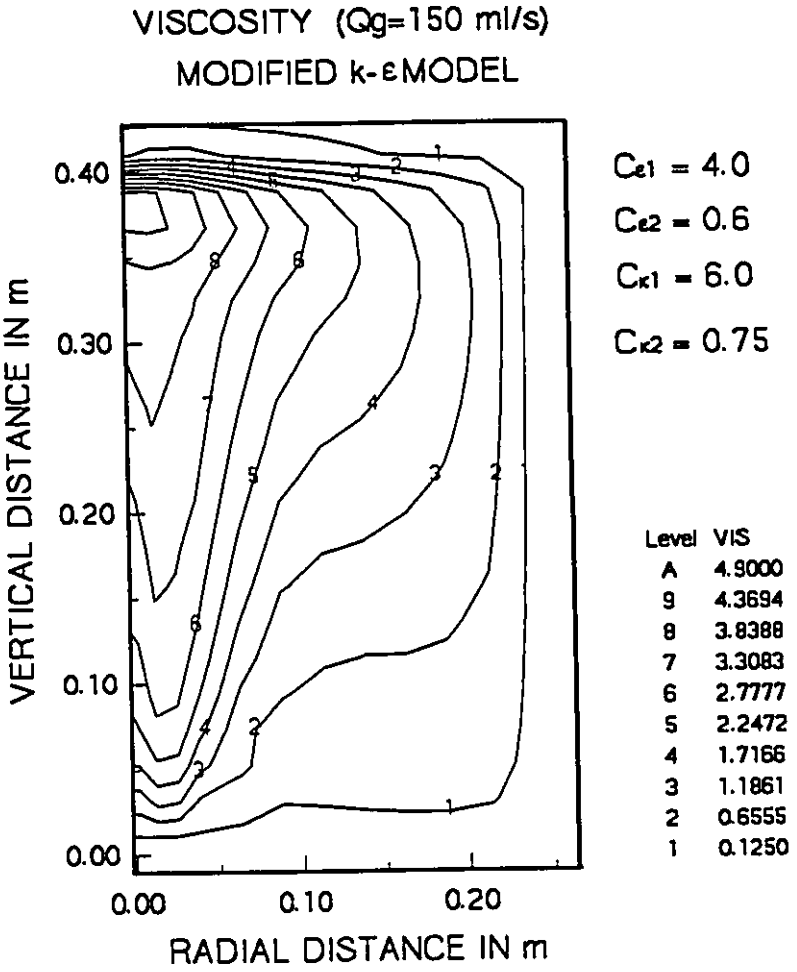

Figure VI.29 Turbulent viscosity predicted with modified k-ε model and optimized constants for extra source terms. This was obtained with the input of the measured α to the program described in Section 6.2. Unit of viscosity is m^2/s. Q_g=150 ml/s.

predicted results of dissipation and viscosity are shown in Figures VI.26, VI.27, VI.28 and VI.29 for gas flowrates of 50 and 150 ml/s, respectively.

6.7.1.2 Conventional k-ε Model

The results predicted with the conventional k-ε model as discussed in Chapter II, and the measured void fraction distribution are shown in Figures VI.30 to VI.33. In the centre of the plume, the liquid velocity is almost twice that of the experimental data when one compares Figure VI.30 with Figure IV.12, while the turbulent kinetic energy (Figure VI.31) is only about the half of the measured data shown in Figure IV.21. The distribution pattern of k around the centerline of the plume is also distorted if compared with the experimental results. The inaccurate prediction using the conventional k-ε model may be explained in the following way. The generation of turbulence resulted from the mean shear flow is accounted for only by the source in the transport equations for both k and ε, while the source for the bubble existence is not taken into consideration. With lower turbulence intensity in the plume zone, the effective viscosity is correspondingly lower, as a result, the entrainment of liquid into the plume is underestimated and the liquid in the plume centre losses less momentum to entrain fresh liquid from the outside of the plume zone with lower velocities. It is interesting to note that some of the predictions using the conventional k-ε model have been claimed to be in good agreement with their experimental measurement (Sahai and Guthrie, 1982b).

6.7.1.3 Bulk Effective Viscosity Model

The effective viscosity calculated with the bulk viscosity model proposed by Mazumdar (1989) is in the range of 0.2 kg/(m•s) inside the plume zone, and its maximum is about 0.8 kg/(m•s) at the place outside of the plume and below the free surface (Figure VI.37), which is even lower than the values obtained with the conventional k-ε model in the two-phase plume zone (Figure VI.33). Local values of the void fractions were used in this computation instead of the cross-section averaged values used by Mazumdar (1989). The difference in the calculated viscosity, however, is negligibly small. For Q_g=50 ml/s, the calculated values of the effective viscosity are 0.25 and 0.27 for the void fractions of 0.5 and 0.1, respectively. The predicted mean flow field (Figure VI.34) and the distributions of turbulent kinetic energy (Figure VI.35) and its dissipation (Figure VI.36) are very similar to the results obtained with the conventional k-ε model.

This model has been extensively used with empirical correlations for the void fraction distribution in the plume; good agreement with the experimental measurements were claimed (Mazumdar and Guthrie, 1985; Sahai and Guthrie, 1982). However, according to the computation results shown in Figures VI.34 through VI.37, some other modifications must be used in the computation to achieve a good agreement with the experimental measurements for both mean velocity and turbulence variables.

6.3.4 Brief Summary

Predictions with experimentally measured void fraction distributions and various turbulence models used for the treatment of turbulence in the bubbly two-phase flows were compared with the experimental data, and the modified k-ε model were found to be the most convenient. The values of the constants of the extra sources used in the modified k-ε model, which are most appropriate to the bubbly plume modelling, were determined based on the comparison with the experimental measurement. The modified k-ε model with the constants determined in this study is able to yield predictions for the bubbly plume flows, which are in good agreement with the experimental measurements in terms of both liquid velocity flow field and the turbulence intensity distribution.

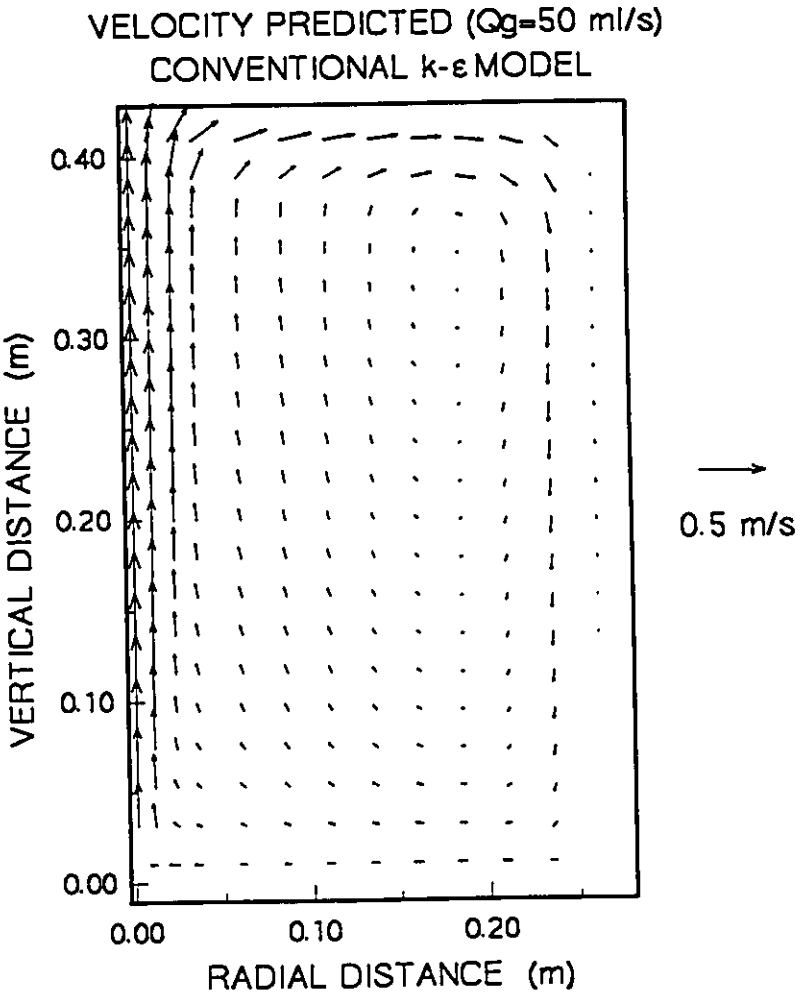

Figure VI.30 Mean flow field predicted with conventional k-ε model. This was obtained with the input of the measured α to the program described in Section 6.2. Q_g=50 ml/s.

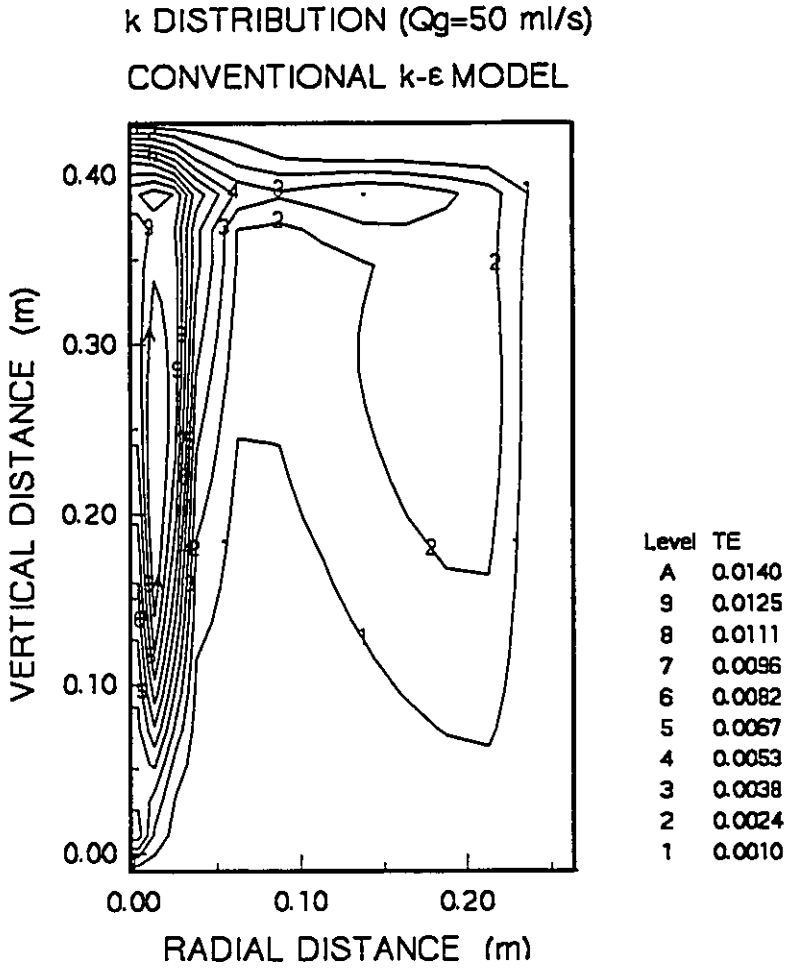

Figure VI.31 Turbulent kinetic energy predicted with conventional k-ε model. This was obtained with the input of the measured α to the program described in Section 6.2. Q_g=50 ml/s.

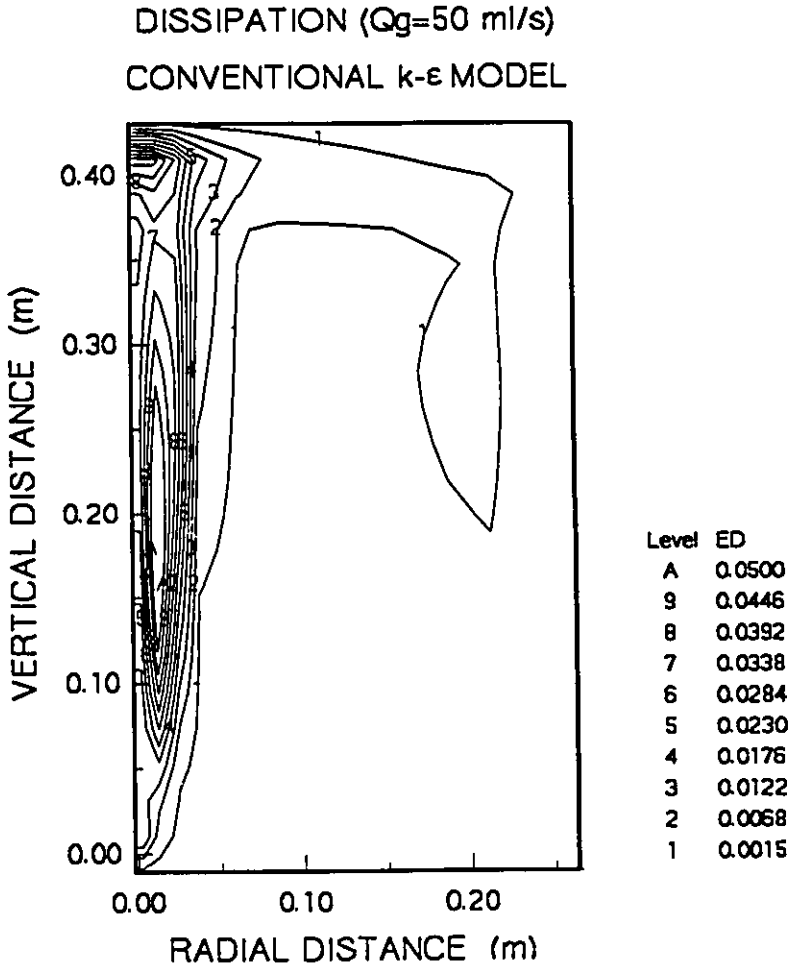

Figure VI.32 Turbulent dissipation predicted with conventional k-ε model. This was obtained with the input of the measured α to the program described in Section 6.2. Q_g=50 ml/s.

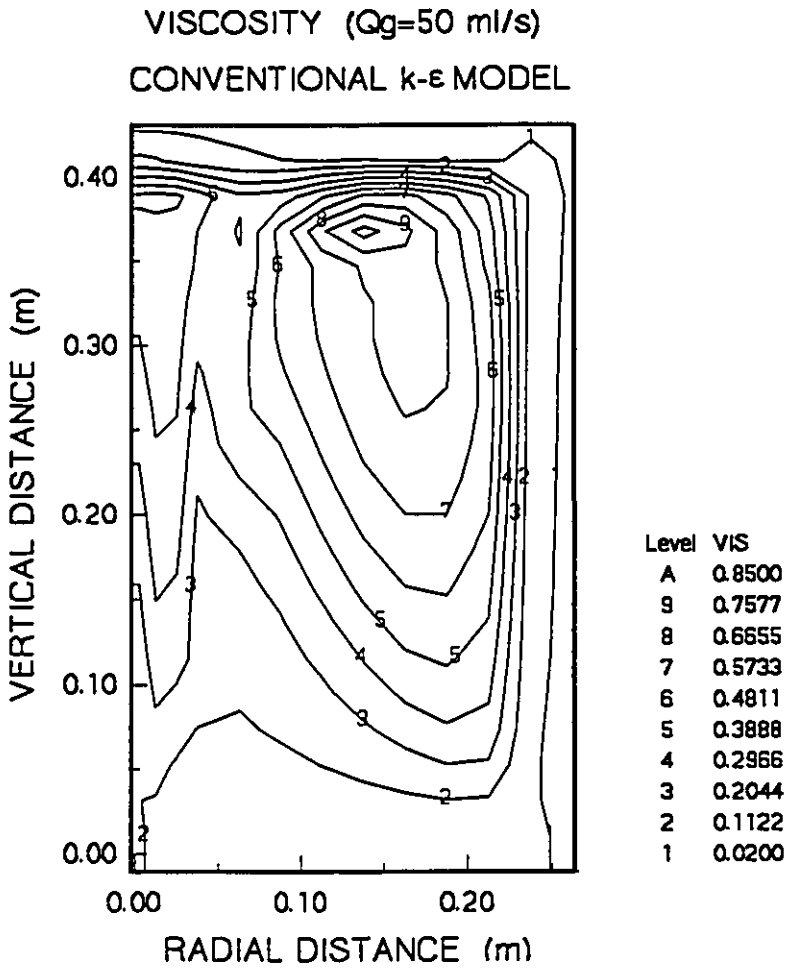

Figure VI.33 Turbulent viscosity predicted with conventional k-ε model. This was obtained with the input of the measured α to the program described in Section 6.2. Q_g=50 ml/s.

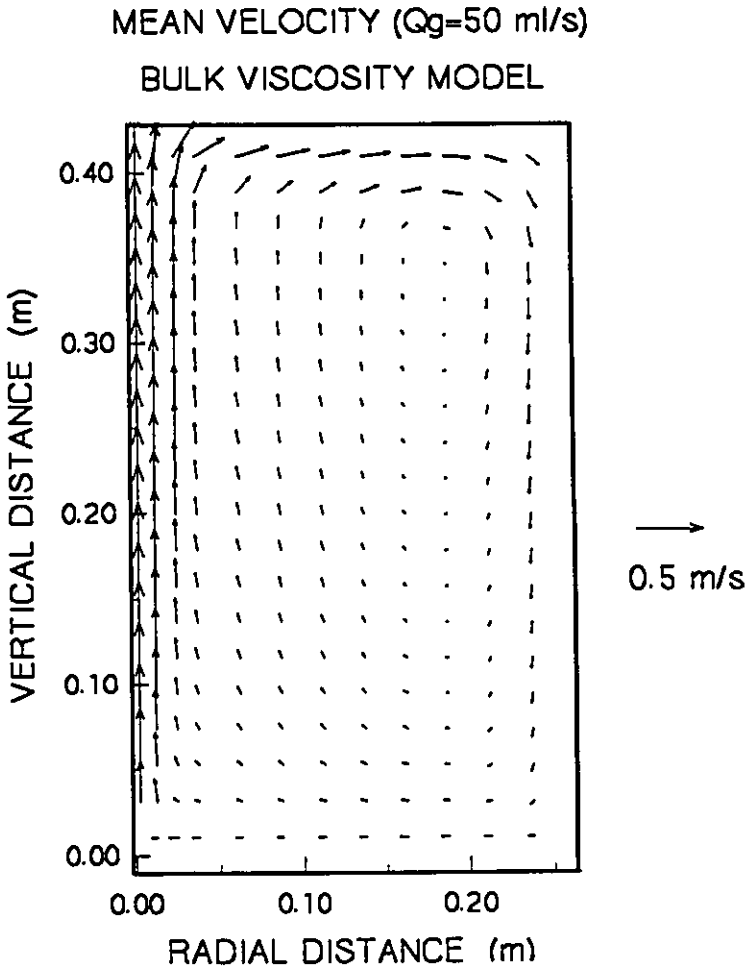

Figure VI.34 Mean flow field predicted with bulk viscosity model. This was obtained with the input of the measured α to the program described in Section 6.2. Q_g=50 ml/s.

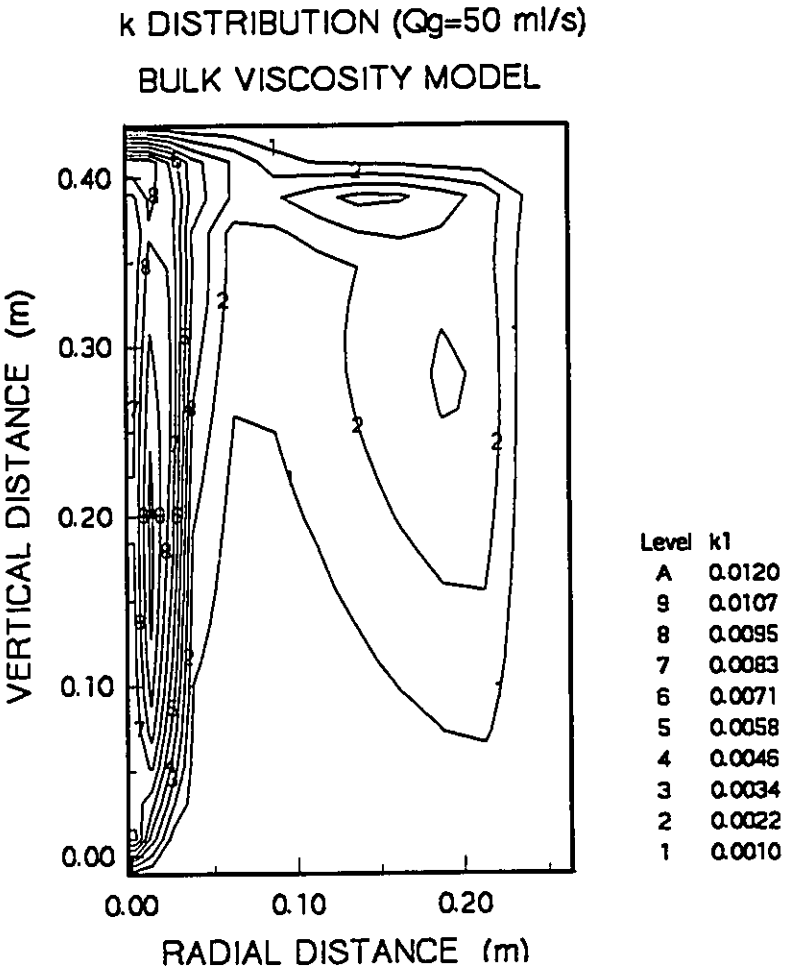

Figure VI.35 Turbulent kinetic energy predicted with bulk viscosity model. This was obtained with the input of the measured α to the program described in Section 6.2. Q_g=50 ml/s.

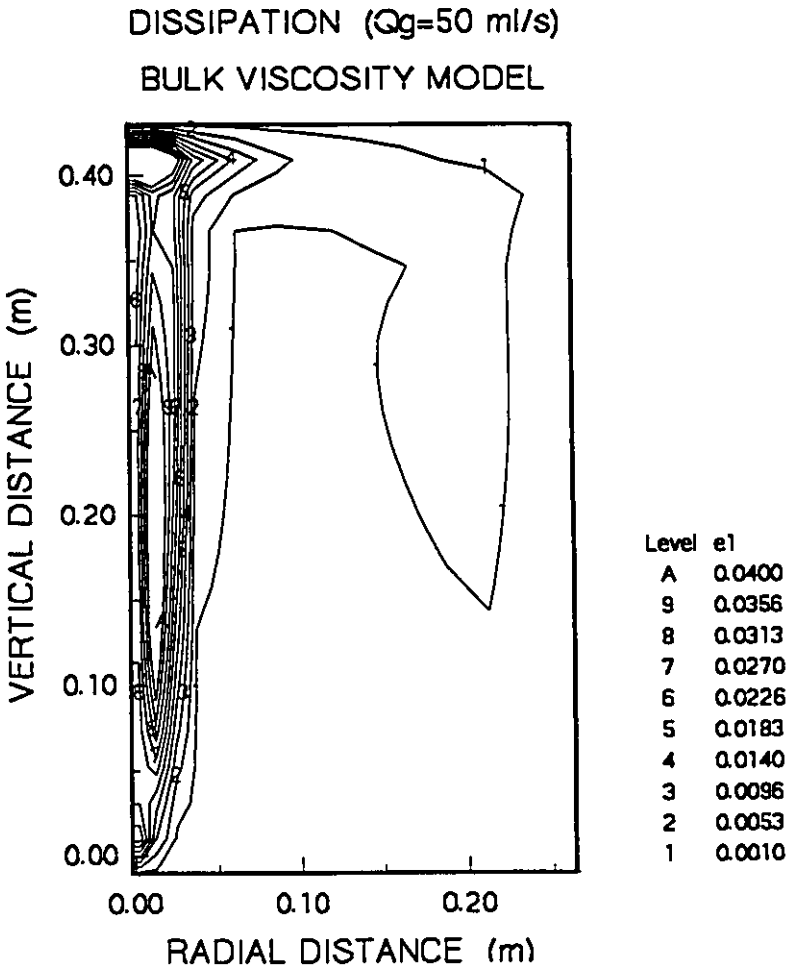

Figure VI.36 Turbulent dissipation predicted with bulk viscosity model. This was obtained with the input of the measured α to the program described in Section 6.2. Q_g=50 ml/s.

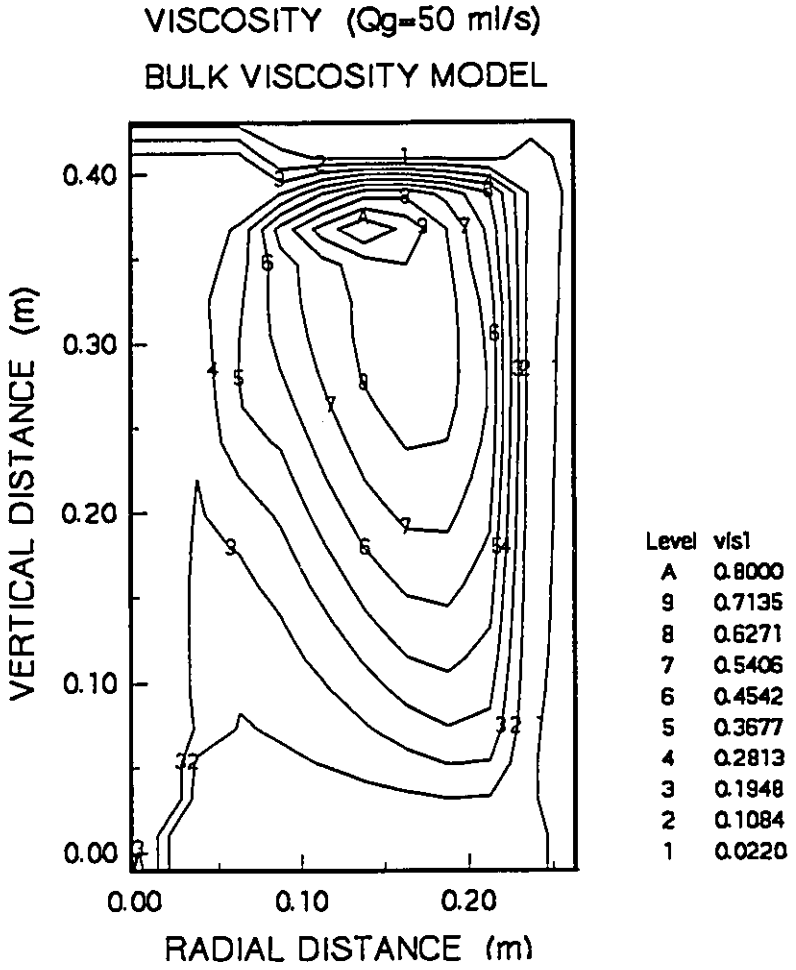

Figure VI.37 Turbulent viscosity predicted with bulk viscosity model. This was obtained with the input of the measured α to the program described in Section 6.2. Q_g=50 ml/s.

6.7.2 Evaluation of the Void Fraction Prediction

The void fraction predictions obtained with the present model are in good agreement with the experimental measurement as discussed in the previous section which is basic for the model to be able to achieve good predictions of the liquid flow field. However, the model has strong reliance on the input of the experimental information in the treatment of the bubble behaviour, which limits the universal applicability of the model. Some of the models on the bubble behaviour in a plume as presented in chapter V and used in the model are still in their early development stage, for instance, the determination of the drag on bubble and the treatment of the bubble breakup process. Although these phenomena certainly need further investigation for the improvement of the present model, the knowledge obtained in this project is very useful to the computer simulation of the process as presented in the above sections. More information is needed for a better understanding of the parameters of the process, such as the effects of the liquid properties and temperature on the bubble shape variation, free rising distance before first break up and the breakup frequency. However, it is certainly a significant improvement in the modelling of the plume flows to take these parameters into consideration. The present model is therefore much closer to reality in revealing those important details of the plume compared with all the previous models.

The void fraction distribution is most sensitive to the breakup and spiral movement of big bubbles rising in the centre of the plume. The breakup of these big bubbles determined the size distribution of bubbles in the plume, which would in turn affect the void fraction distribution significantly. In the present simulation, the breakup was modeled based on the experimental observation which guaranteed reasonable

predictions of the void fraction distributions. The most important factor is the breakup rate as discussed in section 6.3.2.3. Too high a breakup rate of bubble would result in a flatter distribution of bubble size and void fraction along the radial direction than the experimentally measured ones. On the contrary, if the breakup rate is too low, more bubbles would rise through the bath without breaking up to produce an inadequate amount of small bubbles. Consequently, the radial void fraction distributions are too concentrated around the centre line of the plume. In the present computer simulation process, a drop of 50% in the breakup rate would result in 15% to 30% increase of void fraction along the centre line of the plume.

The radial distribution of the void fraction is mainly controlled by the following two factors as observed in the water model experiments:

(1) The swirling movement of big bubbles in the centre of the plume;

(2) The lateral migration of the smaller bubbles resulting from the breakup of big bubble.

To model the swirling movement of the big bubbles, it is critical to determine the most important reason of the swirling. The random interaction of bubbles with the all kind of eddies would result in random variation of the direction of the bubble movement, which is contrary to the regular spiral movement of bubbles as observed in the experiments, and too narrow distributions of the void fraction. The proper treatment of the swirling is therefore based on the random interaction of bubbles with the energy containing eddies, which carry enough energy to change the course of bubble movement, and the wake shedding behaviour of bubbles. It is very interesting that the

two factors yield quite similar characteristic frequencies of bubbles as discussed in section 6.4.3.

For the treatment of the lateral migration of smaller bubbles, there have been different approaches as already discussed in Chapter II. In an Eulerian scheme, the most interesting technique is the adoption of the so-called bubble effective diffusivity concept, which must be determined independently with experiments (Kikuchi et al, 1986). All the factors which affect the lateral migration of bubble, such as the effect of eddies and lateral lift force, are included in the determination of the bubble effective diffusivity. The shortcoming of the technique is its lack of physical significance, and therefore difficulties in properly designing experiments to measure it. In a Lagrangian scheme, all the previous models calculated the bubble trajectories based on the random interaction of the bubbles with turbulent eddies without considering the lateral lift force effect. The lateral lift force also plays important role when a significant radial velocity gradient in the liquid flow field exists. The physical significance of the lateral lift force is not as difficult to understand as the bubble effective diffusivity; and it is also easier to measure experimentally. A better Lagrangian model of the plume, therefore, should include both the effect of the eddies and the effect of the lateral lift force. The remaining problem is the generalization of the experimentally measured lateral lift coefficient, which is 0.1 to 0.15 as measured with the present water model. Further work is needed to determine the coefficient in other physical processes, such as in a molten steel bath.

As a result of the above effort, the predicted void fraction distributions in the radial direction are very close to the measured ones. As in the case of treating bubble breakup process, however, experimental information was needed for the determination of the lift coefficient, C_L, which is one of the limitations of this model to be applied

elsewhere. In most cases, small bubbles away from the plume centre are mostly affected by the lateral lift force, which could drive them laterally for 10 to 30 mm under the present conditions during their rising to the free surface. The contribution of these small bubbles to the void fraction value at the plume boundary, however, is not significant compared to the void fraction values at the centre of the plume. As a result, with the present mathematical model, when C_L increased from 0.0 to 0.1, the predicted void fraction contour line of 0.001 shifted about 10 to 20 mm in the radial direction. Further increases of C_L from 0.1 to 0.15 showed negligible effect on the radial distribution of the void fraction due to the limited amount of void carried by these small bubbles to the boundary zone of the plume.

6.7.3 Features of the Mean Liquid Flow Field

The predicted mean liquid flow fields reflect a very strong upward flow of liquid in the center region of the plume. With the rise of the plume, more and more fresh liquid is entrained into the plume. The treatment of the free surface as a moving solid wall caused this upward flow to decelerate rapidly in the area close to the free surface, which is a distortion to the real situation where a spout would form (Castillejos and Brimacombe, 1987; Brimacombe, 1991). Away from the plume and not very close to the side wall, the recirculation of the liquid is generally weak. The recirculation pattern of the liquid is also affected by the treatment of the free surface as a solid wall. The predicted downward flow along the side walls is usually higher than the measured results, since the momentum dissipated in the spout of the plume in the real process is not totally consumed when the upward plume encounters the free surface in the simulation, part of it is converted into the radial momentum and then further into the

downward momentum. As a result, to better model the recirculation of liquid in this case, the behaviour of the spout formed above the free surface would need careful consideration, even though the heights of the spout are only 0.01 to 0.025 m in the present study.

6.7.4 Predicted Characteristics of the Turbulence

The predicted results obtained in this chapter, together with the experimental measurement discussed in chapter IV, offered a much closer understanding of the topic than any attempt made in the past.

The strongest turbulence is in the center area of the plume. In the predictions, the turbulence is even stronger in the small zone very close to the free surface than in the area close to the nozzle, which is also a distortion by the treatment of the free surface as a moving solid wall. In reality, the strongest turbulence should be in the spout region above the free surface as reported by Sahajawalla and Brimacombe (1989). Both the intensity of turbulence and the dissipation of the turbulent kinetic energy are much stronger in the two-phase plume zone than in the single phase zone. This information is very helpful for the modelling of mass or heat transfer in the plume zone. The transportation of the turbulence by the mean liquid flow is also reflected in the predicted result, as the contours for k, ϵ and μ_T extend along the way of the liquid recirculation.

The predicted results and the convergency of the turbulent variables is more sensitive to the void fraction distribution, which may be due to the fact that the void fraction appears in both of the extra sources for both k and ϵ.

6.7.5 Effect of Grid Size on Predicted Results

The computational results obtained with the solution of the finite difference equations are only approximations to the solutions of the original differential equations. Only when the grid sizes are infinitely small, the approximations may agree perfectly with the real solutions. However, in the computer simulation process, it is impractical to employ infinitely small grid size. To determine an appropriate grid size used for present model, three different grid designs were tested. One design was already shown in Figure VI.1, with 14 grids points along the radial direction and 22 along the vertical direction. The second is the design with all grid sizes double the first design, which yields 9 grids points along the radial direction and 12 along the vertical direction. The third design has 25 grids points along the radial direction and 42 along the vertical direction with each cell size being half of the corresponding grid of the first one. The program used was as the same as that used in the previous sections of this Chapter for the testing of the extra source constants of the modified k-ε model with the experimentally measured void fraction. For the grids where no experimental measurement had made, interpolation was used to assign proper values of void fraction to these points. This treatment was to eliminate the influence from the iteration of the void fraction on the prediction of the flow field. To show the results more clearly, only mean liquid velocity in the vertical direction along the center line of the plume is presented in Figure VI.38 together with the measured velocity data for Q_g of 50 ml/s.

All the three predictions are close to the experimental results, and the predictions based on the 14x22 and 25x42 designs are obviously better than that based on 9x12 design as shown in Figure VI.38. The reason could be twofold. The first is that

the 9x12 design was slightly too coarse to yield accurate prediction. The second, however, is not as straightforward. Since the void fractions used at the center line grids are the same for all three designs, with larger grid size, the void fraction is actually higher than those for smaller grid sizes, considering the radial decrease of void fraction distribution. As a result, the predicted velocity at the center line is also higher.

From the above discussion, it is reasonable to conclude that the predictions using the present computer program depend weakly on the design of the grid size, and grid designs smaller than the 14x22 design would not yield obviously better accuracy when compared to the experimental results.

6.7.6 Convergency Speed

It was relatively easy to obtain the convergency of the mean liquid flow field with the present model. The number of the iterations is usually less than 500 after the first convergency is reached. After each update of the void fraction, a new convergency of the mean liquid flow field would be reached within 50 more iterations. With a IBM compatible 386 PC machine (25 MHz) equipped with a WEITEK math coprocessor and NDP FORTRAN, an iteration of the liquid flow for the 14x22 grid design needs about 2 to 3 seconds. The update of the void fraction for 500 bubbles would require 15 to 30 minutes.

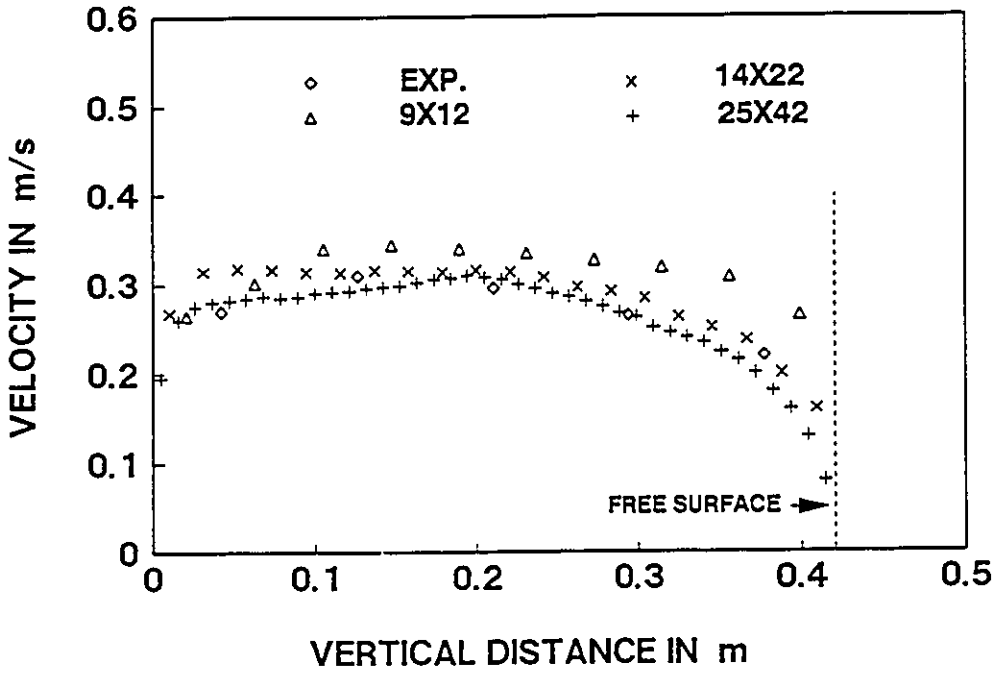

Figure VI.38 Grid size on predicted results with measured void fraction Predictions with three grid designs, 9x12, 14x22 and 25x42 are shown together with the measured velocity for Q_g = 50 ml/s.

CHAPTER VII
FUTURE WORK AND APPLICATIONS

This project has been intended to develop a fundamental understanding of the following practically important subjects:

(1) Behaviour of bubbles in the plume generated under conditions similar to those encountered in the injection metallurgy process;

(2) Turbulent features of the two-phase flow in the plume zone;

(3) Mathematical simulation of the turbulent two-phase flow.

The above mentioned subjects are usually encountered in a bubbly plume flow study and have not received appropriate attention in the literature. In the previous chapters, the results of the experimental measurement and of the mathematical simulation of a water model have been presented. However, the ultimate purpose of the project is to apply these results to benefit steelmaking processes. It is then important to review the significance of the study to the iron and steel industry.

The most important experimental findings of this project are the determination of the drag coefficient for bubbles in water and the turbulent structure

in the plume. Based on the Morton similarity theory discussed in Chapter IV, these findings can be applied directly to industrial processes to determine such important variables as bubble rising velocity and bubble residence time. For various ladle metallurgy processes, to simulate the liquid flow in the ladle, the most appropriate consideration of similarity between a water model and a full scale ladle should be based on the Froude Number, which is the ratio of inertial force to buoyancy force as stressed recently by Mazumdar and Guthrie (1990), who also proposed the following scaling equation for the calculation of the gas flowrate to be used in a water model based on the above consideration:

$$\frac{Q_m}{Q_{fs}} = \left(\frac{L_m}{L_{fs}}\right)^{\frac{3}{2}} \qquad \textbf{(VII.1)}$$

where, Q is the gas flowrate and L is the liquid depth. Subscripts m and fs stand for model and full scale furnace, respectively. The operational conditions of the present water model and the corresponding full scale ladle of 125 ton capacity are listed in Table VII.1.

Table VII.1 Data of water model and full scale ladle

	L, m	R, m	M, ton	Q, ml/s	U_p, m/s	t_B, s
MODEL	0.42	0.25	0.08	50-200	0.20-0.35	0.6-0.9
LADLE	2.5	1.5	125	800-3000	0.70-1.10	1.2-1.8

The average rising velocity of a bubble of size of 0.1 m in a steel making ladle can be estimated with the following equation:

$$U_B = U_p + U_{BT} \qquad \textbf{(VII.2)}$$

where, U_{BT} is the terminal velocity of a single bubble with the same size and U_p is the average rising velocity of the plume. U_{BT} is about 0.70 m/s in this case as calculated with Eq.(VI.31), assuming the surface tension of the steel is 1.5 N/m and the density of the steel is 7000 kg/m^3. U_p can be obtained with the mathematical model presented in the previous Chapter. The calculated mean velocity of the plume, U_p, together with the estimated residence time of bubble based on U_B and the corresponding liquid depth, t_B, are also listed in Table VII.1 for the present water model and its corresponding full scale ladle. The mean plume rising velocity can also be estimated with the following empirical equation proposed by Mazumdar and Guthrie (1990):

$$U_p = 4.5 Q^{1/3} L^{1/4} / R^{1/4} \qquad \textbf{(VII.3)}$$

With the knowledge of the bubble rising velocity and its residence time in the plume, it is then possible to establish such mathematical models as those developed in the present study for the prediction of the turbulent flow field in the ladle, and the various reaction models to predict metallurgical reactions in the plume. It would be possible to construct a mathematical model for the calculation of the flow field of the molten steel and the void fraction distribution in the ladle. The behaviour of bubbles in the ladle can be modelled in the similar way as the model presented in Chapter VI to calculate distributions of bubbles size. Once the flow field of liquid steel and the distribution of bubble size are known, it is then possible to calculate the rising velocity of bubbles with the drag coefficient determined in this project and calculate the residence time distribution of a bubble in the ladle. In the following sections, a brief discussion on the possible application of the findings of this study to various iron and steel making processes will be presented.

7.1 Fundamental Study of Mass and Heat Transfer

Various steel making vessels equipped with gas stirring are actually chemical reactors. The metallurgical reactions in these vessels are governed by mass and heat transfer processes. The rates of these transfer processes can only be obtained after the behaviour of bubble and the turbulence feature in the plume is known. The findings discussed above is therefore very important for controlling and monitoring these metallurgical reactions. In a bottom stirred ladle, for example, the mass and heat transfer in the melt are usually affected by the following factors:

(1) The intensities of the turbulence. Turbulence can affect mass or heat transfer processes either by turbulent diffusion or by turbulent convection processes. Local turbulent properties must be known for the further investigation of local reaction processes.

(2) The mixing conditions in the vessel which depend on both the mean flow field and the turbulence intensity;

(3) The behaviour of bubbles in the plume which include the drag on a bubble, the lateral migration of a bubble and size variation of bubbles as a result of the breakup or coalescence;

(4) The interfacial area supplied by the bubble phases for reaction;

(5) The distributions of the void fraction and the residence time of the bubbles.

The findings of the present work, such as the residence time of bubble, the gas/liquid interfacial area and the turbulence features in the plume, could contribute important information to the estimation of these variables. These would be helpful to the exploration of the mass or heat transfer processes. Take the determination of mass or heat transfer coefficients as example. In most engineering processes, these coefficients are expressed in terms of a group of non-dimensional numbers (Kay and Nedderman, 1985; Geiger and Poirier, 1973). For example, the mass transfer coefficient in a circular pipe with Re > 2100 can be written into the following correlation:

$$Sh = 0.023 Re^{0.83} Sc^{0.44} \qquad \textbf{(VII.4)}$$

where Sh = $k_m D/D$ is the Sherwood Number, Re = UD/v the Reynould Number and Sc = $\mu/(\rho D)$ the Schmidt Number. k_m is the mass transfer coefficient, D, pipe diameter and D the diffusivity. Similar correlation has also been used for the heat transfer coefficient:

$$Nu = 0.023 Re^{0.8} Pr^{0.4} \qquad \textbf{(VII.5)}$$

where Nu = hD/k_t is the Nusselt Number and Pr = $\mu c_p/k_t$, the Prandtl Number. h is the heat transfer coefficient, k_t the thermal conductivity and c_p the specific heat at constant pressure.

The above technique would be also useful if applied to the study of the metallurgical problems. However, due to the usually more complex nature of the metallurgical processes, it is generally more difficult to establish similar dimensionless-number correlations for the calculation of the transfer coefficients. One of the difficulties is the selection of an appropriate length scale. This length scale should be a characteristic length scale of the local turbulence flow, which has not been available

due to the lack of the knowledge of local turbulence. This situation could be improved with the turbulence modelling technique developed in Chapter VI. With the local turbulence variables predicable, the length scales can be also calculated. This would certainly be helpful for the establishment of more plausible correlations to calculate the transfer coefficients.

The findings of the present work can also be directly beneficial to the better understanding and improvement of the steelmaking processes where gas injection is employed as an important refining process. Some of these processes are briefly discussed in the following section.

7.2 Industrial Applications

7.2.1 Ladle Metallurgy

One of the most popular applications of the gas injection is encountered in various ladle metallurgy processes. The operation of most ladle refining processes consists of combinations of the operations such as Degassing, Deoxidation, Desulphurization, Dephosphorization, decarbonization, composition adjustment and temperature control (Szekely et al., 1989). Almost all of these unit operations are affected by such gas blowing operation variables as the position of the lance or the nozzle, the gas flowrate and the blowing time. Although much work has been done in the past for the optimization of these operational parameters, most of these efforts only yielded some macroscopic understanding of the process in terms of the mixing time of the melt. It is still not possible to predict the various metallurgical reactions in terms of

the local variables, such as the local reaction rate and the variation of the composition distribution, due to the lack of the knowledge of the turbulent flow, the behaviour of bubbles and the interaction between the gas and the liquid phase as discussed in the previous section. The design and control of the operation based on such predictions is consequently lacking. Take deoxidation in a ladle furnace equipped with the gas bottom blowing as an example. Basically, the deoxidation can be achieved through three different routes:

(1) Deoxidation with dissolved carbon through the following reactions:

$$[C] + [O] = CO_g \qquad \textbf{(VII.6)}$$

where, [ ] stands for element dissolved in the melt, and subscript g stands for the gas state.

(2) Deoxidation with agents such as Aluminium and Silicon, which are added to the melt in the form of either lumps or powders, and then dissolve into the steel to react with [O]:

$$[Me] + [O] = (MeO) \qquad \textbf{(VII.7)}$$

where, ( ) stands for slag phase and, Me for deoxidation agents.

(3) Deoxidation at the slag/melt interface:

$$[O] + [Fe] = (FeO) \qquad \textbf{(VII.8)}$$

In the first case, the reaction can be significantly improved with inert gas bubbling as a result of the intensified diffusion of both [O] and [C] caused by the inert-gas-driven turbulent recirculation of the melt, and as a result of the inert gas bubbles acting as nucleation sizes for the resultant CO. The void fraction distribution of the inert gas is then the crucial variable needed for the prediction of the reaction. Furthermore, the turbulent diffusion of the dissolved elements is predictable only when the correct turbulence level could be predicted. The techniques developed in the previous chapters for the prediction of the void fraction distribution in the melt and the modified k-ϵ model for the turbulence in the two-phase zone, can therefore contribute to the future work to build such a model for the prediction and monitoring of the reaction process. With this reaction under control, the deoxidation process can then be optimized in terms of the operation time and the energy input with computer simulations instead of the costly industrial experiments.

In the second and third cases, a mass and heat transfer model could be established based on the predictions of the turbulent fluid flow in the steel phase with the mathematical model discussed in chapter VI. It is then possible to calculate the amount of deoxidation agent transported by both the mean flow and the turbulent diffusion from agent-rich zone to other places in the furnace. It is to be noted that all the previous models of the bubbly plume flows as discussed in Chapter II fail to predict correctly the turbulence in the two-phase plume zone, and consequently cannot be used as the base of the models for the prediction of the mass and heat transfer in the zone.

7.2.2 The Electric Arc Furnace

Electric Arc Furnaces (EAF) have been playing a very important role in the steel making industry in recent years, and its steel output has been steadily growing to amount to about 30% of the total world steel production (Berthet and Grosjean, 1990). However, the efficiency of the furnace as a chemical reactor is low due to the shallow furnace hearth and the stagnant melt. The application of bottom gas blowing to the EAF was therefore made to improve the reaction conditions inside the furnace. With the invention of the eccentric bottom tapping and the direct current furnace in recent years, bottom gas blowing has gained more importance in EAF steel making. The apparent benefits from the bottom gas blowing include (Berthet and Grosjean, 1990; Noda et al, 1990):

(1) Lower (FeO) content in the slag phase, which can yield about 1% of Fe saving;

(2) Lower [O] content of the steel, which means better quality of the steel;

(3) Better homogenization of the melt in terms of the temperature and composition distributions. This is most significant when alloying is made inside the furnace. The gas blowing helps the melting and the dispersion of the alloy elements, and therefore shorten the operation.

Although the benefits are obvious, there have been few studies on the optimization of the bottom gas blowing in the EAF. The reason is partly due to the lack of understanding of various dynamic processes inside a two-phase turbulent plume.

The problem could be tackled now with the computation simulation technique developed in this project. With the behaviour of bubbles and the turbulent liquid flow inside the bubbly plume zone being simulated with a computer, it is possible to optimize such operational variables as the number of nozzles to be employed, the distribution of the nozzles in the furnace bottom, and the blowing intensity. As a result, the various reaction rates and the homogenization of the melt can be further improved and the potential benefit of the bottom gas blowing fully exploited.

7.2.3 The Combined Blowing Converter

One of the most important factors which affect the operation of a combined blowing converter is the mixing conditions of the melt and slag during the steel making process. The two-phase plume flow plays an important part in the vessel and have not received adequate attention. Studies performed on cold models yielded only some empirical correlations between the mixing time and the various operational variables (Singh and Ghosh, 1990; Koria and Pal, 1990; Koria and George, 1988). Various mathematical simulations have had difficulties in interpreting the effects of the turbulence caused by the bubbles on the mass and heat transfer processes, such as the effects on the convective diffusion and dispersion of additions in steel melts (Chung and Lange, 1988). The solutions to these problems could be obtained now with the application of the fundamental understandings of the bubbly plume flow developed in the previous chapters. With the turbulent liquid flow in the two-phase zone being better predicted, it is possible to obtain an better estimation of the entrainment rate of the liquid by the plume, and consequently better predict the overall recirculation of the liquid in the furnace to give better estimation of the mixing time. It is also possible to

improve the mixing operation with computer simulations by manipulating various operational variables as the inputs to the computer, instead of expensive and time-consuming physical modelling. To reach this goal, the applicability of the present model to the higher gas flowrate situations should be further investigated.

7.2.4 Non-Ferrous Metallurgical Processes

Gas injection has been used increasingly in the refining and converting of such non-ferrous metals as copper and aluminium (Lehner et al, 1991). The practical purpose of employing gas stirring varies according to different processes. It is used to remove such impurities in the copper or nickel matte as lead, zinc and arsenic (Lehner, 1991), or to enhance smelting or converting reactions of copper in the furnace (Themelis, 1991). It may also be used to reduce thermal stratification in these smelting furnaces which usually have very shallow baths with significant thermal stratification. Gas stirring can evidently improve the temperature distribution in these furnaces and therefore increase the productivity and efficiency of the processes as investigated by Banerjee and Irons (1992).

The mechanisms of the gas stirring in the above mentioned processes are similar to the processes discussed in the previous sections, and therefore can be also simulated with the mathematical model developed in this project. The application of the present model to these non-ferrous metallurgical processes is anticipated to benefit both the theoretical investigations and practical operations in this field.

CHAPTER VIII
CONCLUSIONS

The purpose of this study was to measure the various parameters, which characterize bubbly plume flow with high void fraction and large bubbles, and based on the information obtained from the experiments, develop a new mathematical model for the prediction of both the void fraction distribution and the turbulent liquid flow field. The study is consisted of the following three parts:

1. Analysis of the existing techniques for the bubbly two-phase study, and development of an experimental technique which can be applied conveniently to the bubbly plume measurement.

2. Application of the newly developed technique to the experimental study of the bubbly plume phenomena. The parameters studied include the void fraction distribution, the bubble frequency distribution, mean and fluctuating velocities of the bubble, mean and fluctuating velocities of the liquid, the drag coefficient and the lateral lift coefficient for bubble as well as some of the turbulent features of the liquid flow. With the help of the video camera technique, the information of the shape and size of bubbles was also obtained.

3. Mathematical modelling of the bubbly plume flow. The void fraction distribution

was obtained by tracking the movement of bubbles in a Lagrangian frame, and taking into account of the breakup behaviour of bubbles based on the information obtained in the experimental study. The liquid flow was then computed in an Eulerian frame based on the predicted distribution of the void fraction.

The following conclusions may be drawn from the results obtained in the above mentioned three parts work:

Part I

I.1 Techniques to discriminate between gas and liquid signals based on laser signal waveform analysis or blockage of laser light are difficult to apply to large bubbles at moderate void fraction. The probability distribution function of the mixed velocity of the two-phase also cannot be used for the separation of the two phase velocities in this case.

I.2 For small bubbles (less than approximately 4 mm) and low void fraction (less than approximately 0.4), the mean and RMS values for the gas and liquid velocities can be determined from manipulation of the mixed velocity probability distribution function. The limits of applicability depend on the accuracy required, the uniformity of the bubble size, and the level of the turbulence.

I.3 For large void fractions and large bubbles, a combined Laser Doppler Anemometer and Electric Probe Technique was developed for the simultaneous measurement of the bubble and liquid velocities inside a bubbly two-phase flow. The

void fraction and bubble frequency can be measured at the same time as the velocities of both liquid and gas phases.

Part II

II.1 The void fraction is concentrated in the area close to the centerline of the plume. This is due to the fact that most of the void fraction is contained by the large bubbles rising along the center of the plume. The void fraction decays rapidly in the radial direction. The radial dispersion of the void fraction is a result of the swirling movement of the big bubbles rising in the centre of the plume, and of the lateral migration of the smaller bubbles produced from the break up of the big bubbles.

II.2 The possible reasons for the lateral migration of the small bubbles in the bubbly plume are considered to be the random interaction of the bubbles with the turbulent eddies, and the lift force resulting from the relative movement of the bubbles with respect to the liquid and the radial velocity gradient in the liquid.

II.3 Large bubbles in the center of the plume undergo significant breakup during rise. The following factors play an important role in the breakup process: interfacial instability, the shear forces in the liquid phase and the strong turbulence.

II.4 The relative velocity of bubbles in an unconfined bubbly plume, as well as in a chain of bubbles, is not significantly affected by the void fraction. The difference between the measured relative velocity of bubbles in these cases and the terminal rising velocity of a bubble with the same size is negligible.

II.5 The experimentally measured lateral lift coefficient for small bubbles produced by the fritted glass is in the range of 0.08 to 0.15. It is influenced by such variables as bubble sizes and the vertical slip velocity of a bubble. With the vertical slip velocity of bubble increases from 0.2 to 0.4 m/s, the lateral lift coefficient increases slightly from about 0.1 to 0.13.

II.6 The strongest liquid flow is in the center of the plume. Along the centerline of the plume, the mean vertical velocity of the liquid is almost a constant, with the intensity of turbulence in the range of 0.5 to 0.7. The recirculation of the liquid is caused by the entrainment of the liquid by the bubbly plume, and stronger recirculation is obtained with larger gas flowrates.

II.7 The intensity of turbulence in the two-phase plume zone is generally greater than 0.5 as a result of the strong interaction between the liquid and bubbles. The intensity of turbulence in the single liquid phase, however, is much lower, usually in the range of 0.1 to 0.3.

II.8 The turbulence in the two-phase plume zone is not isotropic; a slightly skew to the vertical direction was observed for all the gas flowrates used in the work. This anisotropy of turbulence is believed to be a result of the much strong flow in the vertical direction, and is weakened with increases of the gas flowrate.

Part III

III.1 Various turbulence models which have been used in the bubbly plume study, such as the bulk effective viscosity model, were found to result in distorted distribution of the turbulent kinetic energy in the two-phase plume zone, when their predictions were compared to the experimental result obtained in this project.

III.2 The modified k-ε model, which takes into account the turbulence generation and dissipation caused by the existence of bubbles, can yield good predictions of both the mean flow field and the distribution of the turbulent kinetic energy in the plume zone when the following values are chosen for the extra source terms in the model based on the experimental measurements made in this project:

$$C_{k1},\ C_{k2},\ C_{\varepsilon 1},\ C_{\varepsilon 2} = 6.0,\ 0.75,\ 4.0,\ 0.6 \qquad \textbf{(VI.46)}$$

III.3 The behaviour of bubbles in the plume was modeled in a Lagrangian frame to yield reasonably good fitting of the distribution of the void fraction. In the model, the bubble motion equations were solved for the trajectories of the bubbles, and the size and shape variation of the big bubble rising in the center of the plume can be approximated with random processes. For the lateral migration of the bubbles, effects of both the turbulent diffusion and the lateral lift force were considered.

III.4 A new mathematical model was developed for the prediction of the bubbly plume flows. In this model, the distribution of the void fraction was first calculated based on an estimated liquid flow field, by solving the bubble motion equations in a Lagrangian frame. The liquid flow field was then calculated in an Eulerian scheme by

solving the turbulent Navier-Stokes Equations using the TEACH computer code and the modified k-ε model. The updated void fraction distribution can be then obtained based on this new estimate of the liquid flow field.

III.5 The predicted distributions of the void fraction with the new mathematical model developed in this project are in good agreement with the experimental measurements. The model also yields good predictions of both the mean liquid flow field and the turbulence distribution in the two-phase plume zone, which agree well with the experimental measurements.

CLAIM TO ORIGINALITY

The following aspects of this thesis constitute, in the Author's opinion, new and distinct contributions to knowledge:

(1) The combined Laser Doppler Anemometry technique for the gas/liquid two-phase measurement. This technique supplied a basic experimental means for the investigation of the gas/liquid two-phase flows in various engineering fields.

(2) The mathematical methods for the separation of the mixed velocity data from gas/liquid flows. The application of this technique is not limited to the gas/liquid flow velocity separation, it can also be used for the separation of a mixture of data from any two Gaussian distribution samples.

(3) This is the first time that the velocities of both the bubble and liquid in a plume flow have been measured. It is also the first time that turbulence characteristics in the plume zone have been revealed experimentally. These findings enlarged the present understandings of the plume phenomena, and are very important to the further investigation of the process.

(4) The results of the present project showed that the relative velocity of bubble in the plume situation is not affected by the distribution of the void faction in the plume, which clarified one of the controversial aspect in the modelling of the plume flows, and

therefore is very important for the further investigation of the bubble behaviour in the plume.

(5) The modified k-ε model for the turbulence modelling in the plume with the experimentally determined coefficients for the extra source terms has supplied a solid base for the further development of computer simulation techniques for the plume flows.

(6) The mathematical model, which employs an Eulerian scheme for the liquid flow modelling and an Lagrangian scheme for the modelling of the bubble behaviour is not the innovation of this project, however, the incorporation of the bubble lateral migration and breakup into the model, though not very mature at this stage, is an important new contribution to the understanding of plume flows. This may represent the most realistic modelling techniques of the plume flows to date.

REFERENCES

Auton., T.R., 1987, Lift Force on a Spherical Body in a Rotational Flow, J. Fluid Mech., Vol.183, Oct. 199-218

Baker, G. R. and Moore, D. W., 1989, The Rise and Distortion of a Two-Dimensional Gas Bubble in an Inviscid Liquid, Physics of Fluid, A Vol.1, No.9, Sept., 1989, p1451

Banerjee, S. and Lahey, R.T., 1981, Advances in Two-Phase Flow Instrumentation, Advances in Nuclear Science and Technology, Vol.13. Edited by Levin, J. and Becker, M., Plenum Publishing Corporation, pp. 227-414

Banerjee, S.K. and Irons, G.A., 1992, Physical Modelling of Thermal Stratification, Bottom Build-up and Mixing in Submerged Arc Electric Smelting, Canadian Metall. Quarterly, in press.

Bankoff, S.G., 1960, J. Heat Transfer, 82(2), pp. 265-270

Berthet, A.J. and Grosjean, J. 1990, The 90's Eletric Arc Furnace Steelmaking Route: The Leap Forward. Proc. of Sixth Intern. Iron and Steel Congress, Nagoya, Japan,

Vol.4, pp. 180-189

Beyerlein, S. W., Cossmann, R. K. and Richter, H 1985, Prediction of Bubble Concentration Profiles in Vertical Turbulent Two-Phase Flow. Int. J. Multiphase Flow, Vol.11, No.5, pp. 629-651

Boerner, T., Martin, W. W., and Leutheusser, H. J. 1984, Comprehensive Measurements in Bubbly Two-Phase Flows Using Laser-Doppler and Hot-Film Velocimeter. Chem. Eng. Commun., Vol.28, pp. 29-43

Boysan, F. and Johansen, S. T., 1985, Int. Seminar on Refining and Alloying of Liquid Aluminium and Ferro-Alloys, Aug.26-28, Trondheim, Norway

Brimacombe, J.K., 1991, Basic Aspects of Gas Injection in Metallurgical Processes, Int. Symp. on Injection in Process Metallurgy, Edited by Lehner, T., Koros, P.J. and Ramachandran, V., A Publication of the Minerals, Metals and Materials Society, pp. 11-23

Burty, M., Fautrelle, Y. and Huin, D., 1990, A Computational Model for the Prediction of Turbulent Recirculating Two-Phase Flows in a Gas-Stirred Steel Ladle. Proc. of the Sixth Int. Iron and Steel Congress, Nagoya, ISIJ, pp. 444-405

Calabrese, R. V., Chang, T. P. K. and Dang, P. T., 1986a, Drop Breakup in Turbulent Stirred-Tank Contactors, Part I: Effect of dispersed-phase viscosity, AICHE J., Vol.32, No.4, pp. 657-666

Calabrese, R. V., Wang, C. Y. and Bryner, N. P., 1986b, Drop Breakup in Turbulent Stirred-Tank Contactors, Part III: Correlations for Mean Size and Drop Size Distribution, AICHE J., Vol.32, No.4, pp. 677-681

Castillejos, A. H. and Brimacombe. J. K. 1987a, Measurememt of Physical Characteristics of Bubbles in Gas-Liquid Plumes: Part I. An Improved Electroresistivity Probe Technique. Met. Trans. B, Vol. 18B, pp. 649-658

Castillejos, A.H. and Brimacombe, J.K., 1987b, Measurement of Physical Characteristics of Bubbles in Gas-Liquid Plumes: Part II. Local Properties of Turbulent Air-Water Plumes in Vertically Injected Jets. Metall. Trans., Vol. 18B, pp. 659-671

Chen, C.P. and Wood, P. E., 1985, Can. J. Chem. Eng., Vol.63, pp. 349-360

Chung, S.H. and Lange, K.W. 1988, Convective Diffusion and Dispersion of Additions in Steel Melts, Ironmaking and Steelmaking, Vol.15, No.5, pp. 244-253

Clark, M. M. 1988a, Drop Breakup in a Turbulent Flow---I. Conceptual and Modelling Considerations, Chem. Eng. Sci., Vol.43, No.3, pp. 671-679

Clark, M. M. 1988b, Drop Breakup in a Turbulent Flow---II. Experiments in a Small Mixing Vessel, Chem. Eng. Sci., Vol.43, No.3, pp. 681-692

Clay, P. H., 1940, Proc. Roy. Acad. Sci. (Amsterdam), 43, pp. 852-865

Clift, R., Grace, J. R. and Weber, M. E., 1978, Bubbles, Drops and Particles. Academic

Press

Collins, S. B. and Knudsen, J. G., 1970, Drop-Size Distribution Produced by Turbulent Pipe Flow of Immiscible Liquids, AICHE, J. Vol.16, No.6, pp. 1072-1080

Coulson, J. M. and Richardson, J. F., 1955, Chemical Engineering, Volume Two, McGraw-Hill Book Co., Inc., New York

Crabtree, J. R. and Bridgewater, J., 1969, Chain Bubbling in Viscous Liquids. Chemical Engineering Science. Vol.24, pp. 1755-1768

Deb Roy, T., Majumdar, A.K. and Spalding, D.B., 1978, Numerical Prediction of Recirculation Flows with Free Convection Encountered in Gas-Agitated Reactors, Appl. Math. Modelling, Vol.2, pp. 146-150

Drain, L. E., 1980, The Laser Doppler Technique, John Wiley and Sons

Drew, D. A., 1988, Lift Force on a Small Sphere in the Presence of a Wall. Chem. Eng. Sci. Vol.43, No.4, pp. 769-773

Drew, D. A. and Lahey Jr., R. T., 1979, Application of General Constitutive Principles of the Derivation of Multidimentional Two-Phase Flow Equations. Int. J. Multiphase flow. Vol. 5, pp. 243-264

Drew, D. A. and Lahey Jr., R. T., 1987, The Virtual Mass and Lift Force on a Sphere in Rotating and Straining Invicid Flow. Int. J. Multiphase Flow. Vol.13, No.1, pp.

113-121

Durst, F. and Zare, M., 1975, Proc. of the LDA Symposium, Copenhagen, pp. 403-429

Durst, F., Schnonung, B., Selanger, K. and Winter, M., 1986, Bubble Driven Liquid Flows, J. of Fluid Mechanics, Vol.170, pp. 53-82

Eichhorn, R. and Small, S., 1964, Experiments on the Lift Force and Drag of Spheres Suspended in a Poiseuille Flow. J. Fluid Mech. Vol.20, Part 3, pp. 513-527

Farias, L.R. and Irons, G.A., 1986, Metall. Trans. B, Vol.17B, pp. 77-85

Fruehan, R. J., 1985, Ladle Metallurgy Principles and Practices, Iron and Steel Society Incorporation

Geiger, G.H. and Poirier, D.R. 1973, Transport Phenomena in Metallurgy, Addison-Wesley Publishing Company, massachusetts

Giddings, J. C., 1988, Continuous Particle Separation in Split-Flow Thin Cells Using Hydrodynamic Lift Forces. Sep. Sci. Technol. Vol.23, No.1-3, pp. 119-131

Govan, A. H., Hewitt, G. F. and Ngan, C. F., 1989, Particle Motion in a Turbulent Pipe Flow. Int. J. Multiphase Flow. Vol.15, No.3, pp. 471-481

Gosman, A.D. and Loannides, E., 1981, Aspects of Computer Simulation of Liquid-Fuelled Combustors, AIAA 19th Aero-Space Science Meeting, St. Louis,

Missouri, U.S.A, Jun.11-15

Gosman, A.D. and Pun, W.M., 1974, Calculation of Recirculating Flows. Report No. HTS/74/12, Department of Mechanical Engineering, Imperial College, London, England

Grace, J. R. , Wairegi, T. and Brophy, J. 1978, Break-up of drops and Bubbles in stagnant media. Can. J. Chem. Eng., Vol.56, pp. 3-8

Grevet, J.H., Szekely, J. and El-Kaddah, N., 1982, An Experimental and Theoretical Study of Gas Bubble Driven Circulation System, Int. J. of Heat Mass Transfer, Vol. 25, No.4, pp. 487-497

Hall, D., 1988, Measurements of the Mean Force on a Particle Near a Boundary in Turbulent Flow. J. Fluid Mech., Vol.187, Feb. pp. 451-466

Halow, J. S. and Wills, G. B., 1970, Radial Migration of Spherical Particles in Couette Systems. J. AIChE, vol.16. No.2, Mar. pp. 281-286

Hardy, J. E. and Hylton, J. O., 1984, Electrical Impedance Probes for Two-phase Poid Fraction and Velocity Measurements. Int. J. Multiphase Flow, Vol.10, No.5, pp. 541-556

Harper, E. Y. and I-Dee Chang, 1968, Maximum Dissipation Resulting from Lift in a Slow Viscous Flow. J. Fluid Mech. Vol.33, pp. 209-225

Hartunian, R. A. and Sears, W. R. 1957, On the stability of small gas bubbles moving uniformally in various liquids. J. Fluid Mechanics, Vol.3, p27

He, Q.L., Pen, Y.C. and Hsiao, T.C., 1984, Proc. Shengyang Symp. on Injection Metallurgy and Secondary Refining of Steel, pp. 98-113, Sept. 19-21, Shengyang, China

Hinze, J. O., 1955, Fundamentals of the Hydrodynamic Mechanism of Splitting in Dispersed Processes. AICHE. J. Vol.1, No.3, pp. 289-295

Hinze, J. O., 1975, Turbulence, 2nd Ed., McGraw-Hill, New York

Hoefele, E.O. and Brimacombe, J.K., 1979, Metall. Trans. B, Vol.10B, pp. 631-648

Huin, D., Reboul, J.P. and Zbaczyniak, Y. 1990, Control of Post-Combustion: A Key Factor of Old and New Refining Process. Proceedings of 49th Ironmaking Conference of ISS. Detroit

Ibaraki, T. Kanemoto, M., Ogata, S. Katayama, H. and Ishikawa, H. 1990, Development of Semlting Reduction of Iron Ore---An Approach to Commercial Iron Making. Proceedings of 49th Ironmaking Conference of ISS. Detroit

Ilegbusi, O.J. and Szekely, J., 1990, The Modelling of Gas-Bubble Driven Circulations Systems. ISIJ Int., Vol. 30, No. 9, pp. 731-739

Irons, G.A., 1986, Ladle Metallurgy of Steel for Continuous Casting and Ingot Teeming, McMaster Symp. on Iron and Steelmaking, No.14, Hamilton, Canada

Irons, G.A. and Guthrie, R.I.L. 1978, Bubble Formation at Nozzles in Pig Iron, Metall. Trans. B, Vol.9B, pp. 101-110

Irons, G.A. and Guthrie, R.I.L. 1981, Canadian Metallurgical Quarterly, Vol. 19, No. 4, pp. 381-387.

Ishii, M. and Zuber, N., 1979, Drag Coefficient and Relative Velocity in Bubbly, Droplet or Particulate Flows, AICHE J. Vol.25, No.5, pp. 843-855

Iwasaki, K., Kawata, H., Yamada, K. and Kitagawa, T. 1989, Integrated Test Plant Work on Smelting Reduction Ironmaking Process. Third Intern. Cong. in New Developments in Metallurgical Technology, Dusseldorf, Germany, pp. 1-15

Johansen, S.T. and Boysan, F., 1988, Fluid Dynamics in bubble Stirred Ladles: Part II. Mathematical Modelling. Metall. Trans. B., Vol. 19B, pp. 755-764

Johansen, S. T., Robertson, D. G. C., Woje, K. and Engh, T. A. 1988, Fuid Dynamics in Bubble Stirred Ladle: Part I. Experiments. Metall. Tran. B, Vol.19B, pp. 745-754

Johansen, S.T., 1986, Fluid Dynamics in Bubble Stirred Ladles, SINTEF Report No. STF34 A86039, Trondheim Norway

Kataoka, H., Takeuchi, H., Nakao, K., Yagi, H., Tadaki, T., Otake, T., Miyauchi, T., Washimi, K., Watanabe, K. and Yoshida, F. 1979, Mass Transfer in a Large Bubble Column. J. Chem. Eng. of Japan. Vol.12, No.2, pp. 105-110

Kawakami, M., Kitazawa, Y., Nakamura, T., Miyake, T. and Ito, K. 1985, Dispersion of Bubbles in Molten Iron and the Nitrogen Transfer in the Bubble Dispersion Zone at 1250 °C. Tran. ISIJ. Vol.25, pp. 394-402

Kay, J.M. and Nedderman, R.M. 1985, Fluid Mechanics and Transfer Processes, Cambridge University Press, London

Kikuchi, A., Taniguchi, S. and Bessho, N., 1986, 5th International Iron and Steel Congress, Process Technology Proceedings, Vol.6, Washington DC, pp. 369-375

Kirkaldy, J.S., 1979, Ladle Treatment of Carbon Steel, McMaster Symposium on Iron and Steelmaking, No.7, Hamilton, Canada

Kitscha, J. and Kocamustafaogullari, G., 1989, Int. J. Multiphase Flow, Vol.15, No.4, pp. 573-588

Kobus, H.E., 1969, Coast Engineering Conference, Vol.II, London

Koide, K., Morooka, S., Ueyama, K., Matsura, A., Yamashita, F., Iwamoto, S., Kato, Y., Inoue, H., Shigeta, M., Suzuki, S. and Akehata, T. 1979, Behavior of Bubbles in Large Scale Bubble Column. J. Chem. Eng. of Japan. Vol.12, No.2, pp. 98-104

Kolmogoroff, A. N., 1949, The breakup of droplets in a turbulent stream, translated from Dok. Akad. Nauk. 66, pp. 825-828, by E. R. Hope, 1956, Directorate of Scientific Information Service, DRB, Canada

Kor, G.J.W. 1989, The AISI Steel Initiative, Steel Research, Vol.60, No.3/4, pp. 122-124

Koria, S.C. and Pal, S. 1990, Model Study on Mixing Condition in Combined Blown Steelmaking Bath, Ironmaking and Steelmaking, Vol.17, No.5, Pp. 325-332

Koria, S.C. and George, A. 1988, Model Study on Mixing Condition in Combined Blown Steelmaking Bath, Ironmaking and Steelmaking, Vol.15, No.3, pp. 127-133

Kuo, J. T. and Wallis, G. B. 1988, Flow of Bubbles Through Nozzles. Int. J. Multiphase Flow. Vol.14, No.5, pp. 547-564

Lehner, T., Koros, P.J. and Ramachandran, V., 1991, International Symposium on Injection in Process Metallurgy, Published by TMS

Lehner, T., 1991, The Industrial Application of Injection Phenomena, International Symposium on Injection in Process Metallurgy, Edited by Lehner, T., Koros, P.J. and Ramachandran, V., Published by TMS, pp. 3-12

Lamb, H. 1945, Hydrodynamics. 6th edition. Dover. New York

Launder, B.E and Spalding, D. B., 1974, The Numerical Computation of Tutbulent Flows. Computer Methods in Applied Mechanics and Engineering, Vol.3, pp. 269-289

Lawn, C.J. 1971, The Determination of the Rate of Dissipation in Turbulent Pipe Flow, J. Fluid Mech. Vol.48, Part 3, pp. 477-505

Lee, S. L. and Srinivasan, J., 1978, Measurement of Local Size and Velocity Probability Density Distributions in Two-Phase Suspension Flows by Laser-Doppler Technique, Int. J. Multiphase Flow, Vol. 4, pp. 41-155

Lee, S. L. and Durst, F., 1982a, On the Motion of Particles in Turbulent Duct Flows, ibid., Vol. 8, No. 2, pp. 125-146

Lee, S. L. and Srinivasan, J., 1982, An LDA Technique for in situ Simultaneous Velocity and Size Measurement of Large Spherical Particles in Two-Phase Suspension Flow. ibid., Vol. 8, No.1, pp. 47-57,

Lee, S. L. and Cho, S. K., 1983, Simultaneous Measurement of Size and Two Velocity Components of Large Droplets in Two-Phase Flow by Laser Doppler Anemometry. Measuring Techniques in Gas-Liquid Two Phase Flow. Edited by Delhaye, J. M. and Cognet, G., Sprinter, New York, pp. 149-164

Lilley, D.G. and Rhode, D.L., 1982, A Computer Code for Swirling Turbulent Axisymmetrical Recirculation Flows in Practical Isothermal Combustor Geometries, NASA Report CR-3442, Grant NAG3-74

Lin, C. J., Peery, J. H. and Schowalter, W. R., 1970, Simple Shear Flow Around a Rigid Sphere: Inertia Effects and Suspension Rheology. J. Fluid Mech. Vol.44, pp. 1-17

Malin, M.R., 1983, Calculations of Intermittency in Self Preserving, Free Turbulent Jets and Wakes. Imperial College CFDU Report CFD/83/10, London

Malin, M.R. and Spalding, D.B., 1984, A Two-Fluid Model of the Turbulence and its Application to Heated Plane Jets and Wakes. PCH PhysicoChemical Hydrodynamics, Vol. 5, No. 5/6, pp. 339-362

Marie, J. L. and Lance, M. 1983, Turbulence Measurements in Two-Phase Bubbly Flows Using Laser Doppler Anemometry. Measuring Techniques in Gas-Liquid Two Phase Flow. Edited by Delhaye, J. M. and Cognet, G., Sprinter, New York, pp. 141-148

Marks, C. H., 1973, Measurements of Terminal Velocity of Bubbles Rising in a Chain. J. of Fluids Engineering. March, pp. 17-22

Martin, W. W., Abdelmessih, A. H., Liska, J. J. and Durst, F., 1981, Characteristics of Laser-Doppler Signals from Bubbles. Int. J. Multiphase Flow, Vol. 7, pp. 439-460

Mazumdar, D., 1989, On Effective Viscosity Models for Gas-Stirred Ladle Systems, Metall. Trans. B., Vol.20B, pp. 967-969

Mazumdar, D. and Guthrie, R.I.L., 1985, Hydrodynamic Modelling of Some Gas Injection Processes in Ladle Metallurgy Operations, Metall. Trans. B., Vol.16B, pp. 83-90

Mazumdar, D. and Guthrie, R.I.L., 1990, Scaling Equations for Gas Stirred Ladle Systems, Proceedings of the Sixth International Iron and Steel Congress, Vol. 1, Fundamentals, Nagoya, Japan, pp. 460-468

McKelliget, J.W., Cross, M. and Gibson, R.D., 1987, Appl. Math. Modelling, Vol.6, pp. 469-480

Meiron, D. I. 1989, On the Stability of Gas Bubbles Rising in an Inviscid Liquid, J. Fluid Mechanics, Vol.198, pp. 101-1114

Momii, K.,Jinno, K., Ueda, T. and Harada, 1986, Study on LDV Measurements and Turbulence Properties in Solid-Liquid Two-Phase Flow. Fluid Control and Measurement. Vol.2, pp. 807-812

Nakanishi, K., Fujii, T. and Szekely, J., 1975, Possible Relationship Between Energy Dissipation and Agitation in Steel Processing Operations, Ironmaking and Steelmaking, No.3, pp. 193-197

Noda, T., Nakayama, S. and Takahashi, M. 1990, Development of the Direct Current Arc Furnace, Proc. of Sixth Intern. Iron and Steel Congress, Nagoya, Japan, Vol.4, pp. 200-207

Oeters, F. 1989, Mixing with Heat and Mass Transfer in Metalurgical Systems, Steel Research, Vol.60, No.3/4, pp. 185-187

Ohba, K., Kishimoto, I. and Ogasawara, M., 1976a, Simultaneous Measurements of Local Liquid Velocity and Void Fraction in Bubbly Flows with a Gas Laser-Part I: Principle and Measuring Procedure. Technology Reports of the Osaka University, Vol.26, No.1328, pp. 547-556

Ohba, K., Kishimoto, I. and Ogasawara, M., 1976b, Simultaneous Measurements of Local Liquid Velocity and Void Fraction in Bubbly Flows with a Gas Laser-Part II: Local Properties of Turbulent Bubbly Flow. ibid. Vol. 27, No. 1358, pp. 230-238

Ohba, K., Yuhara, T. and Matsuyama, H., 1986, Simultaneous Measurements of Bubble and Liquid Velocities in Two-Phase Bubbly Flow Using LDV, Bulletin of JSME, Vol.29, No.254, Aug. 6, pp. 2487-2493

Pan, W. J., 1982, Principle of Fluid Dynamics. Machinery Industry Press, Beijing, China, p170

Parthasarathy, R.N. and Feath, G.M., 1987, Int. J. Multiphase Flow, Vol.13, No.5, pp. 699-716

Patankar, S.V., 1980, Numerical Heat Transfer and Fluid Flow, Hemisphere Publishing Corporation, New York

Pun, W. M. and Spalding, D. B., 1967, Proc. XVIII Int. Astronautical Congress, Pergamon Press, New York, Vol.3, pp. 3-21

Rodi, W., 1984, Turbulence Models and Their Application in Hydraulics, 2nd Edition, State-of-the-Art Paper, Presented by the IAHR-Section on Fundamentals of Division II: Experimental and Mathematical Fluid Dynamics, Delft, Netherland

Saffman, P. G., 1965, THe Lift on a Small Sphere in a Slow Shear Flow. J. Fluid Mech. Vol.22, pp. 385-400

Sahai, Y. and Guthrie, R.I.L., 1982a, Metall. Trans. B. Vol. 13B, pp. 125-127

Sahai, Y. and Guthrie, R.I.L., 1982b, Hydrodynamics of Gas Stirred Melts: Part II. Axisymmetric Flows, Metall. Trans. B. Vol. 20B, pp. 203-211

Sahajawalla, V., Castillejos, A.H. and Brimacombe, J.K., 1991, Basic Aspects of Gas Injection in Metallurgical Processes, International Symposium on Injection in Process Metallurgy, Edited by Lehner, T., Koros, P.J. and Ramachandran, V., Published by TMS, pp. 13-31

Salcudean, M., Low, C.H, Hurda, A. and Guthrie, R.I.L., 1983, Computation of Three-Dimensional Flow and Heat Transfer in Gas Agitated Reactors, Chem. Eng. Commun., Vol. 21, pp. 89-103

Sami, S. M., 1983, Bubble Rise Velocity in Stagnant and Flowing Liquids. Proc. of Inter. Conf. on the Physical Modelling of Multiphase Flow. Coventry, England, April 19-21, pp. 185-198

Sano, M. and Mori, K., 1980a, Dynamics of Bubble Swarms in Liquid Metal, Trans. ISIJ, Vol.20, pp. 668-673

Sano, M. and Mori, K., 1980b, Size of Bubbles in Energetic Gas Injection into Liquid Metals, Trans. ISIJ, Vol.20, pp. 674-685

Sano, M. and Mori, K., 1983, SCANINJECT III, Third Int. Conf. on Refining of Iron and Steel by Powder Injection, Lulea, Sweden, pp. 6:1-17

Schlebusch, W. and Hauck, A., 1989, New Developments of the Combined Blowing Steelmaking Process K-OBM and KMS. Modern Steel Processing, Preprints of Sessions at the 39th Canadian Chemical Engineering Conference, Edited by Kay, D.A.R. and Samson, D.H., Hamilton, Canada

Schlichting, H., 1979, Boundary-Layer Theory, McGraw-Hill,

Serizawa, A., Kataoka, I. and Michiyoshi, I., 1975a, Turbulent Structure of Air-Water Bubbly Flow--I. Measuring Techniques. Int. J. Multiphase Flow, Vol.2, pp. 221-233

Serizawa, A., Kataoka, I. and Michiyoshi, I., 1975b, Turbulent Structure of Air-Water Bubbly Flow--II. Transport Properties. ibid. pp. 235-246

Serizawa, A., Kataoka, I. and Michiyoshi, I., 1975c, Turbulent Structure of Air-Water Bubbly Flow--III. Transport Properties. ibid. pp. 247-259

Sevik, M and Park, S. H., 1973, The Splitting of Drops and Bubbles by Turbulent Fluid Flow. J. Fluid Eng., March, pp. 53-60

Sheng, Y. Y. and Irons, G. A., 1991, Combined Laser Doppler Anemometer and Electric Probe Diagnostic for Bubbly Two-Phase Flow. Int. J. Multiphase Flow, Vol.17, No.5, pp. 585-591

Sheng, Y. Y. and Irons, G. A., 1992a, Measurement of the Internal Structure of Gas-Liquid Plumes, Submitted to Metallurgical Transactions, B.

Sheng, Y. Y. and Irons, G. A., 1992b, Measurement and Modelling of Turbulence in the Gas/Liquid Two-Phase Zone of Gas Injection, To be submitted to Metallurgical Transaction, B.

Sheng, Y. Y. and Irons, G. A., 1992c, Turbulence Modelling of Plume Flows in a Gas Stirred Ladle, Proceedings of the 75th Steelmaking, 51st Ironmaking and 10th Process Technology Division Conferences, Apr. 5-8, Toronto, Canada

Sheng, Y. Y. and Irons, G. A., 1992d, Mathematical Modelling of the Plume Flow in a Gas Stirred Ladle with a Combined Eulerian and Lagrangian Scheme, To be submitted to Metallurgical Transaction, Vol. B.

Sheng, Y. Y. 1992, Determination of the Critical Break-up Bubble Size in an Air-Water System, Unpublished research notes.

Shuen, J.S., Chen, L.-D. and Feath, G.M., 1983, AIChE J., Vol.29, pp. 167-170

Shuen, J.S., Solomon, A.S.P., Zhang, Q.-F. and Feath, G.M., 1985, AIAA J. Vol.23, No.3, pp. 396-404

Simonin, O. and Viollet, P.L., 1988, On the Computation of Turbulent Two-phase Flows in the Eulerian Formulation, Turbulent Two-Phase Flow System, EUROMECH 234, Toulouse, France

Singh, R.P and Ghosh, D.N. 1990, Cold Model Study of Liquid-Liquid Mass Transfer in a Combined Blowing BOS Converter, Ironmaking and Steelmaking, Vol.17, No.5,

pp. 333-342

Southard, J. B., 1971, Lift Forces on Suspended Particles in Laminar Flow: Experiments and Sedimentological Interpretation. J. of Sedimentary Petrology. Mar. pp. 320-324

Standish, N. and He, Q.L. 1989, Drop Generation Due to an Impinging Jet and the Effects of Bottom Blowing in the Steelmaking Vessel, ISIJ Intern., Vol.29, No.6, pp. 455-461

Stone, H. A. and Leal, . G., 1989a, Relaxation and Breakup of an Initially Extended Drop in an Otherwise Quiescent Fluid, J. Fluid Mechanics, Vol.198, pp. 399-427

Stone, H. A. and Leal, . G., 1989b, The Influence of Initial Deformation on Drop Breakup in Subcritical Time-Dependent Flow at Low Reynolds Numbers, J. Fluid Mechanics, Vol.206, pp. 223-263

Sumer, B. M., 1984, Lift Forces on Moving Particles Near Boundaries. J. Hydraul. Eng. Vol.110, No.9, Sep. pp. 1272-1278

Sun, T-Y. and Feath, G.M., 1986a, Int. J. Multiphase Flow, Vol.12, No.1, pp. 99-114

Sun, T-Y. and Feath, G.M., 1986b, ibid., Vol.12, pp. 115-126

Sun, T-Y., Parthasarathy, R.N. and Feath, G.M., 1986, J. Heat Transfer, Vol.108, pp. 951-959

Szekely, J., 1979, Fluid Flow Phenomena in Metals Processing, Academic Press, New York

Szekely, J., Carlsson, G. and Helle, L. 1989, Ladle Metallurgy, Springer-Verlag, New York

Szekely, J., Evans, J.W. and Brimacombe, J.K., 1988, The Mathematical and Physical Modelling of Primary Metals processing Operations. John Wiley & Sons, New York

Szekely, J., Wang, H.J. and Kiser, K.M., 1976, Metall. Trans. B, Vol. 7B, pp. 287-295

Taylor, G.I., 1932, The Viscosity of a Fluid Containing Small Drops of Another Fluid, Proc. Roy. Soc. (London) Ser. A 138, pp. 41-48

Taylor, G.I., 1934, The Formation of Emulsions in Definable Fields of Flow. Proc. Roy. Soc. (London) Ser. A 157, pp. 501-523

Tennekes, H. and Lumley, J.L., 1972, A First Course in Turbulence, The MIT Press, Cambridge, Massachusetts.

Themelis, N.J., 1991, Injection Refining of Directly-Smelted Copper, International Symposium on Injection in Process Metallurgy, Edited by Lehner, T., Koros, P.J. and Ramachandran, V., Published by TMS, pp. 229-252

Themelis, N.J., Tarasssoff, P. and Szekely, J., 1969, Gas-Liquid Momentum Transfer in a Copper Converter. Trans. Metall. Soc., AIME 242, 5, pp. 2425-2433

Thomas, N.H., Auton, T. R., Sene, K. and Hunt, J.C.R., 1983, Int. Conf. on Physical modelling of Multiphase Flow, Apr.19-21, pp. 169-184

Tropea, C., 1986, Measurement Programs for Laser Doppler Anemometry, University of Waterloo

Tropea, C. and Struthers, D., 1987, Microprocessor Based On-Line Measurement System For LDA, Presented at Deutsche-Franzosisches Forschungs institute, Saint-Louis, May 18-20

Tsuji, Y. and Morikawa, Y., 1982, LDV Measurement of an Air-Solid Two-Phase Flow in a Horizontal Pipe. J. Fluid Mech. Vol.120, pp. 385-409

Tsuji, Y., Morikawa, Y. and Shiomi, H., 1984, LDV Measurement of an Air-Solid Two-Phase Flow in a Vertical Pipe. ibid. Vol.139, pp. 417-434

Tsuji, Y., Morikawa, Y. and Terashima, K., 1982, Fluid-Dynamic Interaction Between Two Spheres. Int. J. Multiphase Flow. Vol.8, No.1, pp. 71-82

Tsuji, Y., Morkawa, Y. and Mizuno, O., 1985, Experimental Measurement of the Magnus Force on a Rotating Sphere at Low Reynoulds Numbers. J. Fluids Eng. Trans. ASME, VOl.107, No.4, Dec. pp. 484-488

Ueda, T., Jinno, K., Momii, K. and Nakajima, Y., 1986, Experimental Study on Turbulence in Solid-Liquid Two-Phase Flow with Laser Doppler Anemometer. Technol. Rep. Kyushu Univ. (Japan). Vol.59, No.6, pp. 787-792

Wallis, G.B., 1969, One Dimensional Two-Phase Flow, McGraw-Hill, New York

Walter, J. F. and Blanch, H. W., 1986, Bubble Breakup in Gas-Liquid Bioreactors: Breakup in Turbulent Flows, The Chem. Eng. J. 32, B7-B17

Walters, J. K. and Davidson, J. F., 1962a, The Initial Motion of a Gas Bubble Formed in an Inviscid Liquid, Part.1, The Two-Dimensional Bubble, J. Fluid Mechanics, Vol.12, p408

Walters, J. K. and Davidson, J. F., 1962b, The Initial Motion of a Gas Bubble Formed in an Inviscid Liquid, Part.2, The Three-Dimensional Bubble and the Toroidal Bubble, J. Fluid Mechanics, Vol.12, p408

Wang, C. Y. and Calabrese, R. V., 1986, Drop Breakup in Turbulent Stirred-Tank Contactors, Part II: Relative Influence of Viscosity and Interfacial Tension, AICHE J., Vol.32, No.4, pp. 667-676

Wang, S. K., Lee, S. J., Jones, Jr. O. C. and Lahey, Jr. R. T., 1990, Statistical Analysis of Turbulent Two-Phase Pipe Flow, J. Fluids Eng., Vol.112, 89-95

Wang, J. E., Lee, S.J., Jones Jr, O. C. and Lahey Jr, R. T., 1987, 3-D Turbulence Structure and Phase Distribution Measurements in Bubbly Two-Phase Flows. Int. J. Multiphase Flow, Vol.13, No.3, pp. 327-343

Weber, R., Boysan, F., Ayers, W. H. and Swithenbank, J., 1984, Simulation of Dispersion of Heavy Particles in Confined Turbulent FlowsAIChE J., Vol.30, pp.

490-492

Welle, R. VonDer, 1985, Int. J. Multiphase Flow, Vol.11, No.3, pp. 317-345

Wright, T. 1991, Development of KOBM Practice and Increased Scrap Use, Proc. of Sixth Intern. Iron and Steel Congress, Nagoya, Japan, Vol.3, pp. 86-93

Wygnanski, I. and Fiedler, H., 1969, Some Measurements in the Self-preserving Jet, J. Fluid Mech., Vol.38, Part 3, pp. 577-612

Yamamoto, T. and Ishii, T., 1987, Effect of Surface Active Materials on the Drag Coefficients and Shapes of Single Large Gas Bubbles. Chem. Eng. Sci. Vol.42, No.6, pp. 1297-1303

Yih, C. H., 1980, Stratified Flows, 2nd Edition. Academic Press, New York

Zhao, Y.-F. and Irons, G.A. Irons, 1989, The Breakup of Bubbles into Jets during Submerged Gas Injection, submitted to Metall. Trans. B.

Zun, I., Richter, H. and Wallis, G. B., 1975, The Transverse Migration of Bubbles in Vertical Two-Phase Flow. Dartmouth College, Thayer School of Engineering, Hanover, NH